Experimental studies on the formation of particulate matter in a shock tube

Letícia Carneiro Piton

UNIVERSITÉ D'ORLÉANS

ÉCOLE DOCTORALE
ÉNERGIE, MATERIAUX, SCIENCES DE LA TERRE ET DE L'UNIVERS

Institut de Combustion, Aérothermique, Réactivité et Environnement, CNRS

THÈSE présentée par :

Letícia CARNEIRO PITON

soutenue le : **05 décembre 2022**

pour obtenir le grade de : **Docteur de l'Université d'Orléans**

Discipline/ Spécialité : Énergétique, génie des procédés

Experimental studies on the formation of particulate matter in a shock tube

THÈSE dirigée par :

M. COMANDINI Andrea	Chercheur, ICARE-CNRS, Orléans, France

RAPPORTEURS :

M. PICAUD Sylvain	Directeur de Recherche, UTINAM-CNRS, Besançon, France
M. MATHIEU Olivier	Professeur Associé de Recherche, Texas A&M University, États-Unis

---

JURY :

M. COMANDINI Andrea	Chercheur, ICARE-CNRS, Orléans, France
Mme CHAUMEIX Nabiha	Directrice de Recherche, ICARE-CNRS, Orléans, France
M. PICAUD Sylvain	Directeur de Recherche, UTINAM-CNRS, Besançon, France
M. MATHIEU Olivier	Professeur Associé de Recherche, Texas A&M University, États-Unis
Mme CESSOU Armelle	Directrice de Recherche, CORIA-CNRS, Saint-Étienne-du-Rouvray, France - **Présidente du jury -**

European Research Council
Established by the European Commission

Letícia CARNEIRO PITON

Études expérimentales sur la formation de particules dans les tubes à choc

Résumé : La combustion joue un rôle essentiel dans les secteurs de l'industrie, des transports et de la production d'énergie. Les procédés impliqués dans la conversion d'énergie peuvent conduire à la production et à l'émission de polluants, dont les particules fines (PMs). La chimie de la formation des PMs est un processus complexe, multi-étapes et multi-phases, et malgré des décennies d'études, nos connaissances sont encore incomplètes en raison de la carence de résultats expérimentaux et des limitations des techniques expérimentales. L'objectif de cette thèse est la caractérisation expérimentale de la formation de suie à partir de différentes molécules et mélanges de carburant, dans des conditions typiques rencontrées dans les dispositifs de combustion modernes. Tout d'abord, une nouvelle installation expérimentale basée sur des techniques de tube à choc et de laser a été développée. Les principaux défis et solutions seront abordés. Des techniques d'extinction laser ont ensuite été utilisées afin de dériver des paramètres, tels que les densités optiques, les délais d'induction et les taux de croissance de la suie, à partir de la pyrolyse du toluène, du benzène et du cyclopentène avec et sans l'ajout d'éthylène, d'acétylène, de propène et de propyne. Les profils en fonction de la température de réaction seront comparés pour déduire la tendance des différents combustibles à produire de la suie. La suie a également été collectée pendant les expériences pour des analyses ultérieures par microscopie électronique à transmission, qui ont fourni des informations sur le diamètre et la morphologie des particules de suie ainsi que sur leur structure et leur micro texture. La base de données expérimentale constitue une référence essentielle pour le développement de modèles cinétiques détaillés pour la chimie des particules de suie. En outre, une partie de l'étude s'est concentrée sur l'utilisation d'une installation différente de tube à choc pour la spéciation des molécules de HAP (précurseurs de la suie) provenant de combustibles spécifiques d'intérêt, en particulier le n-heptane et le cyclopentène. Les analyses du modèle cinétique seront également présentées.

Mots clés : tubes à chocs, pyrolyse, formation de suie, diagnostics optiques, extinction laser, rendement en suie, densités optiques, délais d'induction, taux de croissance de la suie, analyse TEM, HAPS, toluène, benzène, cyclopentène, n-heptane, acétylène, éthylène, propène, propyne.

Experimental studies on the formation of particulate matter in a shock tube

Summary : Combustion plays a vital role in the industrial, transportation, and power generation sectors. The processes involved in the energy conversion can lead to pollutant production and emissions, including particulate matters (PMs). The chemistry of PM formation is a complex multi-step, multi-phase process, and despite decades of studies, our knowledge is still incomplete due to the lack of experimental results and the limitations of the experimental techniques. The aim of this thesis is the experimental characterization of soot formation from different fuel molecules and mixtures, at typical conditions encountered in modern combustion devices. First, a new experimental facility based on shock tube and laser-based techniques was developed. The main challenges and solutions will be addressed. Laser extinction techniques were then employed in order to derive parameters, such as optical densities, induction delay times, and soot growth rates, from the pyrolysis of toluene, benzene, and cyclopentene with and without the addition of ethylene, acetylene, propene, and propyne. Profiles as function of the reaction temperature will be compared to derive the tendency of the different fuels to produce soot. The soot was also collected during the experiments for subsequent analyses by transmission electron microscopy, which provided information on the diameter and morphology of the soot particles and their structure and micro texture. The experimental database constitutes an essential reference for the development of detailed kinetic models for soot particle chemistry. In addition, part of the study was focused on the use of a different shock tube facility for the speciation of soot precursor PAH molecules from specific fuels of interest, in particular n-heptane and cyclopentene. The kinetic model analyses will also be presented.

Keywords: shock tubes, pyrolysis, soot formation, optical diagnostics, laser extinction, soot yield, optical densities, induction delay times, soot growth rate, TEM analysis, PAHs, toluene, benzene, cyclopentene, n-heptane, acetylene, ethylene, propene, propyne.

ICARE – CNRS
1C av de la Recherche Scientifique
CS 50060
45071 ORLÉANS Cedex 2

Résumé

La combustion joue un rôle essentiel dans les secteurs de l'industrie, des transports et de la production d'énergie. Cette réaction complexe peut produire de particules de suies. Les préoccupations concernant les effets de la pollution, la santé publique et la qualité de l'environnement ont conduit les gouvernements à réglementer le niveau des émissions des particules suie. Leur formation est un processus complexe qui passe par de nombreuses étapes chimiques et physiques. Les hydrocarbures aromatiques polycycliques (HAP) de grand poids moléculaire sont formés à partir d'espèces aromatiques primaires mettant en jeu leur dimérisation suivie de processus de croissance chimique qui conduisent à la formation de particules précurseurs de suie (particules primaires). Ces précurseurs subissent simultanément une coagulation et une croissance de surface pour former les agrégats finaux. Finalement, lorsque les particules de suie deviennent suffisamment grandes, l'agglomération commence à se produire, donnant lieu à des agrégats macroscopiques en forme de chaîne appelés suie mature. Par conséquent, le but de cette thèse est la caractérisation expérimentale de la formation de suie dans un tube de choc à partir de différentes molécules et mélanges de combustibles, dans des conditions représentatives de celles rencontrées dans les dispositifs de combustion modernes, par le biais de techniques optiques laser. La base de données expérimentales constitue une référence essentielle pour le développement de modèles cinétiques détaillés pour la chimie des particules de suie. Une seconde partie de l'étude s'est concentrée sur l'utilisation d'une seconde installation mettant en œuvre un tube de choc dédié à la spéciation des molécules précurseurs de suie formées lors de la décomposition de combustibles spécifiques d'intérêt pour ce travail.

La spéciation des HAP est réalisée pour la pyrolyse du n-heptane et du cyclopentène, ainsi qu'un modèle cinétique pour les deux combustibles. Concernant la partie solide de la suie, des expériences sur le toluène, le benzène et le cyclopentène ont été réalisées avec et sans ajout d'éthylène, d'acétylène, de propène et de propyne. Des techniques d'extinction laser ont été employées afin de dériver des paramètres, tels que les densités optiques, le rendement en suie, les délais d'induction et le taux de croissance de la suie. La dernière étape de l'analyse a consisté à réaliser une microscopie électronique à transmission (MET), qui a fourni des informations sur le diamètre et la morphologie des particules de suie ainsi que sur leur structure et leur micro texture.

Les résultats obtenus dans ce travail peuvent servir pour les futurs développements de modèles concernant des combustibles et des substituts plus complexes, ainsi que comme base pour la construction de codes de suie pour la simulation de la formation de particules dans les applications de combustion.

Introduction

Le terme "matière particulaire" est utilisé pour décrire un mélange complexe de particules et de gouttelettes liquides extrêmement petites. Elles sont composées d'un certain nombre de composants, dont des acides, des produits chimiques organiques, de suie ou de poussière [1], et peuvent avoir des sources naturelles ou anthropiques. Concernant la suie, elle est définie comme le noyau carboné des particules issues de la combustion incomplète des combustibles. Elle est composée d'agrégats de centaines ou plus de sphérules primaires, appelées particules primaires, presque sphériques.

Le principal problème lié à la présence d'émissions de matière particulaire en suspension dans l'atmosphère est associé au fait qu'elles sont généralement identifiées comme responsables d'impact sur la santé humaine, tels que les problèmes respiratoires, le cancer du poumon et les maladies cardio-pulmonaires [2]. Les effets négatifs sur l'environnement ont également été clairement identifiés [3]–[7]. Ces effets néfastes et la nécessité d'y remédier a été à l'origine de l'intérêt de la communauté scientifique pour l'investigation de la chimie de la formation des suies. L'objectif principal de la recherche dans le domaine de la chimie des particules est l'amélioration des processus de combustion dans tous les systèmes pratiques : moteurs diesel et à essence, turbines à gaz, brûleurs pour chaudières domestiques ou industrielles. Mais aussi, le contrôle des émissions de suie qui nécessitera une meilleure compréhension de la formation et de l'oxydation de la suie dans une variété de conditions de combustion. Cependant, la formation de la suie est encore mal comprise malgré les progrès récents des techniques expérimentales et numériques.

Pour comprendre les processus complexes de formation de la suie, des modèles adéquats sont nécessaires. Ceux-ci doivent être testés en comparant aux mesures des concentrations de particules, des distributions de tailles de particules, des fractions volumiques de suie et d'autres paramètres dans des environnements bien contrôlés. Il est important que ces paramètres soient mesurés in situ par des méthodes non intrusives. Les techniques optiques, en particulier les méthodes de diagnostic par laser, sont les plus adaptées à l'objectif indiqué. En plus d'être non-intrusives, elles ont de hautes résolutions spatiale et temporelle, ce qui est particulièrement utile dans les études de la formation de la suie dans des conditions diluées, où les non-idéalités peuvent être réduites.

Les tubes à choc sont des dispositifs expérimentaux idéaux pour les études cinétiques où le comportement chimique est isolé des processus physiques. Il a été prouvé que l'utilisation de tubes à choc apporte des contributions importantes dans le domaine de la cinétique chimique, car elle permet de travailler dans des conditions contrôlées, à des conditions de température et de pression similaires à celles des systèmes pratiques.

Etude bibliographique

La formation de la suie est un processus complexe, qui passe par de nombreuses étapes chimiques et physiques. La suie constitue l'élément carboné des émissions provenant de la combustion des carburants. Pour caractériser les propriétés de la suie, plusieurs paramètres sont utilisés : i) la fraction volumique de la suie, f_v, qui représente le volume occupé par les particules de suie dans une unité de volume (cm^3/cm^3). Ce paramètre est fonction des propriétés optiques des particules de suie, pour lesquelles on note une divergence importante dans la littérature, notamment en ce qui concerne les particules primaires. Ainsi la densité optique, D_{633}, est souvent employée pour éviter les hypothèses concernant les propriétés optiques des espèces condensées ; ii) le délai d'induction, τ_{ind}, le temps nécessaire à l'apparition des premiers noyaux solides ; iii) le rendement en suie, Y (%), l'efficacité de la conversion du carbone du combustible gazeux en suie ; iv) le diamètre moyen de la particule primaire de suie, d ; et v) la structure interne des particules primaires de suie.

Bien que la chimie des suies ait été largement étudiée au cours des dernières décennies, certains des mécanismes primaires de la formation, de la croissance et de l'oxydation de la suie demeurent incertains. La suie naissante est généralement considérée comme une particule sphérique de petite taille (1-10 nm) produites à partir de grandes espèces organiques de HAP dont le rapport hydrogène/carbone est relativement élevé. La suie mature, cependant, est composée de particules primaires de 10-50 nm de diamètre avec des structures fines similaires au noir de carbone et/ou graphite polycristallin [8].

Le schéma présenté dans la **Figure 1.1** montre que la formation de la suie est un processus complexe, qui passe par de nombreuses étapes chimiques et physiques. Il est généralement divisé en deux parties : phase gazeuse et solide [9], [10]. Les principales étapes de la phase gazeuse sont la pyrolyse des molécules de combustible suivie de la formation de structures aromatiques et d'hydrocarbures lourds. La phase solide comporte quatre étapes au total : la naissance des particules, les réactions de croissance de surface, la coagulation et l'agglomération.

Afin d'étudier les mécanismes de formation de la suie à partir d'hydrocarbures dans différentes conditions expérimentales, plusieurs dispositifs expérimentaux peuvent être utilisés. Les principaux réacteurs de laboratoire sont les flammes, les moteurs, les machines à compression rapide, les réacteurs parfaitement agités et les tubes à choc. En ce qui concerne les carburants, les hydrocarbures aromatiques sont des composants majeurs des combustibles de transport à base de pétrole. Ils sont largement utilisés comme composants majeurs des carburants de substitution pour l'essence, le diesel et le kérosène et jouent un rôle crucial en tant qu'additifs antidétonants pour améliorer l'indice d'octane des carburants, parce qu’ils ont une

grande résistance à l'auto-inflammation [11]. Ils sont également les principaux éléments constitutifs de la formation des HAP typiques, les principaux précurseurs de la suie [12].

Les phénomènes de combustion peuvent être étudiés et caractérisés par techniques de diagnostic optique. Les diagnostics laser sont considérés comme des techniques non intrusives. Elles permettent d'effectuer des mesures à distance, in situ (sur le lieu de la mesure), précises dans l'espace et dans le temps, de paramètres chimiques importants. Le sondage laser présente également plusieurs avantages. Les techniques sont à distance et, presque toujours, non perturbatrices. La température et les concentrations des espèces sont mesurées directement et elles sont caractérisées par de hautes résolutions spatiale et temporelle simultanées. Un autre type d'analyse des suies est l'analyse par microscopie électronique à transmission (MET), qui permet de visualiser la texture de la suie et de déterminer la taille des particules et leur structure interne [13], [14]. Une structure caractéristique avec des plans carbonés (cristallites) peut être décrite. Ces cristallites sont empilées en unités structurelles de base, orientées de manière parallèle dans la couronne extérieure de la suie et de manière aléatoire dans le cœur de la suie.

Etude expérimentale

Le tube à choc est un réacteur idéal. Dans ce dispositif, une onde de choc plane est produite par l'éclatement soudain d'un diaphragme, qui sépare un gaz à haute pression d'un gaz à plus basse pression. Grâce au passage d'une onde de choc, le mélange étudié est amené presque instantanément à une température et une pression connue et contrôlée, jusqu'à des valeurs élevées typiques des moteurs à combustion interne [15], [16]. Le premier tube à choc utilisé dans cette thèse est visible sur la **Figure 3.4**. Il fonctionne en une seule impulsion en raison de la présence d'un réservoir de décharge, qui empêche le réchauffement du mélange de gaz d'essai par des réflexions multiples d'ondes de choc. Deux chromatographes en phase gazeuse et un spectromètre de masse sont couplés au tube à choc afin d'effectuer l'analyse des gaz après le choc.

Le deuxième tube à choc utilisé pour l'étude est illustré sur la **Figure 3.6**. Son principe de fonctionnement est similaire au premier, cependant, celui-ci ne dispose pas d'un réservoir de décharge et n'est pas équipé d'un système d'analyse. Des diagnostics optiques sont effectués dans ce dispositif expérimental. Afin d'effectuer simultanément des mesures d'extinction et de diffusion Rayleigh multi-angle, cinq ports optiques comprenant des fenêtres en quartz sont installés sur le tube à différents angles : 0º, 90º, 180º, 225º et 335º, dans un plan orthogonal à l'axe du tube. L'angle 0º est l'angle d'injection, tandis que les autres sont utilisés pour capturer les signaux. Ils permettent le passage des faisceaux laser et la collecte du faisceau transmis ainsi que des radiations diffusées. Il correspond à l'axe horizontal du faisceau laser d'injection (pour l'extinction et la diffusion Rayleigh). Le 180° correspond à l'axe horizontal des faisceaux directs transmis.

Le 90° correspond à l'axe vertical supérieur. Les 225° et 335° correspondent à des axes symétriques à l'axe vertical. Tous les axes des fenêtres se croisent sur l'axe du tube à choc.

Plusieurs dispositions optiques ont été développées afin de construire une nouvelle méthode pour mesurer l'extinction simultanément avec la diffusion Rayleigh. Au total, quatre approches différentes ont été établies dans la disposition optique.

Première approche - les fibres optiques

La **Figure 3.11** montre un schéma de la première disposition optique développée, où toutes les fibres optiques sont représentées par des flèches orange. Les mesures d'extinction ont été effectuées avec une diode laser à 808 nm, ou un laser Hélium:Néon de 632,8 nm, selon la configuration. Les mesures de diffusion Rayleigh ont été effectuées avec un laser à solide pompé par diode à 532 nm (Laser Quantum, OPUS 532) délivrant jusqu'à 4 Watts. Les deux faisceaux subissent des réflexions à travers les miroirs et sont ensuite superposés via le miroir dichroïque. Une lentille focalise les faisceaux sur le disque rotatif d'un hacheur mécanique (ou chopper, en anglais) qui module l'intensité du faisceau à 40 kHz. Après le chopper, les faisceaux sont collimatés avec autre lentille et injectés dans une fibre optique multimode φ 105 µm connectée à un support de fibre. L'autre extrémité de la fibre optique est connectée à un support de fibre identique fixé à la fenêtre d'entrée (0°) du tube à choc. Les faisceaux sont polarisés horizontalement après traversée d'un cube polariseur, et sont ensuite focalisés sur l'axe du tube à choc avec une lentille convergente de 40 mm de longueur focale.

Les quatre montages optiques montés sur le port fenêtre de 180°, 90°, 225° et 335° sont identiques. Ils consistent en l'assemblage d'une lentille convergente, d'un support de fibre optique et d'une fibre optique multimode φ 200µm. Il est à noter que le support de la fibre comprend une lentille de focalisation. Les faisceaux transmis à 180º sont collimatés à travers un collimateur à fibre et divisés avec un miroir dichroïque, et chaque longueur d'onde passe par son filtre respectif pour finalement atteindre deux photodétecteurs. Les signaux mesurés sont collectés, enregistrés et visualisés sur un oscilloscope. Chacun des trois rayonnements de diffusion de Rayleigh collectés aux 3 angles, est collimaté à la sortie de la fibre optique, et filtré avec un filtre passe-bande de 1 nm de large. Ce rayonnement filtré est ensuite détecté par un tube photomultiplicateur et le signal résultant est collecté, enregistré et visualisé sur un oscilloscope. Afin de réduire et d'éviter toute réflexion du faisceau 532 à l'intérieur du tube à choc, les deux fenêtres et les lentilles sur le 0° et le 180° ont un revêtement antireflet.

Afin de garantir un bon alignement et une bonne superposition des différents volumes de sonde collectés aux différents angles, un outil spécifique a été conçu (**Figure 3.12**). La deuxième étape après l'alignement a consisté à effectuer des tests préliminaires dans l'argon, afin de vérifier la stabilité du dispositif

expérimental (**Figure 3.13**). Des mesures qualitatives ont été retirés de la première approche pour 0,1% de toluène dilué dans de l'argon (**Figure 3.14**). Les signaux bruts de diffusion et l'auto-émission ont également été mesurés lors de cette approche (**Figure 3.15**). Cependant, cette approche n'a pas été poursuivie en raison du manque de répétabilité des expériences et de la qualité du signal. Après plus de 200 chocs, les signaux n'étaient pas cohérents d'un choc à l'autre malgré les efforts pour améliorer l'alignement entre les différents composants (y compris l'injection dans la fibre optique, la focalisation du faisceau au centre du tube de choc, l'ajustement des paramètres des supports) et les tests effectués en remplaçant certains des composants par d'autres (par exemple, le diamètre des fibres). De plus, malgré le fait que les supports sont tous reliés de manière rigide au HPST, de grandes vibrations dans la ligne de base du signal ont pu être observées, ce qui aurait grandement affecté la qualité des mesures.

Deuxième approche - laser infrarouge modifié

La deuxième approche n'est qu'une évolution de la première, comme le montre la **Figure 3.17**. Dans cette configuration, la diode laser a été remplacée par un laser He:Ne de 15 mW et 632,8 nm. Les filtres passe-bande et les miroirs dichroïques associés ont également été modifiés. Concernant les résultats préliminaires, la **Figure 3.18** présente les mesures d'extinction résolues en temps à deux longueurs d'onde différentes pour 0,1% de toluène dilué dans l'argon. La **Figure 3.19** montre les données brutes de diffusion et l'auto-émission à de deux chocs à conditions similaires. On peut voir que la forme et l'amplitude sont tout à fait les mêmes, ce qui signifie que le signal de diffusion mesuré est dominé par l'auto-émission. Ceci peut être interprété par le fait que la densité de particules est trop faible ou que le laser est mal aligné. Néanmoins, nous pouvons observer des signaux de diffusion de particules à 225° et 335° pour t > 2ms, alors qu'il n'y en a pas à 90°. Cela peut s'expliquer par un mauvais alignement de la collection à cet angle. Ce type de différences dans les signaux observés a été fait pour différents tests, montrant l'importance de l'effet des vibrations. L'occurrence et l'amplitude de ces vibrations mécaniques ont été étudiées, en particulier les vibrations transmises sur les ports de fenêtre et les ports de fibre. Pour cette raison, seules des mesures d'extinction ont été envisagées, sans utiliser de fibre optique.

Troisième approche - extinction seule sans fibre optique

La **Figure 3.20** présente la troisième approche optique utilisée. Le faisceau laser He:Ne est injecté directement à travers la fenêtre du tube à choc et l'intensité transmise est filtrée puis focalisée sur une photodiode. Depuis que l'hacheur a été supprimé, le signal brut d'extinction n'est plus modulé, comme on peut le voir sur la **Figure 3.21** (0.1% de toluène dilué dans de l'Argon). Il a été observé un aplatissement très possible de l'intensité laser transmise avant l'apparition de l'onde de choc. Deux problèmes ont été identifiés. Premièrement, le pic à t = 0s, qui est apparu dans plusieurs chocs. Malgré la focalisation du

faisceau sur la partie sensible de la photodiode, la déflexion optique du faisceau induite par la chute de pression était suffisante pour déplacer le faisceau hors de la partie sensible. Le deuxième problème concerne les fluctuations restantes observées sur le signal d'extinction juste après le choc pour t > 0. Des analyses complémentaires ont été réalisées pour cette approche. La fraction volumique de la suie a été calculée (**Figure 3.22**). Les signaux montrent encore certaines vibrations qui pourraient affecter les résultats, dans ce cas provenant du fonctionnement du tube de choc. Afin d'améliorer la qualité des données, une nouvelle structure soutenant le tube de choc lui-même a été conçue (quatrième approche).

Quatrième approche - nouvelle structure ST pour réduire les vibrations

La configuration finale comprend une nouvelle structure pour solidariser le tube à choc avec le sol, que l'on peut voir sur la **Figure 3.23**. La structure maintient le tube dans deux positions différentes, du côté de la haute pression et à la section d'extrémité. Il est constitué de plaques rigidement fixées aux brides du tube de choc, de poteaux verticaux reliés à de grandes bases pour répartir le poids sur la surface du sol, et de poids métalliques modulables. Le poids total des structures est d'environ 1,5 tonne du côté haute pression et d'une tonne du côté basse pression. Ces poids supplémentaires augmentent l'inertie du système et empêchent les vibrations du tube.

Pour confirmer que les dispositifs avec fibres optiques pouvaient également être sources de vibrations, une comparaison a été effectuée (**Figure 3.24**). Deux chocs à l'argon ont été réalisés dans des conditions similaires, sans et avec fibres optiques (**Figure 3.25**). Cette comparaison fait bien apparaître des modulations qui trouvent leur origine dans les vibrations perçues par les montures avec fibre optique. Une approche finale a été conçue sans les fibres en place, **Figure 3.26**. Dans cette solution, les photomultiplicateurs sont montés directement sur la structure du tube de choc. Il est également important de souligner que le faisceau rouge ne passe pas par l'hacheur, ce qui signifie que le signal n'est plus modulé. Le temps d'observation a également changé par rapport aux tests présentés dans les sections précédentes.

Concernant les résultats préliminaires, la **Figure 3.28** montre la fraction volumique de la suie en fonction du temps de six chocs de 0,1% de toluène dans une gamme de température de 1539 à 1991 K et P_5 = 18 bar. De petites vibrations peuvent encore être détectées, en particulier aux temps les plus longs ; cependant, elles sont négligeables par rapport aux niveaux de signal. Des signaux de diffusion ont également été mesurés (**Figure 3.29**).

L'analyse MET

La **Figure 3.30** montre un schéma de l'échantillonnage de particules de suie. Après avoir été générées, les suies se dépose sur les parois du tube à choc. Pour cette raison, la paroi d'extrémité est retirée et placée dans

un bécher avec 1,5 ml d'éthanol ou d'acétonitrile. Le bécher est placé dans un bain à ultrasons pendant trois minutes pour que les suies se détache de la paroi. La solution est ensuite transportée au laboratoire "Interfaces, Confinement, Matériaux et Nanostructures - ICMN" du CNRS à Orléans pour réaliser des analyses par MET et capturer les images de l'organisation des particules de suies (texture et micro-structure).

Résultats et discussions

Dans ce chapitre, les résultats des mesures effectuées dans les deux tubes à choc sont présentés.

Tube à choc à impulsion unique de haute pureté

Un des objectifs de cette thèse est de fournir des bases de données expérimentales sur la chimie de la formation des HAP dans les conditions typiques rencontrées dans les dispositifs de combustion modernes. Sur la base de ces résultats expérimentaux, il est proposé de développer un modèle cinétique détaillé et complet décrivant la formation des HAP qui peut être utilisé comme base pour des modèles de prédiction de suie améliorés. Deux combustibles ont été étudiés : n-heptane et cyclopentène.

Le n-heptane est fréquemment utilisé comme substitut mono-composant du diesel et comme carburant de référence pour l'essence. Il se dissocie en produits hydrocarbonés, principalement C2, C3 et C4, à haute température. Ces composés se polymérisent ensuite pour créer des espèces à forte teneur en carbone comme les HAP. La pyrolyse de l'heptane a été étudiée de manière approfondie afin de révéler les processus qui conduisent à la décomposition et aux processus ultérieurs de croissance du poids moléculaire. Trois concentrations d'heptane ont été investiguées. Cependant, seule la décomposition du combustible à 2000 ppm sera présentée, les deux autres sont présentées en annexe. En général, le modèle est en mesure de reproduire, quantitativement en termes de fractions molaires et domaine de température, la décomposition et la formation des espèces de pyrolyse mesurées en tenant compte des incertitudes expérimentales. Les analyses des taux de production (ROP) et les analyses de sensibilité sont utilisées pour obtenir une compréhension de la chimie de la dégradation de l'heptane et de la croissance des aromatiques.

La **Figure 4.1** présente les profils de fraction molaire expérimentale et simulée du n-heptane et des espèces acycliques en C1-C6. Le modèle cinétique prédit les profils de conversion du combustible mesurés ainsi que la formation de petites espèces intermédiaires dans les différents cas étudiés. Le n-heptane est principalement consommé par la réaction de scission des liaisons C-C, qui produit des radicaux n-propyle (NC_3H_7) et 1-butyle (PC_4H_9), et par les réactions d'absorption de l'hydrogène, qui produisent des radicaux 1-, 2-, 3- et 4-heptyle. Les autres réactions de fission des liaisons C-C qui produisent des radicaux méthyle

et 1-hexyle, ainsi que des radicaux éthyle et 1-pentyle, ne contribuent que légèrement à la décomposition thermique du n-heptane.

La **Figure 4.3** montre les profils de fraction molaire expérimentaux et simulés de plusieurs hydrocarbures mono-aromatiques (HAM) courants et de HAP bicycliques et tricycliques avec une concentration de départ de 2 000 ppm. Le modèle actuel reproduit avec succès les tendances expérimentales pour les formes et les concentrations maximales pour toutes les aromatiques. Grâce aux études ROP, les principales voies de production des aromatiques sont discutées. Cependant, la concentration plus élevée de n-heptane favorise la synthèse de plus d'aromatiques en raison de la quantité accrue de carbone dans le système réactionnel. Les réactions qui clarifient la création de ces aromatiques sont analogues dans tous les systèmes réactionnels. La formation du premier cycle aromatique est l'un des principaux sujets abordés dans les études cinétiques de la consommation de carburant acyclique dans des conditions riches en carburant ou pyrolytiques. Les espèces HAM détectées dans la pyrolyse de l'heptane comprennent le benzène, le toluène, le phénylacétylène, le styrène et l'éthylbenzène.

Concernant le cyclopentène, l'intérêt pour ce carburant provient de son rôle de précurseur d'intermédiaires C5, dont le cyclopentadiène, dont la chimie a un impact important sur la production de HAPs et de suie. La première étape de cette étude consiste à examiner la réactivité de décomposition de 108 ppm de CYC_5H_8 (326 ppm de CYC_5H_8 dans l'annexe) et la spéciation des petits intermédiaires, puis la production d'espèces aromatiques, du plus simple benzène aux plus grands HAP. La **Figure 4.7** montre les profils de fraction molaire du combustible et des espèces C0-C5 en fonction de T_5, y compris les mesures et les simulations utilisant le modèle actuel et les différents modèles cinétiques de la littérature [17], [18]. Le modèle actuel décrit avec précision la réactivité du combustible et la formation du produit principal en ce qui concerne le domaine de température et les concentrations maximales. Selon l'analyse du taux de production, le CYC_5H_8 est principalement consommé par les processus de déshydrogénation et d'isomérisation par ouverture de cycle, qui entraînent la génération de C_5H_6 et de LC_5H_8, respectivement. Les petits hydrocarbures sont formés par d'autres réactions des petits produits de fragmentation, par la consommation d'intermédiaires en C5 ou par des interactions directes du combustible avec les atomes d'hydrogène. La **Figure 4.8** présente les profils de fraction molaire des HAM et des HAP en fonction de T_5. Dans les fenêtres de température et les concentrations maximales, le modèle actuel peut bien reproduire la spéciation des aromatiques. La réaction de C_5H_5 avec de petites espèces conduit à la formation de plusieurs HAM dont le benzène, le toluène, le phénylacétylène et le styrène.

L'objectif de la deuxième partie de l'étude de la pyrolyse du cyclopentène est de démontrer comment les schémas de spéciation sont affectés par l'ajout de C_2H_2. Tout d'abord, l'influence de l'abondant C_2H_2 sur la réactivité de décomposition du CYC_5H_8 est examinée. La **Figure 4.10** montre les concentrations de

combustible dans la pyrolyse du cyclopentène pur et du cyclopentène + C_2H_2 en fonction de la température post-choc. Les voies de production des petits hydrocarbures sont identiques à celles du CYC_5H_8 pur, tant sur le plan qualitatif que quantitatif (**Figure 4.11**). Cependant, l'ajout d'acétylène augmente légèrement la formation de propyne et d'allène à haute température. De plus, la présence de C_2H_2 dans le mélange initial contribue à l'augmentation de la fraction molaire de C_4H_2 à des températures élevées. La **Figure 4.12** présente les mesures quantitatives des composés aromatiques et les simulations correspondantes. Les deux ensembles de données expérimentales ne montrent aucune divergence évidente dans la température de début et les fractions molaires maximales de C_6H_6 et de $C_6H_5C_2H_3$. Par conséquent, le C_2H_2 supplémentaire n'a aucune influence sur la formation de ces hydrocarbures. En revanche, l'ajout de C_2H_2 à CYC_5H_8 amplifie les concentrations de $C_6H_5C_2H$ et de 1-éthynylnaphtalène. Le toluène commence à se former à une température relativement plus basse dans la copyrolyse.

Tube à choc chauffé

L'un des objectifs de cette thèse est de développer et d'évaluer la technique d'extinction pour étudier la formation de suie derrière les ondes de choc réfléchies. Afin de pouvoir remplir cette tâche, il a été décidé d'utiliser le tube à choc chauffé avec les modifications décrites dans la section 3.3.3.4. A partir du comportement en fonction du temps de la fraction volumique de la suie et des section efficaces molaires d'extinction, on obtient des informations sur les paramètres cinétiques globaux de la suie, tels que le rendement de la suie, le délai d'induction et le taux de croissance de la suie.

Le premier paramètre analysé c'était la section efficace molaire d'extinction, elle peut être dérivé des mesures d'extinction. Les cas initiaux considérés sont les carburants cycliques de référence. Tout d'abord, les résultats obtenus avec 0,07% de toluène dilué dans l'argon sont présentés à la **Figure 4.15** pour différentes températures T_5. En effet, le rendement en suie a un comportement caractéristique de dépendance à la température en forme de cloche. Le deuxième combustible aromatique pur de référence est le benzène (**Figure 4.16**). La valeur absolue maximale de D_{633nm} est atteinte à des températures autour de 1680-1740 K, la gamme intermédiaire de notre étude, similaire à celle du toluène. Enfin, le troisième combustible cyclique pur analysé est le cyclopentène (**Figure 4.17**). La valeur absolue maximale de D_{633nm} est atteinte pour 1704 K, la température intermédiaire, similaire à celle du toluène et du benzène. Les rendements en suie de la pyrolyse du cyclopentène sont inférieurs à ceux des aromatiques pour toutes les conditions de température. La **Figure 4.18** présente la comparaison de l'historique du D_{633nm} pour les différents combustibles et à des conditions de température spécifiques (autour de 1650, 1750, 1850 et 1950 K). Cette figure contient également les résultats pour les combustibles acycliques (C_2H_2, C_3H_4 et C_3H_6). Afin de mieux caractériser les résultats présentés, les résultats de D_{633nm} à 2 et 4 ms pour les différents combustibles sont présentés dans la **Figure 4.20** avec les ajustements polynomiaux des points de données.

Les maximales des courbes du benzène et du toluène sont similaires (~ 1700-1750 K), ainsi que les valeurs à des températures plus élevées. En revanche, la croissance initiale de la courbe est décalée vers des températures plus basses pour la pyrolyse du toluène (ou, d'un autre point de vue, les densités optiques pour la pyrolyse du toluène sont plus élevées que celles du benzène à des températures inférieures à 1700 K). Les maximales D_{633nm} dans le cas de la pyrolyse du cyclopentène sont environ 36% et 50% de ceux du benzène et du toluène à 2 ms et 4 ms, respectivement. La fenêtre de température de formation de la suie est également réduite car des quantités discernables du signal d'extinction de la suie à 2 ms ne peuvent être obtenues qu'au-dessus de 1625 K (environ 100 K de plus que dans la pyrolyse des combustibles aromatiques).

L'un des principaux objectifs de la présente étude expérimentale est de comprendre comment l'ajout de combustible (C2s - acétylène et éthylène, et C3s - propylène et propyne) aux combustibles aromatiques peut modifier la propension à la formation de suie. La décomposition thermique du propyne conduit directement à la formation du radical propargyle (C_3H_3), précurseur du benzène par les réactions C3+C3. La croissance ultérieure des HAP et la formation de particules sont favorisées par rapport au cas de la pyrolyse du cyclopentène. Les valeurs D_{633nm} les plus basses ont été obtenues avec l'acétylène comme combustible, car la voie d'accès aux particules repose uniquement sur les réactions C2+C2 qui sont beaucoup moins efficaces pour produire le premier cycle aromatique et les HAP suivants. Les expériences sur les combustibles C2-C3 ont montré que l'ordre dans la tendance à la suie est comme prévu $C_3H_4 > C_3H_6 > C_2H_2 > C_2H_4$.

Le deuxième paramètre analysé est le délai d'induction, qui est l'un des paramètres les plus importants pour caractériser la tendance d'un hydrocarbure à former de la suie. Il représente le temps nécessaire pour que les premières particules de suie apparaissent. La **Figure 4.33** montre les délais d'induction en fonction de l'inverse de la température pour les mélanges toluène et toluène + C2. La courbe ajustée pour le toluène pur a été divisée en 2 : la gamme des hautes températures (1780-1990 K) et la gamme des basses températures (1519-1748 K). L'ajout de C_2H_2 et de C_2H_4 modifie le comportement du délai d'induction par rapport au toluène pur, non seulement d'un point de vue quantitatif, mais aussi dans le fait qu'une seule pente est maintenant discernable. Les deux énergies d'activation sont très similaires pour les deux mélanges, ce qui suggère que la formation des particules est pilotée par un processus commun dans toute la gamme de températures considérée. Lorsque des composés C3 sont ajoutés au toluène (**Figure 4.34**), les mélanges binaires présentent un comportement similaire à celui du toluène pur, avec un double ajustement pour les températures inférieures et supérieures à 1760 K. La **Figure 4.35** montre les résultats de la pyrolyse du benzène, avec et sans ajout d'acétylène et d'éthylène. La première observation est la différence de comportement entre le benzène et le toluène. L'addition d'acétylène et d'éthylène augmente le délai

d'induction, surtout pour l'éthylène, comme dans le cas de l'addition au toluène. La **Figure 4.36** présente les résultats du cyclopentène et du cyclopentène + acétylène. L'ajout de C_2H_2 a eu un faible impact sur le délai d'induction et il ne modifie pas de manière significative les mécanismes de formation de la suie. La **Figure 4.37** montre le délai d'induction en fonction de l'inverse de la température pour tous les carburants purs étudiés avec des concentrations de carbone similaires. Dans la région des hautes températures, les pentes des courbes du cyclopentène, du propyne, du propylène et de l'acétylène sont très similaires, inférieures aux valeurs obtenues pour les combustibles aromatiques. Le seul combustible simple non aromatique qui présente une double pente est le propyne, pour lequel l'ajustement des points de données au-dessous de 1740 K a une pente de 125 kJ/mol. De manière surprenante, cette valeur est beaucoup plus proche de celle obtenue pour le toluène que pour le benzène. D'autre part, les délais d'induction du propyne et du benzène à la plus basse température considérée ici (environ 1600 K) sont très similaires, comme prévu. En résumé, l'ordre de propension à la suie pour les carburants uniques étudiés ici est le suivant : C_7H_8 > C_6H_6 > C_3H_4 > C_5H_8 > C_3H_6 > C_2H_2.

Après la période d'induction, la fraction volumique de la suie croît très rapidement par des réactions de surface et la coagulation. La coagulation devrait fournir une contribution significative au début du processus de croissance, lorsque les particules naissantes sont plus petites (donc plus mobiles) et nombreuses (donc plus promptes à réagir les unes avec les autres). Lorsque les particules augmentent en taille, la croissance de la suie par des réactions de surface devrait être le processus dominant. La **Figure 4.39** montre le taux de croissance de la suie du toluène, toluène + acétylène et toluène + éthylène. Le taux de croissance est normalisé par la concentration du combustible. Le taux de croissance du toluène pur est beaucoup plus élevé que celui des deux mélanges, qui se superposent presque, d'un facteur deux à haute température et d'un facteur cinq à basse température. Les mélanges de C_7H_8 + C_3H_4 et C_7H_8 + C_3H_6 (**Figure 4.40**) ont des taux de croissance très similaires, compte tenu des incertitudes expérimentales. L'addition de propène et de propyne au toluène diminue la valeur absolue du taux de croissance de la suie, mais pas autant que le cas précédent d'addition de C2. En ce qui concerne les résultats relatifs au C_6H_6 (**Figure 4.41**), les données sur le benzène présentent un comportement différent dans les régions à basse et à haute température, comme pour le toluène. La **Figure 4.42** montre la vitesse de croissance de la suie du cyC5H8 et du mélange binaire de cyclopentène et d'acétylène. L'addition d'acétylène conduit à une diminution significative du taux de croissance ainsi qu'à une diminution de l'énergie d'activation globale. La **Figure 4.43** présente une comparaison entre les six carburants purs étudiés à la même concentration en carbone. Le toluène et le benzène sont caractérisés par des taux de croissance de suie similaires pour toute la gamme de température de la présente étude. Le cyclopentène présente des valeurs absolues de densités optiques plus faibles et des délais d'induction plus longs par rapport au toluène et au benzène. La tendance réduite à la formation de particules est également confirmée par un taux de croissance de la suie plus faible. Le seul combustible qui

ne suit pas l'ordre précédent dans la tendance à la suie est le propyne. Le propyne produit effectivement plus de suie que le cyclopentène et plus rapidement, mais le taux de croissance est plus faible. Dans ce cas, nous pouvons observer deux comportements différents à basse et haute température comme pour le benzène et le toluène.

En complément des paramètres mesurés, une étude cinétique préliminaire et qualitative a été entreprise afin de donner un aperçu de la formation de particules lors de la pyrolyse des hydrocarbures cycliques considérés dans ce travail, le toluène, le benzène et le cyclopentène. Les simulations ont été réalisées à l'aide de Chemkin Pro avec le récent modèle cinétique développé à ICARE pour simuler la chimie des HAP à partir de la pyrolyse de nombreux composants et mélanges de carburants. Ce modèle a été validé par rapport aux données de spéciation dans le tube de choc de haute pureté, y compris la chimie détaillée des HAP jusqu'à quatre cycles (le pyrène et le fluoranthène). Le modèle utilisé dans cette analyse ne contient que des réactions à BIN1A et BIN1B, BIN1 correspondant à un composé C20, A et B représentant différents rapports C/H tels que définis dans le modèle CRECK du groupe du Politecnico di Milano. Des travaux sont en cours pour développer le modèle en phase solide à coupler à la chimie des HAP ; néanmoins, la croissance de la suie suivra la formation des HAP et de BIN1, ainsi les analyses sur ces intermédiaires peuvent donner une idée de la quantité de suie qui sera estimée avec le modèle une fois couplé à la chimie de la suie.

Des analyses du taux de production (ROP) à T_5=1750 K, P_5= 18 bars, et un temps de réaction de 4 ms sont effectuées pour le BIN1B, le $C_{18}H_{10}$ groupée, le pyrène ($C_{16}H_{10}$), le fluoranthène ($FC_{16}H_{10}$), le fluorène ($C_{13}H_{10}$), le phénanthrène ($C_{14}H_{10}$), le naphtalène, et l'indène (les principales espèces de PAH). BIN1B est formé pour environ 90% par $C_{18}H_9$+C_2H_2 (voie HACA), environ 1-2% par C_3H_4-P+$C_{18}H_9$, 1,5-3% par C_3H_3+$C_{18}H_9$ pour tous les carburants. Le $C_{18}H_9$, radical du $C_{18}H_{10}$ et intermédiaire clé pour la formation du BIN1, est principalement formé par les réactions d'extraction de l'hydrogène de ses espèces stables. La formation du $C_{18}H_{10}$ dépend de plusieurs voies. Il est principalement produit par les voies HACA, C_2H_2+$C_{16}H_9$ (60% pour le toluène, 47% pour le benzène et 65% pour le cyclopentène) et C_2H_2+$FC_{16}H_9$ (toluène : 30%, benzène : 40%, cyclopentène : 27%). Le $C_{16}H_9$ et le $FC_{16}H_9$ sont produits à partir des réactions d'absorption de l'hydrogène du pyrène et du fluoranthène, respectivement. En ce qui concerne le pyrène, il est principalement formé par la voie HACA C_2H_2+$C_{14}H_9$ (toluène : 77%, benzène : 84%, cyclopentène : 79%) et de façon mineure par les réactions de recombinaison $C_{16}H_9$+H (toluène : 10%, benzène : 10%, cyclopentène : 5%) et C_2H_4+$C_{14}H_9$ (toluène : 9%, cyclopentène : 12%). La voie HACA est principalement responsable de la formation du pyrène. Le $C_{14}H_9$ dérive des réactions d'absorption de l'hydrogène du $PC_{14}H_{10}$. La **Figure 4.46** présente les voies de réaction complexes menant à la formation du $PC_{14}H_{10}$. La deuxième étape HACA vers le $C_{18}H_{10}$ implique le fluoranthène. Les voies de réaction menant

à la formation de naphtalène sont cartographiées sur la base des analyses ROP à 1750 K dans les cas individuels, comme présenté dans la **Figure 4.48**. La formation de $C_{10}H_8$ est régie par l'isomérisation de $C_9H_6CH_2$ et un canal mineur par la déshydrogénation de $C_9H_6CH_3$-1 dans la pyrolyse du toluène et du cyclopentène (66% et 78% du taux de production intégré total, respectivement, **Figure 4.50**).

En complément des mesures d'extinction présentées, l'étude des particules de suie par microscopie électronique à transmission (MET) a été réalisée à deux grossissements : $x2{,}75x10^4$ et $x2x10^5$. L'étude de la texture de la suie (morphologie, taille des particules unitaires) a été réalisée en MET à un agrandissement de $x2{,}75x10^4$ conduisant à des images de moyenne résolution. La micro-structure de la suie (longueur des plans carbonés, distance séparant ces plans) a été étudiée à un grossissement de $x2x10^5$. Les agrégats sont composés de chaînes de sphères primaires et le diamètre moyen des sphères varie avec la température et le combustible. Dans le cas de la pyrolyse du toluène, le diamètre moyen des sphères primaires diminue de 28 nm à 15 nm lorsque la température passe de 1560 à 1930 K. Un comportement analogue a été observé dans le cas du benzène (de 25 à 15 nm). L'addition de C_2H_2 au toluène augmente le diamètre moyen de la particule de 12%, alors que pour le benzène cette augmentation était plus dramatique, presque 40%. Lorsque l'éthylène a été ajouté au C_7H_8, il a également été possible d'observer une légère modification du diamètre de 4 %. Pour la pyrolyse du cyclopentène, le diamètre moyen a diminué de 22 à 18 nm lorsque la température a augmenté de 1550 à 1970K, c'est-à-dire que la variation de la taille des particules est plus faible par rapport au toluène et au benzène. L'addition de C_2H_2 au cyC_5H_8 n'a pas eu d'impact sur la taille de la particule, contrairement aux cas du toluène et du benzène. Pour ces carburants, l'ajout d'acétylène a augmenté le diamètre moyen de la particule, et une mousse a été observée autour des particules.

La microstructure et la micro-texture des particules de suie ont aussi été observées. De ces observations, il est visible que ces deux facteurs sont très fortement influencés par la température de formation des particules. De manière générale, l'organisation des plans carbonés (longueur des plans, parallélisme de ces derniers) sur la couronne externe de la particule augmente avec la température. Pour les températures intermédiaires et élevées, le cœur de la particule est constitué de noyaux qui semblent provenir de la coalescence des premiers noyaux de la particule. Ces observations soutiennent la théorie postulée pour la détermination des constantes de vitesse de croissance selon laquelle la croissance des particules au début est influencée par la coagulation et la croissance de surface, tandis qu'aux stades ultérieurs, seules les réactions de surface sont prédominantes. Concernant les combustibles cycliques, l'espace entre les couches ne varie pas de plus de 10 % d'un combustible à l'autre. Par contre, la température a des effets plus marqués. Pour le toluène, l'addition d'acétylène diminue légèrement de 5% l'espacement entre les couches, mais pour l'éthylène cette valeur est plus élevée : 20%. Cela signifie que l'addition de ces combustibles conduit à un réarrangement différent de la microstructure des particules de suie. Les mêmes phénomènes peuvent être

observés pour $C_6H_6+C_2H_2$ et $C_5H_8+C_2H_2$, une diminution de 6% de l'espacement d pour les deux cas. Les conditions de formation de la suie sont données dans le **Table 4**, ainsi que le diamètre moyen des particules et l'espacement entre les couches avec les incertitudes associées.

Conclusion

Ce travail a été consacré à l'étude de la formation de la suie. Des modèles adéquats sont nécessaires pour comprendre les processus complexes de production de la suie. Ils doivent être testés dans des environnements bien contrôlés par rapport à des mesures de concentrations de particules, de distributions de tailles de particules, de fractions volumiques de suie et d'autres paramètres. Les particules doivent être mesurées in-situ en utilisant des techniques non intrusives. Les techniques optiques, en particulier les techniques de diagnostic par laser, sont idéales dans ce but.

Un des objectifs de cette thèse était de fournir une base de données expérimentales sur la chimie de la formation des HAP dans les conditions typiques rencontrées dans les dispositifs de combustion modernes. Dans la première partie du travail, des expériences de pyrolyse de n-heptane et de cyclopentène ont été réalisées à l'aide d'un tube à choc à impulsion unique sur une plage de température de 940-1680 K pour une pression nominale de 20 bars et un temps de réaction d'environ 4 ms. Les compositions chimiques des mélanges post-choc sont échantillonnées et analysées à l'aide des techniques GC/MS. Des profils de fraction molaire d'espèces en fonction de T_5 sont obtenus. Le n-heptane se dissocie en produits hydrocarbonés, principalement C2, C3 et C4, à haute température. Les espèces de HAP détectées dans la pyrolyse de l'heptane comprennent le benzène, le toluène, le phénylacétylène, le styrène et l'éthylbenzène. L'intérêt du cyclopentène provient de son rôle de précurseur des intermédiaires C5, dont le cyclopentadiène, dont la chimie a un impact important sur la production de HAP et de suie. Le CYC_5H_8 est principalement consommé par les processus de déshydrogénation et d'isomérisation par ouverture de cycle, qui aboutissent à la génération de C_5H_6 et LC_5H_8, respectivement.

L’autre objectif de cette thèse était de développer et d'évaluer la technique d'extinction pour étudier la formation de suie derrière les ondes de choc réfléchies. Afin d'accomplir cette tâche, il a été décidé d'utiliser le tube à choc chauffé. Le comportement en fonction du temps de la fraction volumique de la suie a fourni des informations sur les paramètres cinétiques globaux de la suie, tels que le rendement de la suie, le temps d'induction et le taux de croissance de la suie pour trois combustibles purs : toluène, benzène et cyclopentène. Les résultats de l'addition d'acétylène, d'éthylène, de propène et de propyne aux combustibles précédents ont également été étudiés. Le premier paramètre qui a été examiné est la densité optique. Il a été montré que la valeur absolue maximale de D_{633nm} est atteinte pour la température intermédiaire, donc, il peut être déduit que le rendement en suie a un comportement de dépendance à la température en forme de

cloche, qui est caractéristique du processus de formation de la suie. L'autre paramètre analysé était le délai d'induction. C'est l'un des paramètres les plus importants pour caractériser la tendance d'un hydrocarbure à former de la suie. Le délai d'induction en fonction de l'inverse de la température de tous les combustibles purs étudiés avec une concentration en carbone similaire a été tracé. Après la période d'induction, la fraction volumique de la suie croît rapidement par réactions de surface et coagulations, jusqu'à un point d'inflexion. Au-delà de ce point d'inflexion, on considère que la croissance de la fraction volumique se produit uniquement par des réactions de surface avec les molécules en phase gazeuse. Le taux de croissance de la suie est influencé par la composition des hydrocarbures et la température et sa précision est difficile à évaluer. La vitesse de croissance de la suie est causée par un phénomène complexe et compétitif entre la formation des particules. Enfin, l'étude des particules de suie par microscopie électronique à transmission (MET) a été réalisée à deux grossissements. La longueur des plans de carbone ou la distance entre ces plans ont été caractérisées. Concernant l'organisation interne des plans de carbone, en général, sa longueur et son parallélisme sur la couronne externe de la particule augmentent avec la température.

Dans une perspective de travail, il serait intéressant d'effectuer des mesures de diffusion Rayleigh dans le tube de choc à haute pression. Cela permettrait de dériver le diamètre moyen des particules, qui pourrait ensuite être comparé aux résultats d'analyse MET acquis. Un autre objectif à poursuivre est de réaliser l'analyse MET avec les autres carburants testés, afin d'avoir une description plus précise de chaque hydrocarbure examiné. Enfin, dans le but d'obtenir une compréhension complète de la formation de la suie, il serait utile pour la communauté scientifique d'étudier les conditions d'oxydation dans le tube de choc.

Abstract

Combustion plays a vital role in the industrial, transport and power generation sectors. This complex reaction can lead to particulate matter production. Concerns about the effects of pollution, public health and quality of the environment have led governments to regulate the level of soot emissions. Soot formation is a complex process, occurring through many chemical and physical steps. Large polycyclic aromatic hydrocarbons (PAHs) are formed from primary aromatic species, PAHs dimerization and chemical growth processes lead to the formation of soot precursor particles (primary particles). These precursors undergo simultaneous coagulation and surface growth to form the final aggregates. Eventually, when the soot particles become large enough, agglomeration starts resulting in macroscopic chain-like aggregates called mature soot. Therefore, the aim of this thesis is the experimental characterization of soot formation in a shock tube from different fuel molecules and mixtures, at typical conditions encountered in modern combustion devices, through optical techniques. The experimental database constitutes an essential reference for the development of detailed kinetic models for soot particle chemistry. In addition, part of the study was focused on the use of a different shock tube facility for the speciation of soot precursor molecules from specific fuels of interest.

PAH speciation is performed for n-heptane and cyclopentene pyrolysis, along with a kinetic model for both fuels. Concerning the solid part of the soot, experiments on toluene, benzene and cyclopentene were performed with and without the addition of ethylene, acetylene, propene and propyne. Laser extinction techniques were employed in order to derive parameters, such as optical densities, soot yield, induction delay times and soot growth rate. The last step of the analysis consisted of performing transmission electron microscopy (TEM), which provided information on the diameter and morphology of the soot particles and their structure and micro texture.

The results obtained in this work can serve for future model developments concerning more complex fuels and surrogates, as well as the base for the construction of soot codes for simulation of particle formation in combustion applications.

Keywords: shock tubes, pyrolysis, soot formation, optical diagnostics, laser extinction, soot yield, optical densities, induction delay times, soot growth rate, TEM analysis, PAHs, toluene, benzene, cyclopentene, n-heptane, acetylene, ethylene, propene, propyne.

Acknowledgments

I would like to express my sincere gratitude to my supervisor Dr. Andrea Comandini for his constant support and fruitful discussions during the entire period of the thesis. I am also very grateful to Dr. Nabiha Chaumeix for her endless enthusiasm and constant assistance. Both of them were extremely kind to me during the Ph.D.

A special thanks to Dr. Alaa Hamadi for ongoing supervision, unwavering support, insightful advice, helpful comments and suggestions, encouragement and help. The course of this thesis would be completely different without her, I feel honored to call her my friend.

I want to express my gratitude to Dr. Mahmoud Idir and Dr. Said Abid for all their valuable suggestions, smart ideas, useful comments, and constructive discussions throughout this research work.

I am deeply grateful to Dr. Sharath Nagaraju and Tullio Viola for their constant assistance with the shock tube.

My sincere and special gratitude goes to Dr. Anthony Roque. I have a social life in Orleáns thanks to him, he was my first friend in town. However, he is not the only one. I was lucky to meet wonderful people here, especially Dr. Alka Karan and Fabian Cano. The three of us formed a friendship that I deemed unimaginable in a foreign country, and I am extremely grateful for every experience we had together.

I would like to extend my genuine gratitude to my Brazilian friends, my life would be incomplete without these girls. They have put up with all my dramas and worries over the years. Every text message, advice, and virtual hug they gave me were essential to get me where I am today. They will be forever in my heart.

Most of all, I would like to acknowledge my family. My parents and my brothers were fundamental in this process, both for their moral and emotional support. Thank you for believing in me even when I didn't. I am also thankful to Fernanda, Rafael, Pedro and Júlia for overloading me with cuteness every now and then. You are the most important people in my life.

Any omission in this brief acknowledgment does not mean lack of gratitude and respect.

Contents

Table of Figures

List of Tables

1 Introduction

Combustion science and technology has a significant impact on most fields of society. Cooking food and heating homes have long been two major applications. With the development of the steam engine at the beginning of the eighteenth century, a new use for combustion was found: performing work. Those first engines were employed for burning fuels, usually coal, to produce heat that was used to boil water. Nowadays, combustion still plays an important role in the industrial, transport and power generation sectors. Despite its controlled use has been achieved during the past decades, many areas of the field are still not well understood.

Fuel and oxidizer are necessary elements for a combustion reaction. Fuels can be classified as substances that release heat by reacting with an oxidant. Indeed, their practical applications require them to be economic and comply with the international regulations designed to protect the environment and the public health. Most of the currently used fuels are derived from non-renewable sources. A common example of non-renewable energy source is fossil fuels such as coal, petroleum and natural gas. In ideal conditions, combustion of hydrocarbons leads to the formation of carbon dioxide and water. However, in practical systems, combustion is not complete and other undesired pollutants are formed and emitted. Therefore, the indiscriminate use of this type of fuels needs to be well characterized and controlled for reducing their ecological and social footprint.

Particularly in the last two decades, the level of public awareness regarding environmental issues have increased considerably. Concerns about the effects of pollution, public health and quality of the environment have led governments to regulate the level of emissions. In fact, the main pollutants produced during combustion include hydrocarbons partially or not burned, such as nitrogen oxides (NOx), carbon monoxide, sulfur oxides, and particulate matter/soot. The term “particulate matter”, or PM, is used to describe a complex mixture of extremely small particles and liquid droplets. It is composed of a number of components including acids, organic chemicals, metals and soil, soot, or dust particles [1], and it can have natural or anthropological sources. Dust, volcanoes and forest fires represent the major natural cause, while for human sources combustion processes are the main origin. Soot is defined as the carbonaceous core of the PM derived from the incomplete combustion of fuels. It is composed of aggregates of hundreds or more primary spherules, known as primary particles, nearly spherical.

The main problem for the presence of PM emissions suspended in the atmosphere is associated with the fact that they are usually identified as responsible for a series of specific issues related to human health, such as respiratory problems, lung cancer and cardiopulmonary diseases [2]. The negative effects on the environment have been also clearly identified [3]–[7]. Thus, the study of soot formation chemistry has

sparked interest to the scientific community. The main goal of the research in the field of PM chemistry is the improvement of combustion processes in all practical systems: diesel and gasoline engines, gas turbines, burners for domestic or industrial boilers. On the other hand, controlling soot emissions will require improved understanding of soot formation and oxidation under a variety of combustion conditions. Unfortunately, soot formation is still poorly understood despite the recent advances in experimental and numerical techniques.

Soot formation is a complex process, occurring through many chemical and physical steps. Large polycyclic aromatic hydrocarbons (PAHs) are formed from primary aromatic species (first and second ring); PAHs dimerization and chemical growth processes lead to the formation of soot precursor particles (primary particles). These precursors undergo simultaneous coagulation and surface growth to form the final aggregates. Eventually, when the soot particles become large enough, agglomeration starts resulting in macroscopic chain-like aggregates called mature soot. The description of PM formation is reported schematically in **Figure 1.1** [8].

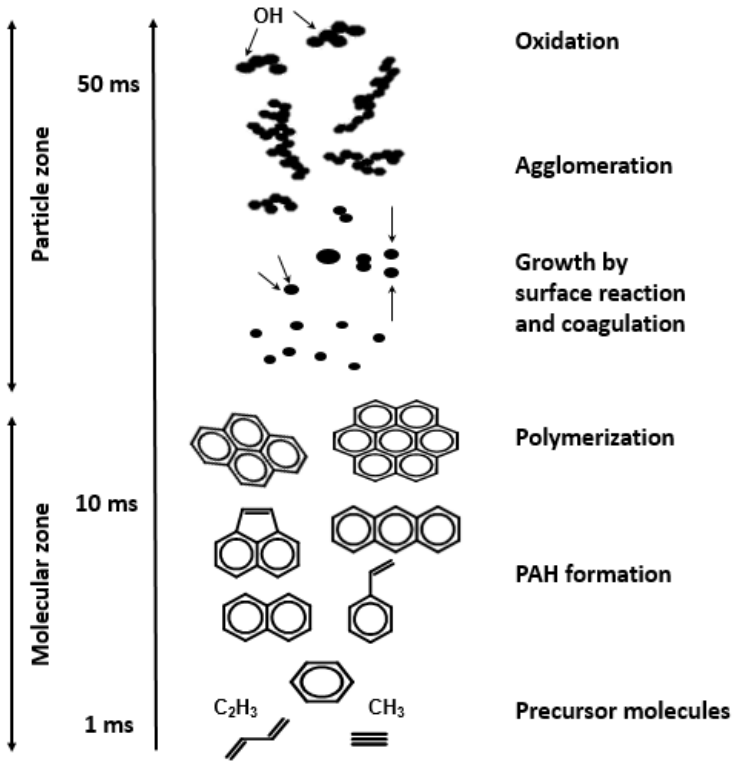

Figure 1.1 *Schematic of soot formation steps [8], [9]*

The soot toxicity is partially attributed to the presence of Polycyclic Aromatic Hydrocarbons (PAHs) condensed and adsorbed on the surface of the soot particles. PAHs are organic compounds formed by several aromatic rings and they are considered the precursors of the nascent soot particles [10], [11]. Many

PAH compounds, formed as a byproduct of incomplete combustion of organic fuels, are considered pollutants with potential carcinogenic and mutagenic effects on living organisms [12]. However, the denomination PAH encompasses different types of chemical compounds that have different properties, depending on their chemical structure and number of rings.

From the brief description above, it is clear that more detailed studies on soot formation are required. The research work carried out for more than thirty years in this field has allowed understanding the main reaction pathways responsible for the formation of soot particles. Nevertheless, predictions from detailed kinetic models are still very unsatisfactory, especially concerning the morphology of soot and the chemical composition of the adsorbed phase. Another very important topic concerns the determination of the optical properties of soot particles, essential because of their impact on the radiative heat transfer [13] but still with large uncertainties.

To understand the complex soot formation processes, adequate models are necessary. These should be tested against measurements of particle concentrations, particle size distributions, soot volume fractions and other parameters in well controlled environments. It is important that these parameters are measured in situ by non-intrusive methods. Optical techniques, especially laser diagnostic methods are the most suitable for the indicated purpose. In addition to being non-intrusive, they have high spatial and temporal resolutions, which is especially useful in studies of soot formation and oxidation in diluted conditions, where the non-idealities can be reduced.

The aim of this thesis is the experimental characterization of soot formation in a shock tube from different fuel molecules and mixtures, at typical conditions encountered in modern combustion devices. The experimental database constitutes an essential reference for the development of detailed kinetic models for soot particle chemistry. In addition, part of the study was focused on the use of a different shock tube facility for the speciation of soot precursor molecules from specific fuels of interest. Shock tubes are ideal experimental devices for kinetic studied where the chemical behavior is isolated from physical processes. The use of shock tubes has been proven to lead to important contributions in the chemical kinetic field, because it permits to work under controlled conditions, at temperature and pressure conditions similar to those of practical systems.

This work is divided in 5 chapters. Chapter 2 presents a review on the state of art concerning particulate matter and soot analyses in different devices, as well as the recent studies performed with the fuels employed in this thesis. In chapter 3 the experimental setup is described, and the principle of the shock tubes is reviewed. The device used in this study is presented, along with the implementation of the technique which is a fundamental part of the current work. In particular, the preliminary experiments fundamental to

characterize the experimental set-up are reported. Chapter 4 is addressed to the results obtained. Fuel and intermediate species, including aromatics, are measured using gas chromatography and mass spectrometry diagnostics. In addition, extinction measurements are performed for different mixtures, using toluene as a reference. Lastly, transmission electron microscopy results are discussed. Conclusions and recommendations for future work are given in Chapter 5.

This project has received funding from the European Research Council (ERC) under the European Union's Horizon 2020 research and innovation programme (grant agreement n◦ 756785), at which the author is very grateful.

2 Literature Review

2.1 Particulate matter, soot properties and formation chemistry

As described in the previous chapter, "particulate matter", also known as particle pollution or PM, generally includes a large number of components in liquid and solid phase. Furthermore, it is classified according to its size, as coarse particles (10 - 2.5 μm, PM_{10}), fine particles (2.5 - 0.1 μm, $PM_{2.5}$) and ultrafine particles (≤0.1μm; nanoparticles, $PM_{0.1}$) [1], [14]. This classification is fundamental as the size of the particles, in addition to their chemical composition, has a strong impact on their effects on human health and the environment. Soot constitutes the carbonaceous element of the emissions from fuel burning. To characterize the soot properties, several parameters are used:

1. Soot volume fraction, f_v, which represents the volume occupied by soot particles in a unit volume (cm^3/cm^3); this parameter is function of the optical properties of the soot particles, which are not well defined at the moment, especially concerning the primary particles, thus the optical density, D_{633} (mol/m^2), is often employed to avoid assumptions concerning the optical properties of the condensed species;
2. Induction delay time, τ_{ind}, the time needed for the inception of the first solid nuclei;
3. Soot yield, Y (%), the efficiency of carbon conversion to soot;
4. The mean diameter of the soot primary particle, d;
5. The internal structure of the soot aggregates.

Although soot chemistry has been studied extensively over decades, some of the primary mechanisms in soot formation, growth, and oxidation are uncertain. Incipient soot is usually considered as spherical, small (1–10 nm) particles produced starting from large organic PAH species with relatively-high hydrogen-to-carbon ratios. Mature soot, however, is composed of primary particles of 10–50 nm in diameter with fine structures similar to polycrystalline graphite [15]. These primary particles are covalently bound into branched-chain aggregates. The aggregates are non-spherical and are characterized by fractal dimensions typically in the range of 1.7–1.9 [16]. It is important to stress that the non-sphericity of these particles makes the optical measurements even more complicated.

The schematic presented in **Figure 1.1** shows how soot formation is a complex process, occurring through many chemical and physical steps. Generally it is divided into two parts: a gas phase chemistry and a solid phase one [17], [18]. The main steps of the gas phase are the pyrolysis of fuel molecules followed by the formation of aromatic structures and heavy hydrocarbons. The solid phase has four steps in total: inception, surface growth reactions, coagulation, and agglomeration.

2.1.1 Gas Phase Precursor Chemistry

In the gas phase, fuel pyrolysis and formation of the precursors take place. Soot precursors are molecular species that compose the basis of soot particles. They play an essential role in the nucleation process (appearance of the first solid structures) but the specific species leading to this process have not been clearly identified. The physical process behind nucleation is also unclear. There could be many different soot precursors, early models assumed these species to be formed starting from small hydrocarbons, such as acetylene and benzene [19], [20].

One of the main and most commonly accepted process responsible for PAH formation and growth is the so-called Hydrogen-Abstraction Carbon-Addition path (HACA) [9]. Previous studies suggested that acetylene was a likely candidate for driving mass growth due to its stability at high temperatures. Hydrogen atoms are also argued to play an essential role for producing the radical species which allows reaction with acetylene and subsequent growth [8], [21]. The hydrogen-abstraction-acetylene-addition mechanism is a repetitive reaction scheme to describe PAH growth from the first aromatic ring. It involves H-abstraction from an aromatic ring by another H atom to create a radical site. This is followed by C_2H_2 addition to the radical site and then ring closure. An example of the HACA mechanism for the formation of two-and three-ring structures from benzene is shown in **Figure 2.1** .

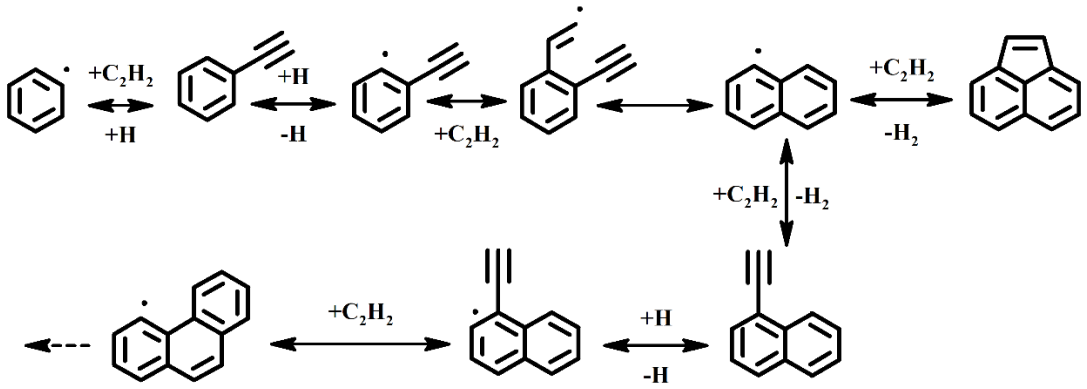

Figure 2.1 *Formation of naphthyl, acenaphthylene and phenanthryl by the HACA mechanism [9]*

For certain conditions, the PAH growth by the HACA route can be overcome by a faster growth pathway involving the direct reaction between two PAH compounds, the so-called reactive coagulation [22]–[24]. In general, the HACA mechanism requires two H-abstraction reactions and two C_2H_2 additions to produce a ring structure to pass for example, from benzene to the naphthyl radical. On the other hand, two PAH compounds can form large structure with a single reaction. For example, the formation of phenanthrene and diphenylacetylene from the reaction of the phenyl radical (C_6H_5) with phenylacetylene ($C_6H_5C_2H$) as

depicted in **Figure 2.2** [25], [26]. In this case, the limiting factor includes the concentration of the PAH radicals and the competition with oxidation reactions and reactions with other abundant intermediate species (as acetylene).

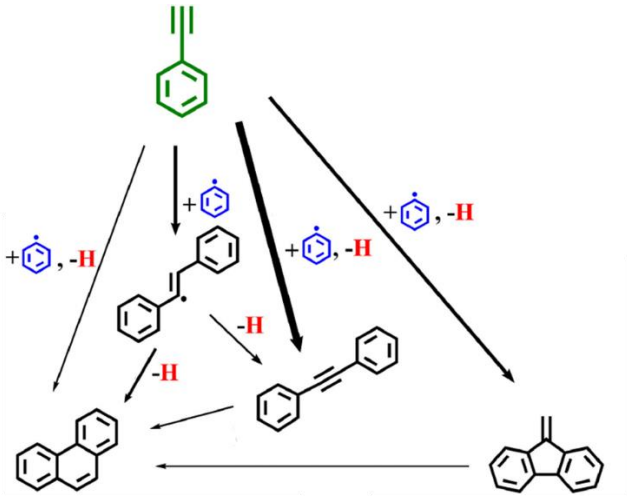

Figure 2.2 *Reaction pathways of species formation from fuel phenylacetylene consumption (adapted from Sun et al.[25])*

Finally, polyynes ($C_{2n}H_2$) have been proposed as PAH growth contributors due to their stability at high temperatures [27]–[29]. This hypothesis has not been proved experimentally, and usually current kinetic models do not largely employ these reaction pathways.

2.1.2 Solid Phase

The formation and growth of soot particles in solid phase can be divided in four stages. The first one is soot particle inception. It represents the transition from gas-phase-precursor species to condensed-phase particles [8], [23], [30]–[33]. Soot particle inception provides the initial particles and growth provides most of the ultimate soot mass [34].

The second stage is surface growth. It consists in the reaction of gas phase species on the surface of the particle and, consequently, their incorporation in the particle itself. This process generates most part of soot, and it is very similar to the reactions in gas phase, with activation of radical sites and addition (HACA route again one of the main paths) or reaction with PAH compounds and radicals.

Third stage is coagulation, which happens at the same time as the surface growth by chemical reactions. During the coagulation, “sticking” collisions between two primary particles take place, followed by sintering to form a single, larger spherical particle. The coagulation results in an increase of the average

particle size, a decrease in the total number of primary particles, while the total soot amount remains the same.

The final stage is aggregation. This process begins with the formation of open clusters, or agglomerates. Aggregates are usually composed of hundreds of smaller spherical particles firmly bound together. The aggregate cannot easily be broken apart. Mature soot particles are formed by the growth of layers of graphene on the surface of primary particle agglomerates [20].

2.2 Different experimental methods applied to soot formation

In order to study soot formation mechanisms from hydrocarbons in different experimental conditions, several experimental set-ups can be employed. The main laboratory-based reactors include flames, engines, rapid compression machines, perfectly-stirred reactors, and shock tubes. A brief overview on some examples of the studies in the literature will be presented in the next section. Indeed, the goal of this section is not to provide a detailed and comprehensive review of the innumerous investigations which have been performed over the past decades, but to depict the different possible set-ups and their main features.

2.2.1 Flames

Laminar flames allow investigating mechanisms of formation, growth, and oxidation of soot particles and their precursors. Typical applications include the determination of the sooting tendencies of fuel/oxidizer mixtures. Kinetics studies have been also performed in flames, although there are several disadvantages compared to other techniques, including non-uniform fields, spatial gradients, coupling of the chemistry with fluidodynamics, uncertainties in the temperature determination along the flame.

For premixed flames, fuel and oxidizer are mixed before the combustion process takes place. Soot can be formed if not enough oxygen is present to oxidize the fuel. In equilibrium conditions, this should correspond to the fuel-rich flames, but the kinetics is dominant soot particles can be formed even at relatively low fuel-lean conditions. On the other hand, for diffusion flames, the fuel and the air are initially unmixed. They are separated and thus the reaction zone is located at their interface. In this flame, combustion is sustained by the diffusion of the fresh mixture in the flame zone. Due to the lack of oxygen, the fuel is pyrolyzed or broken down to smaller molecules and radicals, which results in the formation of soot. Approaching the flame zone, the presence of oxygen allows the products of the pyrolysis to react.

In order to characterize soot particles in terms of concentration and dimension the scattering/extinction technique can be employed in flames. In fact, laser light scattering and extinction measurements in laminar coannular diffusion flames have been reported since 1980 [35]. These techniques were used to determine particle formation and growth as a function of position in the flame. The work also shows measurements of fluorescence and depolarization ratio, which were obtained to provide insight into gas phase processes accompanying particle formation and growth.

Moreover, laser scattering/extinction can be applied to turbulent non-premixed flames, such as the studies on acetylene/air flames in [36], [37]. Mean soot volume fractions, spherule diameters, and aggregate sizes were exclusively characterized based on an optical interpretation that can properly account for the actual particulate morphology. It is important to study non-premixed turbulent flames because turbulence plays a key role in practical combustion systems such as in engines and turbines.

Recent advancements in the technique have leaned towards more accurate particle characterization. For example, Iyer et al. [38] used multiangle scattering at three different height on the burner to determine the total scattering coefficient for ethylene diffusion flames. Coupled to the measurement of local extinction coefficient, the authors were able to estimate the contribution from scattering to extinction without knowledge of the soot primary particle diameter or the morphology of the aggregates. Diameter, number density and the average number of primary particles in the aggregates were obtained.

Laser-Induced Fluorescence (LIF) [39]–[49] and Laser-Induced Incandescence (LII) [50]–[63] are also widely used techniques to characterize soot particles in flames. In fact, Mishra et al. [62] studied laminar Bunsen-type and swirled diffusion flames throughout LIF of Polycyclic Aromatic Hydrocarbons (PAH) and LII of soot particles, simultaneously. The modulated LIF- and LII-signals were acquired together as a single sub-image and then they are spectrally isolated, generating two individual LIF- and LII-images. It was found that PAHs mainly exist in the inner region near the burner and are surrounded by soot and the majority of the OH is distributed on the outer edges of the flame, which represents the reaction zone and soot-oxidation region of the flame.

Mannazhi et al. [49] employed these techniques to measure quantitative soot volume fraction in methane-air diffusion flames at pressures ranging from 0.1 to 0.5 MPa. Similarly, Mishra et al.[62] used LIF for visualization of PAHs and the most mature soot was found at the spatial position of maximum along the central axis and at the flame edges. Indeed, the combination of multiple simultaneous techniques is possible, and it can also provide additional and more complete information on the soot formation. For example, in a recent work multiple optical diagnostic techniques including flame luminosity, light extinction and scattering, spectral soot emission (SSE) as well as LII were used to obtain sooting limit in a

typical counterflow diffusion flames [63]. It was found that the value of sooting limit could be quantitatively different among the used detection techniques, thus proving the importance of the multi-diagnostic approach.

Apart from the in-situ techniques, there is a long history of extractive sampling techniques being used to study flames. The use of such techniques allows for simple particle sizing, soot volume fraction and the ability to identify several species in the same sample. There are, however, as with in-situ measurements, some disadvantages. A key disadvantage is the inevitable perturbation by the physical probe [64], [65].

One commonly employed technique is gravimetric sampling [66]–[70], which involves taking a sample from the flame, achieved by forcing gases through a porous disk in a chimney, and allowing any particulate material attaches itself to the disk [66]. The disk can them be removed for weighing. The flow rate of the gas passing through the disk is a known quantity and thus by weighing the mass of particulates on the disc the mass fraction can be calculated. This is a common method to use for the calibration of laser induced incandescence [70].

A second method which is often seen in the literature is transmission electron microscopy (TEM) [71]–[77]. The method of sampling, which must be employed for this type of analysis, involves placing a fine mesh in the flame for a short period of time, allowing soot to move towards it by thermophoresis and become attached to it. A recent study shows the morphology and structure of soot particles in laminar diffusion flames of anisole/n-heptane [77]. Soot morphology has been analyzed and a set of fractal-based distribution analysis algorithms were proposed by the authors. It was found that the addition of anisole in n-heptane flames greatly influences the soot formation process, which leads to form the soot at the lower part of the flame and subsequently larger primary particle diameters. Moreover, the characteristics of the primary particle diameter distributions, the number of primary particles per aggregate, the aggregate sizes and the fractal dimensions of the flames were disclosed.

An alternative ex-situ technique is scanning mobility particle sizing (SMPS) [78]–[83]. A Scanning Mobility Particle Sizer is an analytical instrument that employ a continuous, fast-scanning technique to provide high-resolution measurements [84] and it has been studied since the early 1990s [82]. Recently, SMPS was shown to be an effective tool to measure the probability density functions (PDFs) of soot nanoparticles in turbulent flames [83] . Time-averaged soot PDFs necessary for validating existing soot models are reported of turbulent, non-premixed, C_2H_4 and N_2 flames. Two differential mobility analyzers (DMAs) with different size ranges were used separately in the SMPS measurements to characterize the entire size range of particles.

In summary, ex-situ techniques have many difficulties associated with them. If the sample is not correctly collected, it will continue reacting and will become unrepresentative of the flame.

2.2.2 Engines

An engine is a machine for converting various forms of energy into mechanical force and motion. The internal combustion engine is perhaps the most common example of a chemical heat engine, in which heat from the combustion of a fuel causes rapid pressurization of the gaseous combustion products in the combustion chamber, causing them to expand and drive a piston, which turns a crankshaft. During this process, soot can be formed as an unwanted element which reduces the efficiency of the cycle and leads to pollutant emissions. Over the last 30 years, research and development has helped manufacturers reduce emissions of these pollutants to comply with EPA emissions standards. The role played by the carbonaceous particles in a diesel engine performance has been studied since the late 1990s [85]. The fuel is introduced in liquid phase and the droplets are progressively vaporized in a high temperature medium. In this case, soot is formed essentially under near pyrolytic conditions.

In general, engines are essential to perform the ultimate tests on soot emissions in practical applications, including characterization of fuels, new designs and operation. On the other hand, the complexity of the system does not really allow for detailed kinetic studies. The laser techniques that will be presented in section 2.4 are widely used on engines where optical access is available. An example is provided here concerning the measurement of soot volume fraction distribution of ethanol blended fuels in an optical direct injection spark ignition engine by combined laser induced incandescence and two-color method [86]. Exhaust PM emissions were also measured by a Combustion Fast Particulate Analyzer, in order to understand the effect of ethanol blending on engine PM.

Ex-situ techniques are also implemented for the analyses of the soot collected at the engine exhaust. For example, Liu et al. [87] investigated the effects of nano-CeO_2 catalytic fuels measuring both in-cylinder soot distribution by visualization methods and exhaust particle characteristics using thermogravimetric analyses in a common-rail engine. In another study, Wang et al. [88] investigated the effect of early-injection on the smoke emissions and engine performance under typical low temperature combustion and reactivity controlled compression ignition. Morphology, nanostructure, and size of the sampled soot particles were studied using different methods, such as high-resolution transmission electron microscopy (HRTEM).

2.2.3 Rapid Compression Machines

Rapid compression machine (RCM) is an experimental device used to simulate a single compression stroke of an internal combustion engine and it can be used for chemical kinetics studies. RCMs are primarily implemented to measure ignition delay times as a function of temperature, pressure, and fuel/oxygen/diluent ratio; further they can be equipped with diagnostics to determine the temperature and flow fields inside the reaction chamber and to measure the concentrations of reactant, intermediate, and product species produced during combustion [89].

Optical devices are employed to study soot formation on RCMs. Simultaneous LII/LIS (laser-induced incandescence/laser-induced scattering) were for example implemented in [90]. Soot was observed distributed in definite clusters, which were linked to slugs of fuel caused by oscillations in the injector needle. Three distinct phases in soot formation could be spotted.

Typical extinction measurements have been also performed, such as in [91], where soot evolution was studied by the line-of-sight absorption method (at 632.8 nm), which measured the soot volume concentration evolution in the initial stage of soot growth before the optical path became opaque. The soot volume fraction showed an initial exponential growth, with a growth rate depending on the compressed charge fuel concentration. A substantial amount of soot was formed after the soot cloud became opaque. Similar methods can be used to determine the soot yield, as in [92].

2.2.4 Stirred reactors

The perfectly-stirred reactor (PSR), well-stirred reactors, or jet-stirred reactors (JSR) are devices used to investigate complex, well-controlled chemical reaction systems [93]. In this system, the temperature, residence time, and the equivalence ratio are fixed, and reaction products can be sampled for subsequent analyses. This apparatus is usually used to investigate the formation of soot precursors at relatively low temperatures. It is particularly interesting for chemical kinetic studies as it allows to obtain stable, well-defined conditions.

The JSR studies can be carried out starting from the first benzene ring, by coupling different diagnostics as gas-chromatography and mass-spectroscopy [94],[95], but also larger PAHs [96]–[100]. In addition, well-stirred reactors were also used to study polycyclic aromatic hydrocarbon (PAH) growth coupled to soot inception [101]–[103]. In this case, soot size distributions were measured using a dilution probe followed by a Nano-differential mobility analyzer (Nano-DMA). Particles were collected from the reactor for transmission electron microscopy analysis.

2.2.5 Shock Tubes

A shock tube is an ideal, totally adiabatic reactor where, due to the passage of a shock wave, the mixture under study is brought almost instantly to a known and controlled temperature and pressure condition. The shock tubes are particularly useful for kinetic studies [104]. The main advantage of this reactor is the capability to study soot formation and its precursors in precise conditions of temperature and pressure, up to high values typical of internal combustion engines. The kinetics is isolated from any other effect (the gases are still behind the reflected shock wave), the conditions are spatially uniform, and the mixture composition can be varied as needed (concentration levels and even at pyrolytic conditions, an essential advantage to study soot formation chemistry).

Since the early 1980s soot formation in shock tubes has been studied. Samples of soot formed during the reaction were taken from the shock tube and examined using a transmission electron microscope to characterize the particles properties [105]. This investigation was undertaken using a reflected shock tube to examine the formation of soot from toluene, benzene and straight-chain heptane. The relative concentrations and type of soot produced were correlated with the reflected temperatures and information derived on the formation of the soot.

Optical access to the shock tube also allows the possibility to apply extinction and scattering techniques, as demonstrated in many experimental investigations in the literature. In particular, De Iuliis et al. [106] performed time-resolved measurements on the pyrolysis of ethylene and toluene at relatively low pressure and for a wide range of temperatures, pointing out the limitations and the difficulties of this combined technique. In general, extinction measurements have also been performed in order to provide global kinetic data concerning the soot formation tendency (soot induction delay time and soot yield), such as in [107] where a diesel fuel surrogate and the hydrocarbon constituents were pyrolyzed in a high-pressure shock tube. Results show that the soot induction delay time and soot yield depend strongly on the structure of the hydrocarbon and on the concentration of oxygen.

This kind of data can be used to test and validate chemical kinetic models for soot formation [21]. For example, in a recent work the influence of oxygenated additives on benzene was considered [108]. The pyrolysis process was investigated behind reflected shock waves at low pressures and wide range temperature. Extinction was measured at 633 nm to determine soot optical densities and soot-inception times. Both, temperature and measured optical densities were compared to simulations based on a detailed chemical kinetics mechanism.

Coupling soot measurements with other laser-based techniques has been also proven to be very effective. For example, soot volume fraction, particle size, and number densities were obtained from the extinction and scattering of benzene and ethylene pyrolysis in [11]. Besides the soot measurements, this work also reports the acetylene mole fraction time-histories. These simultaneous measurements have provided deeper knowledge into soot chemistry and better comprehension of chemical mechanisms.

2.3 Fuels

Aromatic hydrocarbons are major components of petroleum-based transportation fuels and are widely used as major components of surrogate fuels for gasoline, diesel oil, and kerosene. They play a crucial role as anti-knock additives to enhance the octane number of the fuels, as they have high resistance to auto-ignition [109]. They are also the key building blocks for the formation of the typical polycyclic aromatic hydrocarbons, the main soot precursors [110]. The following sections contain a brief summary of the investigations available in the literature concerning the pyrolysis of aromatic hydrocarbons and their mixtures with other fuel molecules relevant to the present thesis, thus at elevated T and P conditions.

2.3.1 Toluene

Toluene (C_7H_8) exists naturally in transportation fuels and it is considered as an important component in surrogate fuels. For example, jet propellants and gasoline contain 20-30% toluene by mole fraction [19]. Being an important combustion intermediate, it has been widely investigated also in relation to the formation and growth of polycyclic aromatic hydrocarbons (PAHs). Indeed, its major initial decomposition product, benzyl radical [111], is a resonantly stabilized radical and thus it is a key intermediate in combustion environments.

To analyze the products the fuel reaction, toluene pyrolysis was performed by Smith [112] in both quartz and tungsten Knudsen cells at very low pressures (10^{-5} to 1 torr) and temperatures up to 1800°C using electron-impact ionization (EI) mass spectrometry (MS). The results for quartz and tungsten Knudsen cells were quite similar. At the lower pressures, only products with molecular weights lower than C_7H_8 were observed, while at higher pressures, these products undergo bimolecular reactions to form heavier compounds up to at least $C_{20}H_{12}$.

Subsequently, other authors performed shock tube pyrolysis studies on toluene [113]–[116]. Pamidimukkala et al. [113] investigated the pyrolysis of toluene at temperatures of 1550–2200 K and pressures from 0.2 to 0.5 atm using two independent shock tube, techniques time-of-flight (TOF) MS and

laser-schlieren densitometry. The primary species observed in these experiments were C_2H_2, C_4H_2, CH_4 and C_7H_7. The proposed mechanism was initiated by two parallel dissociation channels, and the authors were able to define the rate of only one of these channels, the irreversible C-C bond fission. Colket and Seery [114] studied the pyrolysis of 1% toluene in argon using a single-pulse shock tube at pressure of 10 atm, temperature range 1200–1850 K and reaction time of 600 μs. The observed stable products were analyzed using gas chromatography (GC), including some PAHs. Mole fraction profiles of many stable species from H_2 and CH_4 to pyrene were measured. A detailed chemical kinetic mechanism was constructed for describing the formation of aromatics and other species. The work of Sivaramakrishnan et al. [115], [116] was performed at 27 and 45 bar over a wide temperature range (1200–1900 K) with the average reaction time of 2 ms. Stable species were detected using GC combined with MS (GC–MS) only up to indene (C_9H_8). Their model was restricted to depict the formation of PAHs up to naphthalene ($C_{10}H_8$). However, the decay of indene and phenylacetylene observed at the highest experimental temperature conditions could not be captured by the model.

The literature also reports studies of toluene pyrolysis on solid soot particles [105], [106], [117]–[121]. The first work was performed by Graham et al. [117], who reported the formation and growth of soot aerosols in incident shock flows of toluene highly diluted with argon at temperatures in the range 1600-2300 K, at a total carbon concentration in the shock-heated gases of 2.0×10^{17} atoms/cm^3. The soot yield, during the shock flow was determined from extinction measurements at two different visible wavelengths, while the rate of growth of the soot particles was obtained from the variation in the intensity of Rayleigh scattering of a 1 W argon-ion laser beam by the soot particles. It was found that in the light scattering measurements in the early stages of soot formation, a substantial amount of light at both 488 nm and 632.8 nm is absorbed by gas phase molecules and/or radicals rather than by soot particles.

Evans and Williams [105] also performed toluene pyrolysis, to examine the formation of soot in a conventional shock tube. The test gas was 1% of toluene diluted in 99% of Argon, the temperatures range from 715 to 2160 K and the pressure from 40 to 155 kPa. The reflected shock temperature of the gas was determined by measurements of the reflected pressure and the velocity of the incident shock wave and TEM analyses were employed to characterize the particles. The relative concentrations and type of soot produced were correlated to the reflected shock temperatures.

In the early 1990s, Parker et al. [118] analyzed the soot initiation and particle growth in the pyrolysis of C_7H_8 at high inert gas pressures. The experiments were conducted in a conventional shock tube apparatus at low pressure (10, 20, and 30 atm), behind reflected shock waves. Pyrolytic soot formation of dilute fuel systems in Argon between 1500 and 2500 K was examined using multiple wavelength diagnostic capability (389 and 633 nm) and soot yield and induction delay time were measured. What was particularly interesting

in the authors' findings is the soot particle size at 10 to 30 atm: 0.2 to 0.5 μm radius. Alexiou and Williams [119] conducted a similar research. However, their optical set-up was slightly different: soot induction times and rates of soot formation were measured at 633 and 1152 nm by a laser beam attenuation method and these showed an Arrhenius dependence on shock temperature. Soot yields and soot amounts were also measured on high diluted toluene mixtures in Argon (0.5%, 1% and 1.5%). A kinetic model was used to interpret the experimental trends and reasonably reproduced the experimental observations. However, the lack of good quantitative agreement emphasized the urgent need in establishing reliable kinetic data and reaction pathways on the oxidation of the benzyl radical and PAH species. For this reason, other numerical studies were carried out [122]–[127].

More recently, D'Alessio et al. [120] have carried out extinction measurements in the near infrared to follow the formation of carbonaceous particulate in a conventional shock tube. The investigated ranges of temperature and pressure were 1500–2300 K and 8–13 bar, respectively. In addition, through laser techniques, pyrolysis products were characterized by absorption measurements in the wavelength range 300–800 nm, with high time/spectral resolution. Optical diagnostics techniques were also used to study the induction delay time, the soot yield and the particle diameter growth of toluene pyrolysis [106],[121]. De Iuliis et al. [106] performed these measurements at pressure about 500 kPa and for a wide range of temperatures. Xian et al. [121] worked on a lower pressure range: 200-400 kPa. For both works, the dependence of soot yield on the temperature, pressure and fuel concentration was obtained.

2.3.2 Benzene

Benzene (C_6H_6), the simplest aromatic compound, is an essential component of conventional fuels, a relevant intermediate of several combustion processes and a key precursor to soot formation. Several research investigations have suggested that the high temperature chemistry of benzene has significant impact on the formation of heavier PAHs and soot [43].

The identification of gas phase products of benzene pyrolysis is limited even though many studies have been carried out in shock tubes. Kern et al. [129] used shock tube techniques coupled to time-of-flight mass spectrometry (TOF) to investigate the thermal decomposition of benzene (C_6H_6) in dilute inert gas mixtures (21,000 ppm) over a wide range of total pressures (0.21-0.57 atm) and temperatures (1415-2190 K). Concentration profiles were obtained during typical observation times of 700-1000 μs. The major products were C_2H_2 and C_4H_2 with minor amounts of C_6H_2 and C_8H_2 formed at higher temperatures, and no products with molecular weight higher than benzene were observed.

Laskin and Lifshit [130] investigated the thermal decomposition of benzene behind reflected shock waves in a single-pulse shock tube at the pressure of 5 atm, temperatures between 1400 and 2000 K and average reaction time of 2 ms. The major species detected by gas chromatography technique were acetylene (C_2H_2), diacetylene (C_4H_2), biphenyl ($C_{12}H_{10}$) and phenylacetylene (C_8H_6). Sivaramakrishnan et al. [131] studied benzene pyrolysis under elevated pressures (30 - 50 bar) in the temperature range 1200-1800 K for reaction times in the order of 1.2-1.5 ms using a high pressure single pulse shock tube (HPST). The primary species detected using GC were acetylene and diacetylene.

Later, Tranter et al. [132] performed C_6H_5I pyrolysis experiments using a diaphragmless shock tube (DFST) coupled to both a time-of-flight mass spectrometer (TOF-MS) and laser schlieren (LS) densitometry diagnostics for temperatures ranging from 1276 to 1853 K. The LS experiments were carried out at pressures of 22, 54, and 122 Torr, while the TOF-MS experiments were carried out at pressures in the range 500-700 Torr. The authors investigated theoretically and experimentally the self-reaction kinetics of phenyl radicals. In fact, several authors performed kinetic modeling of benzene [26], [116], [133]–[137], but these will not be discussed in the present thesis, once this work is mainly experimental.

Concerning the solid part of the soot, some studies can be found in the literature. Benzene pyrolysis behind a reflected shock wave, similarly to toluene [105], [117], was already described on section 2.3.1. Agafonov et al. [138] analyzed soot formation in the pyrolysis of benzene behind shock waves through an absorption-emission technique, using a 633 nm wavelength laser. The pyrolysis process is accompanied by a decrease in the temperature of the reacting mixture and the soot yield was measured as a function of temperature over wide initial reactant concentration ranges. The benzene concentration varies from 0.18% to 1% and the temperature 1640 – 2680 K. Drakon et al. [139] studied soot formation of C_6H_6/Ar mixtures with addition of H_2, O_2, and CH_4 by laser extinction at the same wavelength as Agafonov et al. [138] and time-resolved temperature measurements via two-color CO absorption using quantum-cascade lasers. The experiments were carried out behind reflected shock waves at temperatures ranging from 1400 to 2600 K and pressure 1.6 – 2.7 bar. A kinetic model of the gas-phase stage of the pyrolysis reactions was also developed and a qualitative kinetics analysis of the effect of various additives on the change in the initial routes of soot formation was carried out based on the gas-phase kinetics simulations. They show that the addition of H_2, O_2, and CH_4 lead only to the suppression of the kinetics pathways towards pyrene formation, which agrees well with experimental observations of a decrease in the measured optical density, hence, soot concentration.

The most recent work on benzene pyrolysis focuses on the influence of the addition of oxygenated hydrocarbons (methanol, ethanol, and n-butanol) and ethers (diethyl ether, dimethoxymethane, furan, and tetrahydrofuran) on soot formation from benzene pyrolysis. Nativel et al. [108] investigated the pyrolysis

process behind reflected shock waves at pressures around 1.4 bar and in the temperature range of 1670–2680 K. Extinction was measured at 633 nm to determine soot optical densities and soot-inception times. Since particle-inception times strongly depend on temperature and the reactive system cannot be considered isothermal because of the high reactant concentration in the shock tube, the temperature was measured as a function of time by two-color infrared absorption based on CO using two quantum-cascade lasers, as previous studies. Both, temperature and measured optical densities were compared to simulations based on a detailed chemical kinetics mechanism from the CRECK Modeling Group.

Toluene

2.3.3 Cyclopentene / Cyclopentadiene

Cyclopentene (CYC_5H_8) is one of the principal cycloalkenes. Its pyrolysis kinetics have been pursued using numerous experimental configurations and methodologies [140]–[152]. Herbinet et al. [141] studied the formation of the first aromatic rings, the thermal decomposition of CYC_5H_8 was examined in a jet-stirred reactor operated at constant pressure (106.7 kPa) and temperature ranging from 773 to 1048 K and under diluted conditions and a residence time of 1 s. Species were quantified using three analytical methods: gas chromatography, synchrotron vacuum ultra-violet photo-ionization mass spectrometry (SVUV-PIMS), and single photon laser ionization mass spectrometry (SPI-MS). The main reaction products found were 1,3-cyclopentadiene and hydrogen and the formation of many unsaturated C2-C6 olefins, di-olefins and alkynes was also observed but in smaller amounts. Besides, benzene, toluene, styrene, indene, and naphthalene were detected from 923 K.

Cyclopentene is consumed mainly through dehydrogenation and ring-opening isomerization reactions leading to the formation of cyclopentadiene (C_5H_6) and pentadiene (LC_5H_8). Interest in cyclopentene originates from its role as precursor of key C5 intermediates, including cyclopentadiene (C_5H_6), whose chemistry strongly affects the formation of PAHs and soot. In general, at typical flame temperatures C_5H_6 is easily converted into cyclopentadienyl radical (C_5H_5), an important intermediate for the formation of high amounts of mono-aromatic hydrocarbons (MAHs) and PAHs [153]–[155].

Cyclopentadiene strongly affects the formation of PAHs and soot as a precursor of naphthalene [156]. For this reason, Roy et al. [157] studied the unimolecular decomposition of C_5H_6 behind reflected shock waves, using shock tube techniques. Atomic Resonance Absorption Spectrometry (ARAS) was used to record the temporal concentration profiles of H-atoms during the pyrolysis of cyclopentadiene under very low concentration conditions. Absorption spectrometry and an optical multichannel analyzer for the detection of acetylene during C_5H_6 pyrolysis were applied. Theory and experiments presented in this work verify quantitatively the decomposition process of the C_5H_5-c radicals. The experiments were carried out in a

temperature that ranged from 1260 to 1600 K and pressures between 0.7 and 5.6 bar. Initial cyclopentadiene concentrations ranged from 0.5 to 120 ppm, diluted in argon.

Before the 2000s, the pyrolysis of cyclopentadiene has been observed in shock waves with two complementary methods: time-of-flight mass spectrometry (TOFMS) and laser-schlieren (LS) densitometry. Kern et al. [158] performed experiments in a conventional shock tube, with pressures ranging from 100 to 450 Torr and temperatures from 1500 to 2500 K. The low-temperature LS experiments show brief, early maxima indicative of chain reaction initiated by C−H fission.

More recent work on cyclopentadiene pyrolysis was not performed in shock tube, but in a tubular continuous flow pyrolysis reactor under both high and low nitrogen dilutions, at a fixed pressure of 1.7 bar and temperature range of 873–1123 K [153]. The new experimental data have been used to further analyze the role of the successive interactions of cyclopentadiene, indene, and naphthalene as well as the recombination and addition reactions of their resonantly stabilized radicals, including revised kinetic parameters.

A detailed experimental and kinetic modeling study of cyclopentadiene (CPD) pyrolysis in the presence of ethene was performed by Vervurst et al. [140]. The copyrolysis of these two fuels was studied in a continuous flow tubular reactor at a pressure of 0.17 MPa and a dilution of 1 mol CPD/1 mol ethene/10 mol N_2. The temperature was varied from 873 to 1163 K, resulting in cyclopentadiene conversions between 1 and 92%. Using an automated reaction network generator, the authors present an elementary step kinetic model for CPD pyrolysis that accurately predicts the initial formation of aromatic products. The model is able to reproduce the product yields measured during the pyrolysis of pure cyclopentadiene and the copyrolysis of cyclopentadiene and ethene.

The latest experimental work on the field presents a novel application of multi-wavelength, multi-species laser absorption methods in the pyrolysis of JP-10 fuel [159]. Two different multi wavelength approaches were used to measure the species from JP-10 pyrolysis in a shock tube at low pressures. A five and seven wavelength (5λ, 7λ) analysis combination produce species time histories for several species, including cyclopentadiene. Details on the cyclopentadiene cross sections are given and numerical simulations are compared to the experimental data.

2.3.4 Ethylene

Ethylene (C_2H_4) is the simplest of the organic compounds known as alkenes, which contain carbon-carbon double bonds. It is produced by heating either natural gas, especially its ethane and propane components,

or petroleum to 800–900°C, giving a mixture of gases from which the ethylene is separated [160]. It is the major intermediate of the fragmentation of large alkanes, thus a fundamental product in pyrolytic and oxidation environments. The pyrolysis of this fuel has been studied since the early 1960s. Skinner and Sokoloski [161] used a single-pulse shock tube to study the kinetics of ethylene pyrolysis in the range 1300 - 1800 K, where the main products were acetylene, 1,3-butadiene and hydrogen. Their goal was to provide the kinetics of acetylene formation and analyze the condensation of butadiene.

Bauerle et al. [162] measured the induction delay time, soot growth rate constants and soot yields were measured at various temperatures, pressures, and C-atom concentrations using light extinction techniques behind a reflected shock wave. The soot produced was also collected on carbon film grids to do transmission electron microscope (TEM) and raster electron microscope (REM) and hence, determine soot particle diameters. The data can be described by a narrow lognormal size distribution, with average diameters of 20-30 nm and the maximum soot yields were observed at temperatures between 1800 and 1950 K.

Ethylene decay reactions by using both time-resolved IR-laser absorption at 3.39 μm and time-resolved IR-emission at 3.48 μm were measured by Hidaka et al. [163]. Pyrolysis of ethylene was studied behind reflected shock waves in the temperature range 1100–2100 K at pressures of 1.5–4.5 atm. The production yields were also analyzed using a single-pulse method and the results were modeled using a kinetic reaction mechanism. C_2H_4 concentration time-histories behind reflected shock waves in ethylene/argon mixture were measured by Pilla et al. [164]. Reflected shock conditions covered temperatures between 1350 and 1950 K, pressures between 1.3 and 3.3 atm, and fuel concentrations of 1% C_2H_4. The experiments were carried out by a 10.5 μm CO_2 laser absorption technique. The absorption cross-section of the fuel was determined over similar pressures and temperatures using both absorption measurements in a heated-cell FTIR and laser absorption/shock tube measurements.

The latest work on ethylene pyrolysis was performed on a shock tube behind reflected shock waves. After completing soot measurements, KC et al. [11] calculated the soot volume fraction, particle size and number densities from the extinction and scattering of a cw Nd:Yag laser at 532 nm. The measured data was then compared against the values simulated using the method-of-moments in Chemkin-Pro and a detailed PAH mechanism.

2.3.5 Acetylene

Acetylene (C_2H_2) is the simplest and best-known member of the hydrocarbon series containing one or more pairs of carbon atoms linked by triple bonds, called the acetylenic series, or alkynes. This fuel is released

to the atmosphere through various industrial waste streams of industries. Because of its vapor pressure (4.04 × 10^4 mm Hg at 25 °C), it exists in the environment exclusively in the form of gas [165], [166].

In the late 1980s, Frenklach et al. [21] demonstrated that soot formation in shock tube pyrolysis of acetylene can be explained by a detailed kinetic mechanism composed of conventional hydrocarbon reactions. The main mass growth was found to proceed through a single dominant route in which fused polycyclic aromatics play a particularly important role: their practically irreversible formation reactions have the effect of "pulling" chains of reversible reactions in which H-atoms reactivate aromatic molecules.

Experimentally, Eremin et al. [167] reported results of time-resolved laser-induced incandescence (TiRe-LII) for particle sizing, laser light extinction for optical density of condensed phase and emission–absorption spectroscopy for the temperature measurements in acetylene pyrolysis. The experiments were carried out behind reflected shock waves in a conventional stainless-steel diaphragm type shock tube in the temperature range of 1600–2400 K and in the pressure range of 5.5–8.5 bar, on a mixture of 3% C_2H_2 diluted in Argon. These techniques were applied simultaneously to study the influence of molecular hydrogen addition on carbon particle formation, 3% of H_2 was then added to the initial mixture. The authors observed that this addition causes a considerable increase of an induction time and a decrease of final particle sizes and optical density of condensed phase. The carbon particle size decreased at about 1.25 times, while the optical density decreased around 2.5 times at the investigated conditions.

Agafonov et al. [168] performed studies of soot formation acetylene pyrolysis behind reflected shock waves over the temperature range from 1700 to 2800 K at a pressure of 3 to 5 bar. The process of soot formation was recorded using the absorption-emission method, which allows to measure the mass of soot particles per unit volume and their temperature. The experimental data was interpreted within a kinetic mechanism that reproduces the time dependence of the soot yield and the temperature of soot particles measured, as well as the concentrations of several key components formed in the early stages of pyrolysis and oxidation of acetylene.

More recently, Drakon et al. [139] worked on the pyrolysis of C_2H_2/Ar behind reflected shock waves. Soot formation was measured by laser extinction at 633 nm. The procedure was already described on section 2.3.2. The formation of PAHs and soot from the pyrolysis of acetylene was also studied in other reactors, such as a quartz tube reactor or flow reactors [169]–[172], through soot-collection and gas-analyses.

2.3.6 Propene

Propene (C_3H_6) is an important intermediate species in many pyrolysis and combustion processes. It has been identified as an intermediate species in the decomposition of propane [173]. Hydrogen abstraction reactions from C_3H_6 or its unimolecular decomposition yield the resonantly-stabilized allyl radical (C_3H_5) which further dissociates to give mainly allene (aC_3H_4) [174]–[178]. The pyrolysis of propene has been the topic of a number of experimental and modeling studies [177], [179], [180].

Propene pyrolysis kinetics was first studied in an atmospheric flow reactor [181]. A relevant study on the field was performed by Kiefer et al. [175]. The authors used laser-schlieren, shock tube methods to determine the rate of initiation in propene pyrolysis. Three different concentrations of propene diluted in Argon were studied (1.834%, 1.997% and 9.998%), in the temperature range of 1670-2460 K. The rate was obtained by a computer simulation assisted extrapolation to the presumed instant of shock heating and the derivation of an initial rate by using calculated frozen reaction conditions.

Recently, Weber et al. [182] analyzed the thermal decomposition of C_3H_6 behind reflected shock waves. The temperature ranges from 1340 to 1910 K and pressures were 0.4, 2.1 and 4.6 bar, while the initial concentrations of propene were in the range 3.5×10^{-11}–1.8×10^{-10} mol/cm^3. Hydrogen atoms were detected time-resolved with atom resonance absorption spectroscopy (ARAS), and rate coefficients of the decomposition reaction $C_3H_6 + M \rightarrow C_3H_5 + H + M$ were determined.

2.3.7 Propyne

Propyne (PC_3H_4) is an alkyne isomer of propadiene and allene. During pyrolysis, propyne undergoes various reactions depending on temperature, partial pressure (when diluted with an inert gas such as argon), and degree of conversion [183]. Several initiation reactions were considered for the thermal decomposition of propyne. These include:

- thermal decomposition to propargyl radical and a hydrogen atom;
- fragmentation reaction with the generation of ethynyl and methyl radicals;
- isomerization to allene.

Further reactions lead to a complex mixture of unsaturated and aromatic compounds. C3 species are involved in important pathways leading to the production of the “first aromatic ring” which is deemed as an essential step in the formation of PAHs and soot. Moreover, the formed aromatics can subsequently react with the C3 species to gain larger aromaticity [184]–[190]. Sun et al.[191] provided experimental and numerical data on the speciation from propylene and propyne pyrolysis by means of shock tube.

Experiments were performed at a nominal pressure of 20 bar over 1050–1650 K. Propyne exhibited a unique two-stage decomposition profile, as the characteristic isomerization to allene dominates in its consumption at moderate temperatures below 1300 K. The authors observed that the formation of benzene is dependent upon the propargyl recombination, and that naphthalene is observed as the most abundant PAH species, followed by acenaphthalene. Besides, indene is formed from the interactions between benzene/phenyl and C3 species, through its non-PAH isomers as intermediates.

Panigrahy et al. [192] provided new experimental data for ignition delay times, pyrolysis speciation profiles and flame speed measurements of propyne. Concerning the pyrolysis, experiments were performed in a single-pulse shock tube at 2 bar pressure and in the temperature range 1000–1600 K. A detailed chemical kinetic model is provided to describe the pyrolytic and combustion characteristics of propyne across this wide-ranging set of experimental data. Important reactions were highlighted through sensitivity and flux analyses. On the other hand, Johnson et al. [193] presented a two novel laser absorption diagnostics for allene and propyne. Quantum cascade lasers (1930.38 cm^{-1} and 1233.3 cm^{-1}) were chosen as the wavelengths for a two-species, two-wavelength diagnostic pair that minimizes interference from other species. Absorption cross sections were measured at different wavelengths over a wide range of temperature (1196–1502 K) and above atmospheric pressure (1.3–1.6 atm). Once characterized, these diagnostics were employed to measure the mutual isomerization rates of propyne over the same temperature range. These rates were found to be in excellent agreement with limited past experimental determinations and recently computed rates. Using these rates, the equilibrium constant is also reported as a function of temperature.

2.3.8 Benzene, toluene, and cyclopentene based mixtures

Real fuels are mostly a mixture of various hydrocarbons ranging from paraffin to aromatics. Blended fuels containing at least two components can have enhanced combustion characteristics than the single components alone [194]–[198], including enhanced PAH formation and soot emissions, fuels' reactivity and so on.

Few previous works studied the binary benzene and toluene-based mixtures through experimental and kinetic modeling approaches. The shock tube co-pyrolysis of benzene and acetylene was studied in the temperature range 1560-2580 K at pressures of 6 and 60 bar, using a light absorption technique [199]. A remarkable increase in soot formation was observed compared to the pyrolysis of pure benzene and pure acetylene. Similar experiments were performed to investigate both pure benzene and benzene + acetylene mixture pyrolysis, however, using flow reactor techniques [133]. C_2H_2 addition to C_6H_6 induced the

production of phenylacetylene and phenanthrene at low temperatures, while no significant influence was observed at high temperatures.

Recently, a single-pulse shock tube facility coupled to the gas chromatography-mass spectrometry was used to study interactions between toluene/benzyl and the common C3 combustion intermediates, toluene-propylene and toluene-propyne co-pyrolysis [191], [200]. Temperature-dependent mole fraction profiles are obtained for numerous species ranging from small-molecule products to three-ring polycyclic aromatic hydrocarbons (PAHs). Increased reactivity is observed in the conversion of toluene with the presence of propylene or propyne, while the consumption rates of the studied C3 fuels are barely influenced by toluene. Benzene formation is facilitated by the C3+C3 reactions introduced by the C3 fuels. The pyrolysis of propylene (or propyne) significantly enhances the level of C1−C3 molecules/radicals that further react with aromatic species.

The influences of acetylene and ethylene addition on the species formation from toluene pyrolysis was also studied in the same experimental set-up. With the neat toluene decomposition profiles as a reference, both fuel components exhibit increased reactivity in the pyrolysis of all studied binary mixtures, indicating the existence of obvious synergistic effects [201]. In particular, such effects become more remarkable when increasing the initial acetylene concentration. This essentially results from the addition-elimination reaction of a toluene fuel radical and a C2 fuel molecule leading to a C9 molecule and a hydrogen atom. A similar study was carried on the pyrolysis of phenylacetylene with and without the presence of C2 hydrocarbons [25]. It was found that the bimolecular reaction between phenylacetylene and hydrogen atom leading to phenyl and acetylene dominates phenylacetylene decomposition throughout the temperature window. The addition/elimination reactions between phenylacetylene and phenyl not only produce hydrogen atoms to maintain the reactivity of the fuel decay, but also directly lead to the formation of several $C_{14}H_{10}$ PAH isomers.

Later on, a combined experimental and kinetic modeling study was carried out to explore the influences of added acetylene, ethylene, propylene, and propyne on the reaction schemes of benzene pyrolysis once again in a single-pulse shock tube coupled to gas chromatography-mass spectrometry technique [202]. Various considerations apply to all studied binary mixtures. The addition of C2- and C3- to the reaction system leads to acetylene formation, and consequently promotes the HACA mechanism. Particularly, in benzene-C_2H_4 co-pyrolysis, naphthalene and acenaphthylene are mainly formed through reactions between PAH radicals and ethylene. Concerning benzene-C3 co-pyrolysis, indene is the major C9 species resulting from the reaction of benzene/phenyl with C3 fuels. All the above studies were performed in the laboratory "ICARE-CNRS" by the 'Onde de Choc' team [25], [191], [200]–[202].

The most recent publication [156] concerns the pyrolysis of cyclopentene with and without the presence of acetylene, new experimental insights on the PAH formation from cyclic C5 species. The kinetic model emphasizing on PAH chemistry can well interpret how cyclopentene is consumed under high-pressure pyrolytic conditions, and how the resulting intermediates react to form PAHs, and furthermore, how the extra acetylene impacts the reaction schemes. In all the investigated cases, cyclopentene mainly decomposes into linear pentadiene and cyclopentadiene. Their consumption mainly contributes to the formation of small hydrocarbons and cyclopentadienyl radical (C_5H_5), respectively. C_5H_5 either decomposes to form small molecules or reacts with other species. When extra C_2H_2 is introduced to the reaction system, cyclopentene decomposition reactivity is negligibly influenced, but the PAH speciation is slightly altered.

2.4 Optical diagnostics techniques

Diagnostics techniques are powerful tools to investigate and characterize combustion phenomena. They can be classified as intrusive and non-intrusive techniques [203]. Physical probing methods are intrusive and present a major disadvantage: combustion processes, despite their hostility, are easily perturbed. Physical probes can alter the fundamental flame behavior they attempt to investigate. In addition, physical probes are generally limited in both their spatial resolution and temporal response.

Laser diagnostics are considered non-intrusive techniques. They supply the capability for remote, in-situ (at the measurement location), spatially and temporally precise measurements of important chemical parameters.

Laser probing also presents several advantages. The techniques are remote and, almost always, nonperturbing. Temperature and species concentrations are measured directly and they are capable of simultaneous high spatial and temporal resolution. On the other hand, a major limitation of this procedure is the requirement for optical access to the test volume. It often requires the addition of windows to an enclosure. In some cases, these can be eliminated by the use of fiber optics or small uncovered apertures if the pressure loss is not a factor to be considered.

Laser techniques permit the investigation of very processes observed at low light intensities. Large amounts of energy can be delivered in very short periods of time permitting instantaneous measurements and freezing of phenomena that quickly change.

There are a large number of laser spectroscopic techniques potentially applicable to analyze the combustion phenomena. In this section an overview of the following soot optical diagnostics is given:

1. Extinction technique
2. Scattering
3. Fluorescence
4. Laser-Induced Incandescence (LII)
5. Two-color emission technique

The techniques listed above are based on different physical phenomena and they are complementary, allowing to obtain different information. More focus will be given on the extinction and scattering techniques, since these were the techniques employed in the present thesis.

The application of one technique instead of another depends on the experimental conditions involved. Light absorption consists in the attenuation of radiation at specific wavelengths as molecules are promoted from lower to higher internal energy states. Then, absorption techniques are mainly used for detection and monitoring of constituents in gas phase. Their spatial resolution is limited as long as they provide measurements averaged over the light path into the absorbing medium.

2.4.1 Extinction technique

Light extinction is the sum of absorption and scattering. Extinction is a well-established technique based on the measurement of a monochromatic light intensity transmitted through a given medium [18], [204]. When laser light passes through an absorbing medium, light extinction occurs. The Beer-Lambert's law relates the attenuation of light to the properties of the material through which the light is traveling. According to this definition, the transmittance TR_λ can be written as:

$$TR_\lambda = ln\frac{I_L}{I_0} = -K_{ext} \cdot L \tag{2.1}$$

where I_L is intensity of the emerging laser beam and I_0 is the incident one. The natural logarithm of these parameters is related to the extinction coefficient K_{ext} (expressed in cm^{-1}) and L (in cm) is the path length in the medium. The extinction coefficient can be expressed as follows:

$$K_{ext} = N_p(\sigma_{scatt} + \sigma_{abs}) = K_{scatt} + K_{abs} \tag{2.2}$$

in which N_p ($\#/cm^3$) is the particle number density and σ_{abs} and σ_{scatt} are the cross sections for absorption and scattering, respectively.

Measuring light extinction results from a combination of absorption and scattering. It provides absolute soot volume fractions (f_v) if the optical properties are known. In particular, in absorbing media the refractive

index can be expressed as a complex number ($m = n - ik$), and its imaginary part k describes the direct attenuation of an electromagnetic wave.

When the particles are monodispersed and spherical and their size is much smaller than the wavelength of the incident radiation, then the absorption coefficient can be expressed as a function of the soot volume fraction, f_v, according to relation (2.3):

$$K_{abs} = \frac{\pi^2 \cdot d^3 \cdot E(m) \cdot N_P}{\lambda} \tag{2.3}$$

In this equation, $E(m)$ is a function of the real, n, and imaginary, k, part of the refractive index m ($m = n - ik$) according to the following expression:

$$E(m) = -Im\frac{m^2 - 1}{m^2 + 2} = \frac{n \cdot k}{(n^2 - k^2 + 2) + 4n^2k^2} \tag{2.4}$$

and the definition of the soot volume fraction, f_v, is

$$f_v = \frac{\pi \cdot d_p^3 \cdot N_p}{6} \tag{2.5}$$

This equation provides the soot volume fraction as function of the total number of primary particles per unit volume and the soot particle diameter, d_p. By taking into account the expressions (2.1), (2.3) and (2.5), the value of f_v can be determined as the classical formula:

$$f_v = \frac{-ln\frac{I_L}{I_0}\lambda}{6\pi LE(m)} \tag{2.6}$$

If L is expressed in meters and λ in microns then f_v is obtained expressed in ppm, which indicates the millionths of the volume occupied by soot. There are some uncertainties regarding this parameter due to *E(m)*. In addition, as mentioned before, the theory behind the measurement of soot volume fraction is based on several assumptions: the medium through which the laser passes is homogeneous, the particles are spherical and monodispersed, the multiple scattering is negligible and the particle diameter is much smaller than the wavelength of the light source. Many of these assumptions are not completely rigorous. Although the diameter of the particles is usually much smaller than the wavelength of the laser, the particles are, on the other hand, neither really monodispersed nor really spherical according to the experimental conditions [205].

Even if the previous hypotheses are valid, the complex refractive index still varies a lot in the literature (30 to 50%) [206] which results in nearly a factor of 4 in *E(m)*. This variation induces a large source of uncertainty in the measurement of the soot volume fraction. A summary of the different refractive indices determined in the visible spectral range is provided in **Table 1**. The refractive index describes the direct

attenuation of an electromagnetic wave in a given medium. $E(m)$ is a function of the real, n, and imaginary, k, part of the refractive index m ($m = n - ik$).

Table 1 *Refractive indexes of soot determined in the visible spectral range*

Authors	Real part	Imaginary Part
Erickson et al. [207]	1.4	1
Dalzell and Sarofim [208]	1.57	0.56
Chippett and Gray [209]	1.9 - 2.0	0.35 – 0.50
Bockhorn et al. [210]	1.1	0.37
Lee and Tien [211]	1.8 – 2.0	0.45 – 0.65
Chang and Charalampopoulos [212]	1.94	0.6

Another parameter that can be derived from extinction measurements is the optical density, D_{633} (m^2/mol), which is a purely experimental property that is not affected by assumptions concerning the optical properties of the condensed species [213], [214]. It can be defined as:

$$D_{633} = \frac{\ln\left(\frac{I_0}{I_L}\right)}{[C]L} \tag{2.7}$$

where [C] is the total carbon concentration related to soot in the mixture.

2.4.2 Scattering

Scattering, as defined in physics, is a change in the direction of motion of a particle because of a collision with another particle [166]. Rayleigh scattering, Mie scattering and Raman scattering are techniques employed in the combustion field, but only Rayleigh scattering will be discussed with deeper details.

Raman scattering is the inelastic scattering of light from molecules. It is ideally suited to combustion diagnostics and has been widely applied in flames [215], [216]. Visible or ultraviolet wavelength lasers are typically employed, but no specific wavelength is required. Raman scattering shows an unearthly reaction that is moved from the laser line. This shift is trademark for the Raman dynamic particles and permits to gauge all significant species focuses on the same time, for example, O_2, N_2 and hydrocarbon fuels. These species can be measured along with the gas temperature. The main disadvantage of this technique in the gas phase is the weakness of the signal, about six orders of magnitude less than Mie scattering.

Mie scattering is the elastic scattering of light from atomic and molecular particles which diameter is larger than the wavelength of the incident light [217]. The Mie signal intensity is proportional to the square of the particle diameter and strongly dependent on the size, shape and density of the diffuser, as well as the scattered angle. It appears then difficult to determine particle dimensions and densities in gaseous mixtures. Nevertheless, one can notice that Mie scattering technique is often developed to measure flow velocities applying Laser Doppler Anemometry (LDA) or Particle Image Velocimetry (PIV). It is important to highlight that Mie scattering is much stronger than Rayleigh scattering. Therefore, a potential source of interference for this weaker light scattering process.

Rayleigh scattering is the elastic scattering of light by particles much smaller than the wavelength of the light. This technique arises from the induced polarization oscillating at the same frequency as the incident radiation. The induced polarization is dependent on the nuclear positions of the molecule and is modulated by the rotation and/or vibration of the molecule. After interaction with the incident photon, the molecules return to the same state they were previously and, since there is no energy exchange, the scattered photons reside at the same frequency as the incoming photons.

This technique can be employed for total density measurements, but generally not for individual species concentrations. Due to its high signal strength, it is a very powerful tool for investigating fundamental turbulent combustion processes in specific experiments. In addition, Rayleigh scattering requires either constant gas composition or known mole fractions of all major species for the density measurement of a gas mixture. In some cases, Rayleigh scattering is stronger for one species than others are, and it can be used to image mixing processes such as fuel – air mixing. It is much weaker than Mie scattering but more than three orders of magnitude stronger than Spontaneous Raman Scattering.

The classical method of scattering allows to derive soot particle diameter and number density applied to a system of isolated and monodisperse spherical monomers. In this technique, a vertically polarized laser light is sent into the probe volume under investigation and the vertically polarized scattered light, usually collected at 90º, is detected [218]. In the Rayleigh regime, the scattering cross section of a single particle is given by [219], [220]:

$$C_{VV}^{p} = C_{p}^{6}\frac{F(m)}{K^{2}} = \frac{\pi^{4}\cdot d_{p}^{6}}{4\,\lambda_{scatt}^{4}}F(m) \tag{2.8}$$

where the particle size parameter is $x_p = {\pi d_p}/{\lambda_{scatt}}$ and $K = {2\pi}/{\lambda_{scatt}}$ is the incident wave vector and $F(m)$ is a function of the refractive index of soot. The cross-section value is used to obtain the scattering intensity measured at the detector, given as:

$$I_{VV} = \eta \cdot I_0 \cdot N_p \cdot C_{VV}^p \tag{2.9}$$

where I_0 is the incident laser intensity and η is the instrumentation efficiency. Combining the extinction with the scattering measurements the particle diameter and the number density can be determined:

$$d_p = \left(\frac{\lambda_{scatt}^4}{\lambda_{abs}}\right)^{\frac{1}{3}} \left(\frac{4E(m)K_{VV}}{\pi^2 F(m)K_{abs}}\right)^{\frac{1}{3}} \tag{2.10}$$

$$N_p = \frac{6f_v}{\pi d_p^3} \tag{2.11}$$

And K_{VV}, the differential scattering coefficient of a calibration gas, is defined as $K_{VV} = N_p \cdot C_{VV}$.

2.4.3 Other soot optical diagnostics

Fluorescence is the spontaneous emission of radiation subsequent to an advancement of the molecule to an excited state. This phenomena can occur by various means, such as electron bombardment, heating, chemical reaction (chemiluminescence) or photon absorption [221]. In other words, fluorescence should be considered as the sequence of an optical absorption process followed by a spontaneous emission event.

Laser-induced fluorescence (LIF) is the spontaneous emission of radiation by atoms or molecules that have been excited by laser radiation. It is applied in combustion processes to measure the concentration of species and temperature, determine pressure and velocity. In this technique, molecules or atoms are excited electronically from the fundamental electronic level by laser radiation absorption. After excited, the species can decay to the fundamental electronic level by the spontaneous emission of photons. Fluorescence is proportional to the number of species that absorb radiation.

LIF should not be mistaken with LII, laser induced incandescence. LII is a technique based on the absorption of high-power laser pulse by particles. As particles interact with the laser and absorb light, their temperatures get higher, leading to a strong non-linear increase in thermal radiation. This results in an increase of the internal energy and on the release of this energy with the emission of a typical grey body thermal radiation. During the laser pulse, the particles reach a temperature well above the flame temperature. This technique is used to measure soot particle sizes.

LII has become a useful tool for in situ measurements of mature-soot particles in combustion and ambient atmospheric environments [15]. There are several key components to an LII setup for either pulsed or continuous-wave (CW) LII, they include a laser system, usually the fundamental and second harmonic of the Nd:YAG laser. The soot aggregates are idealized as composed by particles with the same diameter and touching at one point during LII experiments [222].

Two-color pyrometry has long been used to measure flame temperature and soot concentration from radiative emission in flames [223]. It is a suitable diagnostic for semi-quantitative or qualitative measurements once it requires minimal optical access and can employ high-speed imaging to accomplish remarkable temporal and spatial resolutions. Essentially, soot radiation emitted from a flame is detected at two different wavelengths and compared with the radiation emitted from a calibrated light-source.

2.5 Ex-situ analysis: soot sampling and TEM analysis

The transmission electron microscopy (TEM) analysis allows to visualize the texture of the soot and to determine the size of the particles and the their internal structure [9], [224]. The structure of soot from different fuels and at different conditions has been studied in detail by several authors, i.e. [206], [225]–[227]. In general, a characteristic structure with carbonaceous planes (crystallites) has been described. These crystallites are stacked in basic structural units, oriented in a parallel manner in the outer crown of the soot and randomly in the core of the soot.

The transmission electron microscope uses monokinetic electrons to form the image of an object. The sample is crossed by a part of the emitted electrons with a change of their energy, another part of the electrons is diffracted without change of energy and a last part of these electrons can be transmitted without interaction. In the end, all these electrons allow the formation of an image of the object.

These electrons have the same speed v and by applying the De Broglie's theory, a particle in motion is associated with a wavelength λ:

$$\lambda = \frac{h}{mv} \tag{2.12}$$

Where h is Planck's constant and m is the electron's mass. Thus, for an accelerating voltage of 200 kV, the wavelength is 2.54×10^{-3} nm [206]. The shorter the wavelength, the higher the theoretical resolution. In **Figure 2.3** TEM micrographs of soot primary particles from toluene pyrolysis are presented, as an example. The micro-texture of these primary particles was constituted of a concentric arrangement of basic structural units (BSU) leading to an onion-like micro-texture [228]. In toluene-based mixtures, it was shown that the size of these units increases with temperature whereas mean interlayer spacing decreases.

In principle, from TEM analysis information about essential soot parameters can be derived. This technique, anyway, is intrusive or it requires soot sampling, difficult to be applied in hostile environment, and also time-consuming. For that, usually it is implemented to perform a validation of optical techniques [15].

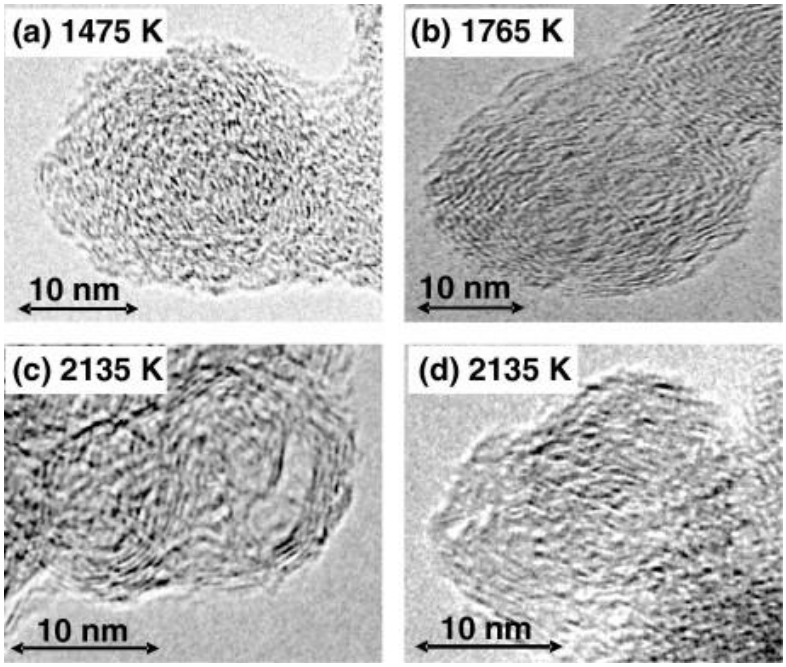

Figure 2.3 *TEM micrographs of soot primary particles from toluene pyrolysis [229]*

3 Experimental Set-Up

3.1 The shock tube theory

The shock tube is an ideal reactor. In this device, a plane shock wave is produced by the sudden bursting of a diaphragm, which separates a gas at high pressure from one at lower pressure. A shock wave is different than a sound wave in the sense that the latter is produced when energy in the form of disturbance propagates and it is carried along due to the particles' vibration [230]. It is a small amplitude compression wave that propagates at the local sound speed and leaves the state of the medium unchanged. A shock wave, however, can only be produced when any object travels faster than the speed of sound. In other words, a shock front is a wave that abruptly changes the state of the supersonic approaching gas. The gas is generally at a higher temperature and pressure after it has passed through the shock compared to its initial state. Furthermore, the shock front is a region where thermodynamic processes are irreversible. In shock tubes, due to the passage of a shock wave, the mixture under study is brought almost instantly to a known and controlled temperature and pressure, up to high values typical of internal combustion engines [231], [232].

It is important to highlight that sound waves and shock waves are co-related. A sound wave is propagated through a gas in the form of a weak isentropic adiabatic compression [231]. The rate at which the sound is propagated is given by equation

$$a = \sqrt{\frac{\gamma\, P}{\rho}} = \sqrt{\frac{\gamma\, RT}{M}} \tag{3.1}$$

The specific heat ratio is given by γ and the other parameters presented on equation 3.1**Error! Reference source not found.** are properties of the ideal gases. The classical ideal gas law may be written as:

$$PV = nRT \tag{3.2}$$

The shock tube is an adiabatic reactor during the typically short observation times negligible energy transfers and molecular diffusion to the wall occur. In addition, the existence of a boundary layer permits to neglect heterogeneous reactions at the walls. In the boundary layer, the gases are at wall temperature and the temperature gradient is very large in relation to the gases in the reactor. These characteristics facilitate the use of shock tube for following the progress of chemical reactions or physical processes.

In the shock tube, the heating occurs almost instantly. This means that the fundamental processes at selected temperature may be studied without interference from surface reactions. A simple scheme of the shock tube is shown on **Figure 3.1(a)**. **Figure 3.1(b)** shows the time evolution of the thermodynamic states as a function of the tube axis, where five different regions can be observed:

- Region 1 - undisturbed low-pressure gas, with initial pressure and temperature, P_1 and T_1;
- Region 2 - between the shock front and contact surface, P_2 and T_2;
- Region 3 - between the contact surface and rarefaction fan, P_3 and T_3;
- Region 4 - high pressure gas, with initial pressure and temperature, P_4 and T_4;
- Region 5 – region behind the reflected shock wave; when the incident shock wave reaches the end of the tube and it is reflected back (reflected shock wave) into the gas at conditions P_2 and T_2, resulting in an additional increase of pressure and temperature, P_5 and T_5.

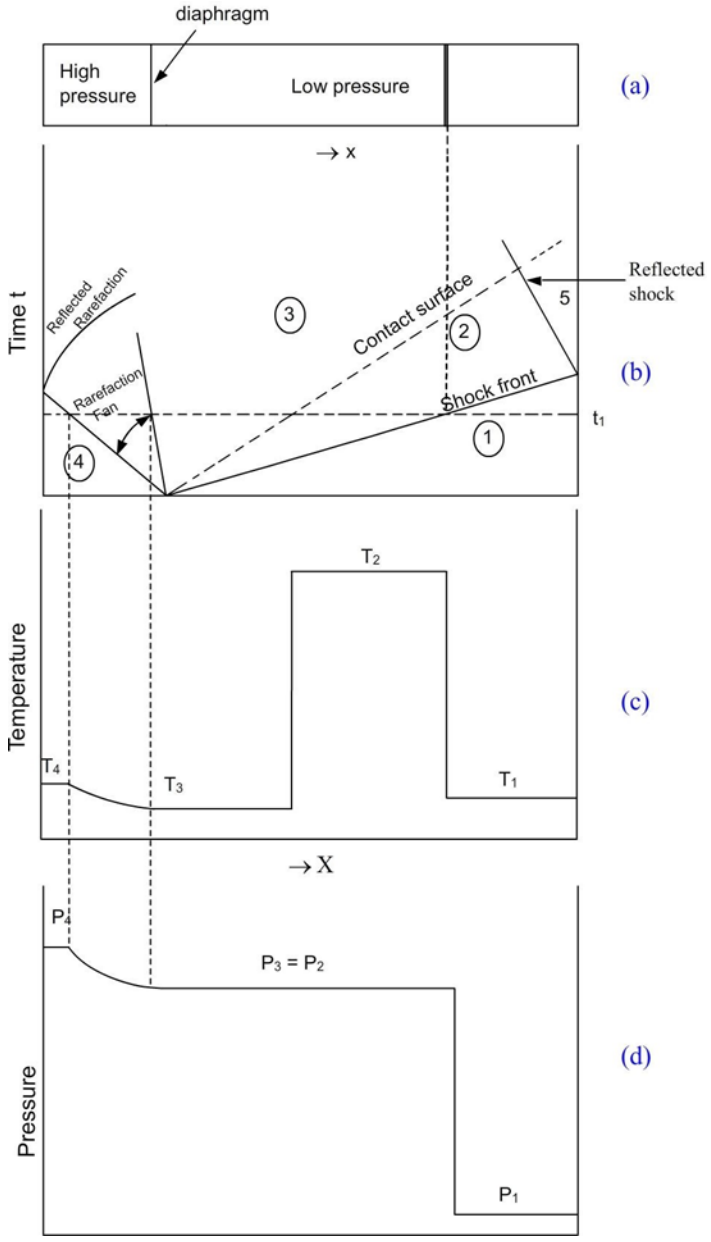

Figure 3.1 (a) *The shock tube,* ***(b)*** *The shock tube wave diagram,* ***(c)*** *Temperature history in the shock tube,* ***(d)*** *Pressure history in the shock tube [233]*

Figure 3.1(c) and **Figure 3.1(d)** show temperature and pressure along the shock tube axis, respectively. At the breaking of the diaphragm at time 0, a series of compression waves are generated traveling along the driven section. These shock waves are of increasing strength; thus, they finally coalesce to form a unique shock wave (incident shock wave). At the same time, a series of rarefaction waves are formed and travel in the opposite side. These rarefaction waves constitute the rarefaction fan. Moreover, in **Figure 3.1** some important concepts are introduced. The first one is the shock front, which can be defined as is the advancing edge of a shock wave. Second is the contact surface, the separation between the driven and driver gases, which follows the shock front.

The formation of a plane shock wave can be seen in **Figure 3.2**. Considering a long tube with a piston at one end and supposing that the piston is capable of accelerating to a constant velocity, $v > a$, with small increments, dv, the shock wave is formed:

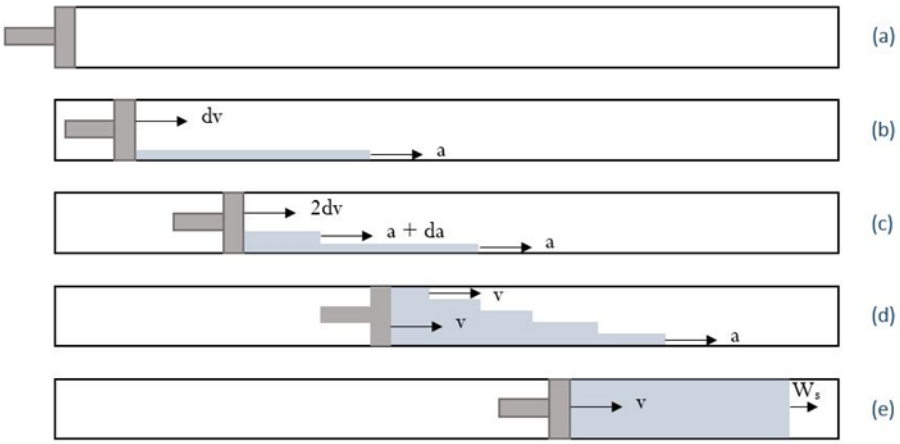

Figure 3.2 *Schematic model of shock-wave formation (adapted from [231])*

After many increments, dv, the gas accelerates and the piston reaches the velocity v. The waves coalesce to form a single step wave front, in which exist large gradients of pressure, density, temperature and moves with a speed, W_S. The gas flow velocity changes across the front due to the collision between molecules. This process is irreversible and an increase in entropy occurs.

In the normal shock tube, a diaphragm holding back a driver gas at high pressure replaces the piston in above example. **Figure 3.3(a)** shows the definition of the gas parameters in the region associated with a shock wave. P, ρ and T are the pressure, density and temperature of the gas and v is the velocity of the gas molecules relative to the shock tube. **Figure 3.3(b)** exhibits the relative velocities u_1 and u_2 in the shock front. It is important to highlight that, for most applications, $v_1 = 0$. W_S is the velocity of the shock front relative to the tube and u is the gas velocity measured in shock-fixed coordinates.

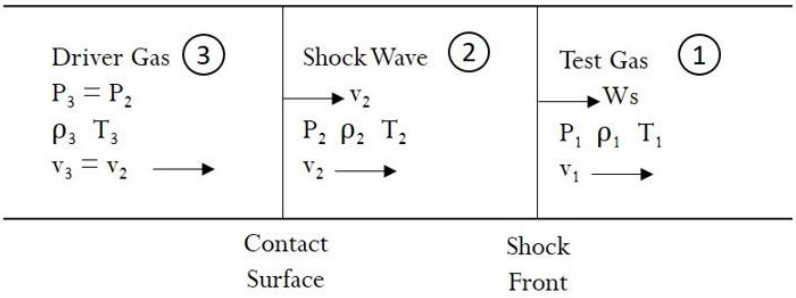

(a) Shock Tube at rest - Laboratory fixed coordinates

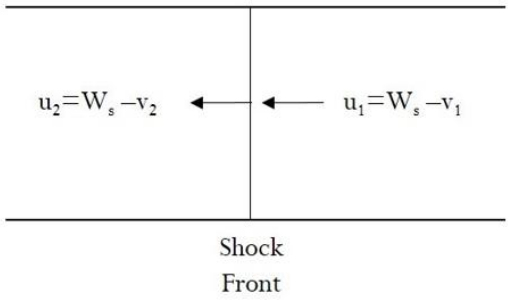

(b) Shock Front at rest - Shock fixed coordinates

Figure 3.3 *Gas parameters associated with shock wave in two coordinate systems (adapted from [233])*

The equations of mass, momentum and energy conservation for the incident shock wave must be considered:

$$\rho_1 u_1 = \rho u_2 \tag{3.3}$$

$$\rho_1 u_1^2 + P_1 = \rho_2 u_2^2 + P_2 \tag{3.4}$$

$$\frac{1}{2}u_1^2 + h_1 = \frac{1}{2}u_2^2 + h_2 \tag{3.5}$$

h_1 and h_2 are the initial and final gas unit mass enthalpies. Equation (3.5) assumes no heat exchange in the shock wave. This is reasonable since the time flow in most shock tubes is usually of the order of milliseconds and heat losses by conduction are consequently negligible. By definition, enthalpy is equal to the system's internal energy plus the product of its pressure and volume. The shock parameters in an ideal gas can be derived from the above equations. For a gas with a constant specific heat ratio, $C_p/C_v = \gamma$, the equation for the enthalpy h can be written as:

$$h = \left(\frac{\gamma}{\gamma - 1}\right) RT = \left(\frac{\gamma}{\gamma - 1}\right)\frac{P}{\rho} \tag{3.6}$$

Rewriting the conservation of energy, equation (3.5), removing u_1 and u_2:

$$\left(\frac{\gamma}{\gamma-1}\right)\frac{P_1}{\rho_1}+\frac{1}{2}u_1^2=\left(\frac{\gamma}{\gamma-1}\right)\frac{P_2}{\rho_2}+\frac{1}{2}u_2^2 \rightarrow \frac{\rho_1P_2-\rho_2P_1}{\rho_2P_2-\rho_1P_1}=\frac{\gamma-1}{\gamma+1} \tag{3.7}$$

Combining equations (3.3) and (3.4) it is possible to find a simpler relation to the pressure ratio:

$$\frac{P_2}{P_1}=1+\frac{\rho_1u_1^2}{p_1}\left(1-\frac{\rho_1}{\rho_2}\right) \tag{3.8}$$

At this point, the Mach number should be considered. This adimensional number provides the ratio of the velocity of a disturbance or a flow and the local speed of sound in the gas, $M_1=u_1/a_1$. When the gas ahead is stationary, $v_1=0$, therefore, $u_1=W_s$. Hence:

$$M_1=\frac{W_s}{a_1}=u_1\left(\frac{\rho_1}{\gamma p_1}\right)^{\frac{1}{2}} \tag{3.9}$$

It is important to take into account the Rankine-Hugoniot equations [234]–[236]:

$$\frac{P_2}{P}=\frac{1-\left(\frac{\gamma-1}{\gamma+1}\right)\frac{\rho_1}{\rho_2}}{\frac{\rho_1}{\rho_2}-\frac{\gamma-1}{\gamma+1}} \tag{3.10}$$

$$\frac{\rho_2}{\rho_1}=\frac{\frac{\gamma-1}{\gamma+1}+\frac{P_2}{P_1}}{\left(\frac{\gamma-1}{\gamma+1}\right)\frac{P_2}{P_1}+1}=\frac{u_1}{u_2} \tag{3.11}$$

Through equation (3.9), it is viable to write the Rankine-Hugoniot equations as functions of the Mach number:

$$\frac{P_2}{P_1}=\frac{2\gamma M_1^2-(\gamma-1)}{\gamma+1} \tag{3.12}$$

$$\frac{\rho_2}{\rho_1}=\frac{(\gamma+1)M_1^2}{(\gamma-1)M_1^2+2} \tag{3.13}$$

$$\frac{T_2}{T_1}=\frac{\left(\gamma M_1^2-\frac{\gamma-1}{2}\right)\left(\frac{\gamma-1}{2}M_1^2+1\right)}{\left(\frac{\gamma+1}{2}\right)^2M_1^2} \tag{3.14}$$

From these three relations, pressure, density and temperature in a shock wave through an ideal gas may be obtained. However, these parameters are found only if the initial conditions and W_S are known, the specific heat ratio is constant.

It is important to consider the dependence of shock strength on diaphragm pressure ratio. In practical applications, this ratio is function of the material of the diaphragm and its thickness. Moreover, the strength

of a shock wave initiated in a gas depends not only on the pressure ratio applied across the diaphragm but also on the physical properties of the two gases used. Therefore, it is required to develop an expression for the pressure ratio between these sections. The process is isentropic, and the gases are ideal:

$$PV^{\gamma} = constant \rightarrow \frac{2a}{\gamma - 1} + v = constant$$

Considering **Figure 3.1(b)**, one can observe that the driver gas at high pressure P_4 in region 4 is expanded through the expansion fan to a lower pressure P_3 behind the contact surface in region 3. On each side of the contact surface the particle and pressures must be continuous because no gas flow takes place across this interface, thus $v_3 = v_2$ and $p_3 = p_2$. For an ideal gas $\gamma_4 = \gamma_3$ and since the unexpanded driver gas in region 4 is still at rest, $v_4 = 0$. These assumptions lead to the following expression:

$$\frac{P_4}{P_2} = \left(\frac{a_4}{a_4 - \frac{\gamma_4 - 1}{2} v_2} \right)^{\frac{2\gamma_4}{\gamma_4 - 1}} \tag{3.15}$$

The last step of this deduction is to derive an expression for v_2. This can be done taking in account the conservation of mass, energy and momentum along with equation (3.13):

$$v_2 = \frac{2a_1}{\gamma_1 + 1} \left(M_1 - \frac{1}{M_1} \right) \tag{3.16}$$

Now all the parameters required to write the pressure ratio as a function of Mach number, specific heat ratio of both gases and their respective sound velocities are given:

$$\frac{P_4}{P_2} = \frac{2\gamma_1 M_1^2 - (\gamma_1 - 1)}{\gamma_1 + 1} \left[1 - \frac{\gamma_4 - 1}{\gamma_1 + 1} \frac{a_1}{a_4} \left(M_1 - \frac{1}{M_1} \right) \right]^{-\frac{2\gamma_4}{\gamma_4 - 1}} \tag{3.17}$$

A low-density such as hydrogen or helium, is most frequently used to drive a shock wave. By increasing the temperature and consequently the sound speed in the driver gas, the shock strength may be also increased. It is crucial to highlight that the incident shock waves can be used as tools to investigate a physical or chemical change in the driven gas. The time during which observations can be made on the gas at the elevated condition T_2 and P_2 behind the shock front is limited by the arrival of the contact surface at the measuring station in the tube. Another factor that needs to be taken in consideration when working behind the incident shock wave is the fact that the gases are in motion with velocity v_2.

When a primary or incident shock wave reaches the end of a shock tube it will be reflected back into the gas which has already been heated by the passage of the incident shock. This results in a further increase of the temperature, pressure and density of the gas. This is how a reflected shock wave is produced. It is a suitable tool to allow high temperature and density to be reached with relatively low P_4/P_1 ratios. In addition,

the speed of the reflected shock front is always less than that of the incident shock and as the gas particles behind the reflected shock wave are at rest relative to the tube, the observations on a fixed group of particles throughout their heating and compression can be carried out. The following equations behind a reflected shock wave:

$$\frac{P_5}{P_1} = \left[\frac{2\gamma M_1^2 - (\gamma - 1)}{\gamma + 1}\right]\left[\frac{(3\gamma - 1)M_1^2 - 2(\gamma - 1)}{(\gamma - 1)M_1^2 + 2}\right] \tag{3.18}$$

$$\frac{T_5}{T_1} = \left[\frac{2(\gamma - 1)M_1^2 - (3 - \gamma)}{(\gamma + 1)^2}\right]\left[\frac{(3\gamma - 1)M_1^2 - 2(\gamma - 1)}{M_1^2}\right] \tag{3.19}$$

These relations are valid only if γ is constant. In the experiments, the variation of γ as a function of the temperature is considered by solving the continuity equation iteratively. The uncertainties in the parameters T_5 and P_5 are related to the uncertainties on the Mach number determination and in the thermodynamics parameters of the investigated gases.

One last parameter to be analyzed is the observation time. It can be referred as the time available for the measurements in the uniform region behind the reflected shock wave. Two events are responsible for the perturbation of the uniform conditions behind the reflected shock wave, which consequently lead to an interruption of the observation time. The first one is the arrival of the reflected rarefaction head to the location where the observation occurs. This event abruptly decreases the pressure and the temperature of the experimental gas and can be manipulated by either increasing the driver section length or adding a portion of heavy gases into the driver gases. Argon or nitrogen is added to the driver gas mixture (originally composed of helium or hydrogen) to slow down the reflected rarefaction head and thus increase the observation time.

The second factor that limits the observation time depends on the nature and the subsequent wave pattern formed by the interaction between the reflected shock wave and the contact surface. In the usual situation when $\gamma_2 = \gamma_3$, the interaction between the reflected shock wave and the contact surface leads to varying results depending on the relative velocities of the gases in region 2 and 3. When $a_2 > a_3$, the reflected shock after passing through the contact surface enters a region of higher Mach number. The resultant properties in the region 3 would be greater than those in region 2. Since, across the contact surface equality of pressure is required, an additional shock is generated in region 5. On the contrary, when $a_2 < a_3$, the Mach number will fall across the interface and an expansion wave is required to restore the pressure equality. Hence in both cases, the reflected shock region is disturbed by an additional waves generated, and the observation time can be obtained using the following expression derived in reference [231].

$$\Delta\tau = \left[\frac{x_1}{M_1 . a_1}\right]\left[\frac{(\gamma - 1)}{2\gamma}\right] \quad (3.20)$$

x_1 is the length of the driven section. In order to have larger observation times behind the reflected shock, a_2 is designed to be the same as a_3. In fact, when a_2=a_3, the pressure across the interface is automatically conserved and no reflected wave results. This is called "tailoring" of the shock tube contact surface. In this case the uniform conditions would in theory persist until the arrival of the reflected rarefaction head.

3.2 High purity single-pulse shock tube at ICARE

The first shock tube used in this thesis can be seen in **Figure 3.4**. The driven section of the shock tube is 6.0 m long and it has an inner diameter of 78 mm with electropolished internal surface. It works in a single pulse-fashion because of the presence of the dump tank, which prevents reheating of the test gas mixture by multiple shock wave reflections [237]–[240]. The dump tank is attached to the driven section close to the diaphragm position and its volume is much larger than the volume of the driven section in order to act as a reservoir (at least 5-6 times larger). The mechanism of the reheating and the function of this specific dump tank are discussed in detail elsewhere [19].

The operation of a single pulse shock tube involves filling the low-pressure section and the dump tank at the same pressure, pressurizing the high-pressure section, and bursting the diaphragm. Sample gas is withdrawn through an orifice located in the center of the end wall of the driven section and through a sampling port for subsequent analyses by gas chromatography and mass spectrometry.

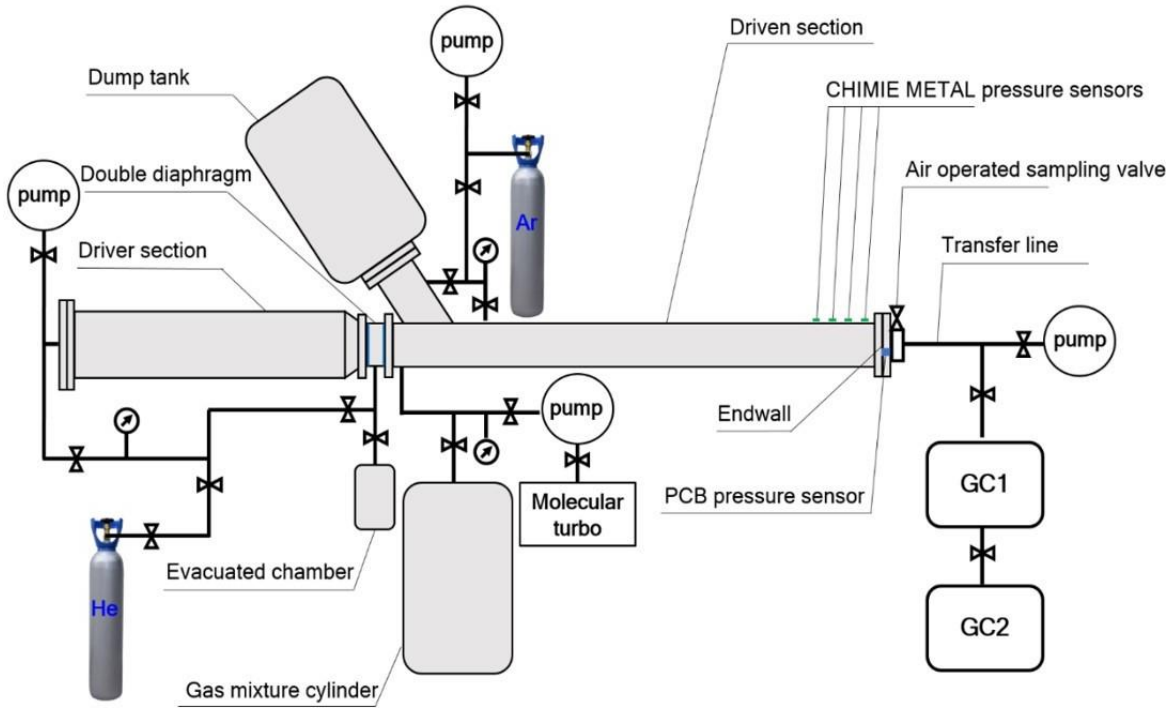

Figure 3.4 *Scheme of the High purity single-pulse shock tube at ICARE [19]*

A series of four pressure sensors (CHIMIE METAL A25L05B) coupled to fast digital oscilloscopes are mounted with a distance interval of 150 mm along the ending part of the driven section, except for the last one, being 82 mm away from the end wall. The times taken for the shock wave to pass at each sensor location are used to calculate the velocity of the incident wave. The speed, initial pressure and temperature conditions and the mixture composition (test gas) are the parameters that allows the determination of the temperature and pressure behind the incident and the reflected shock waves. A PCB pressure sensor shielded by a layer of RTV is located on the end-wall to record the pressure time-history from which the reaction time could be defined. A typical pressure profile with the reaction time is shown in **Figure 3.5**. In the present work, the reaction time is 4 ms.

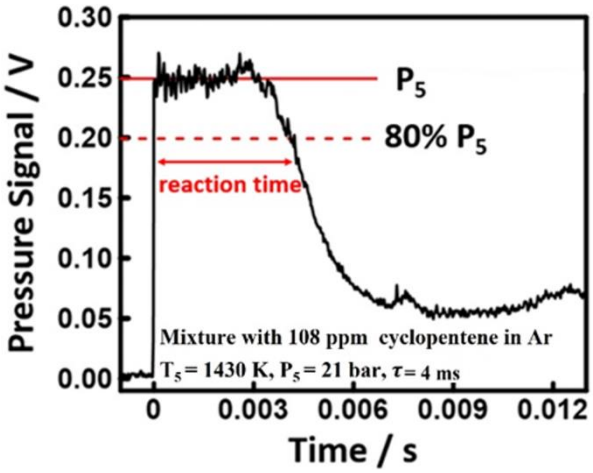

Figure 3.5 *Typical end wall pressure history and the definition of reaction time*

The PCB pressure signal is also used to trigger the operation of an air actuated HIP valve (HIP 30- 11HF4) mounted on the end wall in order to start the sampling process. The post shock gas mixture is analyzed in a GC/GC-MS analytical instrumentation.

Two gas chromatographers and one mass spectrometer are coupled to the single pulse shock tube in order to perform the analysis of the post-shock gases. The first GC, specifically designed to measure PAHs up to four rings, is equipped with a flame ionization detector (FID) coupled to a DB-17ms column for heavy species separation, and a thermal conductivity detector (TCD) coupled to a Molseive 5A column for monitoring the absence of air and the dilution coming from the helium driver gas. The sample loop and the injection lines are located inside an external oven which can be heated up to 320ºC. All the lines are Sulfinert to avoid interaction with the PAH products. The second GC is equipped with an FID detector connected to an HP Plot Q column for measuring light species up to mono-aromatic species and TCD for detecting the internal standard neon, if any. A DSQ mass spectrometer can be connected to the second GC to aid the PAH species identification [19].

The driven section of the shock tube is heated up to a temperature of 90ºC to avoid the condensation of fuels and heavy products. The low-pressure is connected to a turbomolecular pump (LeyBold TURBOVAC 361) which permits to obtain a vacuum below 10^{-5} torr before each experiment. However, the high-pressure section with the diaphragm system (diaphragm-depressurized chamber) and the dump tank are connected to primary pumps. The double diaphragm system uses membranes made of terphane (glycol ethylene poly-terephtalate) of different thickness, from 100 to 225 µm, depending on the load pressure ratio of the two main sections.

The mixtures and the related experimental conditions investigated in the high purity single-pulse shock tube are reported in Table 2. The mixtures are prepared in an electropolished tank by partial pressure method

and left overnight to ensure good homogeneity. The actual composition of the mixture is also tested by GC analyses. n-Heptane (purity higher than 99.5%) and cyclopentene (purity higher than 99.7%) were distributed by Sigma Aldrich. Argon and Helium were distributed by Air Liquide, the purity was higher than 99.999%. The experiments on n-heptane serve at two purposes: 1) as validation of the experimental set-up (n-heptane is a fuel which has been studied for decades now, and its fragmentation chemistry to small products is well understood); 2) probe for the pathways to PAH compounds starting from an alkane component (never observed in the literature studies at pyrolytic conditions). Furthermore, the PAH growth from ring-structures will be sampled using C_5H_8, a precursor of cyclopentadiene and the cyclopentadienyl radical. The reactions with C_2H_2 will also be investigated as relevant to the formation of C7 aromatics.

Table 2 *List of the gas mixtures used in the single-pulse shock tube*

Mixture	Temperature (T_5, K)	Pressure (P_5, bar)
103 ppm NC_7H_{16}	957 - 1652	18.0 – 22.0
502 ppm NC_7H_{16}	941 – 1677	17.8 – 23.5
2000 ppm NC_7H_{16}	885 – 1649	16.4 – 23.7
108 ppm C_5H_8	934 – 1647	17.3 – 21.9
326 ppm C_5H_8	943 – 1624	18.4 – 22.0
111 ppm C_5H_8 + 517 ppm C_2H_2	940 – 1657	17.9 – 23.4

3.3 Heated Shock Tube

The second shock tube used for the study is illustrated on **Figure 3.6**. The operation principle of the heated shock tube (HST) is similar to the high purity single-pulse shock tube. However, this one does not have a dump tank and is not equipped with an analytical system.

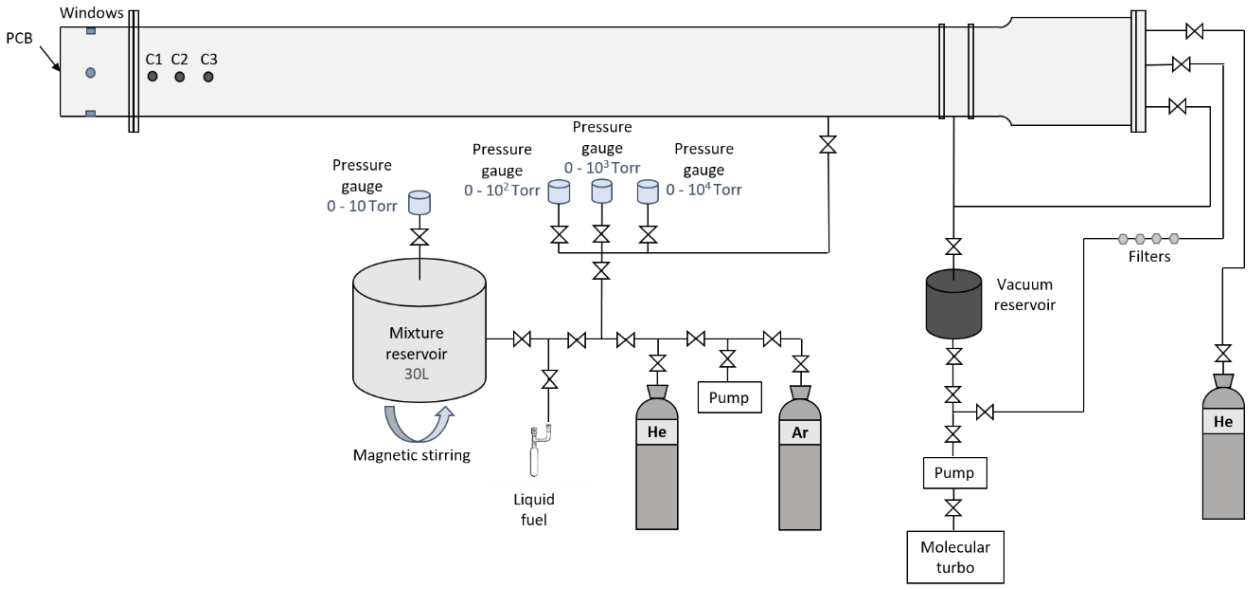

Figure 3.6 *Scheme of the heated shock tube*

The low-pressure side measures 5.25 meters and its inner diameter is 52.5 mm. Its inner wall has been polished in order to limit molecule adsorption and avoid disturbances in the flow behind the shock wave. The driven section is pumped with a turbomolecular pump (LeyBold TURBOVAC 361) that reaches minimal pressures of the order of 10^{-4} mbar. Two pressure gauges (MKS), 0-100 torr and 0-1000 torr are installed close to the double diaphragm, to measure the pressure of the test gases. The high-pressure side measures 2 meters and its inner diameter is 114.3 mm. A rotary vane pump is attached to this side for reaching primary vacuum. Four soot filters are fixed to this part in order to collect the soot produced at each shock. The double diaphragm system consists of two terphane membranes, and the thickness of the sheets varies between 50 to 200 µm. They are mounted on a metal support and stretched between two O-rings and a sudden depressurization of the space between the two membranes (initially loaded at a pressure equal to half P4) causes the successive rupture of the sheets.

As for the case of the single-pulse shock tube, the velocity of the incident shock wave is measured by taking the time intervals of the passage of the wave between pressure sensors located towards the end of the tube (three pressure sensors CHIMIE METAL A25L05B) and a PCB installed at the endwall. The distances between the sensors are 150 mm, 152 mm and 160 mm. Their response time is very short and they are aligned with the inner wall of the tube, therefore do not interfere with the passage of the shock wave. The PCB pressure sensor (PIEZOTRONICS Model482C series) shielded by a layer of RTV is also used to record the pressure time-history. A typical pressure profile with the reaction time is shown in **Figure 3.7**.

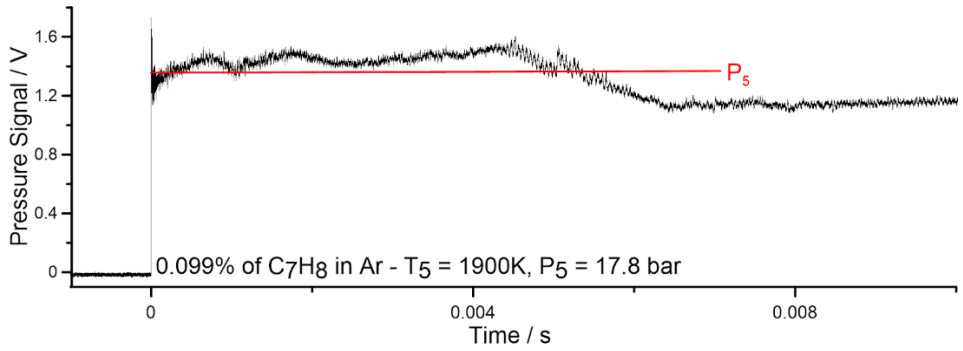

Figure 3.7 *Typical end wall pressure history*

As described previously (section 623.1), the observation time depends of the length of the tube, the thermodynamic properties of the test gases and the speed of the shock wave. In this thesis, the experimental set up is adapted in a way that the observation time is at the same order of magnitude as the time necessary to obtain the maximum soot volume fraction, f_v, and optical density, D_{633}. This time is 2 ms in the preliminary results and 4 ms in the final results.

To extend the test time usable in chemical kinetics studies, the use of "tailored" driver-driven gas interface to prevent interaction between the reflected shock and the contact surface has been well-established for conventional shock tubes areas [241]–[244]. At the tailoring condition the reflected shock wave passes through the tailored contact surface with unchanged shock strength [242]. When the reflected shock interacts with the mixing zone a pressure bump can appear, indicating that even though a contact surface disturbance occurred, the contact surface tailoring condition has still been achieved [241]. In order to avoid this bump, a characterization of the shock tube was performed. It was found that:

- If the desired T_5 is low, between 1520 and 1750K, 20-23% of Helium must be added to the low pressure and 12.5-20% of N_2 to the high pressure;
- If the desired T_5 is high, between 1750 and 2000K, 23-25% of Helium must be added to the low pressure and 10-12.5% of N_2 to the high pressure.

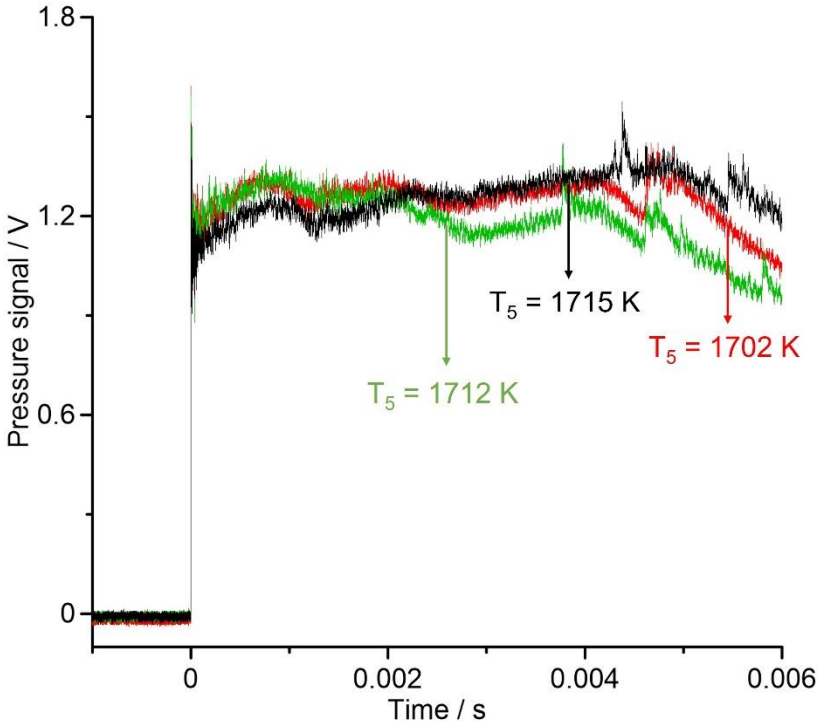

Figure 3.8 *Pressure histories in the HPST behind reflected shocks of 0.1% C_7H_8 diluted in Argon*

In **Figure 3.8**, the black curve shows the pressure profile of 0.1% C_7H_8 diluted in Argon, where T_5 is 1715 K and P_5 is 16.4 bar. For this test, 24% of Helium was added to the low pressure and 10% of N_2 was added to the high pressure. There was no equilibrium between He/N_2, for this reason, it is possible to observe that the curve goes up after 2 ms. A counter bump can be spotted in the green curve. For this particular pressure profile, 24% of Helium was added to the low pressure and 13% of Nitrogen was added to the high pressure (T_5=1712 K and P_5=16 bar). The red profile, however, shows a perfect balance of Helium and Nitrogen, which provides a flat curve. For this specific run, 27% of Helium was added to the low pressure while 10% of N_2 was added to the high pressure and T_5 is 1702 K and P_5 is 17 bar.

For the present study, a new end-wall section was designed (**Figure 3.9**). In particular, five windows are located close to the end wall in order to allow the passage of the laser beams and signal acquisition. They are located at the angles 0º, 90º, 180º, 225º and 335º, and more details will be given on section 3.3.3. Two additional caps are present for installation of sensors, if needed. The end-wall plug was replaced by an end-wall element with a movable plate (for easy removal during soot collection) and possibility to mount the PCB sensor at the center. The entire section was blackened to reduce the light reflections inside the shock tube.

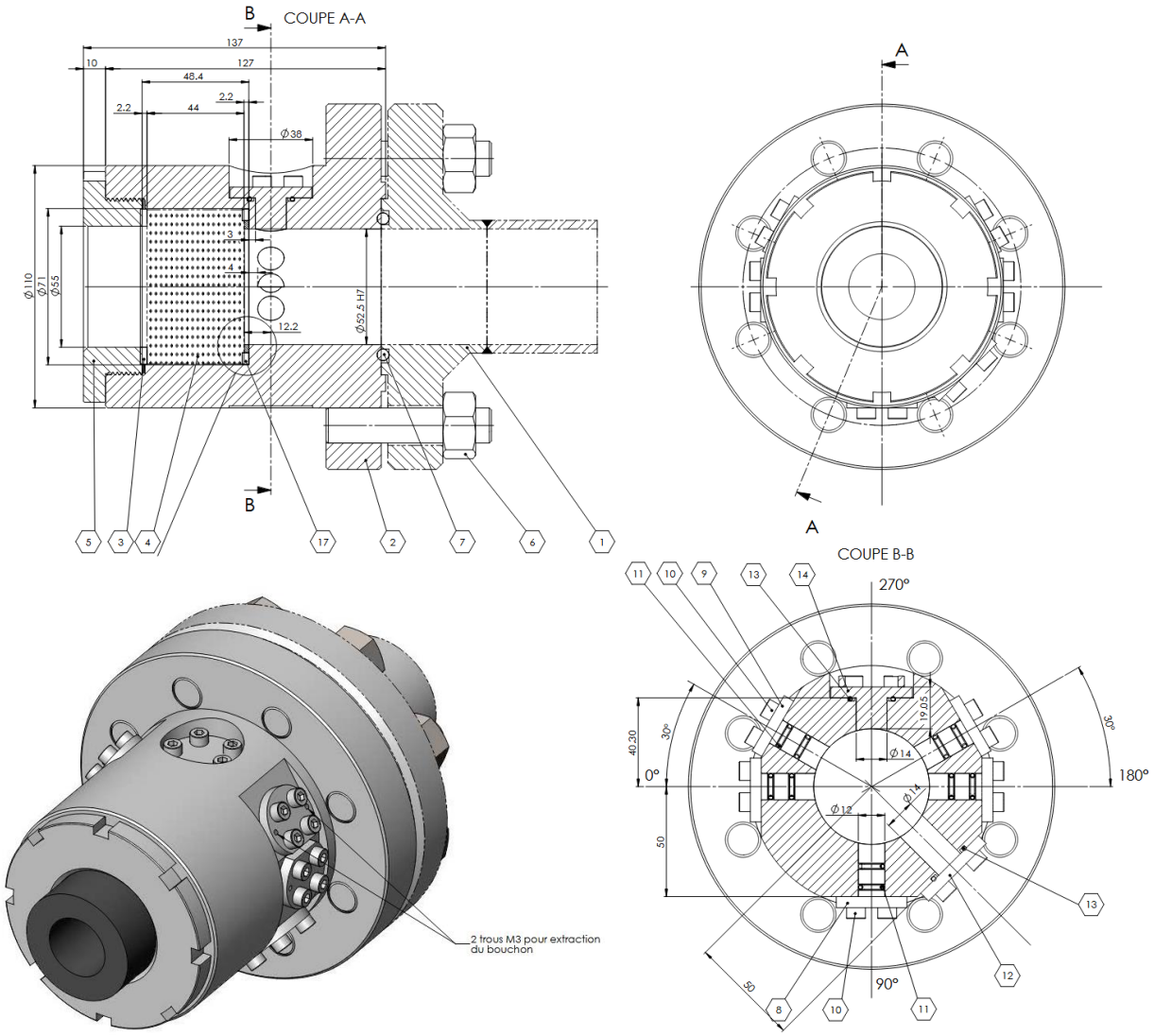

Figure 3.9 *End-wall section with optical access*

After each experiment, the tube is pumped through the soot filters by means of rotary pumps to eliminate the gaseous products of combustion. The tube is then opened and cleaned several times, to ensure that the inner surface is free of soot particles with an acetone-soaked cloth. The windows are also meticulously cleaned with a cotton swab. The end wall plate is removed so the soot can be collected for the TEM analysis, discussed in section 3.3.4.

3.3.1 Gas mixture preparation

In order to acquire kinetic data, the preparation of gas mixtures is a relevant and delicate step. In fact, it must be as precise as possible. The mixtures always consist of a hydrocarbon or a mixture of hydrocarbons diluted in argon, without the presence of oxygen, as the goal of this thesis is to analyze pyrolysis data.

Degassing the liquid samples is an important step before preparing a mixture. From its name, it consists in the removal of the air and the dissolved gases present in the liquid fuels through a freeze and thaw procedure. The sample to be degassed is placed in a Schlenk tube and frozen using liquid nitrogen. The headspace above the sample is then evacuated using a vacuum pump. Afterward, the sample is sealed and thawed allowing the dissolved gases to migrate into the evacuated head space. This process is typically repeated three times in order to have a good degasification efficiency.

The experimental device for the preparation of gas mixtures consists of a 30 L stainless steel cylindrical tank, pipes, also made of stainless steel, several valves and various different pressure gauges (MKS), with specific pressure ranges, 0-10, 0-100, 0-1000, and 0-10000 Torr. The different ranges are necessary to guarantee accurate measurements at any desired pressure. The tank is pumped with a primary pump before the beginning of the mixture preparation. Then the tank is filled with argon and pumped down again to around 1.5 Torr. This procedure guarantees the flushing of the tank from the previous gas mixture. After the fuel introduction into the mixing tank, the tank is filled with argon up to the total pressure, typically.

$$[fuel] = \frac{p_{fuel}}{P_{total}} \tag{3.21}$$

The mixing of the reagents is ensured by a magnetic stirring system. The mixing tank contains a central axis with a series of six blades, which, rotating, allow mixing of the gases and thus a good homogeneity of the gas mixture.

3.3.2 Experimental conditions

The mixtures and the related experimental conditions investigated in this study are reported in **Table 3Table 3** . The concentrations of the mixtures were chosen in such way that the carbon concentration was similar in all cases studied. The reference was toluene, for which extinction reached around 90%. The only exception is C_2H_4, which carbon concentration is higher. This is justified by the fact that a small amount of soot was observed when experiments were performed with this fuel, so it was decided to increase the initial concentration. Multiple sets were also performed with acetylene.

Air Liquide distributed ethylene, propylene, propyne, argon and helium, the purity was higher than 99.999%. Acetylene by Air Liquide is dissolved in acetone for stability issues. To remove traces of acetone, a Matheson filter was employed, together with a flame arrestor for safety purposes. Toluene, benzene and cyclopentene were distributed by Sigma Aldrich, the purity was higher than 99.7%.

Table 3 *List of the gas mixtures used in the heated shock tube*

Mixture	Temperature (T_5, K)	Pressure (P_5, bar)	[C]x10^{-17} (atoms/cm^3)
0.07% C_7H_8 + 99.93% Ar	1518 – 1990	16.4 – 18.2	3.03 – 3.92
0.03% C_7H_8 + 0.15% C_2H_2 + 99.82% Ar	1607 – 1916	17.0 – 18.0	3.34 – 3.87
0.03% C_7H_8 + 0.15% C_2H_4 + 99.82% Ar	1571 – 1978	16.2 – 18.6	3.05 – 3.68
0.02% C_7H_8 + 0.11% C_3H_6 + 99.87% Ar	1609 – 1978	16.7 – 18.9	3.24 – 4.07
0.02% C_7H_8 + 0.11% C_3H_4 + 99.87% Ar	1562 - 1960	16.3 – 18-7	3.20 – 4.16
0.082% C_6H_6 + 99.918% Ar	1537 – 1967	16.4 – 18.3	3.06 – 3.90
0.03% C_6H_6 + 0.15% C_2H_2 + 99.82% Ar	1582 – 1975	16.7 – 18.6	3.23 – 3.85
0.03% C_6H_6 + 0.15% C_2H_4 + 99.82% Ar	1645 – 2017	16.1 – 18.7	3.10 – 3.71
0.098% C_5H_8 + 99.902% Ar	1551 – 1968	16.6 – 18.6	3.21 – 3.85
0.03% C_5H_8 + 0.16% C_2H_2 + 99.81% Ar	1576 – 1953	16.6 – 18.6	3.27 – 3.81
0.245% C_2H_2 + 99.755% Ar	1750 – 1989	16.8 – 18.1	3.09 – 3.63
0.35% C_2H_2 + 99.65% Ar	1603 – 1980	16.7 – 18.2	4.47 – 5.55
0.7% C_2H_4 + 99.3% Ar	1685 – 2017	16.9 – 20.7	8.95 – 11.2
0.16% C_3H_6 + 99.84% Ar	1598 – 1968	16.0 – 18.6	3.07 – 3.99
0.16% C_3H_4 + 99.84% Ar	1586 – 1951	16.8 – 19.4	3.32 – 4.11

3.3.3 Optical layouts and preliminary results

In order to perform simultaneously extinction and multi-angle Rayleigh scattering measurements five optical port including quartz windows are installed on the tube at different angles 0º, 90º, 180º, 225º and 335º, in a plane orthogonal to the tube axis, around 1 cm from the end wall of the shock tube. The 0º is the injection angle, while the others are employed to capture the signals. They allow the passage of the laser beams and collection of the transmitted beam as well as the scattered radiations. The 0º corresponds to the horizontal injection laser beam (for extinction and Rayleigh scattering) axis. The 180° corresponds to the horizontal direct transmitted beams. The 90° corresponds to the top vertical axis. The 225° and 335°

correspond to axis symmetric to the vertical axis. All windows axes intersect on the shock tube axis. Each window has 4 mm of diameter and 3 mm of thickness.

Laser beams for extinction and Rayleigh scattering measurements are coincident. They enter the ST along the 0° axis window and are focused on the ST axis. They exit the ST along the 180° axis window. The beams are collected, attenuated, split and measured with specific detectors. Rayleigh scattering radiation originating from the laser focal point is collected with 3 identical specific optical setups installed on the 3 windows port at 90°, 225° and 335°.

Whereas absorption/extinction measurements in shock tubes have been successfully made for years, implementing simultaneous multi-angle Rayleigh scattering measurements appeared challenging, in terms of thermomechanical stability. As the focused beam has a diameter of a few dozens of µm, the mechanical adjustments of the optical setup need to be fine and accurate, and moreover, non-sensitive to vibrations.

The laser power for each laser needs also to be very stable. During the shock the tube is subject to vibrations for duration longer than the studied process. Then the collection volume seen by each optical collection setup should remain the same; and include the laser probe volume.

When optical fibers are used to bring the laser to the shock tube and/or collect the signal from the shock tube, special custom-made assemblies were designed and constructed to allow flexibility (modular pieces) and easy alignment. The assembly for beam injection into the shock tube is presented in **Figure 3.10**. The other holders are similar but without the polarizing element. Fiber optics is used for long-distance and high-performance data networking [245]. A fiber optic cable contains a varying number of glass fibers. Surrounding the glass fiber core is another glass layer, the cladding. Another layer, the buffer tube, protects the cladding, and a jacket layer acts as the final protective layer for the individual cable. This cable transmits photons. The glass fiber core and the cladding have a different refractive index that bends incoming light at a certain angle. When light signals are sent through the fiber optic cable, they reflect off the core and cladding in a series of zigzag bounces, adhering to a process called total internal reflection. The light signals do not travel at the speed of light because of the denser glass layers, instead traveling about 30% slower than the speed of light.

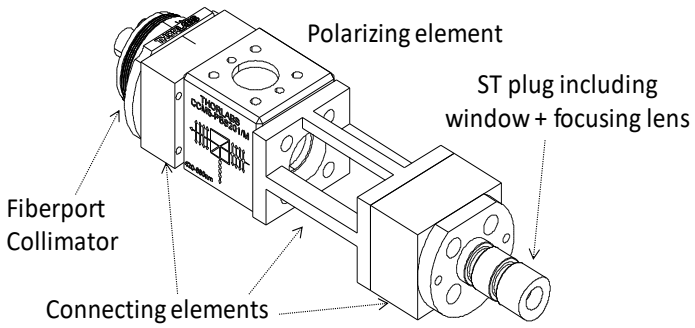

Figure 3.10 *Optical fiber shock tube holder*

Several optical layouts were developed in order to build a new method to measure extinction simultaneously with Rayleigh scattering. In total, four different approaches were established in the optical layout.

3.3.3.1 First approach – optical fibers

Extinction measurements were performed with a 808 nm laser diode, or a 632.8 nm Helium:Neon laser, depending on the configuration. Rayleigh scattering measurements were conducted with a DC 532 nm diode pumped solid state laser (Laser Quantum, OPUS 532) delivering until 4 Watts. Both beams undergo reflections through the mirrors (M1, M2, M3) and then are superimposed via the dichroic mirror (DM1). In the scheme, the laser beams are not superimposed for a clearer image. A lens (L1) focuses the beams on the rotating disk of a mechanical chopper (SCiTec 300CD). The chopper modulates the beam intensity at 40 kHz. For such high frequencies the slit width apertures of the chopper is smaller than the laser beam diameter. That is why the beams are focused in order to ensure a total obstruction of the beams. Following the chopper, the beams are collimated with the lens (L2) and injected in multimode optical fiber (105 µm diameter) connected to a fiber-port (Thorlabs, AF2S-18A). The other extremity of the optical fiber is connected to an identical fiber-port attached to the entrance window port (0°) of the ST. The two exiting beams from the optical port are collimated with 3 mm diameter. As the beams at the exit of the fiber are not polarized a polarizing splitting cube (PSC, model: PBS052, **Figure 3.10**) is mounted between the fiber-port and the 0° window port. The beams are horizontally polarized and then focused on the axis of the ST with a 40 mm focal length converging lens. In such condition, the beam waist at the focal point is less than 10 µm.

The four optical setups mounted on the 180°, 90°, 225° and 335° window port are identical. They consist in the assembly of a 40 mm EFL converging lens, an optical fiber port (Thorlabs, PAF2S-18A) and a φ 200 µm multimode optical fiber (Thorlabs, M25L05). It has to be noted that the fiber port includes an 18 mm focusing lens. Then the field of view collected by the optical setup is 440 µm wide (i.e., $200 \times 40/18$).

The transmitted beams at 180º are collimated through a fiber collimator (Thorlabs, F220SMA-532) and split with a dichroic mirror (DM2), and each wavelength undergoes its respective filter (F532 and F808) to finally reach two photodetectors (Thorlabs, model: PDA10A2). The measured signals are collected, recorded and visualized on an oscilloscope (Rohde & Schwarz, RTB2004). Each of the three Rayleigh scattering radiation collected at the 3 angles, is collimated at the exit of the optical fiber (Thorlabs, F220SMA-532), and filtered with a 1 nm bandpass filter (Thorlabs, FL05532-1). This filtered radiation is then detected by a photomultiplier tube (PMT, HAMAMATSU R5938P) and the resulting signal is collected, recorded and visualized on an oscilloscope (Rohde & Schwarz, RTB2004). In order to reduce and avoid any reflection of the 532 beam inside the ST, both windows and lenses on the 0° and 180° have an antireflective coating.

Figure 3.11 shows a scheme of the first optical layout developed, in which all the fibers are represented as orange arrows.

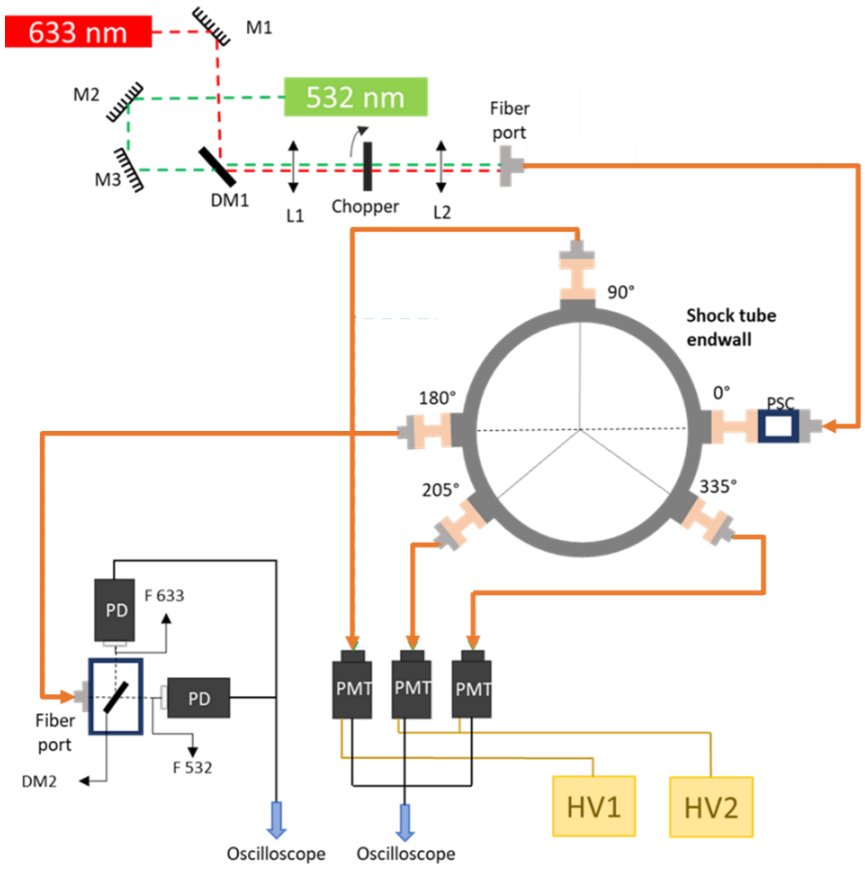

Figure 3.11 First approach of optical layout

In order to guarantee a good alignment and superimposition of the different probe volumes collected at the different angles a specific tool was designed, which can be seen on **Figure 3.12**.

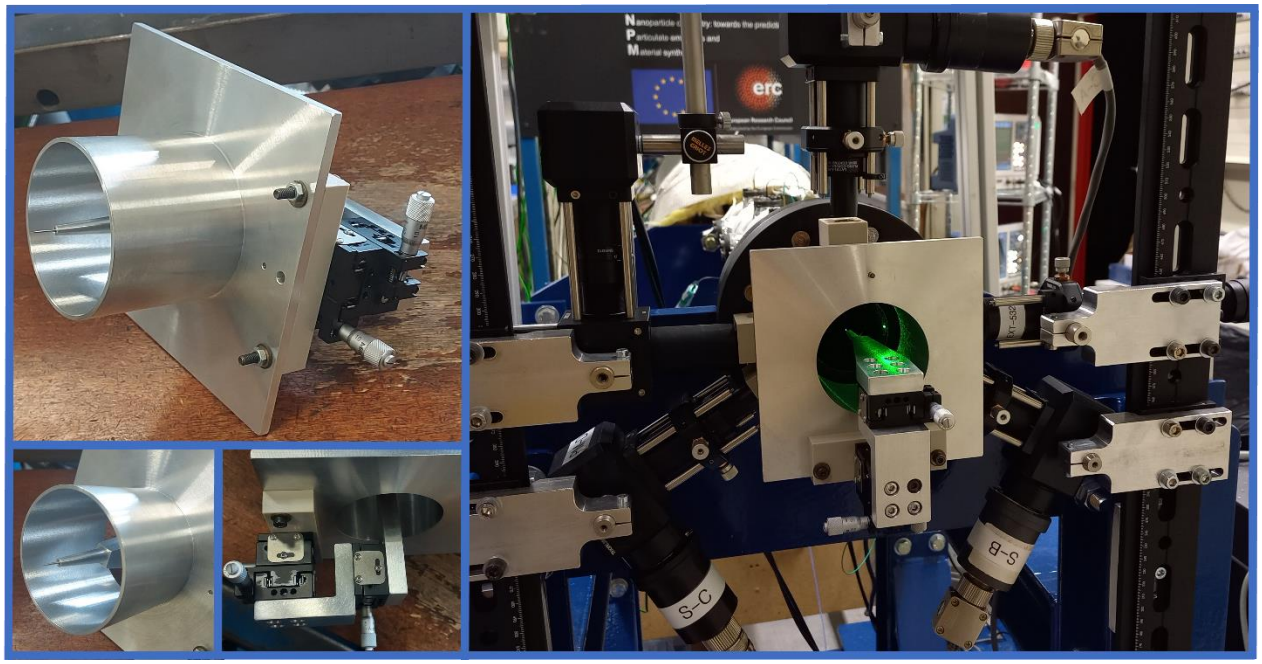

Figure 3.12 *Tool designed for alignment procedure*

This tool consists in a fine needle mounted on a three-axis translation table with micrometer adjusters that can be inserted inside the ST. Once the 2 coincident beams are centered and focused on the axis of the ST the needle is installed and translated until its tip is in contact with the laser beams at their focal point. The laser beam is then reflected and scattered in all directions, allowing to locate the probe volume. Each fiber-ports can be adjusted with precision in order to collect and optimize the acquired signal.

The second step after the alignment was to do preliminary tests in argon, to check the stability of the experimental set-up. **Figure 3.13** displays an example of it, whereby T_5 is 1962 K and P_5 is 17.5 bar.

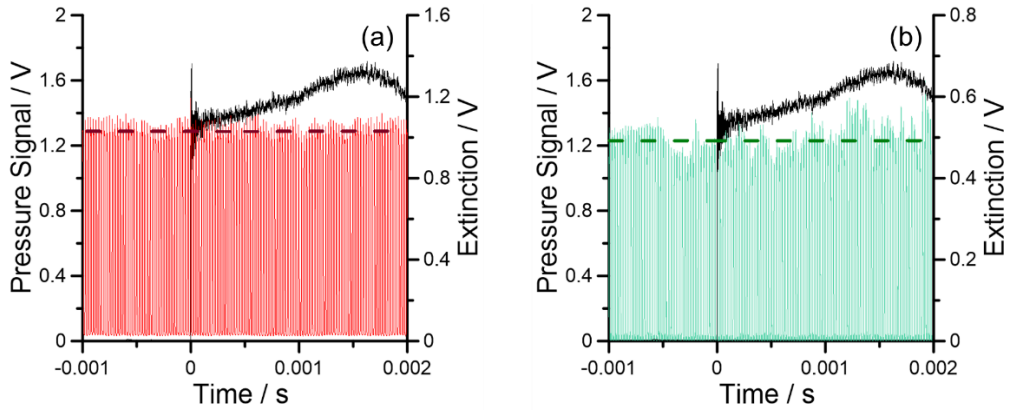

Figure 3.13 *Time-resolved extinction measurements of an Argon shock, at T_5 = 1962 K and P_5 = 17.5 bar*

Figure 3.13(a) represents the extinction signal of 808 nm infrared laser while **Figure 3.13(b)** is the extinction signal of the 532 nm laser at 1 W power. The dashed red and green lines represent the envelope of the signals, which are flat, consistent with Argon shocks. It is also possible to observe that both graphs present good stability, which allowed to run tests with hydrocarbon mixtures.

Preliminary results were obtained with the first approach and raw extinction signals are presented in **Figure 3.14**. This particular experiment, T071, is 0.1% of toluene diluted in argon, with T_5 = 1730 K and P_5 = 17.5 bar. It is important to highlight that both graphs contain raw extinction signals. As in **Figure 3.13**, the dashed red and green lines represent the envelope of the signals which allow to consider or not the contribution of self-chemiluminescence at the 2 laser wavelengths originating from the reactive mixture for in the treatment of the data. Also, the decay of the signal after t=0 on the red plot represents the induction delay time of this shock.

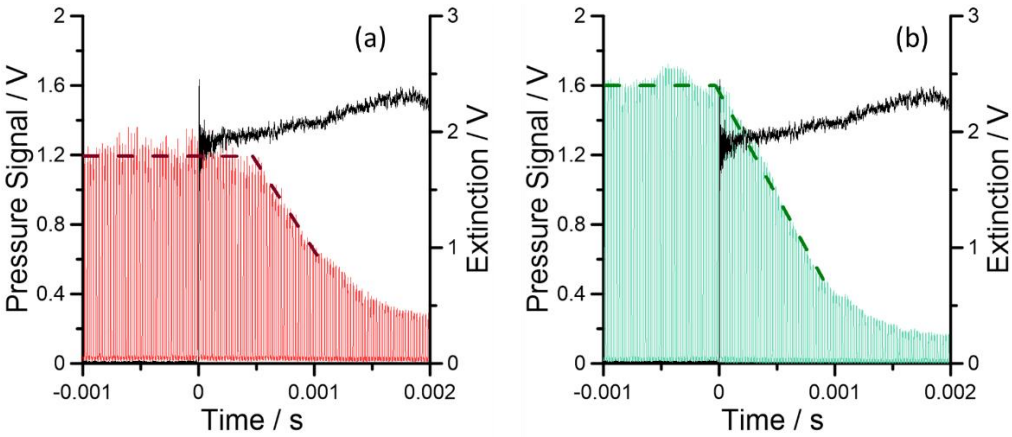

Figure 3.14 *Time-resolved extinction measurements – raw data. T071 - 0.1% C_7H_8 in Ar; at T_5 = 1730 K and P_5 = 17.5 bar*

Scattering raw signals and self-emission have also been measured at this approach and can be seen on **Figure 3.15**. **Figure 3.15(a)** represents the scattering of the run T071, mentioned above. The graph on the

top is the pressure profile, up to 4 ms and the three below are the scattering raw signal of each individual angle. Once again, the dashed blue, green and yellow lines represent the envelope of the scattering measurements.

Figure 3.15(b) is the profile obtained when the 532 nm laser is off, in other words is the self-emission of the shock (T212). This run has similar conditions to T071, T_5 = 1724 K and P_5 = 17.6 bar, which allows to make a reasonable comparison. This signal, which is not modulated and consequently not related to the laser, is a consequence of the emission from soot or other gas-phase species produced in the tube at high temperature, such as PAHs.

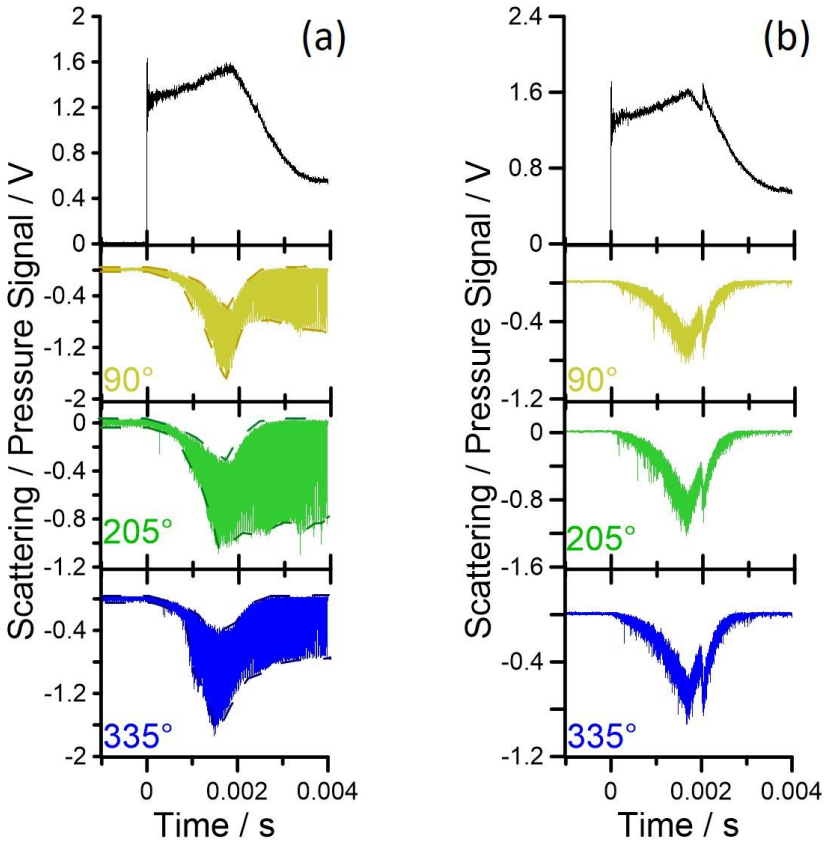

Figure 3.15 *Raw data - 0.1% C_7H_8 in Ar:* ***(a)*** *Time-resolved scattering measurements at T_5 = 1730 K and P_5 = 17.5 bar (T071);* ***(b)*** *Emission at T_5 = 1724 K and P_5 = 17.6 bar (T212)*

This approach was not pursued due to the lack of repeatability in the experiments and quality of the signal. After more than 200 shocks, the signals resulted not consistent from shock to shock despite the efforts in improving the alignment between the different components (including injection into the optical fiber, focusing of the beam at the center of the shock tube, adjustment of the holders' parameters) and the tests performed replacing some of the components with different ones (i.e., the diameter of the fibers). In

addition, despite the fact that the holders are all rigidly connected to the HPST, large vibrations in the signal baseline could be observed which would greatly affect the quality of the measurements.

The vibration of the optical fibers themselves (without the shock tube in operation) caused large variations in the signal. In order to minimize the vibrations, a structure where the optical fibers could be attached was built solidly to the optical table and surrounding the shock tube end section. The signals improved but not sufficiently, as shown in **Figure 3.16**. Both graphs represent the raw extinction data of two similar 0.1% toluene shocks. The green profiles are the 532 nm laser at 1.4 W signals, while the red are the infrared laser signals. The difference between **Figure 3.16(a)** and **Figure 3.16(b)** is the structure built to the optical table. The graph on the left presents less vibration due to the presence of the structure. The vibration is clear in the figure on the right, it is possible to observe a variation of the red signal around t=0.

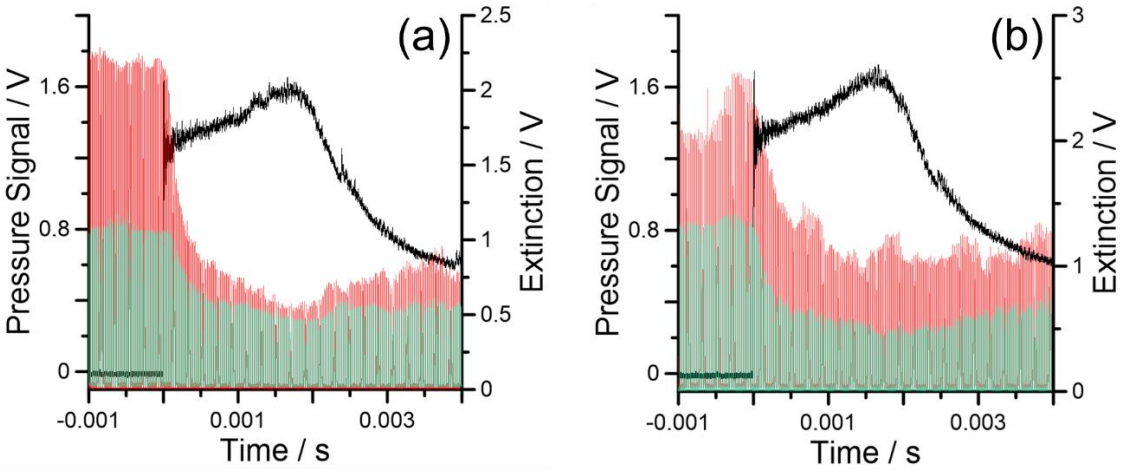

Figure 3.16 *Time-resolved extinction measurements, raw data - 0.1% C_7H_8 in Ar;* ***(a)*** *T109 – with bosh profile structure, at T_5 = 1946 K and P_5 = 17.6 bar;* ***(b)*** *T115 – without bosh profile structure, at T_5 = 1957 K and P_5 = 17.9 bar*

This problem is thought to be associated with the characteristics of the multimode fibers compared to the single mode ones, as only in the single mode fibers the beam travels in the core without interaction with the cladding. On the other hand, no single mode fiber can sustain the high power required for the scattering measurements. For these reasons, the method was not pursued.

3.3.3.2 Second approach – infrared laser changed

The second approach is just an evolution of the first one, as presented on **Figure 3.17**. In this configuration, the laser diode was replaced by a 15 mW, 632.8 nm He:Ne laser. The associated bandpass filters and dichroic mirrors were also changed. In addition, only one high voltage box is used in this set-up, the three PMTs are connected to it. Apart from these changes, the optical table remains similar, with the presence of optical fibers (in orange).

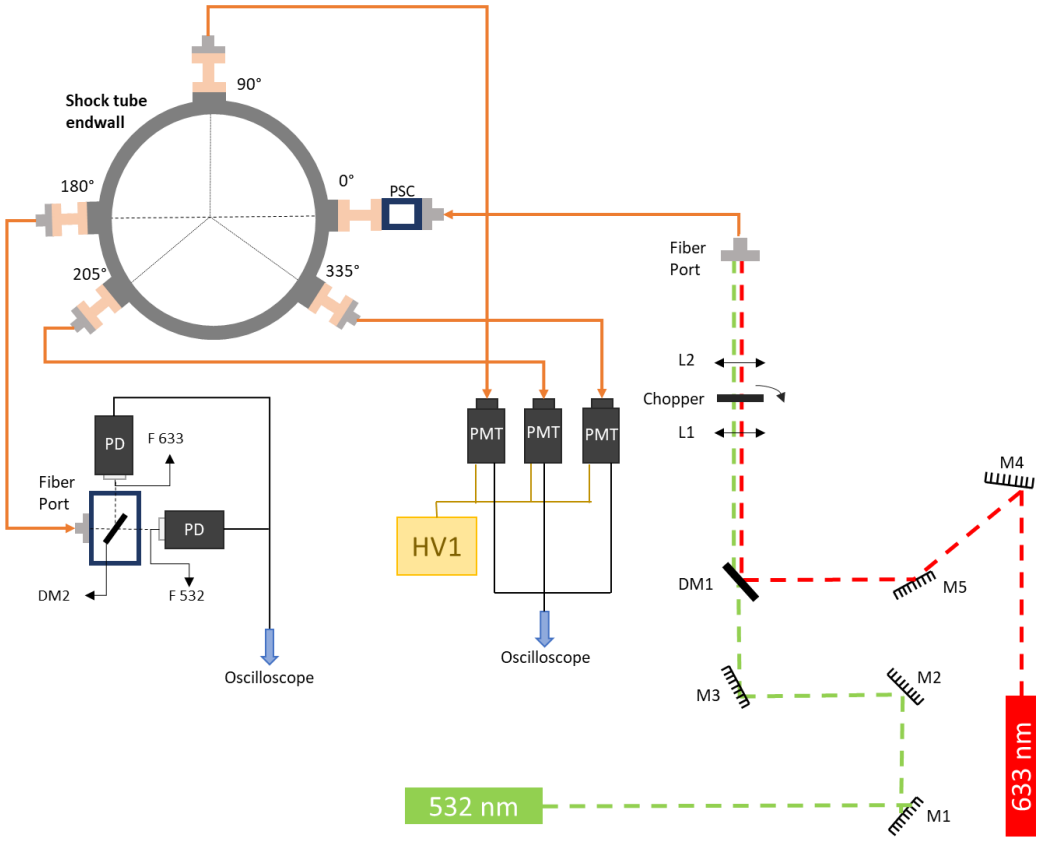

Figure 3.17 Second approach of optical layout

Concerning the preliminary results, **Figure 3.18** presents the time-resolved extinction measurements in two different wavelengths. This is the raw data of run T238, with 0.1% of toluene diluted in Argon at T_5 = 1731 K and P_5 = 18.0 bar. Comparing figures **Figure 3.14** and **Figure 3.18**, the shape of the curve remains the same but

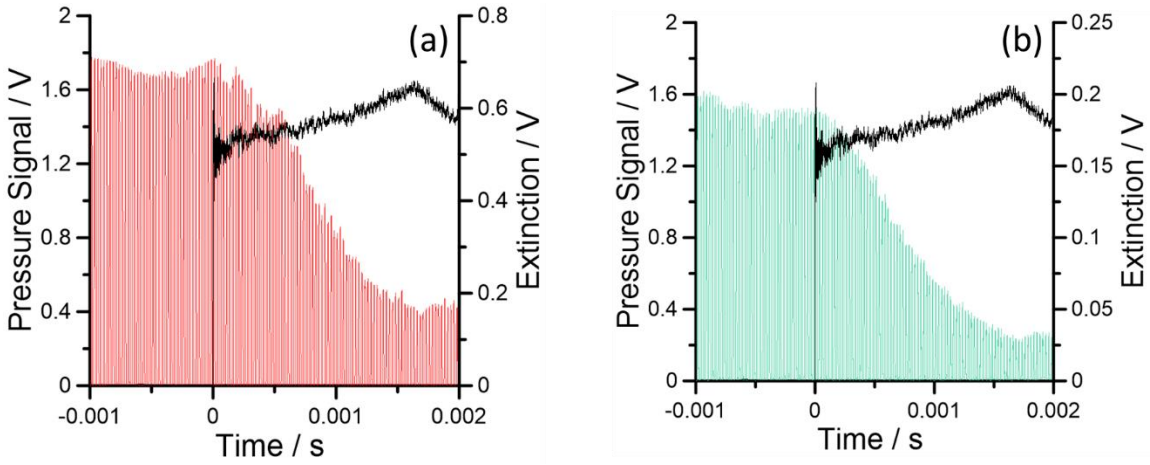

Figure 3.18 Time-resolved extinction measurements – raw data. T238 - 0.1% C_7H_8 in Ar; at T_5 = 1731 K and P_5 = 18.0 bar

the absolute value of the maximum signal changes. It is also possible to spot some vibration in the signals, they are not completely flat before t = 0.

Moving to the scattering results, **Figure 3.19(a)** shows the raw scattering data of shock T238 and **Figure 3.19(b)** the self-emission at T_5 = 1747 K and P_5 = 18.1 bar (run T229). From both figures **Figure 3.19(a)** and **Figure 3.19(b)** one can see that the shape and amplitude are quite the same, meaning that the measured scattering signal is dominated by the self emission. This can be interpreted by the fact that the particles density is too weak or that the laser is quite misaligned. Nevertheless, we can observe scattering signals from particles at 225° and 335° for t > 2 ms, whereas there is no at 90°. This can be explained by a misalignement of the collection at this angle. This kind of differences in the observed signals were made for different tests, showing the importance of the effect of vibrations.

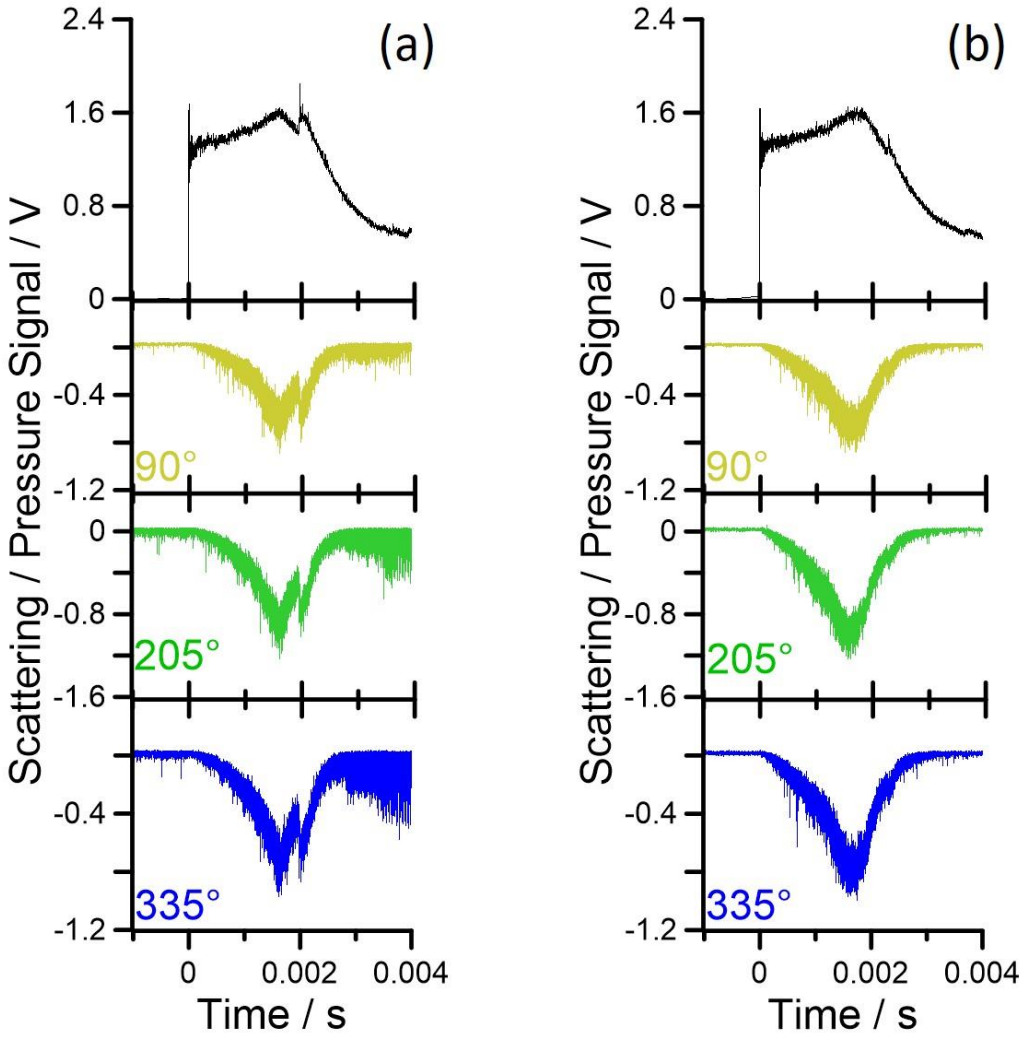

Figure 3.19 *Raw data - 0.1% C_7H_8 in Ar:* ***(a)*** *Time-resolved scattering measurements at T_5 = 1731 K and P_5 = 18.0 bar (T238);* ***(b)*** *Emission at T_5 = 1747 K and P_5 = 18.1 bar (T229)*

The occurence and amplitude of these mechanical vibrations were studied, especially the transmitted vibration on the window ports and fiberports. For this reason, only extinction measurements were considered, without using any optical fiber (see **Figure 3.20**).

3.3.3.3 Third approach – extinction only without optical fibers

Figure 3.20 exhibits the third optical layout employed. The laser beam from the He:Ne laser is injected directly through the window of the shock tube and the transmitted intensity is filtered and then focused on a photodiode.

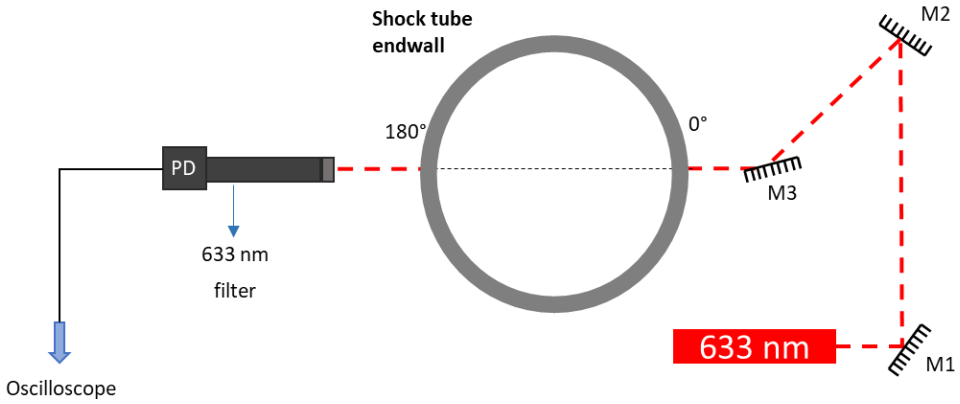

Figure 3.20 Third approach of optical layout

Since the chopper was removed, the extinction raw signal is no longer modulated, as seen in **Figure 3.21**. This shock, run T326, is 0.1% of toluene diluted in Argon, at T_5 = 1748 K and P_5 = 18.2 bar. It was observed a very could flatness of the transmitted laser intensity before the occurrence of the shock wave. Two problems have been identified. First, the spike at t = 0, which appeared in several runs. Despite the focusing of the beam on the sensitive part of the photodiode, the optical deflection of the beam induced by the pressure drop was enough to shift the beam out of the sensitive part. This problem was fixed by replacing the photodetector (PD) by a photomultiplier tube (PMT), as will be seen in section 3.3.3.4.

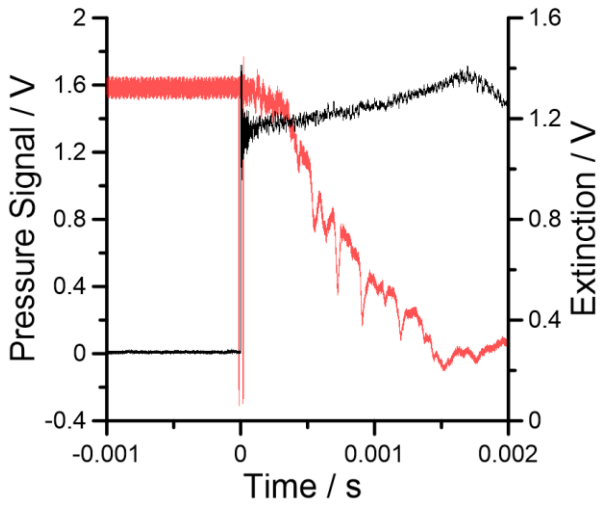

Figure 3.21 *Extinction measurements – raw data. T326 – 0.1% C_7H_8 in Ar; at T_5 = 1748 K and P_5 = 18.2 bar*

The second problem concerns the remaining fluctuations observed on the extinction signal right after the shock for t > 0.

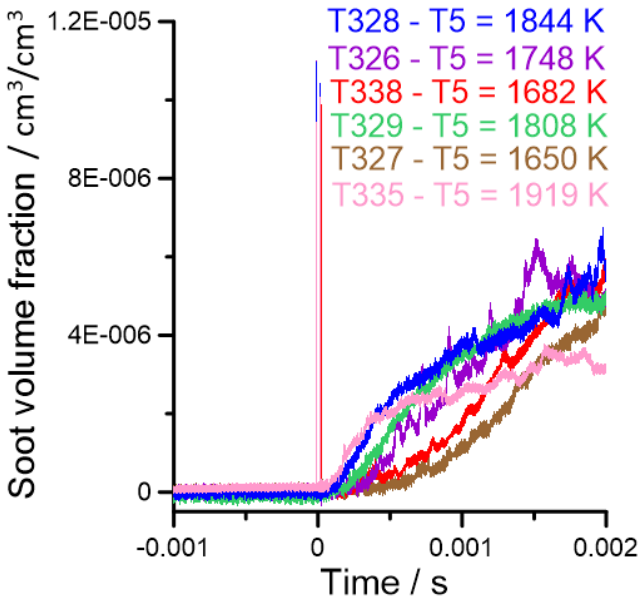

Figure 3.22 *Soot volume fraction of 0.1% C_7H_8 in Ar and P_5 = 18 bar*

Further analyses have been performed for this approach. The soot volume fraction was calculated according to equation (2.6) and the refractive index used in this study is of Lee and Tien [211]. **Figure 3.22** displays this parameter as a function of time of six 0.1% toluene shocks in a temperature range of 1650 to 1919 K and P_5 = 18 bar. Each curve represents a different temperature condition. The results follow the expected behavior, with induction reducing along with the temperature. The peak volume fraction increases up to a temperature of around 1844 K, before decreasing at higher temperatures. On the other hand, the signals still

show certain vibrations which might affect the results, in this case coming from the operation of the shock tube. In order to further improve the quality of the data, a new structure sustaining the shock tube itself was designed as in the next section.

3.3.3.4 Fourth approach – new ST structure for reduced vibrations

The final configuration includes a new structure to block the shock tube, which can be seen on **Figure 3.23**. In order to build it, all the devices were dismounted, the optical table and the shock tube. The frame holds the tube in two different positions, at the high-pressure side and at the end section. It is made of plates rigidly attached to the shock tube flanges, vertical posts which are connected to large bases to spread the weight over the floor surface, and modulable metallic weights. The total weights of the structures are around 1.5 tons in the high-pressure side and 1 ton in the low-pressure side. These additional weights increase the inertia of the system and prevent vibrations of the tube.

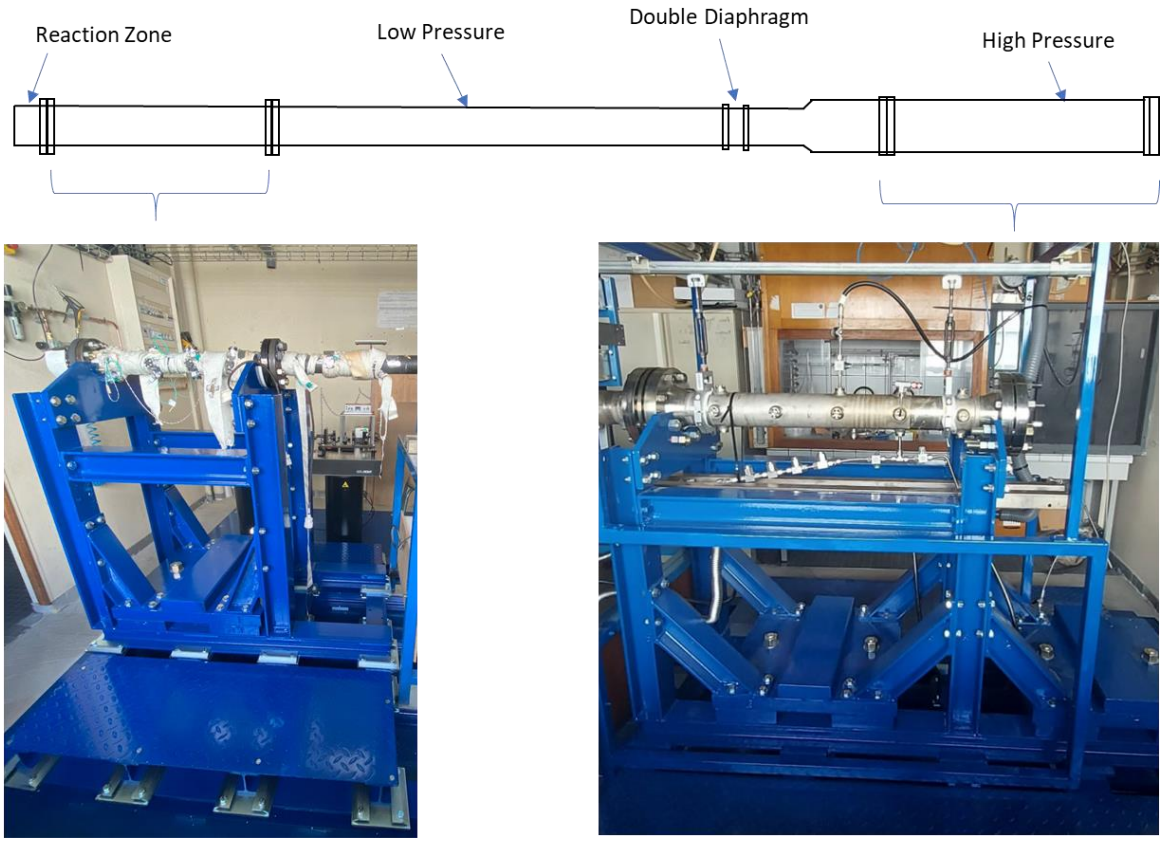

Figure 3.23 *Structure to hold the shock tube*

To confirm that the fiber could also be a source of vibration, a comparison was carried out. **Figure 3.24** shows two preliminary optical layouts after the frame holding the shock tube was built. **Figure 3.24(a)** is

the layout of extinction measurements without optical fiber, while **Figure 3.24(b)** is with optical fiber in place only for the injection of the beam into the shock tube. Two Argon shocks were run in similar conditions, without the optical fiber (T360) and with it (T361). In **Figure 3.25**, the green lines are associated with the optical fiber and the red lines related to the run without it.

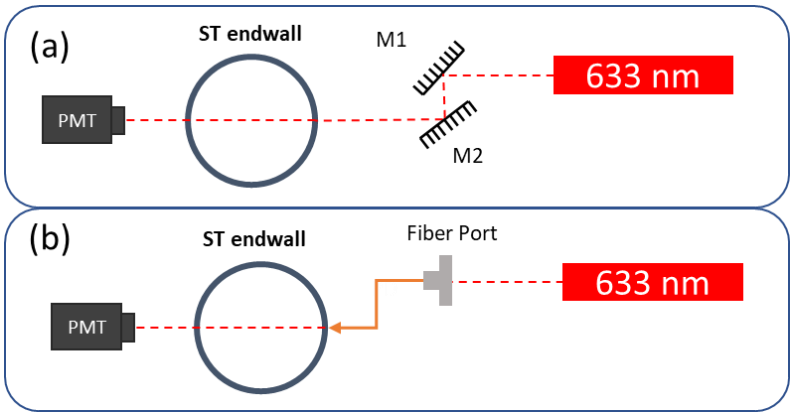

Figure 3.24 *Preliminary optical layouts after structure: extinction measurements (a) without optical fiber, (b) with optical fiber in injection*

The comparison below proves that the optical fiber was also a source of vibration as hypothesized in section 3.3.3.1, thus a final approach was designed without fibers in place, as in **Figure 3.26**. In this solution, no photodetectors are used, only photmultipliers and they are all mounted directly to the shock tube structure.

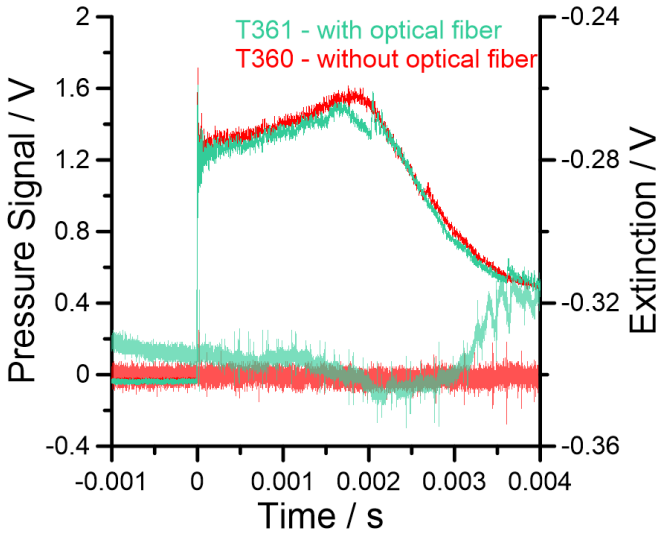

Figure 3.25 *Raw extinction signals of two Argon shocks in similar conditions: T_5 = 1620K and P_5 = 17.1 bar; T361 with optical fiber and T360 without it*

Hence, if still the shock tube slightly vibrates, the PMTs will vibrate at the same frequency of the tube, reducing the effects on the signal.

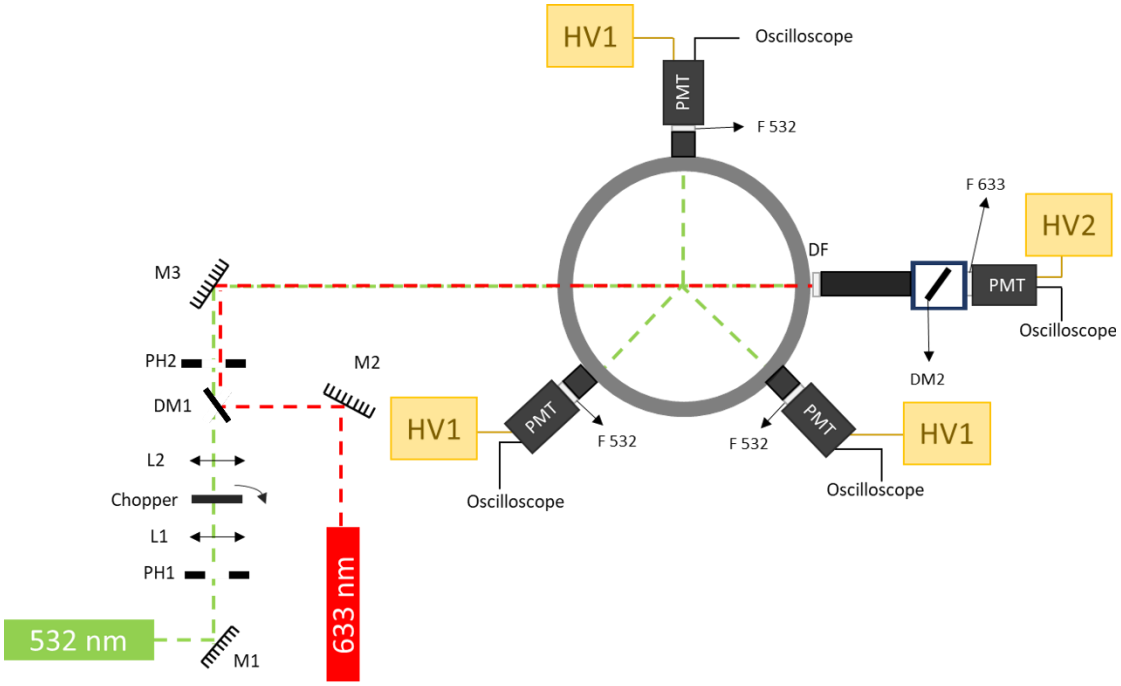

Figure 3.26 Final approach of optical layout

It is also important to highlight that the red beam does not go through the chopper, which means that the signal is no longer modulated, as shown in **Figure 3.27**. The observation time has also changed compared

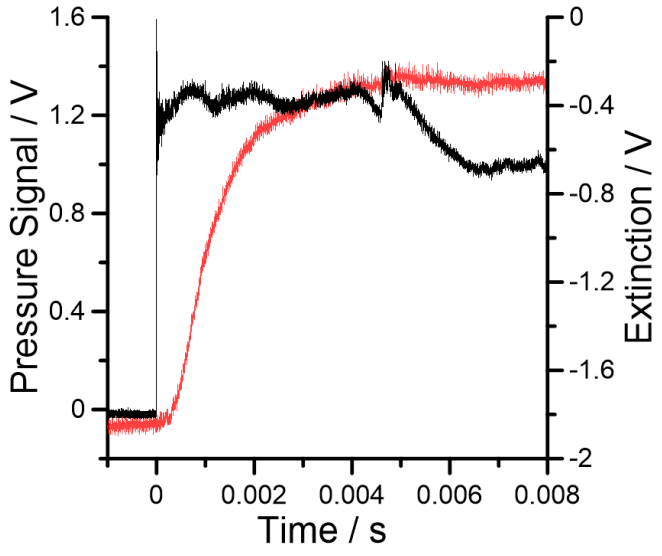

Figure 3.27 Extinction measurements – raw data. T468 - 0.1% C_7H_8 in Ar; at T_5 = 1702 K and P_5 = 17.0 bar

to the tests presented in the previous sections. The tailoring was performed by adding 24% of buffer gas (Helium) to the mixture and 2-3 bar of Nitrogen to the high-pressure helium gas.

Several tests were run for the same mixture, but different temperatures, and the soot volume fraction was calculated. **Figure 3.28** displays this parameter as a function of time of six 0.1% toluene shocks in a temperature range of 1539 to 1991 K and P_5 = 18 bar. Small vibrations can be still detected especially at longer times; however, these are negligible compared to the signal levels.

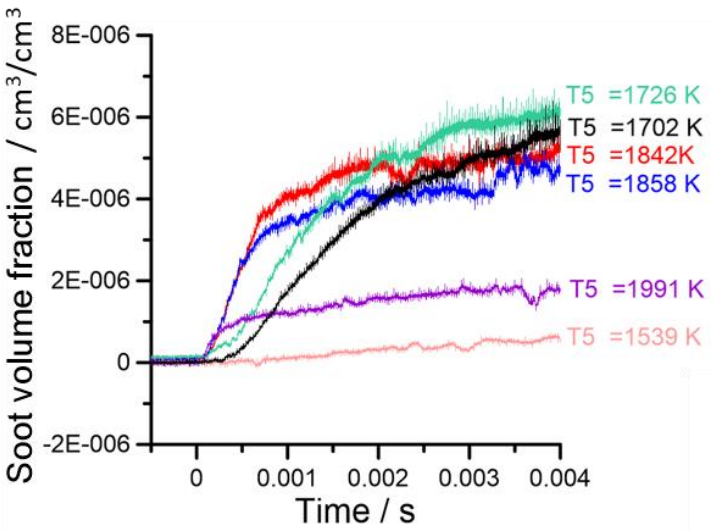

Figure 3.28 *Soot volume fraction of 0.1% C7H8 in Ar and P5 = 18 bar*

Scattering signals were also measured for run T468, as shown in **Figure 3.29**. The three angles collected modulated signals, once the green beam goes through the chopper. The self-emission is still observed in the shape of the curve. It is also remarkable that the minimum absolute value differs between the angles: for 90º and 335º is around -1.2 V, while for 205º is -1.7 V. This difference appears in several experiments, with no clear pattern. Future work will include the identification of the problems related to such lack of repeatability in the scattering signals. For the moment, it has been decided to perform only with extinction measurements to obtain induction delay time, growth rate and optical densities, which will be discussed on chapter 4.

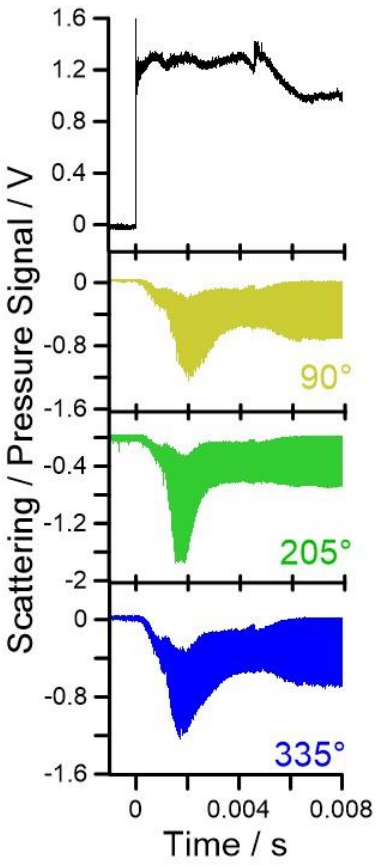

Figure 3.29 *Scattering measurements – raw data. T468 - 0.1% C_7H_8 in Ar; at T_5 = 1702 K and P_5 = 17.0 bar*

3.3.4 TEM Analysis

Transmission electron microscopy (TEM) provides information on the diameter and morphology (texture) of the soot particles and their structure (atomic scale organization) and micro texture (spatial organization of basic structural units). Besides the interest of knowing the evolution with temperature of the average diameter of the particles and their structures, these data are important because they allow validating experimentally the theory related to the determination of the volume fraction in soot. In this section, the principle of the transmission electron microscope will be briefly explained and the method of sampling soot for observation will be described.

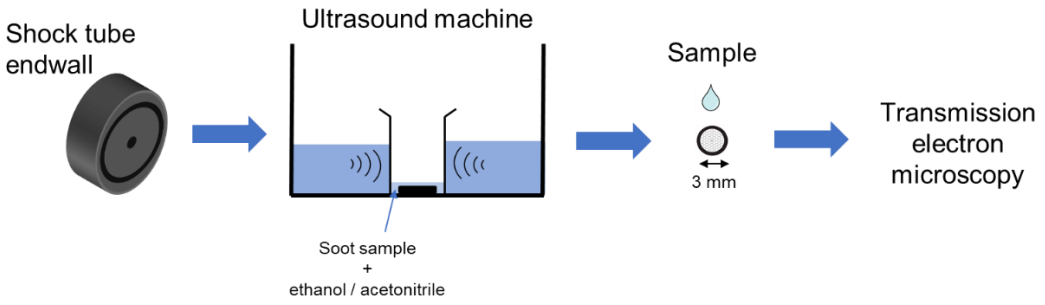

Figure 3.30 Scheme of soot sample preparation

Figure 3.30 shows a scheme of the soot sampling. After being generated, the soot is deposited in the walls of the shock tube. For this reason, the endwall is removed and put in a beaker along with 1.5 ml of ethanol or acetonitrile. The beaker is placed in an ultrasound bath (Fischerbrand FB15050) for three minutes for soot detachment from the wall. The resulting solution is kept in the fridge in small dark vials to avoid its interaction with light and heat.

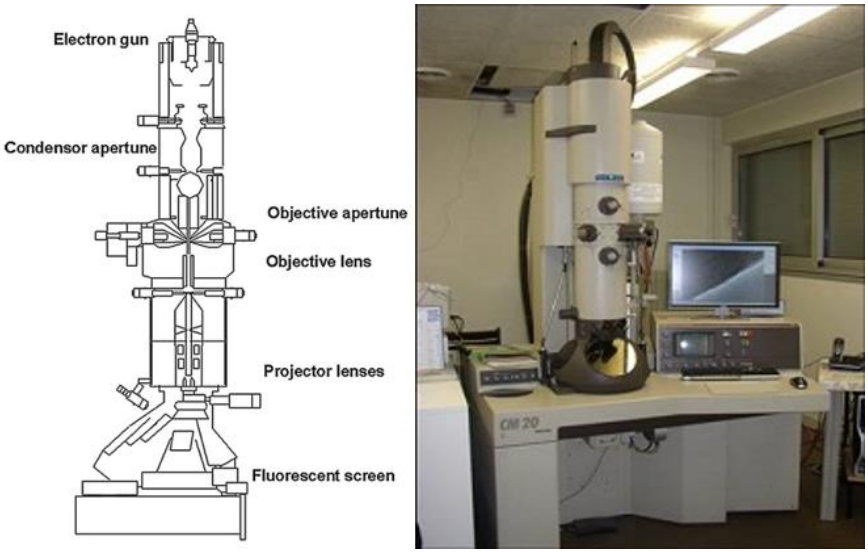

Figure 3.31 Schematic diagram of transmission electron microscope [246], [247]

The solution is then transported to the "Interfaces, Confinement, Matériaux et Nanostructures – ICMN" laboratory in CNRS, Orléans. One drop is deposited on a 3 mm metal mesh grid specific for electronic microscopy. After the liquid has evaporated from the grid, the sample is introduced inside of the microscope chamber. The measurements were performed with a Philips CM20 equipped with a LaB6 filament and coupled with EDX energy-dispersive X-ray spectrometry [Si(Li) detector], operated at 200 kV [247], as displayed on **Figure 3.31**.

Figure 3.32 shows a picture of a 0.1% toluene soot particles in high temperature, T_5 = 1954K. In this image, the grid is visible, along with the aggregates. On the other hand, the analyses are performed on the soot which is not attached on the grid, thus suspended in the void, in order to avoid any interference of the grid.

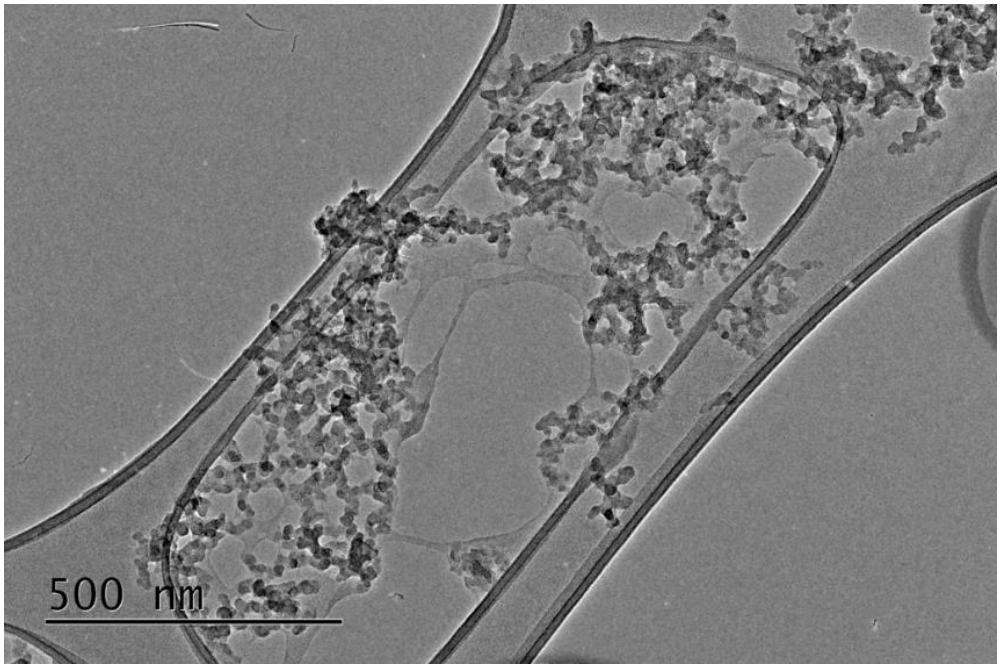

Figure 3.32 *Toluene soot particles in ethanol, T_5 = 1954K*

In the following sections, the diameter of the primary particles, images of the clusters and the internal organization of the carbon layer will be discussed for the different fuels tested.

4 Results and discussion

In this chapter, the results of the measurements performed in both shock tube are presented. The chapter is essentially divided in two sections. In the first part, the pyrolysis of n-heptane and cyclopentene are investigated in the single-pulse shock tube. To this purpose, fuel and intermediate species, including aromatics up to phenanthrene, are measured using gas chromatography and mass spectrometry diagnostics.

In the second section, measurements performed in the heated shock tube are displayed. Extinction measurements are performed for 14 different mixtures, using toluene as reference, as many works can be found in the literature, and consequently many data are available for the comparison. In particular, information about global soot growth parameters, as soot yield and induction delay time, as well as the soot structure and dimension are presented. In order to analyze the morphology of soot particles, TEM analysis is performed.

4.1 High purity single-pulse shock tube results

One of the goals of this thesis is to provide experimental databases for PAH formation chemistry at typical conditions encountered in modern combustion devices. Based on such experimental results, develop a detailed comprehensive kinetic model describing PAH formation that can be used as a base for improved soot prediction models. This work is part of a series of studies on the pyrolysis of fuels and fuel mixtures conducted at ICARE in the framework of the ERC Starting Grant FUN-PM. In particular, the data presented here concerns the pyrolysis of n-heptane (reference alkane), and cyclopentene (precursor of cyclopentadiene, and consequently the second ring) with and without the addition of acetylene. A single pulsed shock tube coupled with gas chromatography – mass spectrometry diagnostics was employed to measure stable intermediates, including large PAHs up to four rings, at high pressure, high temperature, and highly diluted conditions. These data were used for the extension of the comprehensive, detailed chemical kinetic model developed in the sequential studies.

My specific contributions to this work mainly regard developing and conducting the shock tube experiments for all the fuel mixtures presented (**Table 2**). Dr. Alaa Hamadi has performed the kinetic modeling. Thus, the details on the kinetic model development will not be provided here.

4.1.1 n-Heptane pyrolysis

n-Heptane is frequently utilized as a single-component substitute for diesel fuel and as a crucial gasoline reference fuel [248]. It dissociates into small hydrocarbon products, primarily C2, C3, and C4, when subject to high temperature conditions. These compounds can then react leading to the formation of larger species such as the polycyclic aromatic hydrocarbons, PAHs. n-Heptane pyrolysis can be thoroughly studied to reveal the processes that lead to the breakdown of the chain structure and subsequent molecular weight growth processes.

n-Heptane pyrolysis kinetics have long been pursued using numerous experimental configurations and methodologies that cover a wide range of pressure, temperature, and initial fuel concentration conditions [125], [164], [249]–[263]. For this reason, n-heptane can also be used as a target to validate a specific experimental set-up, by reproducing well-characterized experiments and/or by kinetic modeling analyses. On the other hand, past research has focused on the fuel decomposition reactivity and the formation of small hydrocarbons rather than the formation of PAHs, though this latter is necessary for the development of clean combustion technologies. For this reason, in this section, shock tube speciation datasets spanning from small hydrocarbons to three-ring aromatics from n-heptane pyrolysis experiments relevant to modern combustion devices will be provided.

4.1.1.1 Fuel decomposition and formation of small hydrocarbons

To demonstrate the predictive capabilities of the kinetic model, experimental and simulated species concentrations as a function of post-shock temperature T_5 will be presented. Three n-heptane concentrations have been studied, however only the fuel decomposition at 2000 ppm will be displayed for clarity of discussion. The data obtained with 103 ppm and 502 ppm provide similar results and they can be found in the This work was devoted to study soot formation at typical conditions encountered in modern combustion devices. Soot is a toxic compound, and its toxicity is partially attributed to the presence of PAHs condensed and adsorbed on the surface of the particles. PAHs are also the building blocks for the appearance of the nascent nanoparticles. The denomination PAH encompasses different types of chemical compounds, that have different properties, depending on their chemical structure and number of rings, as function of the fuel and the thermodynamic conditions. Particularly with regards to the morphology of soot and the chemical composition of the adsorbed phase, but also to the fundamental principles of soot formation chemistry, predictions from comprehensive kinetic models are still unsatisfactory. Adequate models are required to comprehend the intricate soot production processes. These models should be tested in well controlled environments against measurements of PAH precursors from fuel molecules and mixtures and particle

concentrations, particle size distributions, soot volume fractions, and other parameters which characterize the solid-phase chemistry.

One of the objectives of this thesis is to provide an experimental database on the chemistry of PAH formation from the pyrolysis of important fuel components at high-pressure and high-temperature conditions. In the first part of the work, pyrolysis experiments of n-heptane (from 100 to 2000 ppm in argon bath gas) and cyclopentene with and without the addition of acetylene (100 and 300 ppm cyclopentene and 100 ppm cyclopentene + 500 ppm acetylene in argon bath gas) were carried out using a single-pulse shock tube over a temperature range of 940-1680 K for a nominal pressure of 20 bar and a reaction time of around 4 ms. Chemical compositions of the post shock mixtures were analyzed using the GC/MS techniques. Species mole fraction profiles as a function of T_5 were obtained, the base for the extension of a comprehensive chemical kinetic model for PAH chemistry. n-Heptane dissociates into hydrocarbon products, mainly C2, C3 and C4, at high temperatures. These compounds then react to form larger multi-ring species (PAHs). In general, the model can capture the decomposition and formation temperature windows of the reported pyrolysis species and match their mole fraction profiles while accounting for experimental uncertainties. Analytical modeling techniques such as rate of production (ROP) analyses and sensitivity analyses were used to obtain an understanding of the chemistry of n-heptane fragmentation and aromatics growth. n-Heptane is primarily consumed by the C-C bond scission reaction, which produces n-propyl and 1-butyl radicals, and by hydrogen abstraction reactions, which produce 1-, 2-, 3-, and 4-heptyl radicals. Other C-C bond fission reactions that produce methyl and 1-hexyl radicals, as well as ethyl and 1-pentyl radicals, contribute only slightly to the thermal decomposition of n-heptane. The experimental and simulated mole fraction profiles of several common mono-aromatic hydrocarbons (MAHs) and bicyclic and tricyclic PAHs were also shown and analyzed. Through the ROP studies, the major pathways of aromatics production were presented and discussed. MAHs species detected include benzene, toluene, phenylacetylene, styrene and ethylbenzene. Concerning the soot precursor PAH molecules, the central tole of indene and the indenyl radical was highlighted for the formation of numerous species including naphthalene, acenaphthylene and fluorene. The naphthyl radical also contributes to the formation of large PAHs products such as 1-methyl naphthalene and 1-ethynyl naphthalene, while the benzyl radical self-recombination is the major reaction contributing to the three-ring structures.

The second fuel studied in the single pulse shock tube was cyclopentene with and without the addition of acetylene. The interest in cyclopentene stems from its role as a precursor to C5 intermediates, including cyclopentadiene, whose chemistry has a significant impact on PAH and soot production. The decomposition reactivity of CYC_5H_8 was studied along with the speciation of small intermediates, followed by the production of aromatic species, from the simplest benzene to the largest PAHs. The model developed

accurately describes the fuel reactivity and the formation of the main product with respect to temperature windows and peak concentrations. According to the ROP analysis, CYC_5H_8 is mainly consumed by the dehydrogenation and ring-opening isomerization processes, which result in the generation of C_5H_6 and LC_5H_8, respectively. Smaller hydrocarbons are formed by other reactions of small fragmentation products, consumption of C5 intermediates, or direct interactions of the fuel with hydrogen atoms. The reaction of C_5H_5 with small species leads to the formation of several MAHs including benzene, toluene, phenylacetylene, and styrene, while the C5+C5 mechanisms were validated for the formation of different PAH such as indene and naphthalene. Further growth to acenaphthylene and phenanthrene is the result of the indenyl radical reacting with C_3H_3 and C_5H_5, respectively. Once acetylene is added to cyclopentene, the production pathways for the small hydrocarbons did not significantly change compared to those of pure CYC_5H_8, both qualitatively and quantitatively, though the addition of C_2H_2 to CYC_5H_8 amplifies the concentrations of $C_6H_5C_2H$ and 1-ethynylnaphthalene while reducing the naphthalene concentration.

Another aim of this thesis was to develop, implement and characterize the laser-based technique to study soot formation behind reflected shock waves (scattering + extinction). In order to accomplish this task, it was decided to use the heated shock tube present at ICARE. A new end-section was designed to allow multiple optical fibers to be connected to the shock tube for delivery and collection of two laser beams. The preliminary measurements showed large vibrations in the signals. Several solutions were implemented to improve the method, which resulted in the construction of a rigid frame for blocking the shock tube, and the use of classical optical systems without optical fibers. The extinction technique was completely developed and characterized.

The new technique was then used to measure the time-dependent behavior of the soot volume fraction from numerous fuels and fuel mixtures, including benzene, toluene, cyclopentene, acetylene, ethylene, propylene, propyne, and the mixtures between the cyclic compounds and the C2/C3 intermediates, at temperatures between 1500 and 2000 K, pressures between 16 and 20 bar, and similar carbon concentrations. The first parameter that was examined was the optical density. It was shown that the maximum absolute value of D_{633nm} is reached for the intermediate temperature, hence, it can be inferred that the soot yield has a bell-shaped temperature dependence behavior, which is characteristic of the soot formation process. Similar optical densities were obtained for benzene and toluene, pyrolysis. The third pure fuel analyzed was cyclopentene and the general behavior of this fuel does not differ much from the two aromatic fuels, however, the absolute value of the optical density decreased to around half. The addition of C2 and C3 fuels to toluene, benzene, or cyclopentene lead to a significant decrease in the absolute value the optical densities. Acetylene, propyne and propylene were also studied as single fuels at similar concentrations. The single fuels can be classified as it follows concerning the propensity to form soot

particles: toluene = benzene > propyne > cyclopentene > propylene > acetylene. In order to be able to study ethylene, experiments at higher initial fuel concentrations were performed.

Another parameter derived from the extinction measurements was the induction delay time. This is one of the most important parameters to characterize the tendency of a hydrocarbon to form soot, as it is the time necessary for the first soot particles to appear. The induction times as a function of the inverse of the temperature of toluene, toluene + C2 and toluene + C3 were analyzed. The fitted curve of neat toluene was split into two parts, fitting the data in the high-temperature and low-temperature ranges. Their pre-exponential factors and their activation energies differ, suggesting the existence of two mechanisms, probably associated with the aromatic-aromatic reactions at lower T or with aromatic-aliphatic reactions at high T. The addition of C_2H_2 and C_2H_4 increases the induction delay times, especially C_2H_4, and it changes the behavior compared to neat C_7H_8 as the data can be fit with a single curve. The binary mixture of toluene and propyne or propylene shows similar behavior to neat C_7H_8, i.e., the data needs to be described with two curves, although the difference in the activation energies is less significant than for the neat toluene. Again, an increase in the induction times was observed for the mixtures. In the case of benzene, the fitted curve of the neat fuel is divided into two parts, similarly to toluene, but with a less marked difference in the activation energies. The addition of acetylene and ethylene increases the induction times, but it modifies the behavior as only a single curve could be used to fit the data. For cyclopentene, the addition of C_2H_2 had a small impact on the induction delays with a slight increment observed. Considering the C2 and C3 fuels, the order for the tendency to form particles follows a similar trend than the optical densities: toluene > benzene > propyne > cyclopentene > propylene > acetylene. Among the non-cyclic fuels, only propyne shows a double-stage behavior as the aromatic fuels, possibly due to the formation of large amounts of benzene from the C3+C3 reactions.

After the induction period, the soot volume fraction grows quickly by surface reactions and coagulations. With the assumption that beyond the inflection point of the curve the growth of the volume fraction occurs mainly by surface reactions with the gas phase molecules, the soot growth rate was derived considering a first-order Arrhenius law. The results showed that the addition of C_2H_2 and C_2H_4 to benzene and toluene have the same consequences on the soot growth rates, with a similar decrement in the absolute value. The same for the addition of propyne and propylene to toluene. The comparison between the different single fuels leads to the following ranking in the propensity to form particles toluene > benzene > cyclopentene > propyne > propylene > acetylene. Thus, in this case, cyclopentene has a faster growth rate than propyne. Among the different fuels and mixtures, only the curves for toluene, benzene, and propyne were described by two different fitting curves. The activation energy of the high-temperature regions for such fuels, and the activation energies of the remaining fuels show similar values.

Lastly, the study of soot particles by transmission electron microscopy (TEM) was performed at two magnifications: $2.75x10^4$ (soot texture: morphology, primary particle size) and $2x10^5$ (microstructure: length of carbon planes, distance between these planes). For pure fuels (toluene, benzene and cyclopentene), three temperatures were analyzed: minimum, intermediate (at the maximum optical densities) and maximum. Once C_2H_2 or C_2H_4 was added, only the intermediate temperature was analyzed. The particles are composed of chains of primary spheres and the average diameter of the spheres strongly varies with the temperature. On the other hand, the three cyclic fuels have similar values. For toluene and benzene, the addition of acetylene and ethylene lead to an increase of the particle size, while no significant variation could be obtained when acetylene was added to cyclopentene. The analyses on acetylene pyrolysis showed very large primary particles compared to the other fuels. Concerning the internal organization of the carbon planes, in general, its length and parallelism on the external crown of the particle increases with temperature. For intermediate and high temperatures, the core of the particle is made of different nuclei that seem to come from the coalescence process.

As a perspective work, the Rayleigh scattering measurements will be implemented in the heated shock tube for complementing the extinction and TEM data. This would allow to derive the mean diameter of the particles as a function of time. Another objective to pursue is to do the TEM analysis for other fuels tested, in order to have a more mapping of the influence of the fuel composition on the soot structure. The work of course could be extended to other fuels of interest, including important aromatic intermediates, aliphatics, and naphthenes, as well as real fuels including the new generation biofuels. In addition, with the intention of obtaining a complete understanding of the soot formation, it would be useful for the scientific community to investigate the soot formation in oxidation conditions. Lastly, the development of a soot code for simulation of the particle formation in pyrolytic conditions is an ongoing effort as part of a different thesis work at ICARE.

Appendix.

In general, the model can capture the decomposition and formation temperature windows of reported species and it can match their mole fraction profiles within the experimental uncertainties. Modelling analyses such as rate of production (ROP) analyses and sensitivity analyses will be used to obtain understanding of the chemistry of n-heptane fragmentation and aromatics growth.

Figure 4.1 (**Figure A. 1** and **Figure A. 2**) presents the experimental and simulated mole fraction profiles of n-heptane and C1–C6 acyclic species. The kinetic model accurately predicts the measured fuel conversion profiles as well as the formation of small intermediates in the individual studied cases. In particular, it can be clearly observed that as soon as n-heptane decomposes, olefins start to be produced in large amounts.

To determine the correlation between various alkene production and the fuel consumption, **Figure 4.2** displays initial fuel decomposition pathways based on integrated ROP analyses over 4 ms in the three reaction systems. The temperatures chosen to perform these ROP calculations are 1160 K for 103 and 502 ppm heptane pyrolysis, and 1130 K for 2000 ppm heptane pyrolysis, where approximately half of the fuel is consumed in each case.

n-Heptane is mainly consumed via the C-C bond scission reaction producing n-propyl (NC_3H_7) and 1-butyl (PC_4H_9) radicals, and via the H-abstraction reactions to 1-, 2-, 3-, and 4-heptyl radicals. Other C-C bond fission reactions that produce methyl and 1-hexyl radicals, along with ethyl and 1-pentyl radicals, contribute only slightly to the thermal decomposition of n-heptane.

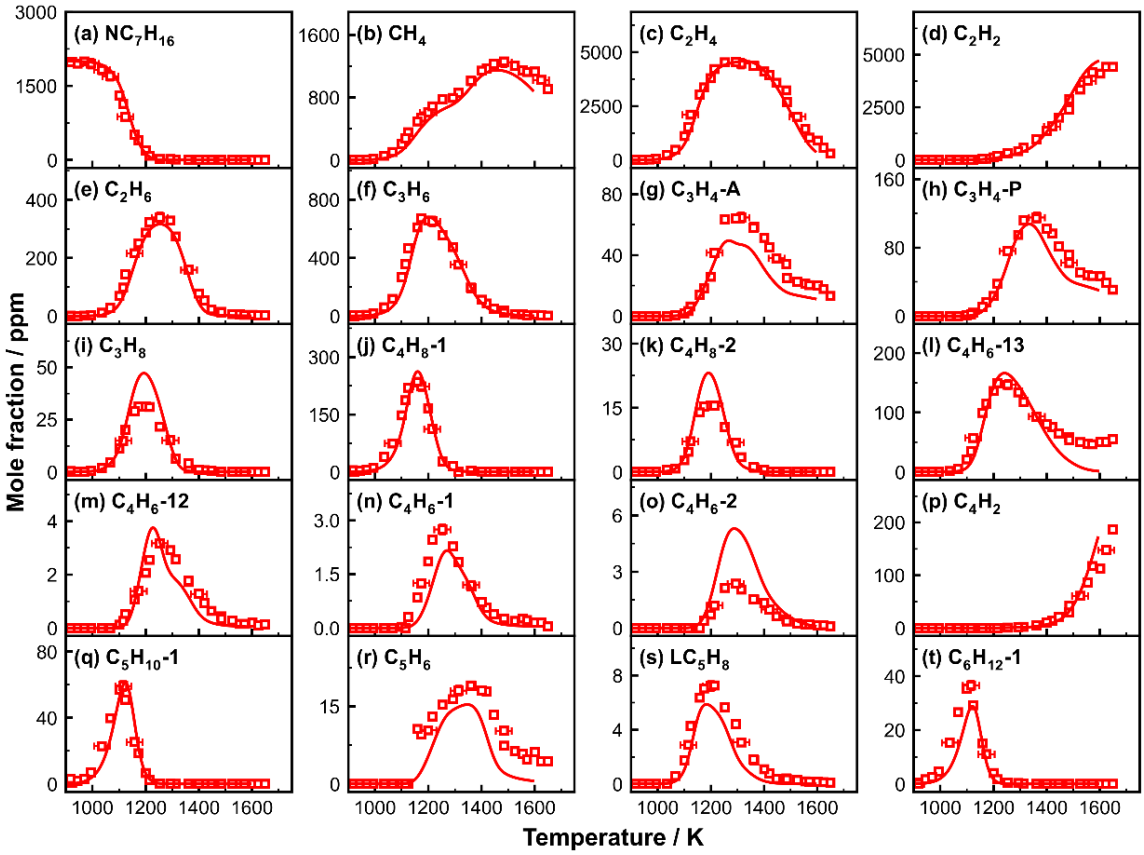

Figure 4.1 *Measured (symbols) and simulated (lines) mole fraction profiles of fuel and small intermediates as a function of post-shock temperature T_5 in heptane pyrolysis, 2000 ppm*

The numerous alkene products derive from the decomposition of the principal heptane radicals. Propylene (C_3H_6), **Figure 4.1(f)**, and 1-pentene (C_5H_{10}-1), **Figure 4.1(q)**, are straight formed through the unimolecular decomposition of 2- and 4-heptyl radicals, respectively. The 3-heptyl radical permits a substantial fraction of methyl radical (CH_3) and l-hexene (C_6H_{12}-1), **Figure 4.1(t)**, to be formed in favor of NC_3H_7 and l-butene (C_4H_8-1), **Figure 4.1(j)**. The allyl (C_3H_5-A) + CH_3 recombination reaction is the second important C_4H_8-1 formation channel at 1160 K (around 30% according to the ROP analyses).

The majority of C_3H_5-A is produced by the unimolecular breakdown of C_5H_{10}-1 and C_6H_{12}-1 and a small amount is produced from C_3H_6 through H-abstraction processes involving the methyl radical and hydrogen atom.

The other butene isomer, 2-butene (C_4H_8-2), **Figure 4.1(k)**, is produced mainly through isomerization and H-assisted isomerization of C_4H_8-1, with slight contribution from C_3H_5-A + CH_3 recombination reaction in 100 ppm n-heptane pyrolysis. However, as the n-heptane concentration rises, the latter contributes more to become a significant contributor in 2000 ppm n-heptane pyrolysis.

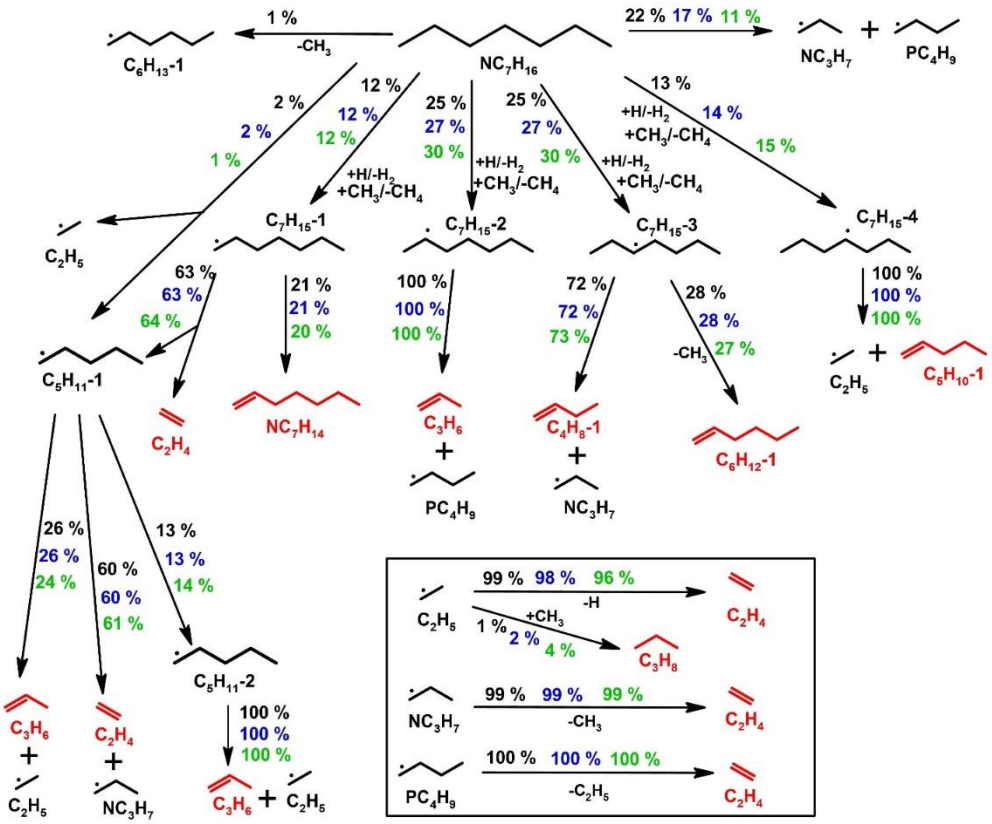

Figure 4.2 *Fuel consumption pathways at 1160 K in 103 and 502 ppm heptane pyrolysis and at 1130 K in 2000 ppm heptane pyrolysis. The percentage numbers (103 ppm heptane: black normal; 502 ppm heptane: blue normal; 2000 ppm heptane: green normal) are the contributions by the corresponding reactions to the consumption of the species on the source side. The reaction path analyses are based on the integrated ROP analyses over 4 ms*

Ethylene (C_2H_4), **Figure 4.1(c)**, is formed via several reaction pathways, as presented in **Figure 4.2**. These reactions include the direct decomposition of 1-heptyl, and thermal fragmentation of 1-pentyl (C_5H_{11}-1), 1-butyl, l-propyl, and ethyl radicals, these radicals derive from 1-,2-,3-and 4-heptyl decomposition, respectively. The leading C_2H_4 consumption route is the unimolecular breakdown reaction into vinyl radicals (C_2H_3) and H-atoms.

The recombination between methyl and ethyl radicals leads to propane formation (C_3H_8), **Figure 4.1(i)**, starting in the low temperature region of the current study. Pentadiene (LC_5H_8), **Figure 4.1(s)**, is the result of the unimolecular decomposition of pentenyl (NC_5H_9-3) and heptenyl radicals (NC_7H_{13}), which are formed through dehydrogenation of C_5H_{10}-1 and 1-heptene (NC_7H_{14}), respectively. The unimolecular breakdown of C_7H_{15}-1 produces entirely NC_7H_{14}, as shown in **Figure 4.2**.

Successive reactions produce the remaining small hydrocarbons. In particular, the major products methane (CH_4), **Figure 4.1(b)**, and ethane (C_2H_6), **Figure 4.1(e)**, result from the abundant CH_3 production via:

- $NC_3H_7 = CH_3 + C_2H_4$ reaction at low temperatures (>1200 K),

- $H + C_3H_6 = CH_3 + C_2H_4$ reaction at moderate temperatures (1200-1350 K),
- and unimolecular decomposition of C_2H_6 at high temperatures (> 1400 K).

Acetylene (C_2H_2), **Figure 4.1(d)**, is predominantly formed by the decomposition of C_2H_3 and slightly by the reaction of H atoms with allene (C_3H_4-A), **Figure 4.1(g)**, and propyne (C_3H_4-P), **Figure 4.1(h)**, which are C_3H_4 isomers. These isomers are also created through the consumption of C_3H_6.

Other complex isomer product mixtures are observed in n-heptane pyrolysis, including the C_4H_6 isomers which are: 1-butyne (1-C_4H_6), **Figure 4.1(n)**, 2-butyne (2-C_4H_6), **Figure 4.1(o)**, 1,2-butadiene (1,2-C_4H_6), **Figure 4.1(m)**, and 1,3-butadiene (1,3-C_4H_6), **Figure 4.1(l)**. Previous studies on heptane pyrolysis have rarely reported quantitative mole fraction profiles for these isomers. The current model captures 1,3-C_4H_6, 1,2-C_4H_6, and 1-C_4H_6 profiles well; nonetheless, divergences exist between the experimental and simulated 2-C_4H_6 speciation profiles. The peak mole fraction of 1,3-C_4H_6 is fifty times larger than that of the other three isomers. To explain the larger peak mole fractions of 1,3-C_4H_6 more effectively in comparison to the other C_4H_6 isomers, ROP analyses are conducted across the temperature formation windows. The formation of the dominant isomer 1,3-C_4H_6 mainly depend on the 1-C_4H_8 consumption through the di-dehydrogenation via 1-buten-3-yl ($C_4H_71–3$) radical as an intermediate. 1,2-C_4H_6 is primarily formed through CH_3 + propargyl (C_3H_3) reaction, where C_3H_3 derived from the decomposition of allene and propyne. Reactions between CH_3 and C_3 molecules/radicals (C_3H_4-A and C_3H_3) govern the formation of 1-C_4H_6. The production of 2-C_4H_6 mostly depends on the isomerization reactions of 1,2-C_4H_6 and just moderately by 1,3-C_4H_6 isomerization reactions.

Regarding C5 species, cyclopentadiene (C_5H_6), **Figure 4.1(r)**, is primarily formed by dehydrogenated of cyclopentadiene (CYC_5H_8) and slightly through the reaction C_3H_5-A+C_4H_6=C_2H_5+C_5H_6. The 1-penten-4-yl radical ($C_5H_9$14) formed by the C_3H_5-A+C_2H_4 recombination reaction can undergo cyclization reaction to produce cyclopentenyl radical (cyC_5H_9), which is the key source of CYC_5H_8 through its β-C–H scission.

4.1.1.2 Aromatic growth

Figure 4.3 shows the mole fraction profiles for both experimental and simulated mole fraction profiles of several common mono-aromatic hydrocarbons (MAHs) and bicyclic and tricyclic PAHs with a starting fuel concentration of 2000 ppm. The aromatic growth of 103 and 502 ppm can be found in the Appendix (**Figure A. 3** and **Figure A. 4**). The current model successfully reproduces the experimental trends for the shapes and peak concentrations for all the aromatics.

Through ROP studies, the major aromatic production pathways will be now discussed. The reactions that lead to the creation of these aromatics are analogous in all reaction systems. However, the higher n-heptane concentration favors the formation of higher concentrations of aromatics due to the increased amount of carbon in the reaction system.

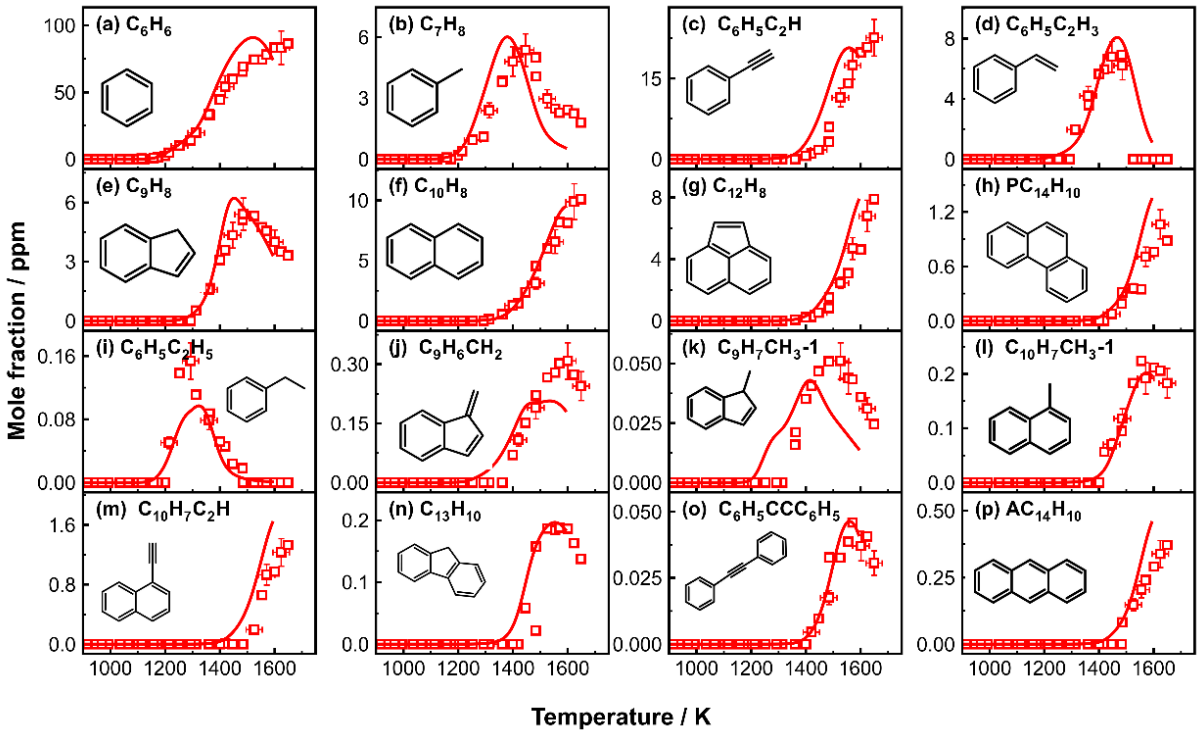

Figure 4.3 *Measured (symbols) and simulated (lines) mole fraction profiles of MAHs and PAHs as a function of post-shock temperature T_5 in heptane pyrolysis, 2000 ppm*

The formation of the first aromatic ring is one of the main topics discussed in kinetic studies of acyclic fuel consumption under fuel-rich or pyrolytic conditions. The MAH species detected in n-heptane pyrolysis include benzene (C_6H_6), **Figure 4.3(a)**, toluene (C_7H_8), **Figure 4.3(b)**, phenylacetylene ($C_6H_5C_2H$), **Figure 4.3(c)**, styrene ($C_6H_5C_2H_3$), **Figure 4.3(d)**, and ethylbenzene ($C_6H_5C_2H_5$), **Figure 4.3(i)**.

The most predominant MAH species produced is C_6H_6. The reaction pathways leading to the formation of C_6H_6 are mapped using integrated ROP studies at 1250 K and 1450 K as illustrated in **Figure 4.4**. Three sources are responsible for C_6H_6 production in heptane pyrolysis:

- the dehydrogenation of 1,4-cyclohexadiene (CYC_6H_8) that is mainly produced from C_2H_3+C_4H_6 recombination followed by cyclization, H-abstraction and β-scission [149],
- the reaction sequence $2C_3H_3 \rightarrow$ fulvene $\rightarrow C_5H_5CH_2$-1/$C_5H_5CH_2$-2 $\rightarrow C_6H_6$ [264],
- and the C_3H_3 self-recombination**.**

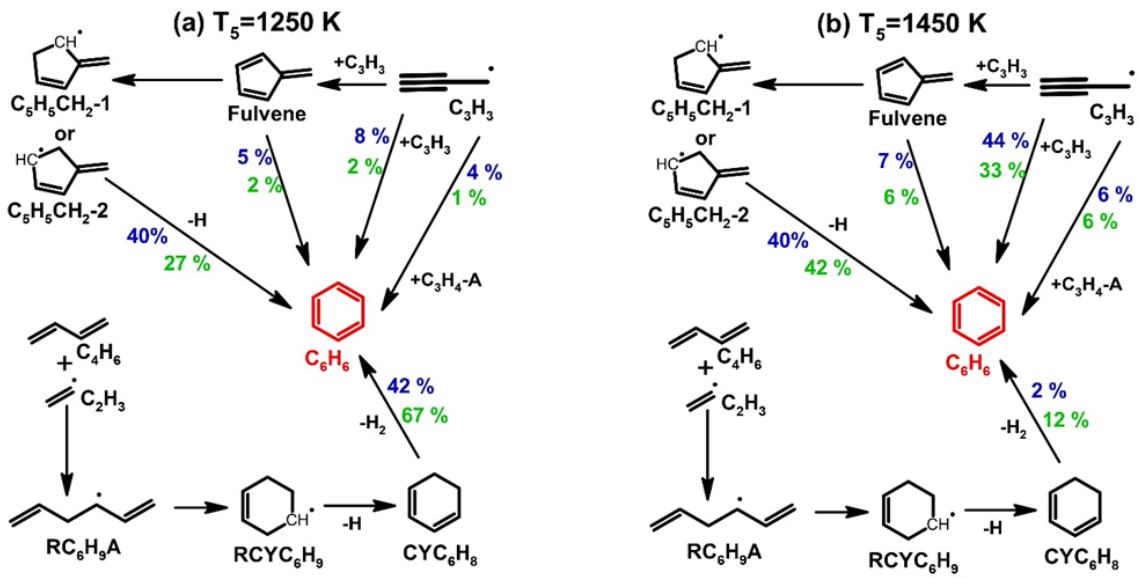

Figure 4.4 *The reaction pathways leading to benzene formation at* ***(a)*** *T_5 = 1250 K,* ***(b)*** *T_5 = 1450 K in the pyrolysis of heptane. The percentage numbers (502 ppm heptane: blue normal; 2000 ppm heptane: green normal) represent the contributions to benzene formation*

According to the temperature, the relative relevance of the above-mentioned channels changes. At low temperatures, the first two pathways control C_6H_6 formation, whereas at high temperatures, the last two channels govern its formation. Additionally, the C_3H_5-A+C_3H_3 recombination and the fulvene isomerization have minor effects on C_6H_6 throughout the temperature range.

Concerning toluene, its formation depends mainly on the reactions of C_3H_3 with C_4H_6 and but-2-yn-1-yl radical (C_4H_5-2). The formation of $C_6H_5C_2H$ and $C_6H_5C_2H_3$ largely relies on the reactions of phenyl with C_2H_2/C_2H and C_2H_4, respectively. C_5H_5+C_3H_3 reaction and C_4H_6 self-recombination also slightly contribute to $C_6H_5C_2H_3$ at low temperatures. $C_6H_5C_2H_5$ is mainly formed through benzyl (C_7H_7) + CH_3. C_4H_6 self-recombination also has a non-negligible contribution to $C_6H_5C_2H_5$.

The smallest PAH detected in this study is indene (C_9H_8), **Figure 4.3(e)**. C_9H_8 mainly originates from the bimolecular reaction C_9H_7+H=C_9H_8 at low temperatures (T_5 < 1400 K), where C_9H_7 is exclusively formed from C_4H_2+C_5H_5 reaction. As the temperature increases, the isomerization of 1-phenyl-propyne ($C_6H_5C_3H_3$P_1) and phenyl-allene ($C_6H_5C_3H_3$A), and C_7H_7+C_2H_2 reaction become the dominant C_9H_8 formation channels. $C_6H_5C_3H_3$P_1 is mainly formed through the reaction $C_6H_5C_2H$+CH_3, whereas the recombination reaction C_6H_5 + C_3H_3 is the major source of $C_6H_5C_3H_3$A.

C_9H_8 consumption mostly yields indenyl radical (C_9H_7) through H-abstraction and unimolecular decomposition. C_9H_7 participates in the formation of the other PAHs, including naphthalene ($C_{10}H_8$), **Figure 4.3(f)**, and acenaphthylene ($C_{12}H_8$), **Figure 4.3(g)**, which were found to be the most predominant

multi-ring products. The formation mechanism of $C_{10}H_8$ includes several possible reaction pathways that are displayed in **Figure 4.5**, based on ROP analysis at 1525 K. $C_{10}H_8$ mainly comes from the isomerization of benzofulvene ($C_9H_6CH_2$), **Figure 4.3(j)**. According to the ROP results, the formation of $C_9H_6CH_2$ relies on three major channels:

- the unimolecular decomposition of methyl-indene radical ($C_9H_6CH_3$-1) following the production of 1-methyl-indene ($C_9H_7CH_3$-1) through C_9H_7+CH_3 recombination;
- the recombination between fulvenallyl (C_7H_5) and C_3H_3;
- the bimolecular reaction between o-benzyne (o-C_6H_4) and vinylacetylene (C_4H_4).

Besides the above-mentioned pathway to naphthalene, the consumption of methyl-indene radicals ($C_9H_7CH_2$ and $C_9H_6CH_3$-1) and C_7H_5+C_3H_3 reaction are also potential sources of $C_{10}H_8$ (**Figure 4.5**).

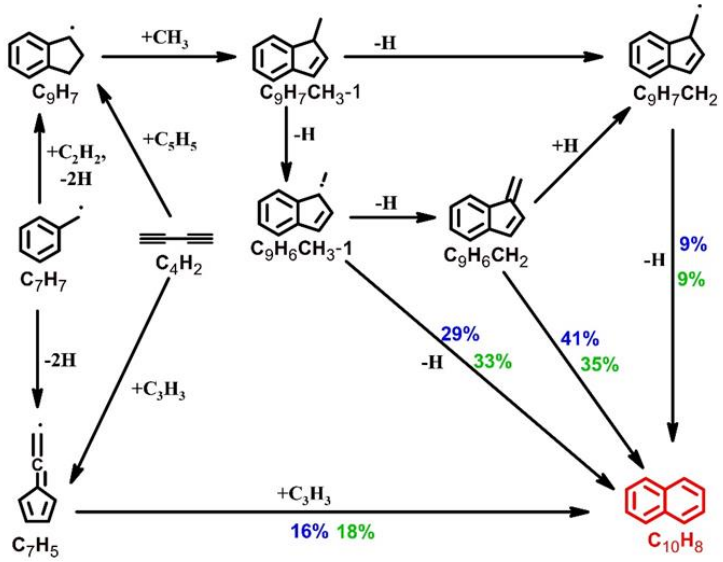

Figure 4.5 *The reaction pathways leading to naphthalene formation at T5 = 1525 K in the pyrolysis of heptane. The percentage numbers (502 ppm heptane: blue normal; 2000 ppm heptane: green normal) represent the contributions to naphthalene formation by the corresponding reactions*

1-methyl-indene ($C_9H_7CH_3$-1), **Figure 4.3(k)**, 1-methyl naphthalene ($C_{10}H_7CH_3$-1), **Figure 4.3(l)**, acenaphthylene ($C_{12}H_8$), **Figure 4.3(g)**, 1-ethynyl-naphthalene ($C_{10}H_7C_2H$_1), **Figure 4.3(m)**, and fluorene ($C_{13}H_{10}$), **Figure 4.3(n)**, are among the major C_{10}–C_{13} PAHs identified. As previously stated, $C_9H_7CH_3$-1 is a key precursor for the naphthalene-benzofulvene isomer pair. The C_9H_7 + CH_3 recombination produces the majority of $C_9H_7CH_3$-1.

In the pyrolysis of n-heptane, $C_{12}H_8$ is one of the most abundant PAHs. Throughout the temperature range, $C_{12}H_8$ production is dominated by the C_9H_7+C_3H_3 recombination and consequent dehydrogenation and ring-rearrangement processes [265].

The formation of the remaining PAHs involves the participation of naphthyl radical ($C_{10}H_7$-1): $C_{10}H_7$-1+CH_3 recombination is the primary source of $C_{10}H_7CH_3$-1; the HACA route $C_{10}H_7$-1+C_2H_2 = $C_{10}H_7C_2H$_1+H controls the formation of $C_{10}H_7C_2H$_1 and partly accounts for $C_{12}H_8$ formation (27% at 1525 K); $C_{10}H_7$-1+C_3H_4-P is a minor route leading to $C_{13}H_{10}$. However, the C_9H_7+vinylacetylene (C_4H_4) reaction governs the $C_{13}H_{10}$ formation in n-heptane pyrolysis throughout the temperature range.

Four distinct $C_{14}H_{10}$ species, including the predominant phenanthrene ($PC_{14}H_{10}$), **Figure 4.3(h)**, and its isomers, diphenylacetylene ($C_6H_5CCC_6H_5$), **Figure 4.3(o)**, 9-methylene-fluorene ($C_{13}H_8CH_2$), and anthracene ($AC_{14}H_{10}$), **Figure 4.3(p)**, are detected and measured. The reaction pathways leading to $C_{14}H_{10}$ isomers formation at 1500 K are presented in **Figure 4.6.** $C_6H_5CCC_6H_5$ and $C_{13}H_8CH_2$ are the products of the $C_6H_5C_2H$+C_6H_5 addition-elimination reaction [266]. $AC_{14}H_{10}$ is totally formed from C_7H_5 self-recombination.

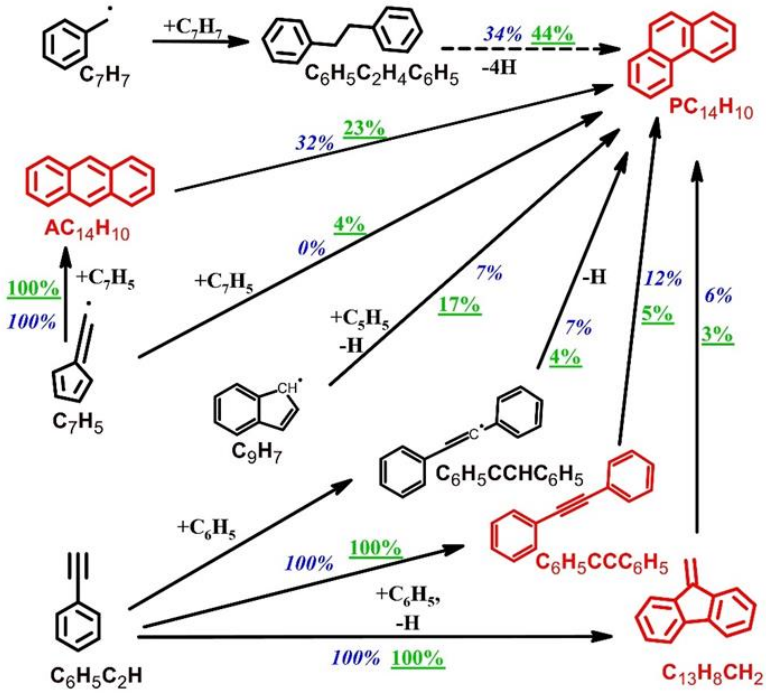

Figure 4.6 *The reaction pathways leading to the formation of C14H10 isomers at T5 = 1500 K in the pyrolysis of heptane. The percentage numbers (502 ppm heptane: blue italic; 2000 ppm heptane: green underlined) represent the contributions to C14H10 isomers formation by the corresponding reactions. The dashed arrows represent multi-step reaction*

The main sources of $PC_{14}H_{10}$ are $AC_{14}H_{10}$ isomerization and C_7H_7 self-recombination. The self-recombination of C_7H_5, the H-assisted isomerization of $C_6H_5CCC_6H_5$ and $C_{13}H_8CH_2$, and the reaction of C_9H_7 with the cyclopentadienyl radical (C_5H_5), which is produced by the consumption of C_5H_6 and the addition of C_3H_3 to C_2H_2, are additional reaction pathways that also contribute to the formation of $PC_{14}H_{10}$.

In conclusion, the combination of experimental findings and additional modeling analyses have been used to show the creation paths of PAH species during n-heptane pyrolysis. The results will enable researchers to comprehend better the formation of PAHs during the combustion of surrogate fuels which generally contain n-heptane as a component. The data on the n-heptane thermal decomposition could also be used to test the accuracy of our single-pulse shock tube experimental facility.

4.1.2 Cyclopentene pyrolysis with and without acetylene addition

Interest in cyclopentene originates from its role as precursor of key C5 intermediates, including cyclopentadiene (C_5H_6), whose chemistry has a significant impact on the production of PAHs and soot. Indeed, at typical flame temperatures, C_5H_6 is easily converted into cyclopentadienyl radical (C_5H_5), an important intermediate for the formation of mono-aromatic hydrocarbons (MAHs) and PAHs [153]–[155]. As was previously mentioned in section 2.3.3 many experimental setups and approaches have been used to investigate the reactions involving C5 species. The present work aims at further improving our fundamental understanding of the related molecular weight growth processes at high-pressure, high-temperature conditions frequently encountered in combustion devices.

Only two kinetic studies focused on the pyrolysis of cyclopentene are available in the literature [140], [141] . The single-pulse shock tube experiments at highly diluted conditions presented here complement the previous studies. In addition, to investigate the effects of acetylene addition, co-pyrolysis experiments of cyclopentene plus acetylene were performed. It is important to emphasize that recent kinetic mechanisms developed by Herbinet et al. [141] and Vervust et al. [140] are used to simulate the current experiments for comparison purposes. In reality, the model by Vervust et al. [140] has not been validated against cyclopentene data, but only against results involving cyclopentadiene and ethene. On the other hand, the chemistry for the formation of the second-ring naphthalene by C5+C5 reactions is similar to all these reaction systems, thus the model by Vervust et al. [140] will be used only to evaluate such portion of the kinetic scheme relevant to naphthalene formation.

4.1.2.1 Fuel decomposition and formation of small hydrocarbons

In this section, the first step is to examine the CYC_5H_8 decomposition reactivity and the speciation of small intermediates, and then put emphasis on the production of aromatic species, from the simplest benzene to larger PAHs. For clarity of discussion, only the data from 108 ppm CYC_5H_8 pyrolysis are presented in the discussion, while the ones for 326 ppm are given in the Appendix.

Figure 4.7 (and **Figure A. 8**) shows the mole fraction profiles of the fuel and the C0-C5 species as a function of T_5, including measurements and simulations using the current model and the different kinetic models from literature [140], [141].

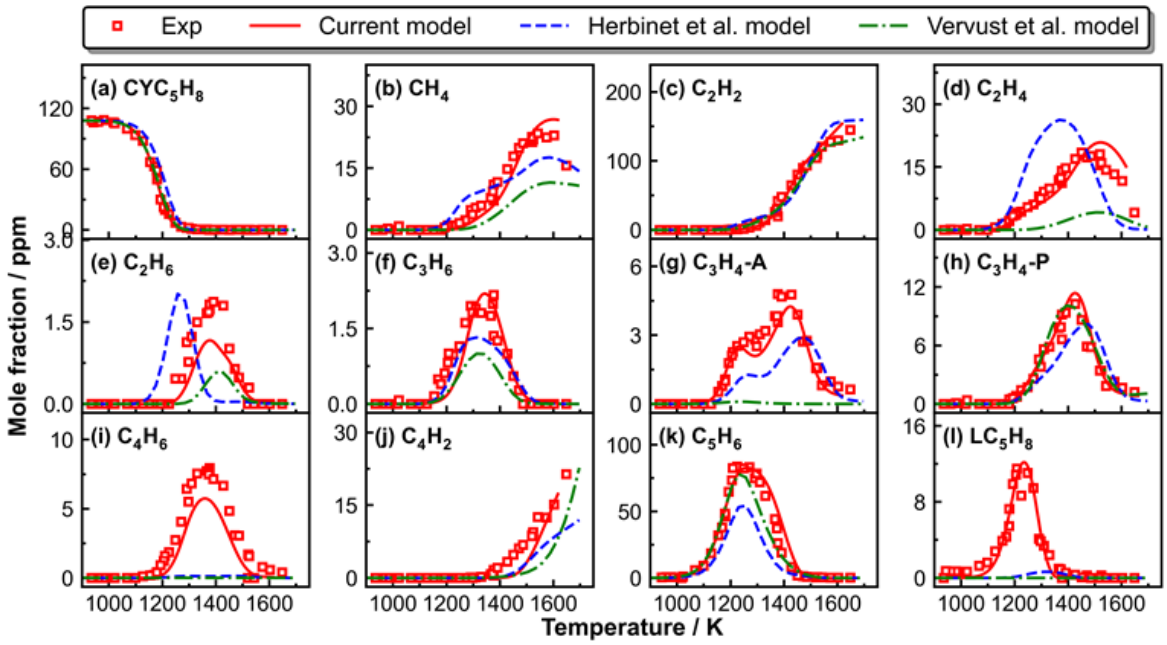

Figure 4.7 Measured (symbols) and simulated (lines) profiles of fuel and the C0-C5 species as a function of T_5 in 108 ppm cyclopentene pyrolysis. Thick solid red lines: simulations using the current kinetic model; thin dashed blue lines: simulations using the Herbinet et al. [141] model; thin dot dashed green lines: simulations using the Vervust et al. [140] model

The current model accurately depicts the fuel reactivity and formation of major product with respect to both the temperature windows and the peak concentrations. According to the rate-of production (ROP) analysis, CYC_5H_8, **Figure 4.7(a)** is mostly consumed through dehydrogenation and ring-opening isomerization processes, which result in the generation of C_5H_6, **Figure 4.7(k)**, and LC_5H_8, **Figure 4.7(l)**, respectively (CYC_5H_8=C_5H_6+H_2: 84% and CYC_5H_8=LC_5H_8: 11% throughout the conversion range).

Small hydrocarbons are formed through further reactions of the small fragmentation products, consumption of C5 intermediates, or direct fuel interactions with H atoms. The primary products of LC_5H_8 consumption are 1,3-butadiene (C_4H_6) and propene (C_3H_6) [267]. **Figure 4.7(i)** shows the profile of C_4H_6 which is predominantly formed through the H-addition reaction to LC_5H_8 (H+LC_5H_8=C_4H_6+methyl (CH_3)). On the other hand, C_3H_6, **Figure 4.7(f)**, is mainly produced through the reaction LC_5H_8=C_2H_2+C_3H_6, and minorly through H+LC_5H_8=C_3H_6+vinyl (C_2H_3).

The predominant pathway leading to the synthesis of allene (C_3H_4-A), **Figure 4.7(g)**, at low temperature (around 1200 K) is the dehydrogenation of allyl (C_3H_5-A), which is formed from C_3H_6, and H-addition to CYC_5H_8/LC_5H_8 (H+CYC_5H_8/LC_5H_8=C_3H_5-A+C_2H_4). The C_5H_6 unimolecular decomposition into

C_2H_2+C_3H_4-A also slightly contributes to C_3H_4-A (6 % at 1250 K). At higher temperatures, these pathways have equivalent contribution (55% for the former one and 41 % for the latter one at 1400 K). Through isomerization, the consumption of C_3H_4-A leads to the formation of propyne (C_3H_4-P), **Figure 4.7(h)**. C_5H_6 unimolecular decomposition into C_2H_2+C_3H_4-P is also a crucial step in the production of C_3H_4-P.

The C3 products propene and propyne, as well as C_4H_6 are consumed through H-abstractions, producing CH_3. Methane (CH_4), **Figure 4.7(b)**, is formed through the H+CH_3 recombination reaction and the hydrogen abstraction reactions by CH_3 from C_5H_6. Ethane (C_2H_6), **Figure 4.7(e)**, is solely produced from the self-recombination of CH_3. The C_2H_6 consumption afterwards contributes to C_2H_4 production, **Figure 4.7(d)**. Other important pathways for C_2H_4 formation include the H-addition reactions to CYC_5H_8 (H+CYC_5H_8=C_3H_5-A+C_2H_4), LC_5H_8 (H+LC_5H_8= C_3H_5-A+C_2H_4), C_4H_6 (H+C_4H_6=C_2H_3+C_2H_4), and C_3H_6 (H+C_3H_6=CH_3+C_2H_4).

C_2H_2, **Figure 4.7(c)**, can be formed through a variety of pathways. The C_5H_5 unimolecular decomposition (C_5H_5=C_2H_2+C_3H_3), C_2H_3 unimolecular decomposition (C_2H_3=C_2H_2+H), C_5H_6 decomposition (C_5H_6=C_2H_2+C_3H_4-P), and the H-atom addition fragmentation of C_3H_4-P (H+C_3H_4-P=C_2H_2+CH_3) produce most of the C_2H_2. The generation of vinyl radical is mainly done via the consumption of both C_4H_6 and C_2H_4.

Although the kinetic model by Herbinet et al. [141] slightly underpredicts the fuel's reactivity, it accurately reproduces the formation of key intermediates including acetylene, C3 fuels, and cyclopentadiene (although with slight under-prediction). Larger discrepancies can be seen for C_2H_4, C_2H_6 and CH_4, as well as for C_4H_6 and linear C_5H_8 whose production is not predicted. On the other hand, the model by Vervust et al. [140] captures correctly the reactivity of the fuel as well as the initial formation and peak concentration of cyclopentadiene, hence it can be used to further test the pathways involving the cyclic C5 + cyclic C5 reaction pathways to naphthalene.

4.1.2.2 Aromatic growth

Figure 4.8 (and **Figure A. 9**) presents the mole fraction profiles of MAHs and PAHs as function of T_5. Within the temperature windows and peak concentrations, the current model can well reproduce the aromatics speciation. **Figure 4.9** shows the aromatic formation pathways based on integrated ROP analysis at T_5 = 1400 K when the majority of aromatics have high concentrations. The shown pathways start from C_5H_5 that is formed through H-abstraction reactions from C_5H_6, the most abundant product in CYC_5H_8 pyrolysis (**Figure 4.7**).

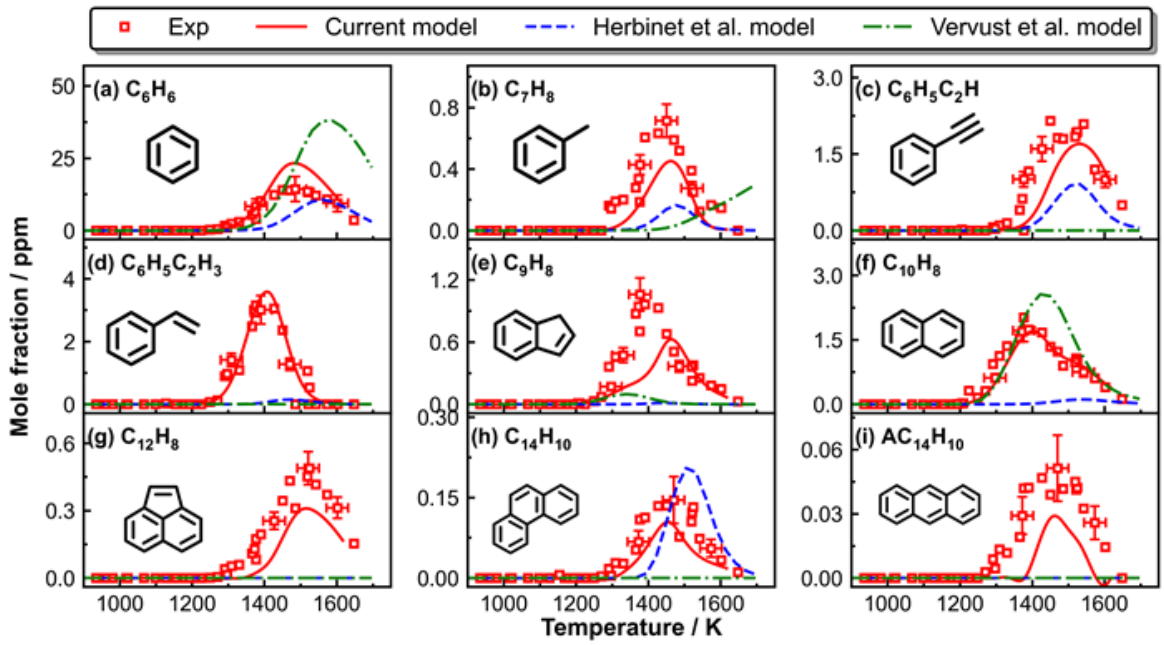

Figure 4.8 *Measured (symbols) and simulated (lines) mole fraction profiles of the aromatic species as a function of T_5 in 108 ppm cyclopentene pyrolysis. Thick solid re d lines: simulations using the current kinetic model; thin dashed blue lines: simulations using the Herbinet et al. [141] model; thin dot dashed green lines: simulations using the Vervust et al. [140] model*

The reaction of C_5H_5 with small species leads to the formation of several MAHs including benzene (C_6H_6), **Figure 4.8(a)**, toluene (C_7H_8), **Figure 4.8(b)**, phenylacetylene ($C_6H_5C_2H$), **Figure 4.8(c)**, and styrene ($C_6H_5C_2H_3$), **Figure 4.8(d)**. Three C_6H_7 isomers ($C_5H_5CH_2$-1, $C_5H_5CH_2$-2, and $C_5H_4CH_3$) are produced as a result of the C_5H_5 recombination with CH_3 and hydrogen elimination. These isomers then go through C-C beta scission with ring expansion and a C-H beta scission to give C_6H_6 and H atom. Propargyl recombination is a significant additional mechanism for the production of benzene (**Figure 4.9**).

Propargyl with C_4H_6 and but-2-yn-1-yl radical ($\dot{C}H_2C\ CCH_3$) recombination reactions are the main sources of C_7H_8 formation. The formation of C_7H_8 through C_5H_6+C_2H_2 reaction is only 5% at 1400 K. The reduced toluene production through this channel and the under-predication of the model to C_7H_8 peak mole fraction in both sets (**Figure 4.8(b)** and **Figure A. 9(b)**) indicate that either more theoretical work on C_5H_6+C_2H_2 is needed or formation channels are missing. $C_6H_5C_2H_3$ is primarily produced through C_5H_5+C_3H_3 reactions, and slightly through C_6H_5+C_2H_4 reaction.

The two most abundant PAHs found in the current study, (C_9H_8), **Figure 4.8(e)**, and naphthalene ($C_{10}H_8$), **Figure 4.8(f)**, are formed from C_5H_5. Fulvalane is produced by the C_5H_5+C_5H_5 recombination reaction, and they decompose into fulvalanyl radicals. According to the modeling analysis, fulvalanyl radicals undergo gradual isomerization to create $C_{10}H_8$ [268], and this reaction sequence is the main pathway for $C_{10}H_8$ formation in cyclopentene pyrolysis (**Figure 4.9**).

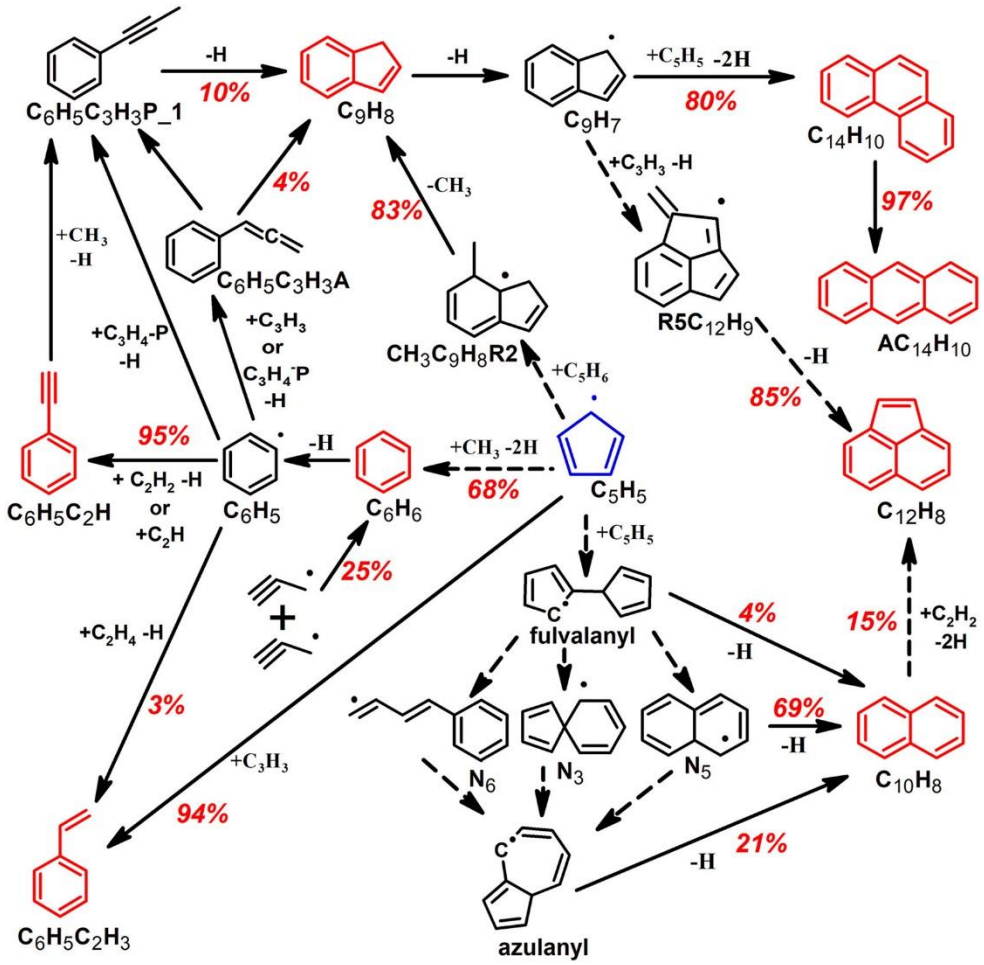

Figure 4.9 *The reaction pathways leading to aromatics formation based on integrated ROP analyses at T_5 of 1400 K in the pyrolysis of CYC_5H_8. The percentage numbers represent the contributions of the corresponding reactions in aromatic formation. The dashed arrow resembles multi-step reactions*

Indene is primarily formed through the addition of C_5H_5 to C_5H_6 through the intermediate methylindanyl ($CH_3C_9H_8R2$) [269]. The modeling analysis demonstrates that, in the context of the current investigation, the kinetic parameters of the first step (addition of C_5H_5 to C_5H_6) are extremely sensitive. Indene is formed in part as a result of a different series of reactions beginning with the addition of phenyl radical to propyne/propargyl. Following the formation of indene, indenyl is crucial in aromatic growth. In fact, the interactions of indenyl with propargyl and C_5H_5 dictate the formation of acenaphthylene ($C_{12}H_8$), **Figure 4.8(g)**, and phenanthrene ($PC_{14}H_{10}$), **Figure 4.8(h)**, respectively. The HACA pathway through naphthyl ($C_{10}H_7$)+C_2H_2 and bibenzyl dehydrogenation [111] also contribute around 15% and 18 % in $C_{12}H_8$ and $PC_{14}H_{10}$ formation, respectively. 15% of $C_{12}H_8$ is formed during the post-shock quenching, mainly through the C_9H_7+C_3H_3 recombination [270]. Anthracene ($AC_{14}H_{10}$), **Figure 4.8(i)**, is totally formed from phenanthrene isomerization. The cyclopenta-ring species are further demonstrated to be significant precursors to the development and expansion of aromatic rings based on the discussion above.

The experimental profiles of the mono- and poly-aromatics are not accurately described by the models from the literature. On the other hand, it is possible to observe how the model by Vervust et al. [140] correctly depicts the synthesis of naphthalene. This finding further validates the accuracy of the reactions and associated kinetic parameters involving two cyclic C5 compounds and resulting in the appearance of the second-ring structure (**Figure 4.7**).

4.1.2.3 Impacts of added acetylene on C_5H_8 pyrolysis

The purpose of the second part of the cyclopentene pyrolysis investigation is to demonstrate how the speciation patterns are affected by the addition of C_2H_2, paying special attention to the pathways that lead to the creation of PAHs. To this end, the species pools and reaction schemes of CYC_5H_8+C_2H_2 pyrolysis will be compared with those of neat CYC_5H_8 pyrolysis.

First, the influence of the abundant C_2H_2 on CYC_5H_8 decomposition reactivity is examined. **Figure 4.10** shows the fuel concentrations in neat cyclopentene and cyclopentene + C_2H_2 pyrolysis as function of the post-shock temperature T_5. The measured fuel conversion profiles in the studied cases are successfully predicted by the kinetic model. The findings of the modeling and experimental studies show that the addition of C_2H_2 has no effect on the reactivity of CYC_5H_8. C_2H_2 remains unreactive at temperatures below 1250 K. The reference simulated profile of neat C_2H_2 is also displayed in **Figure 4.10(b)** to further highlight the interactions between the binary fuel components. C_2H_2 begins forming at temperatures above 1300 K due to its production from the yielded small intermediates in CYC_5H_8 decomposition.

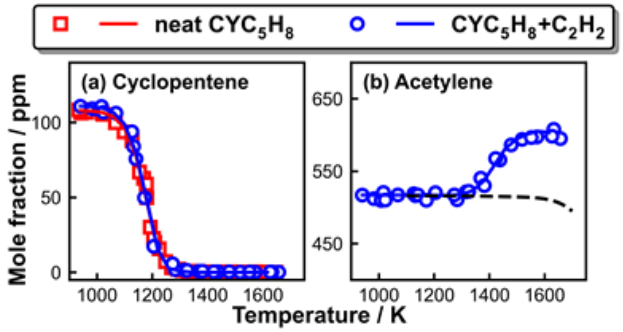

Figure 4.10 *Experimental (symbols) and simulated (solid lines) mole fractions of* ***(a)*** *CYC_5H_8 in the two investigated cases,* ***(b)*** *C_2H_2 in the pyrolysis of 111 ppm CYC_5H_8 + 526 ppm C_2H_2 mixture. The dashed line in (b) represents the simulated mole fractions of C_2H_2 when CYC_5H_8 is absent from the corresponding mixture.*

As shown in **Figure 4.11**, the production pathways of the small hydrocarbons are identical to those in neat CYC5H8 both qualitatively and quantitatively. However, the addition of acetylene slightly increases the formation of propyne and allene at high temperatures through the reaction CH_3+C_2H_2=C_3H_4-p/C_3H_4-A +H (**Figure 4.11(f)** and **(g)**). This reaction pathway inhibits the CH_3 self-recombination reaction, which lowers

the peak mole fraction of C_2H_6 (**Figure 4.11(d)**). Additionally, the presence of C_2H_2 in the initial mixture contributes to the build-up of C_4H_2 mole fraction (**Figure 4.11(j)**) at elevated temperatures due to the increased number of carbon atoms.

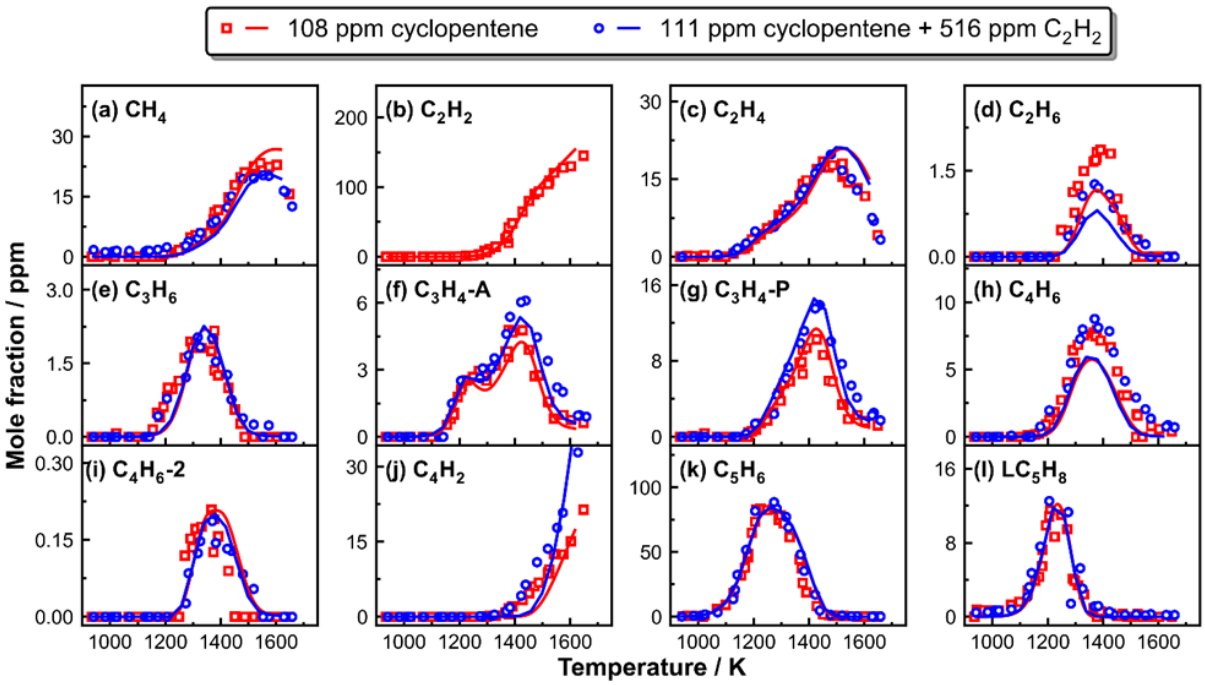

Figure 4.11 Measured (symbols) and simulated (lines) mole fraction profiles of small hydrocarbons in the pyrolysis of 108 ppm cyclopentene and 111 ppm cyclopentene+ 517 ppm acetylene

Figure 4.12 displays quantitative measurements of the aromatic compounds and their corresponding simulations. The two experimental data sets show no evident discrepancies in the onset temperature and the peak mole fractions of C_6H_6 (**Figure 4.12(a)**) and $C_6H_5C_2H_3$ (**Figure 4.12(d)**). Hence, the extra C_2H_2 has no influence on C_6H_6 and $C_6H_5C_2H_3$ formation as they are primarily formed through C_5H_5+CH_3 and C_5H_5+C_3H_3, respectively. The addition of C_2H_2 to CYC_5H_8 increases the concentrations of $C_6H_5C_2H$ (**Figure 4.12(c)**) and 1-ethynylnaphthalene ($C_{10}H_7C_2H$, (**Figure 4.12(h)**). In fact, the formation of $C_6H_5C_2H$ and $C_{10}H_7C_2H$ largely depends on the C_6H_5/$C_{10}H_7$+C_2H_2 reactions, and the presence of C_2H_2 in the initial mixture facilitates their production. C_7H_8 starts forming at relatively lower temperature in CYC_5H_8/C_2H_2 co-pyrolysis (**Figure 4.12(b)**). Indeed, the carbon flux into C_7H_8 through C_5H_6+C_2H_2 recombination is increased from 5% in neat cyclopentene to 40% at T_5=1400K.

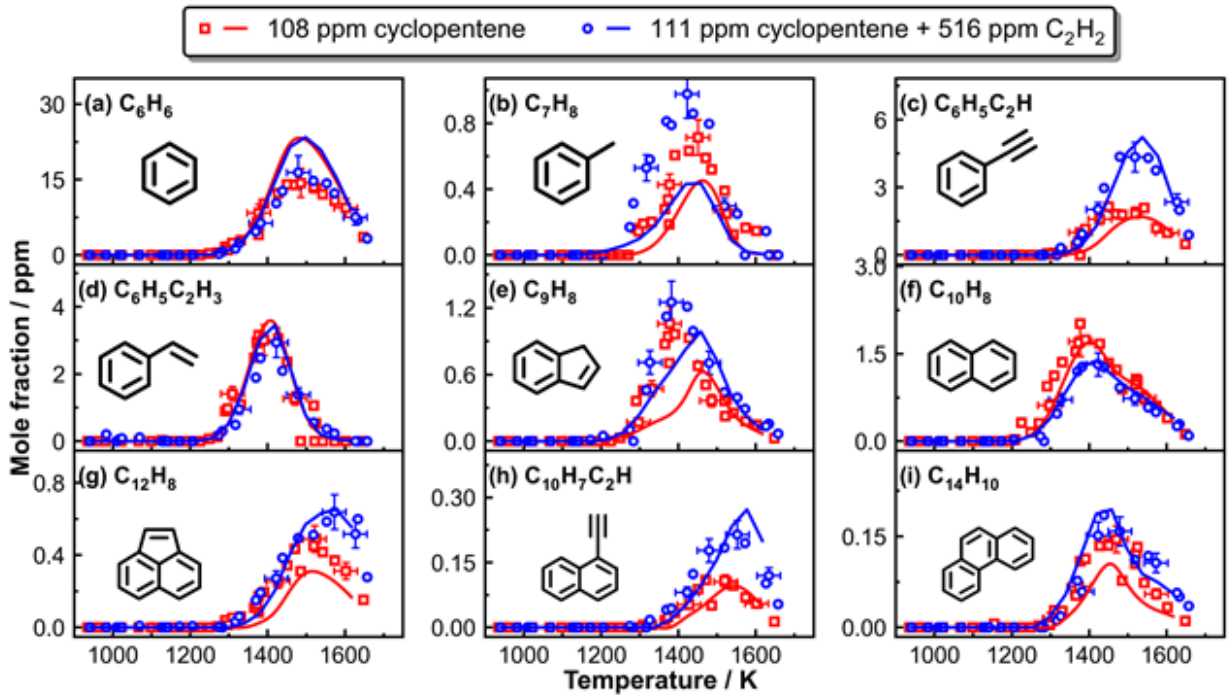

Figure 4.12 *Measured (symbols) and simulated (lines) mole fraction profiles of aromatics in the pyrolysis of 108 ppm cyclopentene and 111 ppm cyclopentene+ 517 ppm acetylene*

Regarding other significant PAHs, the addition of C_2H_2 in the initial mixture increases the peak mole fraction of indene, **Figure 4.12(e)**, and this effect is more prominent in the simulation results compared to the experimental ones. In neat CYC_5H_8, C_9H_8 formation is governed by C_5H_5+C_5H_6 reaction. However, in CYC_5H_8+C_2H_2 co-pyrolysis, a newly introduced channel is essential in C_9H_8 formation through the reaction sequence starting from C_5H_5+C_2H_2 proposed by da Silva et al. [151] and Fascella et al.[152]. The enhanced indene formation in the binary mixture clearly rises the peak concentrations of acenaphthylene, **Figure 4.12(g)**, and phenanthrene, **Figure 4.12(i)**, as they mainly originate from reactions involving indenyl. Compared to case of neat cyclopentene pyrolysis, the presence of C_2H_2 slightly limits the formation of naphthalene, **Figure 4.12(f)**, owing to the fact that the predominant reaction sequence through C_5H_5 self-recombination is hindered by the lowered C_5H_5 level as a small part of C_5H_5 reacts with C_2H_2.

In conclusion, to better understand the formation of PAHs from neat cyclopentene and cyclopentene/C_2H_2 mixtures, a combined experimental and kinetic modeling investigation was presented. In all the investigated cases, it is noted that the cyclopentadienyl radical largely participate in the formation of MAHs (benzene and styrene) and PAHs (indene, naphthalene and phenanthrene).

4.2 Heated shock tube results

One of the main objectives of this work is to develop and to assess the extinction technique to study soot formation behind reflected shock waves. In order to be able to fulfill this task, it was decided to use the heated shock tube with modifications described in section 3.3.3.4. For each run the following measurements are obtained:

- four pressure signals from the corresponding pressure transducers (CHIMIE METAL, C1 to C3) and the PCB;
- extinction signal across the tube with the red laser beam at 632.8 nm (Helium:Neon).

For signals acquisition, two different fast digital oscilloscopes were used (Rohde & Schwarz, RTB2004), both triggered by the signal from the PCB positioned at the end wall. **Figure 4.13** shows typical pressure signals versus time. Starting from the bottom, the signals detected from the pressure transducers C1, C2, C3, and PCB are presented. These curves allow to evaluate the time of the passage of the incident shock wave at the specific location. Afterwards, by knowing the distance between two consecutive pressure transducers, for each run the shock wave velocity is calculated, and then P_5 and T_5 can be derived by solving the conservation equations.

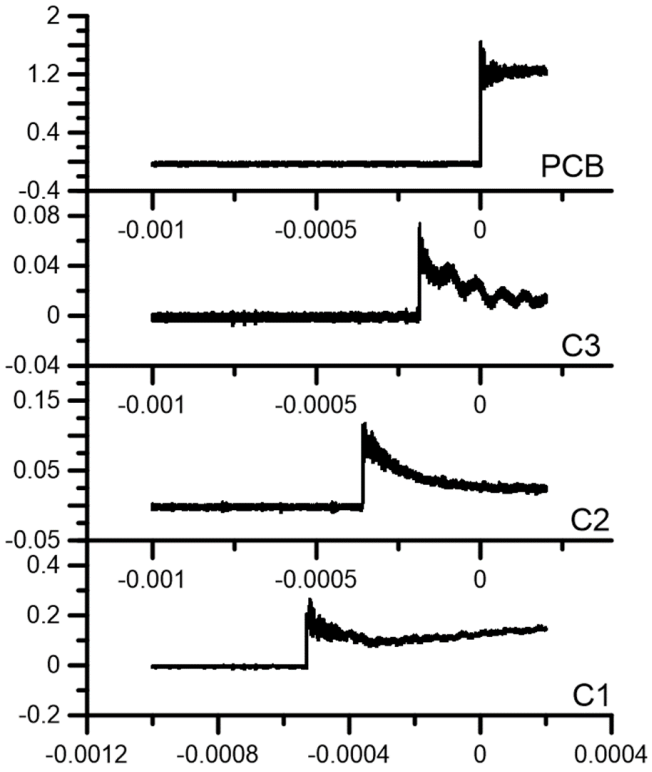

Figure 4.13 *Pressure signals versus time – 0.1% C_7H_8 in Ar, at T_5 = 1732 K and P_5 = 18.0 bar*

The transmitted intensity of the 632.8 nm laser beam is reported in **Figure 4.14** together with the pressure profile. In the figure, the parameters are the following:

- I_0= the signal intensity corresponding to 0% absorption (which is the incident laser beam intensity value);
- I_{100} = the signal intensity corresponding to 100% absorption (obtained blocking the laser beam at the shock tube entrance);
- I_L= the signal intensity of the transmitted laser beam, depending on time.

The monochromatic transmittance, TR_λ is calculated as

$$TR_\lambda = \frac{I_L - I_{100}}{I_0 - I_{100}} \tag{4.1}$$

Subsequently, applying equations (2.6) and (2.7) the soot volume fraction and the optical densities can be calculated. It is clear from this example how the rarefaction waves arrive at the end-wall ~4.5 ms after the arrival of the shock wave. A second shock due to the interaction between the reflected shock wave and the contact surface is also present (the shock conditions have not been tailored but experimentally determined in order to obtain reaction times of around 4 ms). The signals after 4.5 ms cannot then be used for data treatment and analysis.

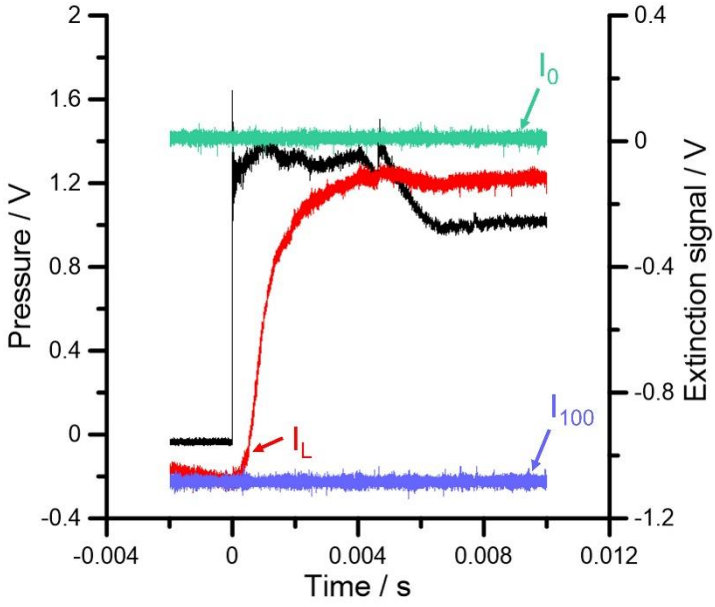

Figure 4.14 *Time-resolved extinction measurements, raw data - 0.1% C_7H_8 in Ar, at T_5 = 1732 K and P_5 = 18.0 bar*

From the time-dependent behavior of the soot volume fraction and optical densities, information about global soot kinetic parameters, such as the soot yield, the induction delay time, and soot growth rate are obtained. In the following subsections, results of toluene, benzene, cyclopentene and their respective

mixtures with C2 and C3 components will be presented. Soot optical densities at 2 ms and at 4 ms, induction delay times, and soot growth will be discussed. This choice is due to the fact that these properties do not depend on the optical properties of the soot particles, for which large uncertainties still exist especially considering that they vary as a function of the fuel, the temperature, the pressure, and the time (nascent particles vs larger primary particles vs aggregates). The soot volume fractions obtained with an *E(m)* equal to 0.19 (average value among the ones proposed in various literature studies) will be presented in the Appendix.

4.2.1 Optical densities

The optical density consists on a logarithmic intensity ratio of the beam light to the light transmitted through an analyzed material [271]. This parameter can be derived from extinction measurements, as seen in section 2.4.1, equation (2.7). The carbon concentration, [C], is given by:

$$[C] = \frac{x_{hc} P_5}{k_B T_5} n_c 10^{-6} \tag{4.2}$$

Where x_{hc} is the molar fraction of the hydrocarbon, k_B is the Boltzmann's constant (k_B = 1.38·10^{-23} J·K^{-1}) and n_c is the initial number of carbon atoms. The initial concentration of carbon was chosen in order to avoid saturation of the absorption signal for the aromatic fuels, which have more tendency to form particles (**Table 3**).

The initial cases considered concern the reference cyclic fuels. The analyses will be done by taking into consideration the time-history profiles as well as the values of D_{633} at specific times, in particular 2 and 4 ms. First, the results obtained with 0.07% of toluene diluted in argon are presented in **Figure 4.15** for different T_5 temperatures. The optical densities are expressed in m^2/mol, (**Figure A. 10** for f_v in cm^3/cm^3) and calculated according to equation (2.7). The pink line represents the lowest temperature (1518 K) for which the soot produced is the lowest (D_{633} ~ 15 m^2/mol at 4 ms), while the black line is the profile obtained at the highest T_5 (1940 K). The maximum absolute value of D_{633nm} is reached at 1716 K (~ 70 m^2/mol at 4 ms), the intermediate temperature. Indeed, the soot yield has a characteristic bell-shaped temperature dependency behavior.

The second neat reference aromatic fuel is benzene. **Figure 4.16** presents the optical densities for different temperatures with an initial fuel mole fraction of 0.082% in argon (**Figure A. 11** for f_v). Once again, the pink and black line represent the lowest and highest temperatures (1518 K and 1940 K, respectively). The maximum absolute value of D_{633nm} is reached at temperatures around 1680-1740 K, the intermediate range

of our study, similar to toluene. The value of this maximum is also comparable with the toluene case (around 70 m^2/mol for benzene).

Finally, the third neat cyclic fuel analyzed is cyclopentene, 0.098% in argon bath gas. **Figure 4.17** displays the optical density profiles of different experiments at various temperatures versus time (**Figure A. 12** for the soot volume fraction). The maximum absolute value of D_{633nm} is reached for 1704 K, the intermediate temperature, similar to toluene and benzene. However, this value is considerably lower than the previous fuels (around 35 m^2/mol). Similarly, the soot yields from cyclopentene pyrolysis are lower than the aromatic cases for all the temperature conditions. The reason of such difference will be analyzed in the following section with kinetic analyses on the soot precursor molecules.

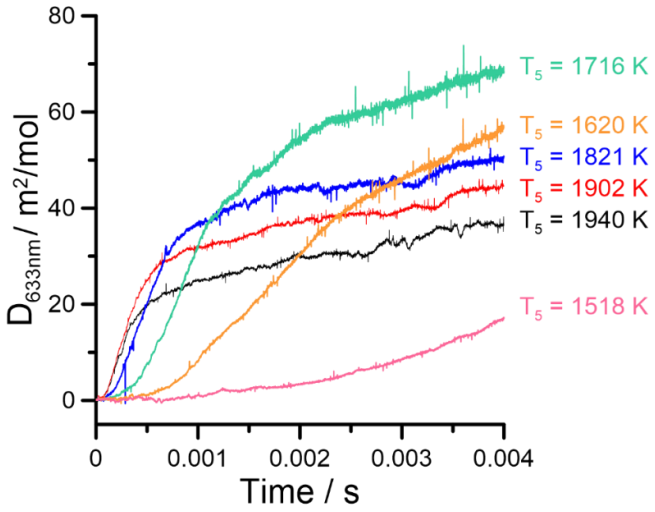

Figure 4.15 *Optical densities versus time of 0.07% C_7H_8 in Argon for different temperatures*

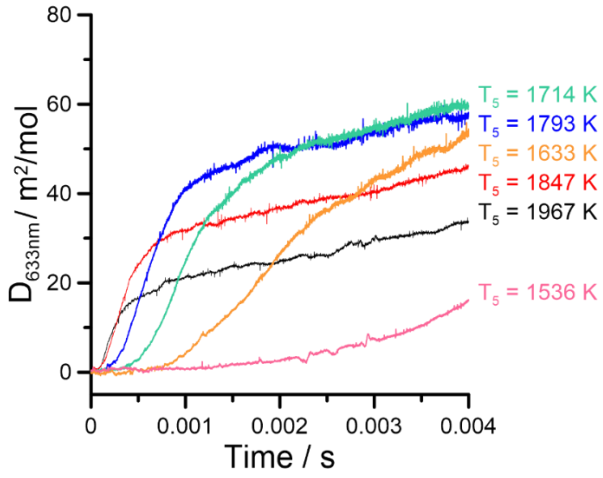

Figure 4.16 *Optical densities versus time of 0.08% C_6H_6 in Argon at different temperatures*

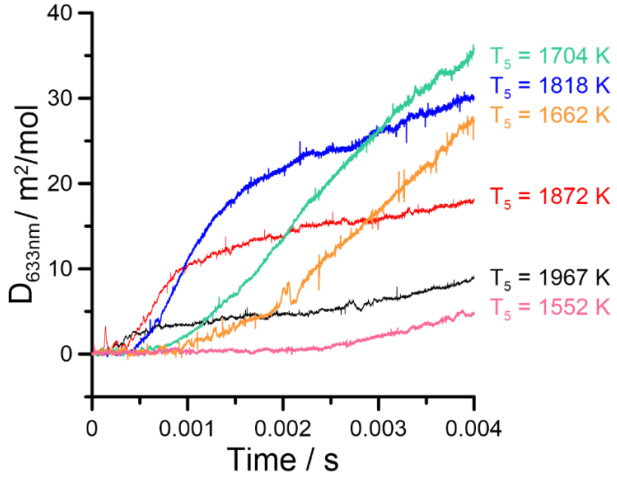

Figure 4.17 *Optical densities versus time of 0.098% C_5H_8 in Argon at different temperatures*

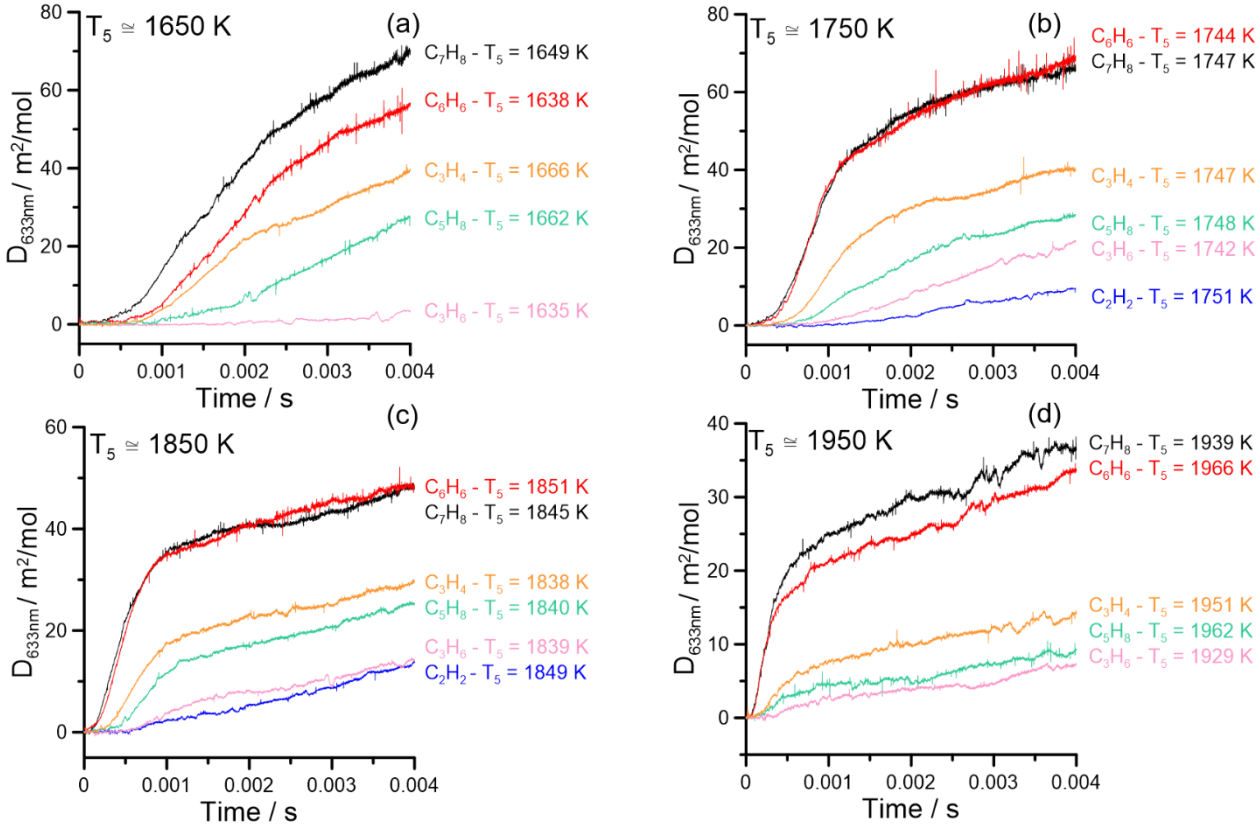

Figure 4.18 *Optical densities versus time of different fuels at similar temperatures - in black: 0.07% C_7H_8 in Ar, in red: 0.08% C_6H_6 in Ar, in orange: 0.16% C_3H_4 in Ar, in green: 0.098% C_5H_8 in Ar, in pink: 0.16% C_3H_6 in Ar and in blue: 0.245% C_2H_2 in Ar.* ***(a)*** *$T_5 \approx 1650K$,* ***(b)*** *$T_5 \approx 1750K$,* ***(c)*** *$T_5 \approx 1850K$ and* ***(d)*** *$T_5 \approx 1950K$*

Figure 4.18 contains the comparison of the D_{633} time-histories for the different fuels and at specific temperature conditions (around 1650, 1750, 1850, and 1950 K). This figure contains also the results for the acyclic fuels which will be discussed later, although for the moment the focus will be on the experiments with toluene (in black), benzene (in red), and cyclopentene (in green). In general, there is no discernable difference between toluene and benzene above 1750 K (the 30 K difference in the experimental T_5's of **Figure 4.18(d)** may explain the reduced D_{633} for benzene). On the other hand, the soot formation from toluene pyrolysis at around 1650 K is clearly promoted compared to the benzene case (D_{633} around 70 and 55 m^2/mol, respectively). The soot formation from the cyclopentene pyrolysis is limited compared to the aromatic cases for all temperatures.

In order to have a better characterization of the results presented above, the D_{633} results at 2 and 4 ms for the different fuels are shown in **Figure 4.20** together with polynomial fits of the data points. This figure contains once again the results for the acyclic fuels discussed in the following sections. The "bell-shaped" pattern of optical density is similar to the soot yield behavior, which have been observed by many authors [117], [272]–[274]. This pattern was first suggested by Graham et al. in 1975 [117] and it is due to the competition between two reaction pathways:

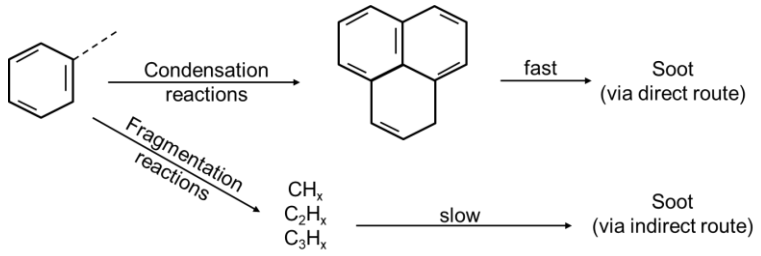

Figure 4.19 *Reaction scheme of soot formation (from [117])*

Thus, the decrease in the optical density when the temperature increases is due to the fact that fragmentation reactions become predominant, while at lower temperatures, condensation reactions between aromatics and between aromatics and small fragments are prevalent. According to Frenklach et al [272], this shape is characteristic of an auto-catalytic process.

With more details on the results presented in **Figure 4.20** and considering the experimental uncertainties, the maxima of the benzene and toluene curves are similar (~ 1700-1750 K), as well as the values at higher temperatures. On the other hand, the initial growth of the curve is shifted to lower temperatures for the toluene pyrolysis (or, from another perspective, the optical densities for toluene pyrolysis are higher than the ones for benzene at temperatures below 1700 K). This may be due to two factors:

- the thermal fragmentation of toluene occurs at lower temperatures compared to benzene;

- the increased stability of the benzyl radical compared to the phenyl radical.

The D_{633} maxima in the case of cyclopentene pyrolysis are around 36% and 50% of those of benzene and toluene at 2 ms and 4 ms, respectively. The soot formation temperature window is also reduced as discernable amounts of soot extinction signal at 2 ms could be obtained only above 1625 K (around 100 K more than in the pyrolysis of the aromatic fuels).

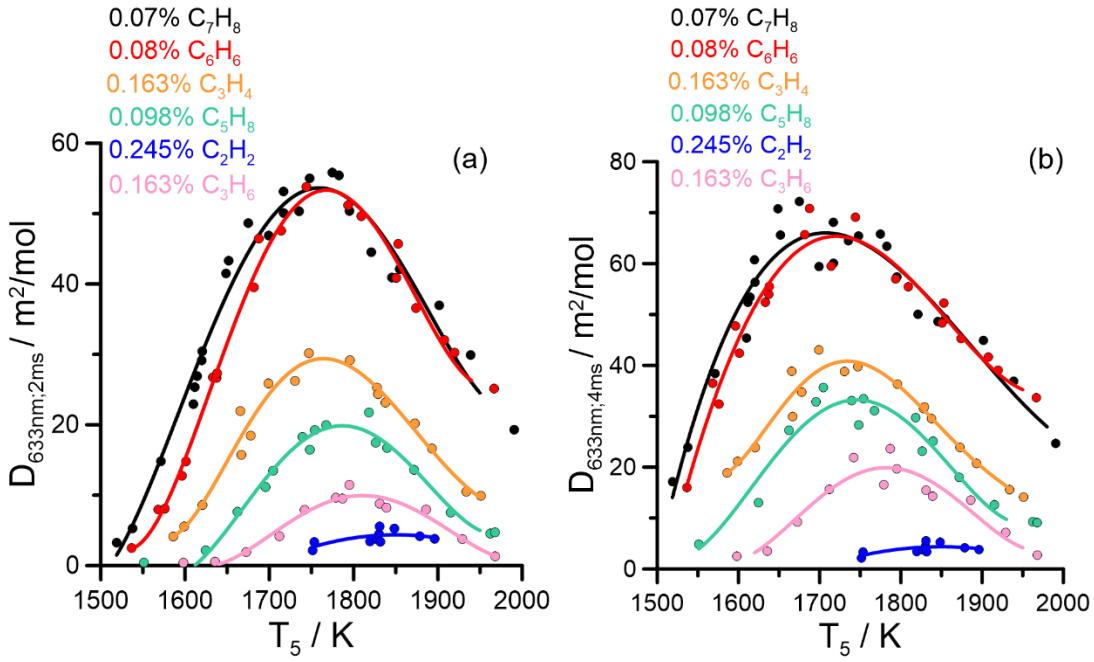

Figure 4.20 *Dependence of the optical densities from the temperature of different fuels – in black: 0.07% C_7H_8 in Ar, in red: 0.08% C_6H_6 in Ar, in orange: 0.16% C_3H_4 in Ar, in green: 0.098% C_5H_8 in Ar, in pink: 0.16% C_3H_6 in Ar and in blue: 0.245% C_2H_2 in Ar;* ***(a)*** *at 2ms;* ***(b)*** *at 4ms*

One of the main goals of the present experimental investigation is understanding how the addition of small fuel fragments (C2s - acetylene and ethylene, and C3s - propylene and propyne) to aromatic fuels might alter the soot formation propensity. First, the soot formation from the pyrolysis of the single components needs to be evaluated. **Figure 4.18** contains the D_{633} time-history profiles for the C3 fuels (0.163% in argon) and acetylene (0.245% in argon), when available. Indeed, soot formation from acetylene pyrolysis is limited, and reasonable results could be obtained over a small temperature range. In addition, ethylene pyrolysis could not be studied at the concentration of carbon atoms comparable with the other fuels. The curves obtained from the thermal decomposition of propyne (orange curves) lie between the curves of the aromatic fuels and those from the cyclopentene pyrolysis. The thermal decomposition of propyne leads directly to the formation of propargyl radical (C_3H_3), precursor of benzene through the C3+C3 reactions. The subsequent PAH growth and particle formation are favored compared to the case of cyclopentene pyrolysis. On the other hand, the formation of the propargyl radical from propylene requires a much less effective step-wise dehydrogenization. As a consequence, the optical densities from the propylene pyrolysis

(pink curves) are much lower than the previous cases; in addition, soot formation starts at higher temperatures. The lowest D_{633} values were obtained with acetylene as a fuel, as the pathway to the particles rely only on the C2+C2 reactions which are much less effective in producing the first aromatic ring and the subsequent PAHs.

These considerations reflect in the experimental curves of D_{633} vs T_5 presented in **Figure 4.20**. The maximum values in the case of propyne pyrolysis reach ~ 30 m^2/mol at 2 ms and ~ 40 m^2/mol at 4 ms (around 55% and 57% of the aromatic maxima, respectively). The shape of the curve is very similar to the ones obtained for benzene and toluene. The peaks in the case of propylene pyrolysis are instead shifted towards higher temperatures (between 1750 and 1800 K), while the maxima reach around 10 m^2/mol at 2 ms (one third of the propyne value) and ~ 22 m^2/mol at 4 ms (around half of the propyne case). The signal levels obtained from the pyrolysis of 0.245% acetylene are relatively low, and thus the quantification might be affected by larger uncertainties compared to the other cases. In the temperature range considered, no clear peak could be defined, with maximum values at 2 and 4 ms of around 5 and 12 m^2/mol, respectively.

In order to provide more accurate experimental results for kinetic model validation, additional experimental sets were obtained on the C2 fuels with increased initial fuel concentrations. The acetylene concentration was first increase from 0.245% to 0.35%, while the experiments on ethylene pyrolysis were obtained with 0.35% and 0.70% fuel in argon.

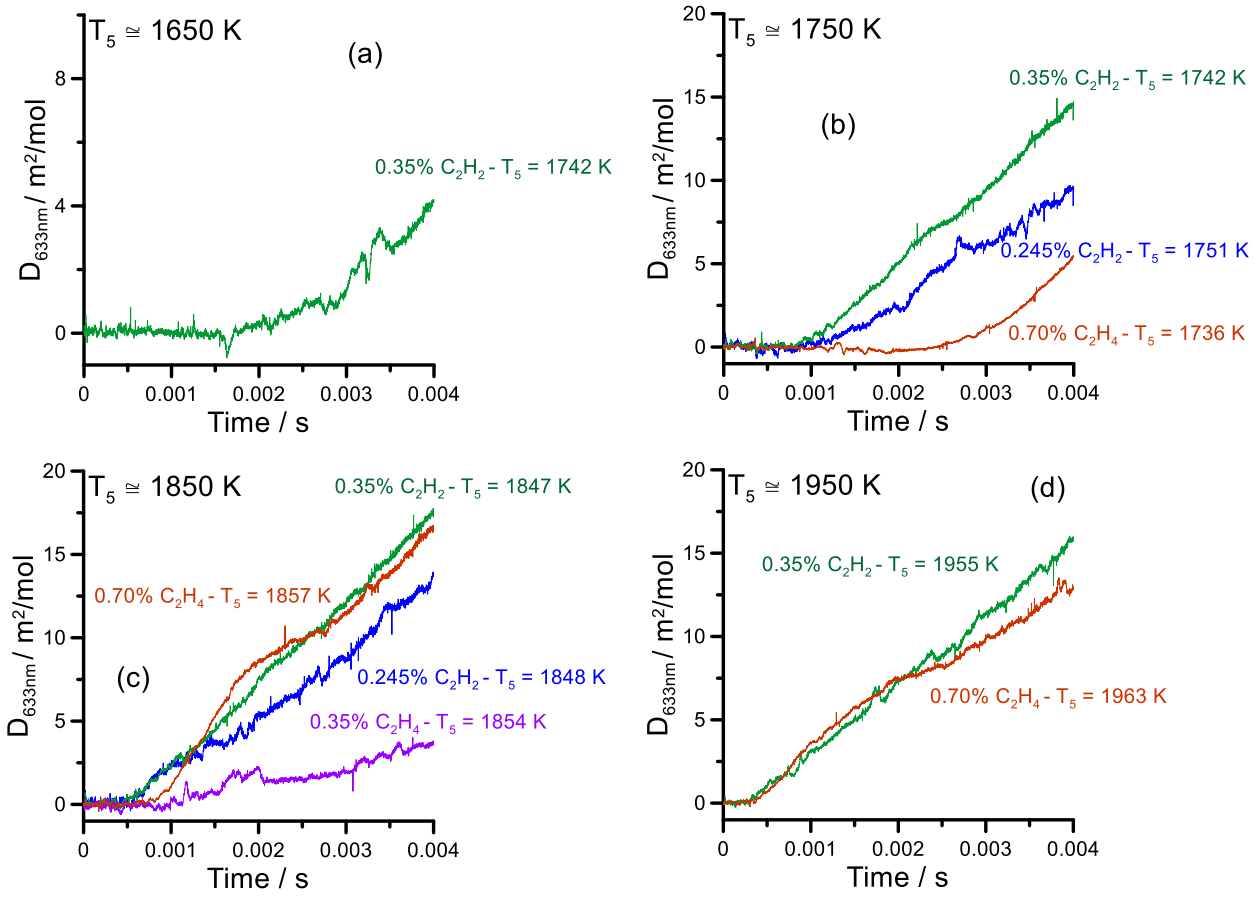

Figure 4.21 *Optical densities versus time of different fuels at similar temperatures - in blue: 0.245% C_2H_2 in Ar, in green: 0.35% C_2H_2 in Ar, in purple: 0.35% C_2H_4 in Ar, in brown: 0.70% C_2H_4 in Ar.* ***(a)*** *$T_5 \approx 1650K$,* ***(b)*** *$T_5 \approx 1750K$,* ***(c)*** *$T_5 \approx 1850K$ and* ***(d)*** *$T_5 \approx 1950K$*

Figure 4.21 contains the time-history profiles of the optical densities for the C2 fuel mixtures, when available. Soot formation in the mixtures with acetylene starts at similar times but the optical densities of the mixture with 0.35% acetylene are clearly higher than those with 0.245% acetylene (around 30-50% increment). The experiments with 0.70% ethylene have optical densities which are comparable with those obtained with half of the acetylene initial concentration, although the formation of soot starts at later times. The extinction signal obtained with 0.35% C_2H_4 is the lowest and it reaches only 5 m^2/mol at its maximum.

The profiles as function of the temperature T_5 are presented in **Figure 4.22**. The profile of the experiments with 0.7% ethylene peaks at around 1900-1950 K at 2 ms and at around 1850-1900 K at 4 ms. In this case, soot starts forming in discernable amounts at around 1700 K. On the other hand, the experiments with 0.35% acetylene show optical densities which are nearly constant above 1800 K, with soot production at lower temperatures compared to the ethylene case.

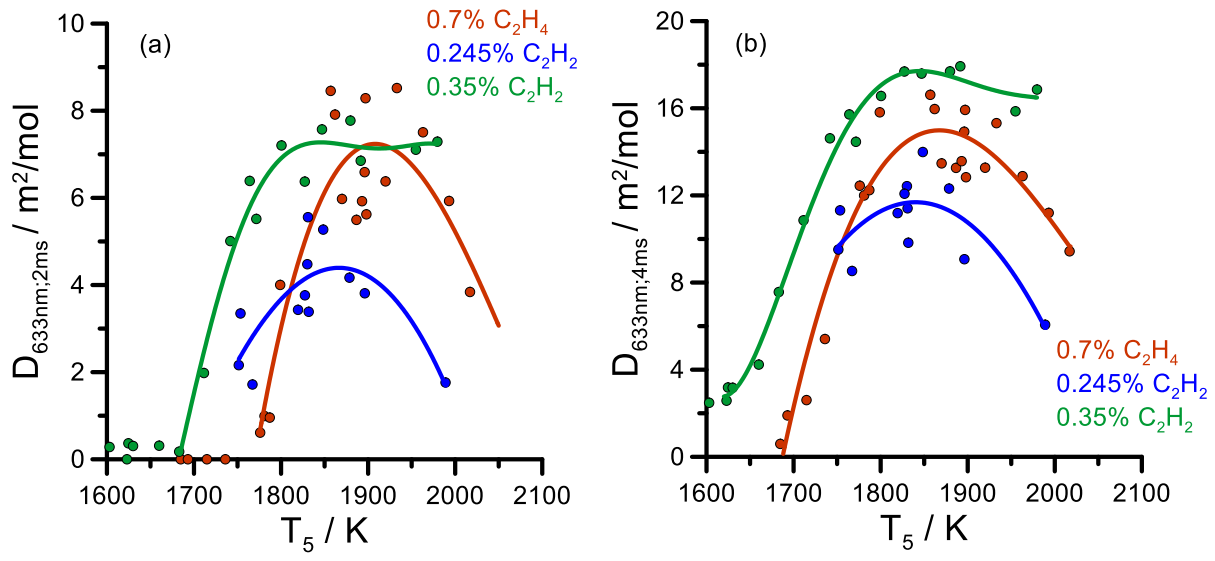

Figure 4.22 *Dependence of the optical densities from the temperature of different fuels – in blue: 0.245% C_2H_2 in Ar, in green: 0.35% C_2H_2 in Ar, in brown: 0.70% C_2H_4 in Ar* ***(a)*** *at 2ms;* ***(b)*** *at 4ms*

The experiments on the small C2-C3 fuels showed how the order in the soot tendency is as expected C_3H_4 > C_3H_6 > C_2H_2 > C_2H_4. Such order is also followed when the C2-C3 fuels are added to toluene (**Figure 4.23**), with the exception for the addition of C_3H_6 and C_2H_2 which seems to have similar effects at temperature above 1750 K (within the experimental uncertainties), while at even lower T_5s the addition of C_2H_2 leads to larger optical densities than propylene. This behavior will need to be analyzed by kinetic modeling, although two contributions can be hypothesized:

- the different synergy between toluene and C_2H_2 or C_3H_6 (benzyl radical + acetylene is a major direct pathway to indene, one of the main building blocks for particle formation);
- the percentage of toluene in the C_7H_8+C_2H_2 is higher compared to the C_7H_8+C_3H_6 mixture (0.03% and 0.02%, respectively).

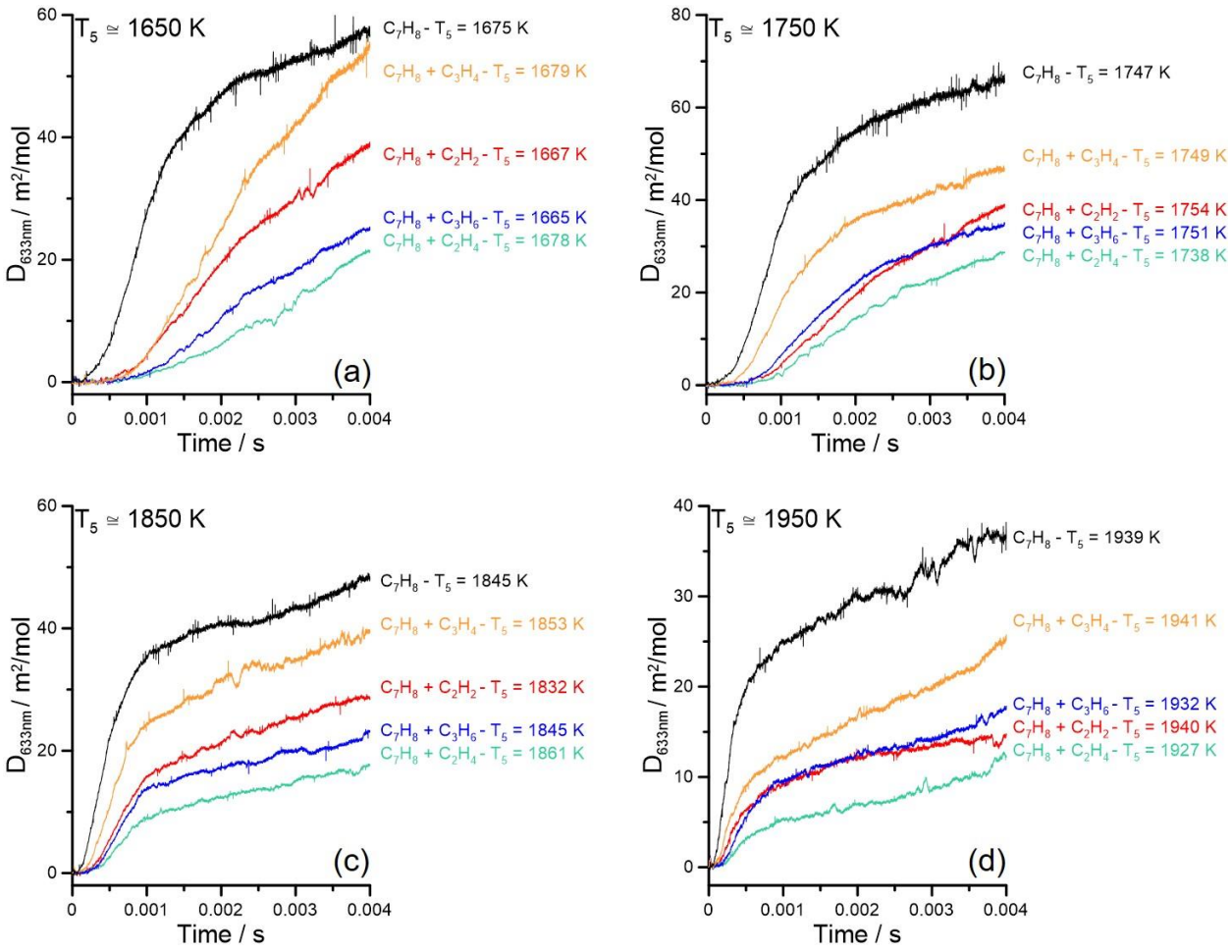

Figure 4.23 *Optical densities versus time of different fuels at similar temperatures - in black: 0.07% C_7H_8 in Ar; in red: 0.03% C_7H_8 + 0.15% C_2H_2 in Ar, in green: 0.03% C_7H_8 + 0.15% C_2H_4 in Ar; in orange: 0.02% C_7H_8 + 0.11% C_3H_4 in Ar; in blue: 0.02% C_7H_8 + 0.11% C_3H_6 in Ar.* ***(a)*** *$T_5 \approx 1650K$,* ***(b)*** *$T_5 \approx 1750K$,* ***(c)*** *$T_5 \approx 1850K$ and* ***(d)*** *$T_5 \approx 1950K$*

The optical densities of the toluene + C2 mixtures as function of the temperature T_5 are reported in **Figure 4.24** for reaction times of 2 and 4 ms. The reduction in the peak D_{633} values is around 50%-54% and 64%-73% for addition of acetylene and ethylene, respectively, while the peak temperatures do not vary significantly. **Figure 4.25** contains similar results for the addition of the C3 fuels. As for the C_2H_2 addition, the reduction of the maximum values of the optical densities is around 64%-73%, while higher D_{633} were obtained with propyne as a fuel component. In the latter case, the maximum optical densities decrease by a factor between 21% and 33%. As for the case of the C2 fuels, the addition of propylene and propyne does not significantly vary the shape of the curves.

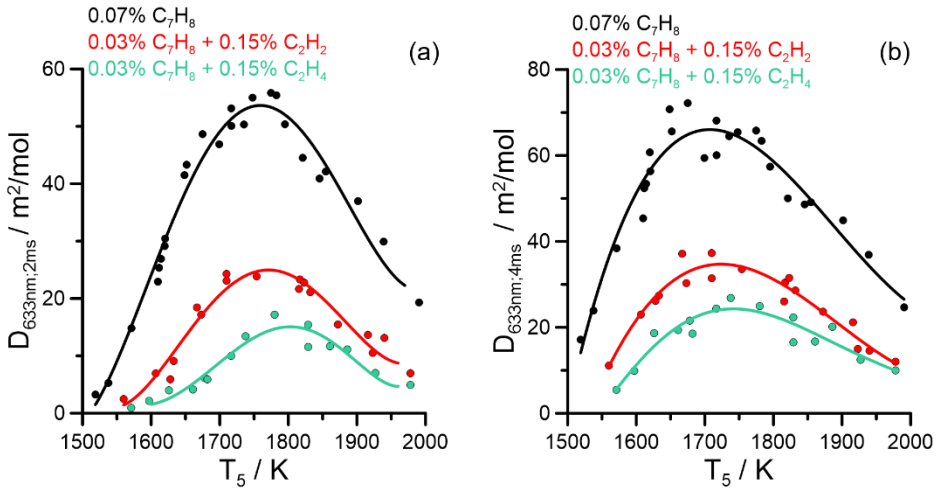

Figure 4.24 *Dependence of the optical densities from the temperature – in black: 0.07% C_7H_8 in Argon, in red: 0.03% C_7H_8 + 0.15% C_2H_2 in Argon, in green: 0.03% C_7H_8 + 0.15% C_2H_4 in Argon;* ***(a)*** *at 2ms;* ***(b)*** *at 4ms*

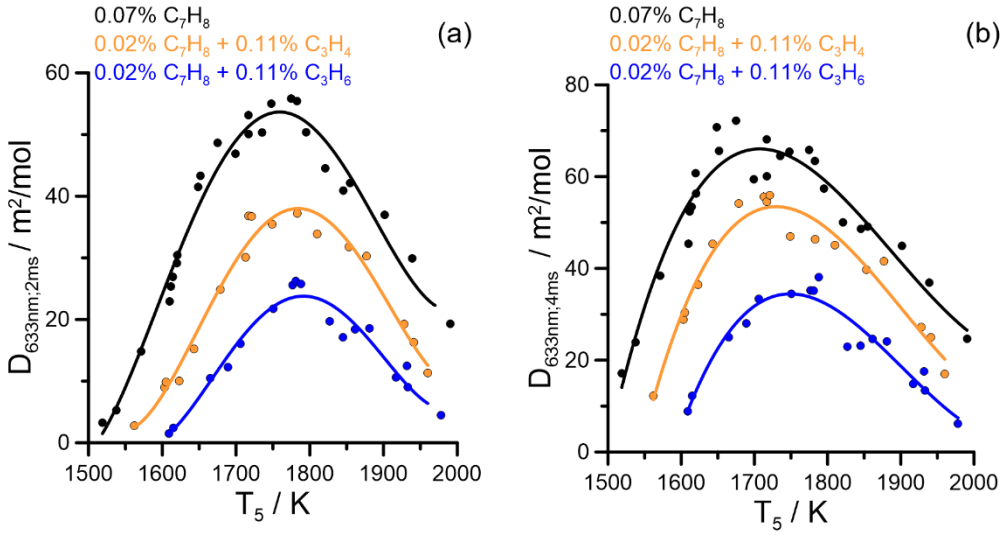

Figure 4.25 *Dependence of the optical densities from the temperature – in black: 0.07% C_7H_8, in orange: 0.02% C_7H_8 + 0.11% C_3H_4, in blue: 0.02% C_7H_8 + 0.11% C_3H_6 in Argon;* ***(a)*** *at 2ms;* ***(b)*** *at 4ms*

In order to better appreciate the difference between the results obtained with the C_7H_8+C_2H_2 and the C_7H_8+C_3H_6 mixtures, the two datasets are compared in **Figure 4.27**. It is clear how soot starts forming at lower temperatures in the C_7H_8+C_2H_2 mixture, with significant increment of the optical density values compared to the C_7H_8+C_3H_6 case for temperatures below 1750 K. Above this temperature condition, the two curves converge.

Figure 4.26 presents the optical densities versus time of benzene + C2 at similar temperatures ($T_5 \approx$ 1650K, 1750K, 1850K and 1950K). In black, neat C_6H_6, in red C_6H_6 + C_2H_2 and in green C_6H_6 + C_2H_4. In **Figure 4.29** where the values as function of the initial temperature T_5s are plotted for the different cases. Compared to the pure benzene case, the maximum optical densities are reduced by a factor of 41%-52% in the case of

acetylene addition, and 57%-67% in the case of ethylene addition. This is comparable with the values obtained in the toluene + C2 co-pyrolysis. Finally, experiments were conducted in order to understand the influence of acetylene addition on the pyrolysis of cyclopentene. The results are presented in **Figure 4.30** and **Figure 4.31**. In this case, the reduction of the optical density at the peak is around 50% with no influence on the shape of the D_{633} profile vs temperature at 2 and 4 ms. As expected, the addition of ethylene leads to a more significant reduction in the optical densities compared to the acetylene case, although the difference between the two experimental datasets tend to reduce at temperatures higher than 1820-1850 K.

In summary, extinction measurements were performed on the pyrolysis of cyclic fuels (toluene, benzene, and cyclopentene) and small C2-C3 intermediates, which were also subsequently added to the cyclic species to test the synergetic effects between the different fuels. Neat toluene and benzene pyrolysis resulted in very similar optical densities in terms of absolute values, although soot particles start forming at lower temperature in the toluene case. Soot formation from cyclopentene is much reduced compared to the aromatic fuels. A significant decrease in the absolute values of the optical densities is observed when C2 and C3 are added to the cyclic fuels. The synergetic effects are not sufficient to compensate for the decrement in the aromatic content of the fuel mixtures. In particular, the reduction in D_{633} follows the expected trends, C_2H_4>C_2H_2 (addition to toluene and benzene) and C_3H_6>C_3H_4 (addition to toluene). Future analyses will clarify the importance of the chemistry between the different fuels compared to the results of the difference in the aromatic content.

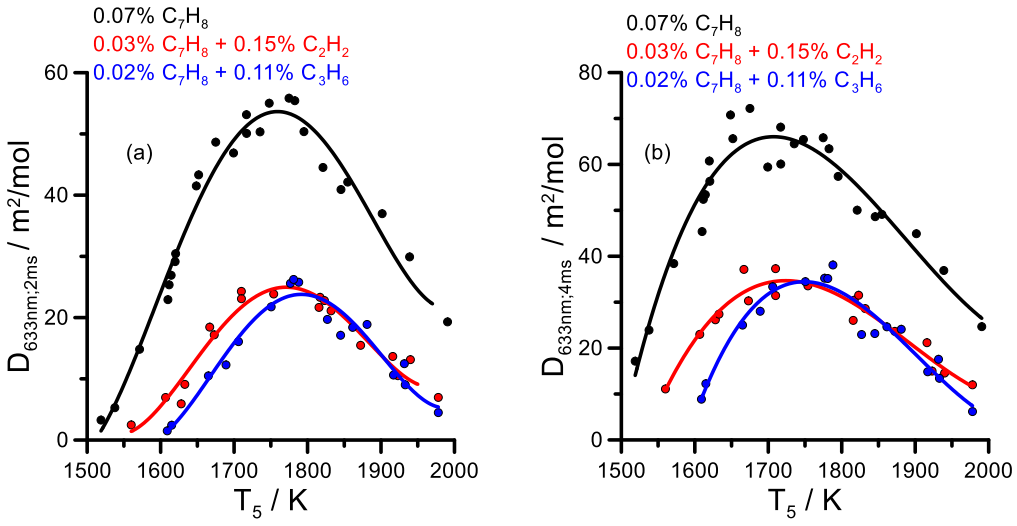

Figure 4.27 *Dependence of the optical densities from the temperature – in black: 0.07% C_7H_8, in red: 0.03% C_7H_8 + 0.15% C_2H_2 in Argon; in blue: 0.02% C_7H_8 + 0.11% C_3H_6 in Argon;* ***(a)*** *at 2ms;* ***(b)*** *at 4ms*

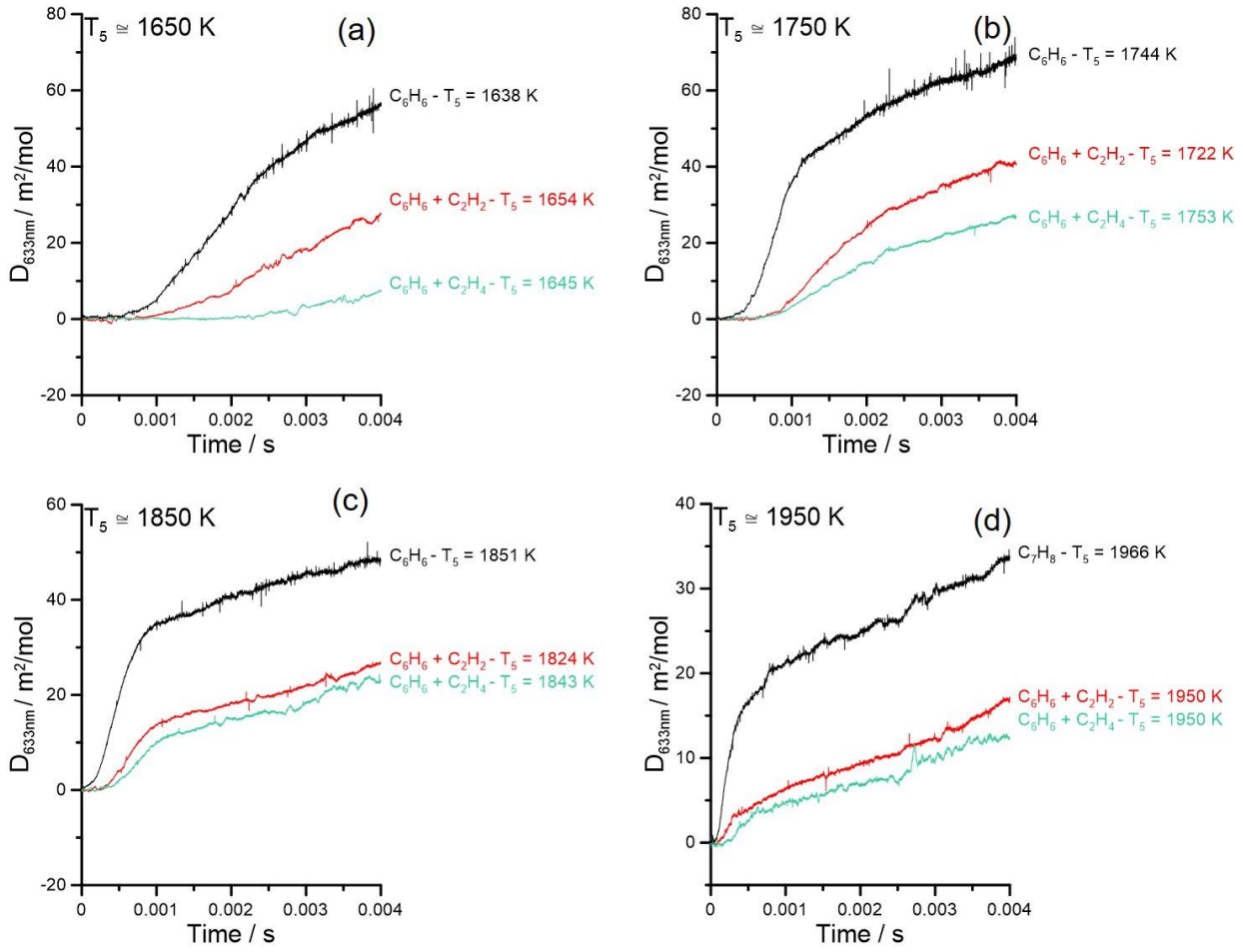

Figure 4.28 *Optical densities versus time of different fuels at similar temperatures - in black: 0.082% C_6H_6 in Ar; in red: 0.03% C_6H_6 + 0.15% C_2H_2 in Ar, in green: 0.03% C_6H_6 + 0.15% C_2H_4 in Ar.* ***(a)*** *$T_5 \approx 1650K$,* ***(b)*** *$T_5 \approx 1750K$,* ***(c)*** *$T_5 \approx 1850K$ and* ***(d)*** *$T_5 \approx 1950K$*

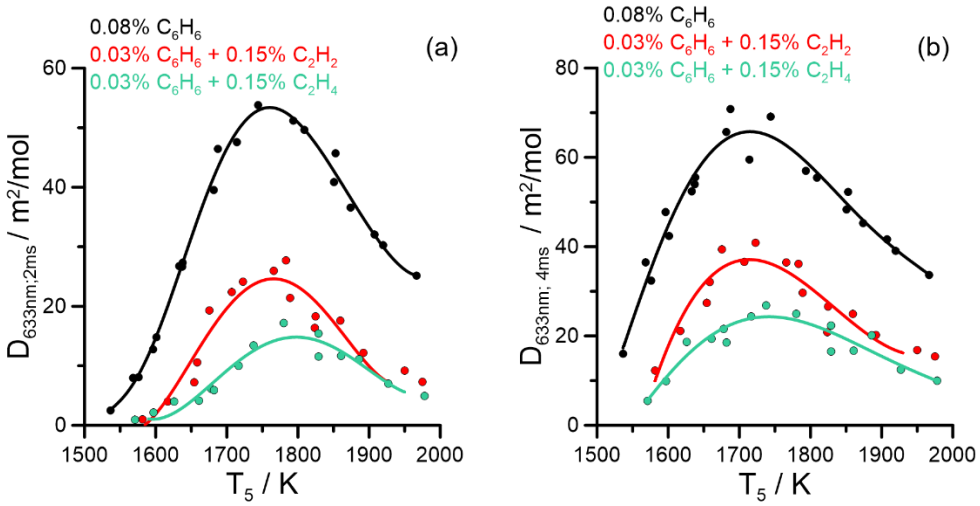

Figure 4.29 *Dependence of the optical densities from the temperature – in black: 0.08% C_6H_6 in Argon, in red: 0.03% C_6H_6 + 0.15% C_2H_2 in Argon, in green: 0.03% C_6H_6 + 0.15% C_2H_4 in Argon;* ***(a)*** *at 2ms;* ***(b)*** *at 4ms*

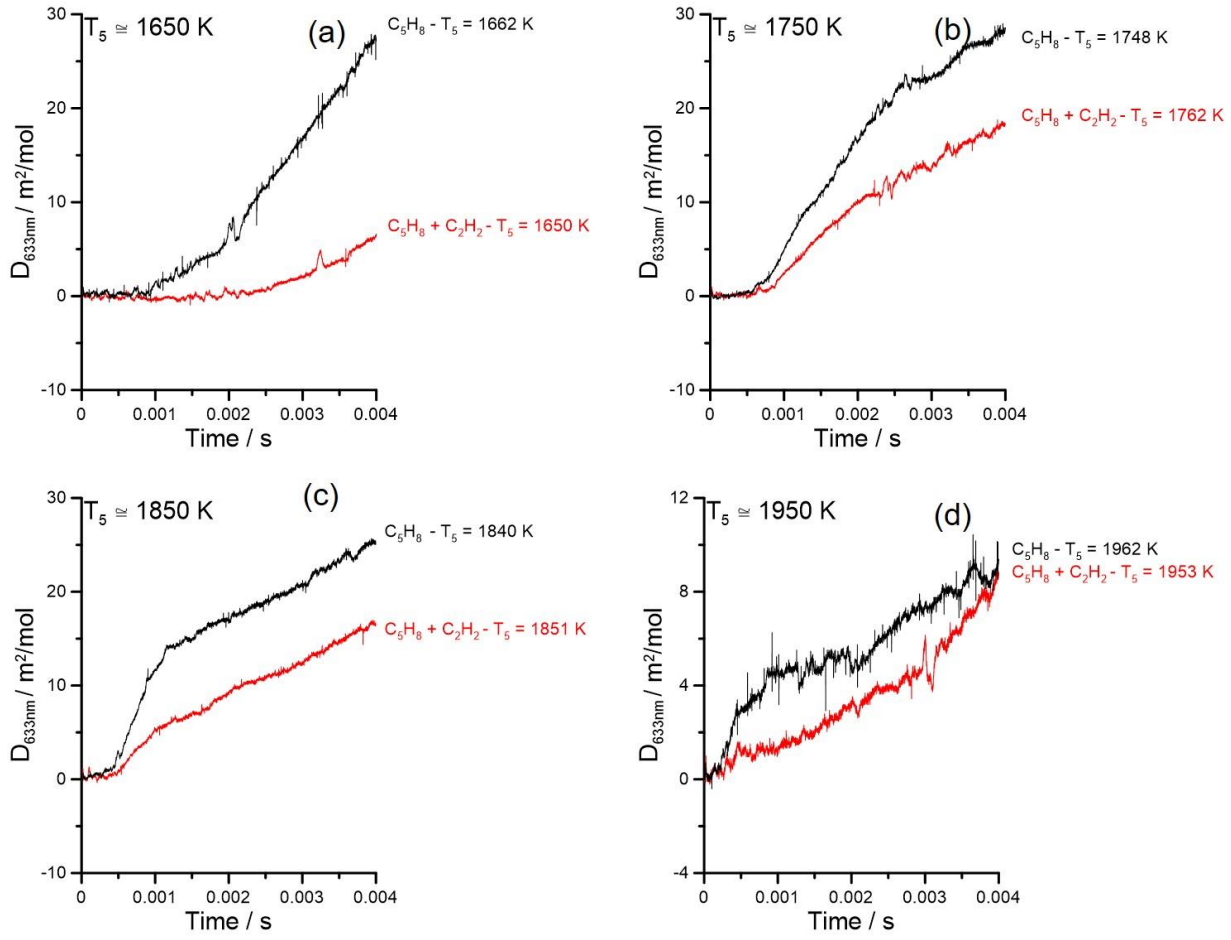

Figure 4.30 *Optical densities versus time of different fuels at similar temperatures - in black: 0.098% C_5H_8 in Ar; in red: 0.03% C_5H_8 + 0.16% C_2H_2 in Ar.* ***(a)*** *$T_5 \approx 1650K$,* ***(b)*** *$T_5 \approx 1750K$,* ***(c)*** *$T_5 \approx 1850K$ and* ***(d)*** *$T_5 \approx 1950K$*

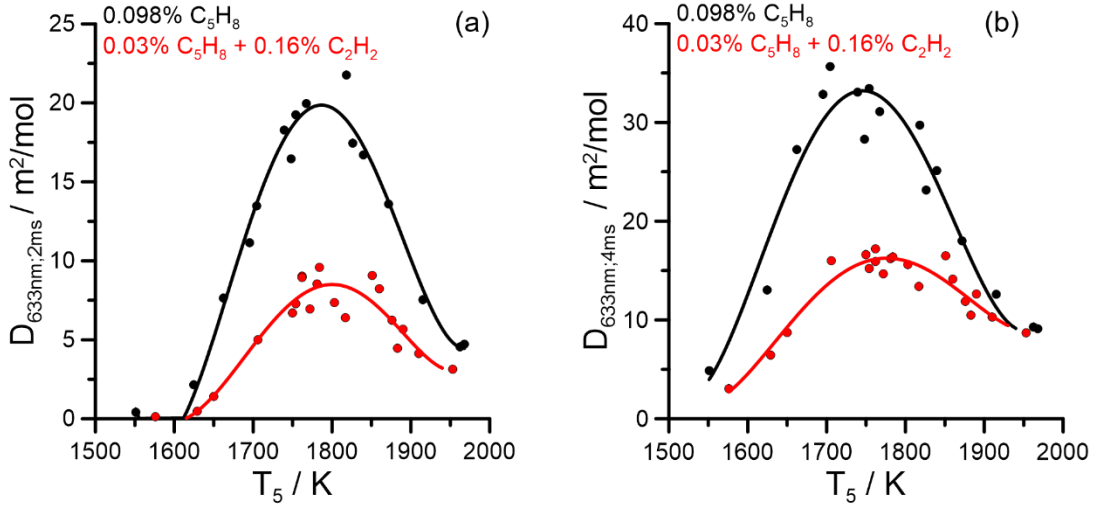

Figure 4.31 *Dependence of the optical densities from the temperature – in black: 0.098% C_5H_8 in Argon, in red: 0.05% C_5H_8 + 0.23% C_2H_2 in Argon;* ***(a)*** *at 2ms;* ***(b)*** *at 4ms*

4.2.2 Induction delay times

The induction delay time is one of the most important parameters to characterize the tendency of a hydrocarbon to form soot, as it represents the time necessary for the first soot particles to appear. The induction time encompasses the different stages of soot particle formation, which include the formation and growth of soot precursors (polycyclic aromatic hydrocarbons) in gas phase, and the nucleation and the initial growth of the particles. In **Figure 4.32** the definition of the induction delay time is shown. It is the time interval between the wave front of the reflected shock wave arriving at the endwall and the extrapolation of the maximum soot volume fraction growth to the baseline.

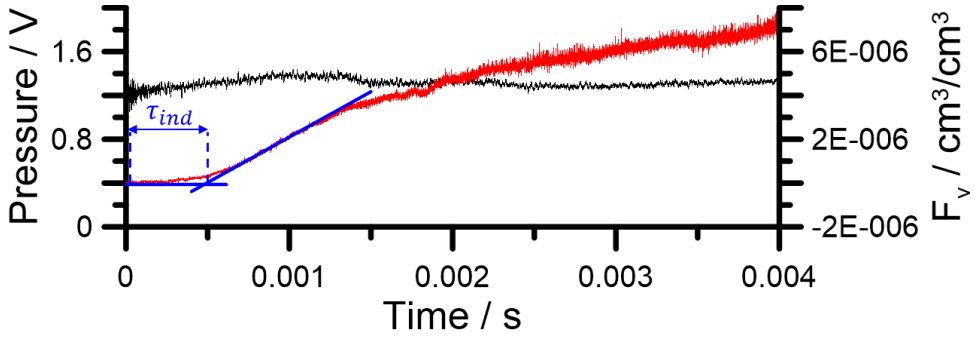

Figure 4.32 *Induction delay time obtained from f_v time-dependent profile – 0.1% C_7H_8 in Ar, at T_5 = 1732 K and P_5 = 18.0 bar*

In general, the delay can be represented by a modified Arrhenius expression which allows to account for the impact of different parameters such as temperature, pressure and initial concentration of reactants:

$$\tau_{ind} = A[Hydrocarbon]^a[Diluent]^b \exp(E_{ind}/RT) \quad (4.3)$$

In equation (4.3) A is the pre-exponential factor, [Hydrocarbon] and [Diluent] are the concentration of the fuel and the diluent (function of the total pressure) (mol·m^3), E_{ind} is the activation energy of the induction delay (J·mol^{-1}), R is perfect gas constant (= 8.314 J·K^{-1}·mol^{-1}) and T is the temperature (K). The coefficients a and b allow for normalization of the results obtained at different initial fuel concentrations and pressures, for the same fuel molecule. In the present study, the pressure is maintained nearly constant for all experiments, while no fuel concentration-dependent study is performed. Thus, a and b are zero in our case.

Figure 4.33 shows the induction delay times versus inverse of the temperature for the toluene and toluene + C2 mixtures. The black points represent the experimental data obtained for neat toluene shocks. The fitted curve, however, was split into 2: one black line for the high-temperature range (1780-1990 K) and one grey line for the low-temperature range (1519-1748 K). Their pre-exponential factors differ in magnitude by a factor 10^4. Their activation energy is equally different: E_{ind}= 259 kJ/mol for the black curve and decreases to 112 kJ/mol for the grey one. The soot formation process is probably driven by two complementary reaction mechanisms: the pathways involving reactions between the aromatic rings at relatively low temperatures, where the lifetime of the radicals (especially the resonantly stabilized ones as the benzyl

radical from the toluene decomposition) is long enough to allow their reactions with stable intermediates, and the growth by addition of small species to the aromatic stable intermediates (including the HACA pathway). These hypotheses need to be confirmed through kinetic modeling. The addition of C_2H_2 and C_2H_4 are also represented in **Figure 4.33**, red and green lines, respectively. The addition of these fuels changes the behavior of the induction delay time when compared to neat toluene, not only from quantitative point of view, but also in the fact that only one single slope is now discernable. The two activation energies are very similar for the two mixtures (around 175 KJ/mol) which suggests the particle formation to be driven by one common process throughout the entire temperature range considered. This process should include the reactions between aromatics and C_2H_2 (HACA) as ethylene fast decomposes to acetylene at high temperatures. On the other hand, the presence of acetylene as a reactant leads to a faster formation compared to ethylene, as acetylene would be readily available for reactions with the benzyl radicals to indene and the following PAH growth reactions. Other kinetic aspects which may slow down the formation of the particles in the C_7H_8+C_2H_4 system include:

- the presence of larger amounts of hydrogen in the system from the thermal fragmentation of ethylene;
- the H-abstraction reactions between the aromatic radicals (including benzyl radical) and C_2H_4;
- the reduced efficiency of the growth reactions between C_7H_7 and ethylene compared to the acetylene case.

All these considerations have been analyzed in the experimental and modeling work on PAH formation from toluene + C2 [201].

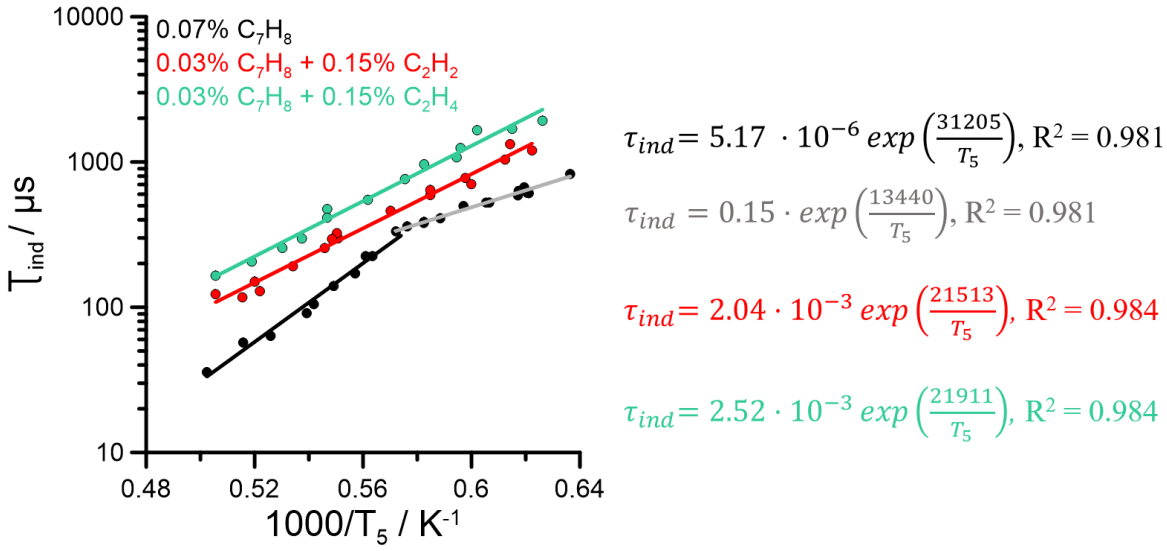

Figure 4.33 *Induction delay time versus inverse of the temperature – in black: 0.07% C_7H_8, in red: 0.03% C_7H_8 + 0.15% C_2H_2 and in green: 0.03% C_7H_8 + 0.15% C_2H_4 diluted in Argon*

Figure 4.34 displays the induction delay time versus the inverse of the temperature when C3 compounds are added to toluene. The addition of C_3H_4 and C_3H_6 are represented in orange and blue, respectively. The binary mixtures present similar behavior as neat toluene, with a double fitting for temperatures below and above 1760 K. For the toluene + propyne experiments, in the high temperature region, E_{ind} = 236 kJ/mol, while in the low temperature the induction energy decreases to 154 kJ/mol. In the case of propene addition to toluene, these two values become 216 kJ/mol and 144 kJ/mol, respectively, thus very similar activation energies were measured for the C3 fuels additions. At high temperatures, the activation energies are slightly lower compared to the pure toluene case (9% and 17% lower for C_7H_8 + C_3H_4 and C_7H_8 + C_3H_6, respectively) while in the low temperature range the energies are higher by 38% and 29%, respectively. The activation energies of the toluene + C3 mixtures are indeed much closer to the values of benzene, as the decomposition of the C3 fuels results in large amounts of benzene through the C3+C3 reactions involving the propargyl radical. Once again, the low-temperature mechanism could be driven mainly by aromatic-aromatic reactions (toluene and benzene as main building blocks), while the high-temperature one by aromatics reacting with the fragmentation products.

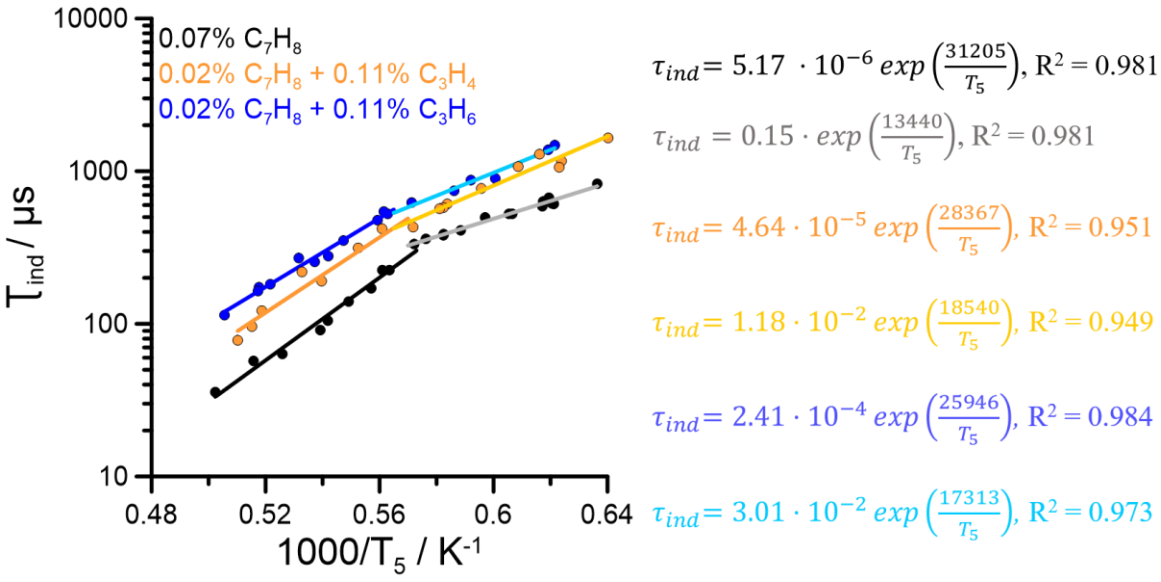

Figure 4.34 *Induction delay time versus inverse of the temperature – in black: 0.07% C_7H_8, in orange: 0.02% C_7H_8 + 0.11% C_3H_4, in blue: 0.02% C_7H_8 + 0.11% C_3H_6 in Argon*

Figure 4.35 shows the results on benzene pyrolysis, with and without the addition of acetylene and ethylene. The black dots and curve represent neat benzene, the red C_6H_6+C_2H_2 and the green C_6H_6+C_2H_4. Their respective Arrhenius correlations of the curves are presented in the same colors. The first observation is the difference between the behavior of benzene compared to toluene. Althought the experiments can be fit with two curves, the corresponding slopes are much more similar to each other (238 kJ/mol above 1740 K and 171 kJ/mol below 1740 K) compared to toluene. This is possibly due to the fact that the phenyl

radical is not as stable as the benzyl radical, thus the influence of the aromatic-aromatic reactions is less important. The addition of acetylene and ethylene increase the induction delay time, especially for ethylene, as for the case of the addition to toluene. The slopes of the curves are slightly higher than the slopes of the curves for the toluene + C2 case (201kJ/mol and 224 kJ/mol vs 175 kJ/mol).

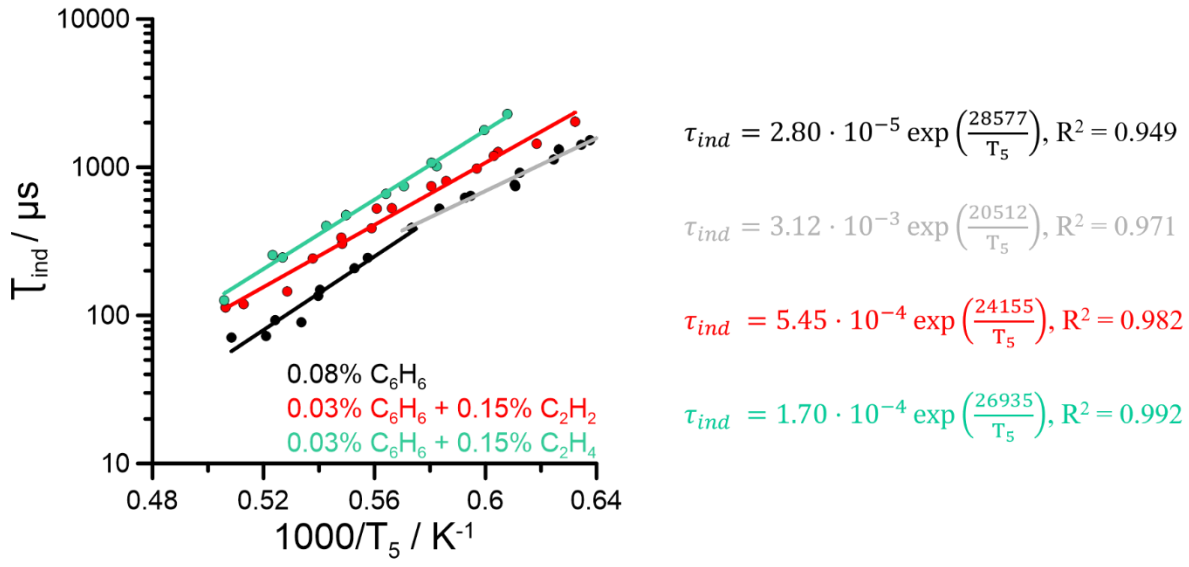

Figure 4.35 *Induction delay time versus inverse of the temperature - in black: 0.08% C_6H_6, in red: 0.03% C_6H_6 + 0.15% C_2H_2 and in green: 0.03% C_6H_6 + 0.15% C_2H_4 diluted in Argon*

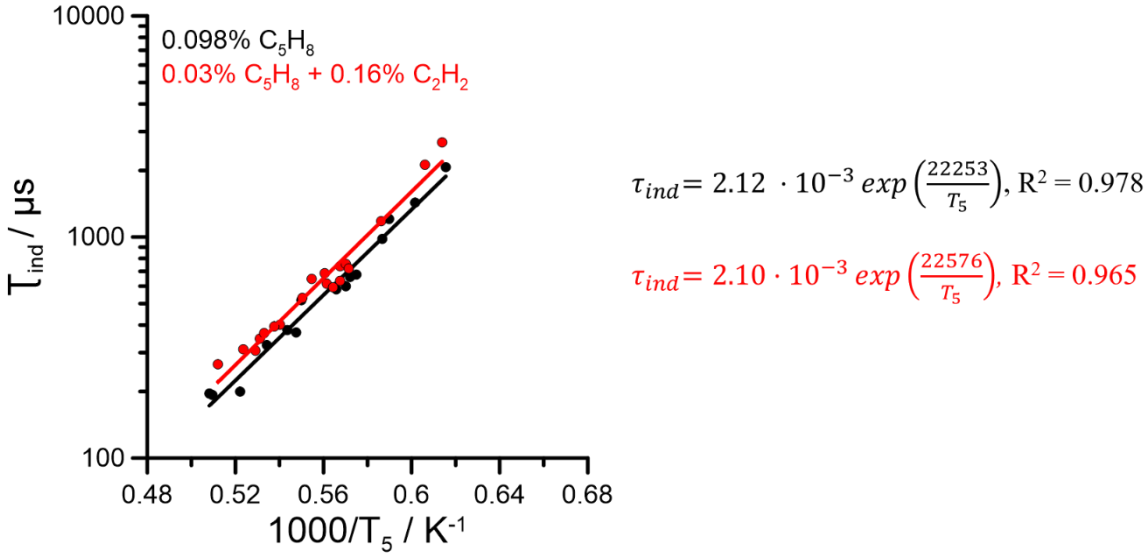

Figure 4.36 *Induction delay time versus inverse of the temperature - in black: 0.098% C_5H_8 in Argon, in red: 0.03% C_5H_8 + 0.16% C_2H_2 in Argon*

Figure 4.36 displays the results of cyclopentene and cyclopentene + acetylene. The addition of C_2H_2 had a small impact on the induction delay time. The formation of PAH products is limited in the case of neat cyclopentene, thus the soot formation chemistry mainly depends on the addition of small fuel fragments to

the aromatic molecules; addition of acetylene does not vary significantly the mechanisms of soot formation. In particular, the induction energies are essentially the same (185 kJ/mol and 188 kJ/mol). On the other hand, the presence of lower concentrations of cyclic fuels does increase the induction times for the C_5H_8+C_2H_2 mixture compared to the pure cyclopentene experiments.

Lastly, **Figure 4.37** displays the induction delay time versus inverse of the temperature all the neat fuels studied with similar carbon concentrations. Toluene is presented in black, benzene in red, cyclopentene in green, propene in pink, propyne in orange and acetylene in blue.

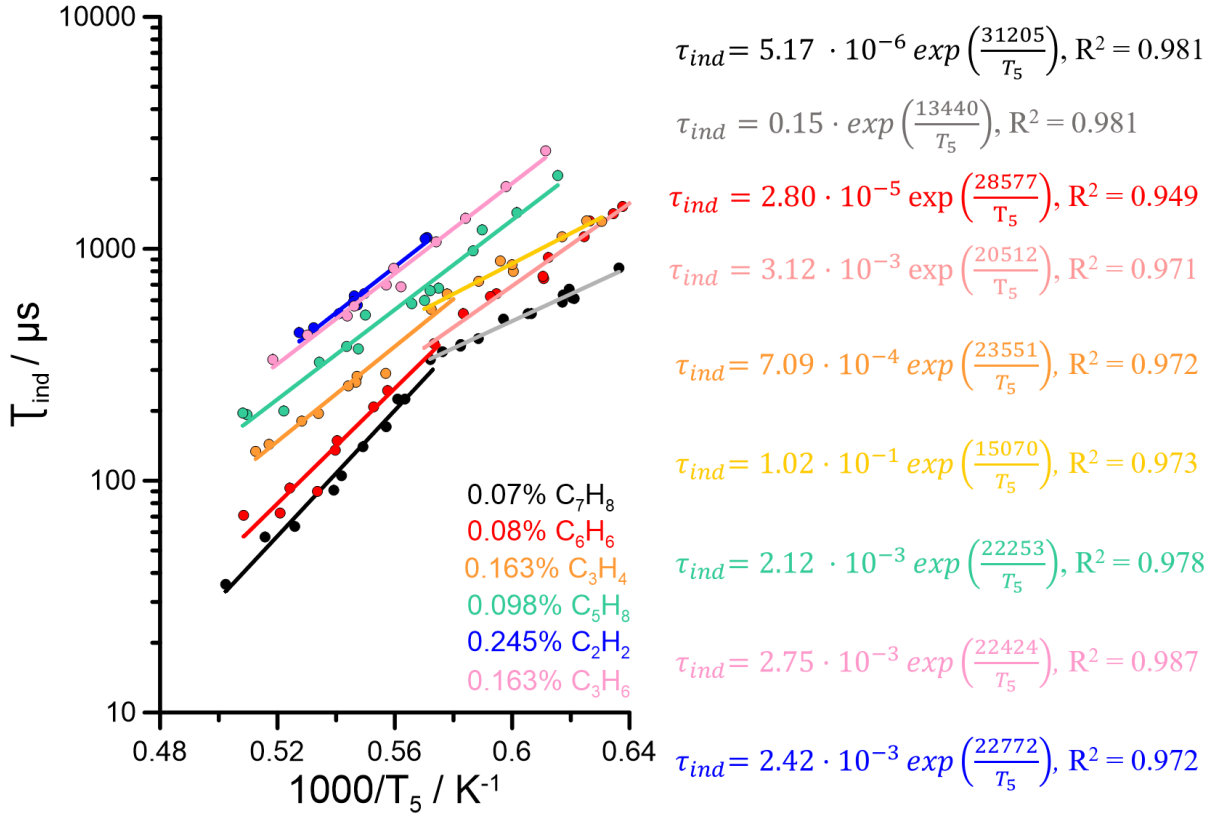

Figure 4.37 *Induction delay time versus inverse of the temperature, in black: in black: 0.07% C_7H_8 in Ar, in red: 0.08% C_6H_6 in Ar, in orange: 0.16% C_3H_4 in Ar, in green: 0.098% C_5H_8 in Ar, in pink: 0.16% C_3H_6 in Ar and in blue: 0.245% C_2H_2 in Ar*

In the high-temperature region, the slopes of the curves of cyclopentene, propyne, propylene, and acetylene are very similar (185 kJ/mol, 196 kJ/mol, 186 kJ/mol, 189 kJ/mol, respectively), lower than the values obtained for the aromatic fuels (259 kJ/mol for toluene, 238 kJ/mol for benzene). The only non-aromatic single fuel which presents a double slope is propyne, for which the fit of the data points below 1740 K has a slope of 125 kJ/mol. Surprisingly, this value is much closer to the value obtained for toluene than for benzene. On the other hand, the induction delay times of propyne and benzene at the lowest temperature considered here (around 1600 K) are very similar, as expected. Future kinetic analyses will try to provide a rational explanation to such observations.

Concerning the absolute values of the induction delay times, toluene is the fuel which shows the shortest times over the entire temperature range, followed by the other aromatic fuel, benzene. This is clearly due to the fact that the thermal decomposition of toluene leads to the formation of the resonantly stabilized benzyl radical, compared to the phenyl radical which has much shorter life span at high temperature conditions. The third cyclic fuel, cyclopentene, has induction times which are 2 to 5 times longer than the toluene ones. The fact that this fuel does produce a large quantity of resonantly stabilized C_5H_5 radicals does not trigger fast pathways to the soot particles. This may be due to different reasons:

- part of the ring opens forming linear C5 intermediates;
- the PAH growth mechanism involving C5 cyclic intermediates are not as efficient as the ones involving C6 and C7 aromatics.

The results on propyne pyrolysis lie between the cyclopentene and the benzene curves, thus the pathway starting with C_3H_4 to C_3H_3 to benzene is quite effective in leading to the soot particles, more than the cyclic C5 mechanism. Finally, acetylene and propylene show similar induction delay times, a factor 3-6 times higher than the toluene curve.

In summary, the order of soot propensity for the single fuels studied here is the following: $C_7H_8 > C_6H_6 > C_3H_4 > C_5H_8 > C_3H_6 > C_2H_2$. The induction delay times of toluene, benzene, and propyne show typical behaviors in the low-temperature and high-temperature ranges, which can be attributed to two different soot formation mechanisms involving reactions between aromatic compounds or between aromatic compounds and small intermediates, respectively. For the other fuels, only one curve can fit the experimental data. At high temperature, the slopes of the induction curves for non-aromatic fuels are very similar, suggesting a common soot formation mechanism. Concerning the fuel mixtures, the addition of C2 intermediates to toluene and benzene leads to longer induction delay times compared to the aromatic fuel, with similar activation energies for acetylene or ethylene (one single curve for all the T range). Acetylene addition to cyclopentene does have a minor influence on the induction of the neat cyclic fuel. When C3 fuels are added to toluene, the double curve behavior is maintained due to the fast pathway from C3 fuels to benzene, although the induction delay times are longer compared to the pure toluene case.

4.2.3 Soot growth rates

After the induction period, the soot volume fraction grows very rapidly by surface reactions and coagulation. The coagulation should provide a significant contribution at the beginning of the growth process, when the nascent particles are smaller (thus more mobile) and numerous (thus more prompt to react one with each other). When the particles increase in size, the soot growth by surface reactions should

be the dominant process. The growth of the volume fraction by surface reactions can be described by a first order law in first approximation, which follows the initial particle detection [275]–[277]. This law can be written as it follows:

$$\frac{df_v}{dt} = k_f \cdot (f_{v\,max} - f_v) \tag{4.4}$$

where k_f is the growth rate constant. The interpretation of this law assumes that the coalescence and agglomeration of particles are negligible during this phase (total number of particles, N, constant and particles always in the form of elementary spherules). The growth rate constant can also be written as an Arrhenius relation:

$$k_f = A \exp\left(-\frac{E_f}{RT}\right) \tag{4.5}$$

where A is the pre-exponential factor and E_f in the activation energy of the soot growth. The results of the present study will be correlated with the first order kinetic law defined above (4.4). In integrated form, this law is written as:

$$\ln\left(\frac{f_{v\,max}}{f_{v\,max} - f_v}\right) = k_f \cdot t = f(t) \tag{4.6}$$

which can be defined as a function f(t). This function can be derived from the soot volume fraction profile and plotted as a function of time, as shown in **Figure 4.38**. The slope of this curve will provide the value of k_f. On the other hand, the slope varies with time. The assumption used in this analysis is that beyond the inflection point, the particles will be large enough and the process will be driven by the surface reactions. Thus, only the experimental points following the inflection will be used to derive the soot growth rate.

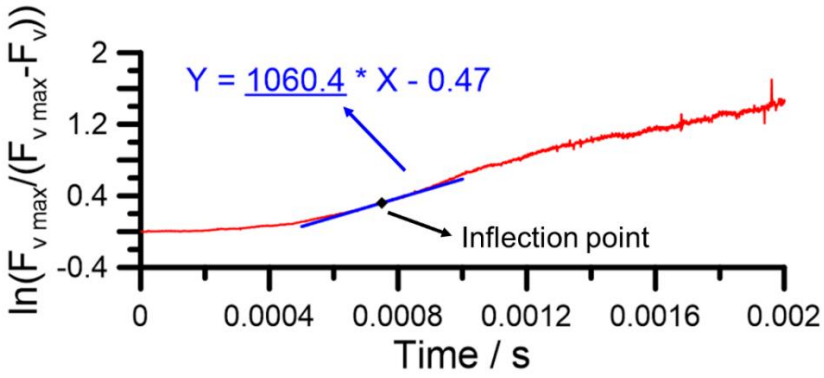

Figure 4.38 *Soot growth rate obtained from the fitted curve of f_v time-dependent behavior – 0.07% C_7H_8 in Ar, at T_5 = 1735 K and P_5 = 18.0 bar*

Figure 4.39 shows the soot growth rate of neat toluene in black, the binary mixture of toluene and acetylene in red, and toluene + ethylene in green. The growth rate is normalized by the fuel concentration as in

previous literature works. The growth rate constant, activation energy and correlation coefficients are displayed for each curve in their respective colors. In general, the soot growth rates have a larger dispersion and uncertainties compared for example to the induction delay times, the R^2 of the correlations especially when few points are available may be relatively low. On the other hand, the qualitative behavior of the different curves can be easily derived and compared.

The growth rate of pure toluene is much higher compared to the ones for the two mixtures, which nearly superimpose, by a factor of two at high temperatures and a factor of five at low temperatures. The toluene data have been divided into two parts, following the same data ranges as in **Figure 4.33**. The global activation energy of the growth process of the two mixtures is very similar to the one for toluene pyrolysis in the high temperature range (around 8 kJ/mol for the mixtures and 7 kJ/mol for neat toluene). On the other hand, the activation energy of pure toluene at low temperatures is much larger, around 18 kJ/mol. Once again, the two values for toluene pyrolysis might reflect the two growth mechanisms by addition of aromatics or smaller fuel fragments.

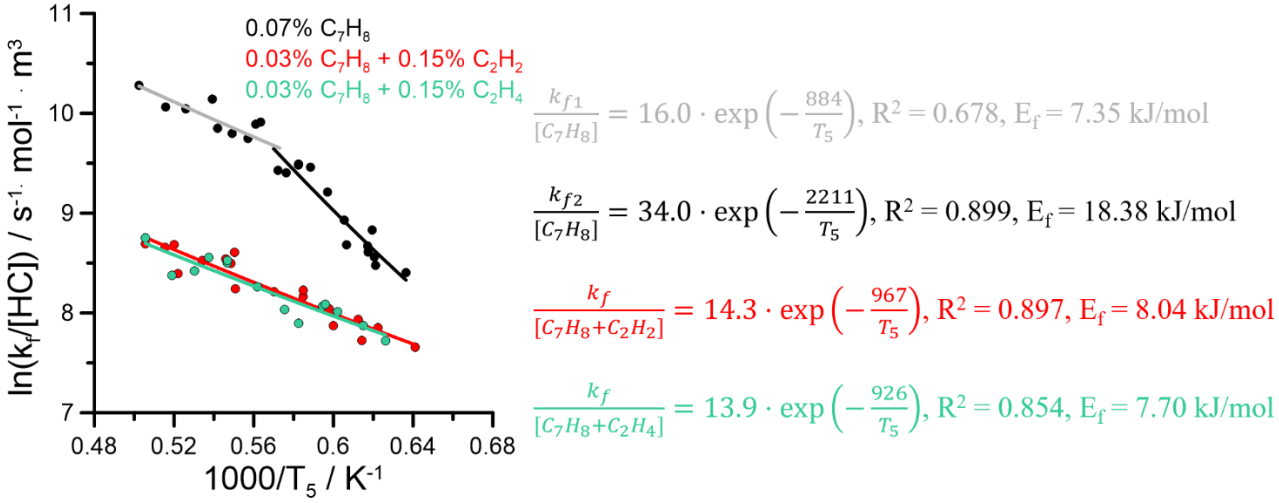

Figure 4.39 *Soot growth rate versus inverse of the temperature – in black: 0.07% C_7H_8, in red: 0.03% C_7H_8 + 0.15% C_2H_2 and in green: 0.03% C_7H_8 + 0.15% C_2H_4 diluted in Argon*

Figure 4.40 displays the soot growth rate of C_7H_8 + C_3H_4 in orange and C_7H_8 + C_3H_6 in blue. The growth rate constant, activation energy and correlation coefficient are displayed for each curve in their respective colors. The two mixtures have very similar induction delay times, considering the experimental uncertainties. The addition of propene and propyne to toluene decreases the absolute value of the soot growth rate, but not as much as the previous case of C2 addition. In this case, the ratio between the toluene rates and the mixtures rates vary from 1.7 to 2.7 from the lowest temperature conditions to the highest ones. Differently from the results on the induction delay times, only one curve can be used to fit the experimental data. The global activation energies of the growth process for the two mixtures are very similar, 11 kJ/mol

and 12 kJ/mol for C_7H_8 + C_3H_4 and C_7H_8 + C_3H_6, respectively. These values are intermediate between the energies of the low-temperature and the high-temperature regimes for toluene pyrolysis.

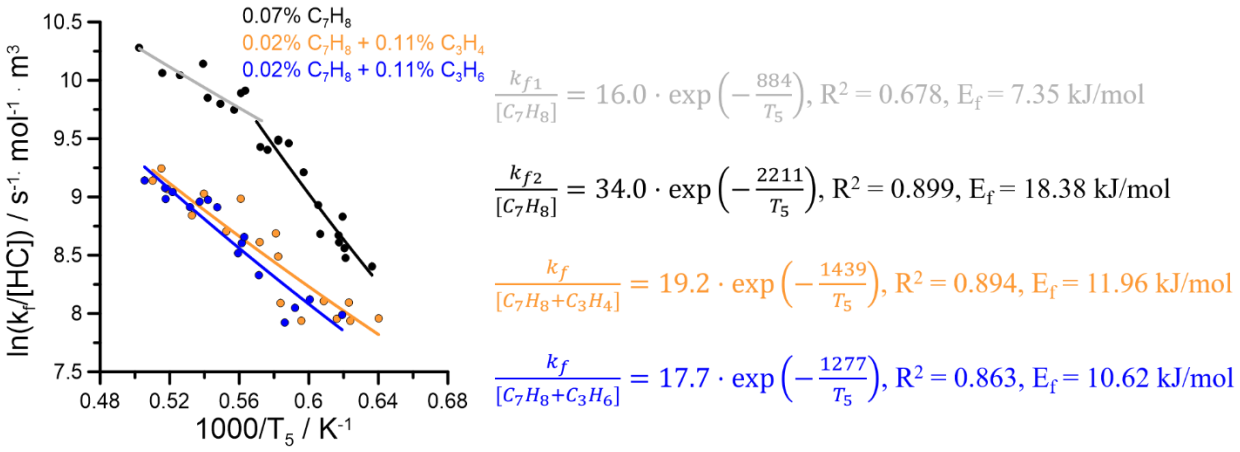

Figure 4.40 *Soot growth rate versus inverse of the temperature in black: 0.07% C_7H_8, in orange: 0.02% C_7H_8 + 0.11% C_3H_4, in blue: 0.02% C_7H_8 + 0.11% C_3H_6 in Argon*

Moving to C_6H_6 results, **Figure 4.41** shows the soot growth rate of neat benzene in black and the binary mixtures with C_2H_2 and C_2H_4 in red and green, respectively. The benzene data exhibit a different behavior in the low-temperature and the high-temperature regions, as for toluene and for the data on the induction delay times (**Figure 4.35**). The two activation energies are 14 kJ/mol at low temperatures vs 6 kJ/mol in the high temperature range. Once again, the addition of acetylene or ethylene has the same cosequences on the absolute growth rate. The ratio between the growth rates for neat benzene and benzene + C2 varies between 2 at high temperatures to 4 at low temperatures, similar to toluene and toluene + C2. The activation energy is 8 kJ/mol and 9 kJ/mol for C_6H_6 + C_3H_4 and C_6H_6 + C_3H_6, respectively.

Figure 4.42 shows the soot growth rate of neat cyC_5H_8 in black and the binary mixture of cyclopentene and acetylene in red. The global activation energy is around 8 kJ/mol for the neat C5 fuel, thus comparable with the values presented above for the toluene-based and benzene-based mixtures as well as for the aromatic fuels in the high temperature regions. The addition of acetylene leads to a significant decrement in the growth rate as well as a decrease of the global activation energy (around 4 kJ/mol, but subject to large uncertainties due to the small values and the limited temeprature range of the dataset).

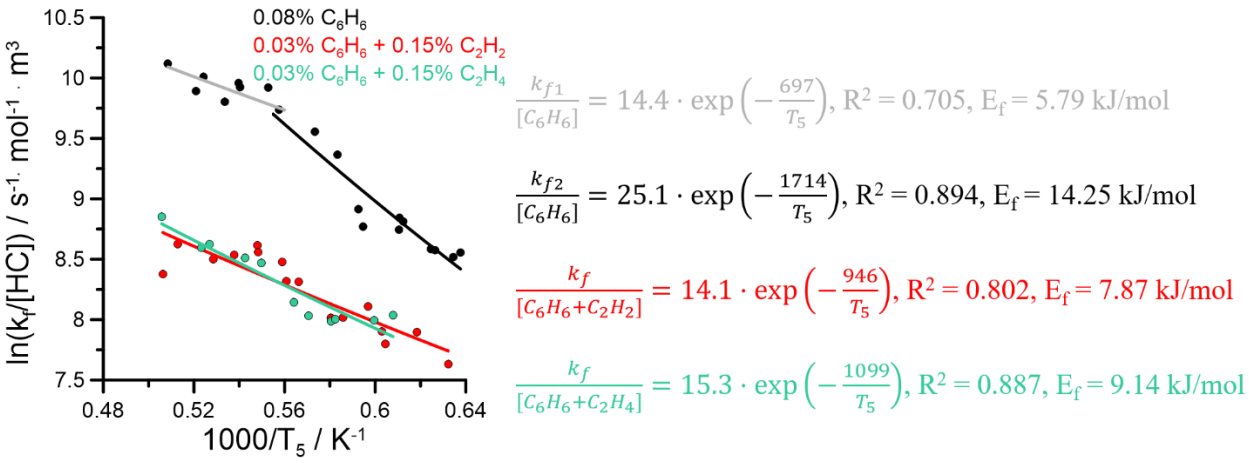

Figure 4.41 *Soot growth rate versus inverse of the temperature - in black: 0.08% C_6H_6 in Argon, in red: 0.03% C_6H_6 + 0.15% C_2H_2 in Argon, in green: 0.03% C_6H_6 + 0.15% C_2H_4 in Argon*

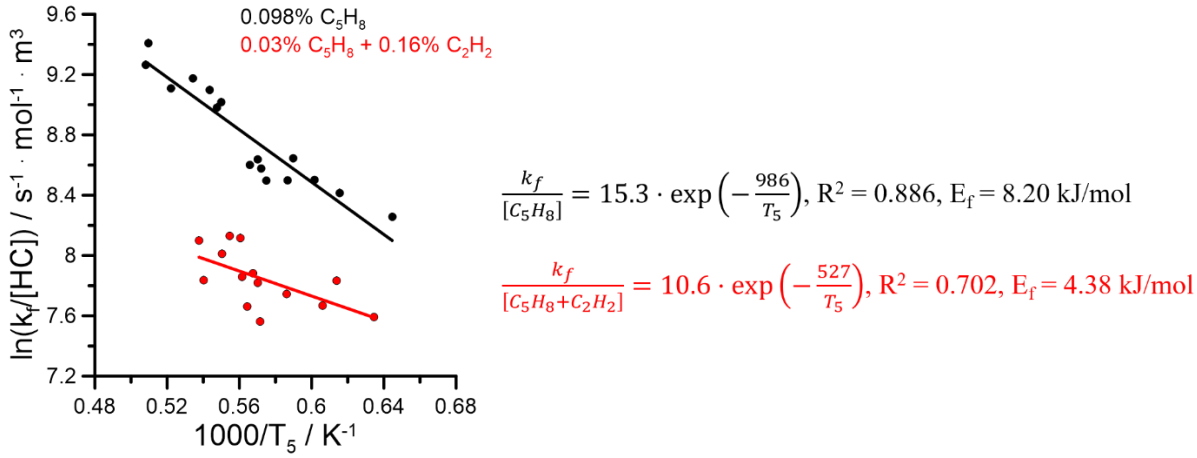

Figure 4.42 *Soot growth rate versus inverse of the temperature - in black: 0.098% C_5H_8 in Argon, in red: 0.03% C_5H_8 + 0.16% C_2H_2 in Argon*

Figure 4.43 shows a comparison between the six neat fuels studied at the same carbon concentration. Toluene is presented in black, benzene in red, cyclopentene in green, propene in pink, propyne in orange, and acetylene in blue. Toluene and benzene are characterized by similar soot growth rates for the entire temperature range of the present study. As seen in the previous sections, cyclopentene presents lower absolute values of optical densities (**Figure 4.20**) and longer induction delay times (**Figure 4.37**) when compared to toluene and benzene. The reduced tendency to form particles is also confirmed by a lower soot growth rate. The only single fuel which does not follow the previous order in soot tendency is propyne. Propyne does produce more soot than cyclopentene (**Figure 4.20**) and faster (**Figure 4.37**), but the growth rate is lower. In this case we can observe two different behaviors in the low-temperature and high-temperature range as for benzene and toluene. It should be noted that the activation energies for the high-temperature regions of toluene, benzene, and propyne and the growth rate of cyclopentene, propene, and

acetylene are very similar (7 kJ/mol, 6 kJ/mol, 6 kJ/mol, 8 kJ/mol, 11 kJ/mol, 11 kJ/mol, respectively). On the other hand, the slopes in the low-temperature range for the aromatic fuels and propyne are higher, 18 kJ/mol for toluene and propyne and 14 kJ/mol for benzene.

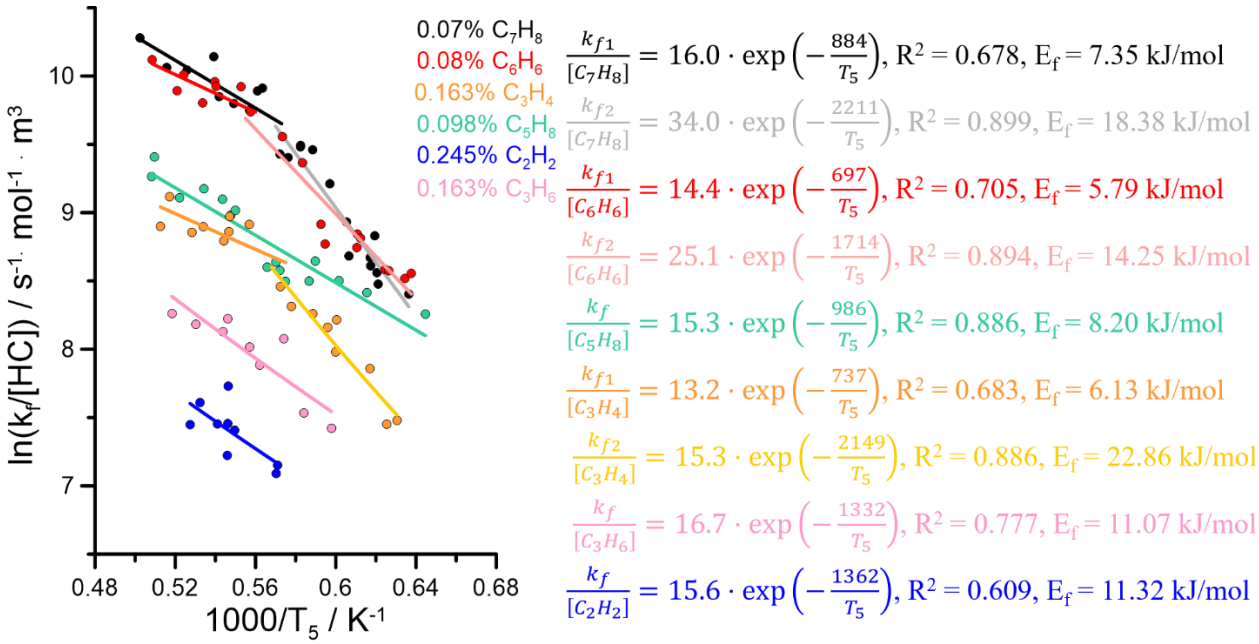

Figure 4.43 *Soot growth rate versus inverse of the temperature - in black: in black: 0.07% C_7H_8 in Ar, in red: 0.08% C_6H_6 in Ar, in orange: 0.16% C_3H_4 in Ar, in green: 0.098% C_5H_8 in Ar, in pink: 0.16% C_3H_6 in Ar and in blue: 0.245%*

In summary, the soot growth rate is influenced by the fuel type and the temperature condition. Toluene, benzene and propyne profiles show a two-stage behavior corresponding to the one observed in the induction delay times for reactions relevant to aromatic-aromatic interactions or aromatic-aliphatic growth. The data on the other fuels and mixtures can be fit with only one curve. The propyne pyrolysis shows global growth rates which are lower than the cyclopentene case, which is opposite to what observed for the optical densities and induction delay times. The mixtures with C2 and C3 additions to toluene, benzene, and cyclopentene are characterized by lower growth rates compared to the neat fuels. It is interesting to notice how the addition of acetylene and ethylene leads to a similar decrement in the growth rate compared to toluene and benzene, while the effects on the optical densities and induction delay times are very different, as seen in previous sections. Similar considerations apply for the addition of propyne and propylene to toluene.

There is not a lot of data available on the literature concerning this parameter. Knorre et al [278] analyzed the temperature dependence of the normalized soot growth rate for benzene, acetylene, benzene/acetylene, and acetylene/hydrogen mixtures at 6 bar and 60 bar at a wide range of carbon concentrations. Bauerle et al. [162] studied this parameter for benzene, ethylene and n-hexane, also for wide ranges of pressure and

carbon concentrations. The trend found for toluene is in agreement with previous studies carried out in the laboratory on the same experimental set-up [279]. This parameter was also studied for n-haxadecane, decahydronaphthalene, n-heptylbenzene and 1-mehylnaphtalene. Later, Mathieu [206] analyzed the soot growth rate of the pyrolysis of the fuel Fisher-Tropsch, propyl-cyclohexane, butylbenzene, heptamethylnonane, ternary mixture mimic of a regular gas oil (22% of heptamethylnonane, 31% of butylbenzene and 47% of propyl-cyclohexane) and also toluene, however in much higher concentrations compared to the present study, which led to a different trend of soot growth rate.

4.2.4 Kinetic modeling analyses

A preliminary, qualitative kinetic investigation has started in order to provide some insights on the particle formation from the pyrolysis of the cyclic hydrocarbons considered in the present work, toluene, benzene, and cyclopentene. The simulations were performed using Chemkin Pro [280] with the recent kinetic model developed at ICARE for simulating the PAH chemistry from the pyrolysis of numerous fuel components and mixtures, including the ones presented in chapter 4.1. Such model was validated against speciation data in the high-purity shock tube, including detailed chemistry for PAHs up to four rings (i.e. pyrene and fluoranthene). The model also contains larger gas-phase species, but lumped. In fact, the number of species of similar mass and the number of structural isomers increase quickly with molecular mass. Therefore, lumped PAH species (i.e. $C_{18}H_{10}$) and classes (BINs) of very large PAHs and particles covering certain mass ranges have been defined by Richter et al [281]. The model used in this analysis contains only reactions to BIN1A and BIN1B, BIN1 corresponding to a C20 compound, A and B representing different C/H ratios as defined in the CRECK model from the group at Politecnico di Milano. Work is ongoing to develop the solid-phase model to be coupled to the PAH chemistry; nevertheless, the soot growth will follow the formation of the PAHs and BIN1, thus the analyses on such intermediates can give an idea of the quantity of soot that will be estimated with the model once coupled to the soot chemistry. **Figure 4.44** shows the mole fraction in ppm versus time in seconds of BIN1B, from benzene pyrolysis in red, toluene in black and cyclopentene in green, at a constant pressure of 18 bar and initial temperature of 1750 K. The formation of BIN1B starts at earlier time for toluene compared to benzene, although the maximum values are comparable. On the other hand, the mole fraction from cyclopentene pyrolysis is much lower compared to the curves for the aromatic fuels. This agrees with the results observed in **Figure 4.20** (optical densities vs temperature) and **Figure 4.37** (induction delay times vs (1000/T)).

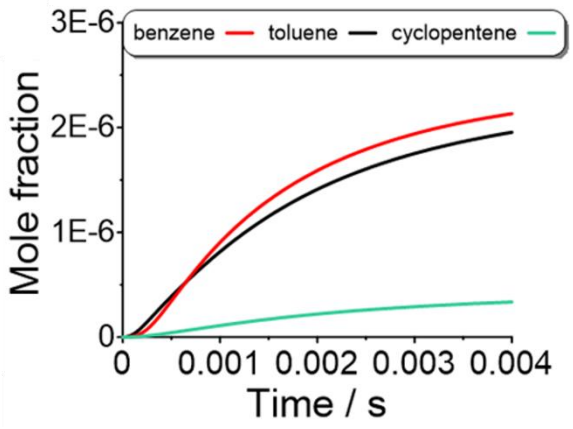

Figure 4.44 *Mole fraction in ppm versus time in seconds of BIN1B – benzene in red, toluene in black and cyclopentene in green*

It is now of interest to investigate the kinetic reasons behind this difference in behavior, in particular how BIN1B is produced for the different fuels. For this purpose, rate of production analyses (ROP) at T_5=1750 K, P_5= 18 bar, and reaction time of 4 ms are performed for BIN1B, lumped $C_{18}H_{10}$, pyrene ($C_{16}H_{10}$), fluoranthene ($FC_{16}H_{10}$), fluorene ($C_{13}H_{10}$), phenanthrene ($C_{14}H_{10}$), naphthalene, and indene (the major PAH species). The percentages provided in the following sections are integrated values over the 4 ms time of the simulations. BIN1B is formed for around 90% through $C_{18}H_9$+C_2H_2 (HACA route), around 1-2% through C_3H_4-P+$C_{18}H_9$, 1.5-3% through C_3H_3+$C_{18}H_9$ for all fuels. Fuel dependent pathways include reaction of indene with the $C_{10}H_7CH_2$ (1% of the total ROP for toluene and cyclopentene), and, only for cyclopentene, the recombination between 2 naphthyl radicals (1.5%) and the reaction between benzene and $C_{18}H_9$ (1%). $C_{18}H_9$, radical of $C_{18}H_{10}$ and key intermediate for the formation of BIN1, is predominantly formed through the H-abstraction reactions from its stable species.

The formation of $C_{18}H_{10}$ depends on several pathways. It is mainly produced through the HACA routes, C_2H_2+$C_{16}H_9$ (60% for toluene, 47% for benzene and 65% for cyclopentene) and C_2H_2+$FC_{16}H_9$ pathways (toluene: 30%, benzene: 40%, cyclopentene: 27%). C_9H_7+$C_{10}H_7$-1 also slightly contributes to $C_{18}H_{10}$ formation (8% for toluene and benzene, 6% for cyclopentene). $C_{16}H_9$ and $FC_{16}H_9$ are produced from the H-abstraction reactions of pyrene and fluoranthene, respectively. Concerning pyrene, it is mainly formed through the HACA pathway C_2H_2+$C_{14}H_9$ (toluene: 77%, benzene: 84%, cyclopentene: 79%) and minorly through the recombination reactions $C_{16}H_9$+H (toluene: 10%, benzene: 10%, cyclopentene: 5%) and C_2H_4+$C_{14}H_9$ (toluene: 9%, cyclopentene: 12%). **Figure 4.45** shows the mole fraction versus time of $C_{16}H_{10}$. $C_{16}H_{10}$ is formed very rapidly in the toluene case, and it reaches the highest value among the different fuels (around 0.18 ppm) compared to 0.14 ppm for benzene and 0.03 ppm for cyclopentene. The peak of the profile for benzene is also shifted to longer times compared to the other fuels.

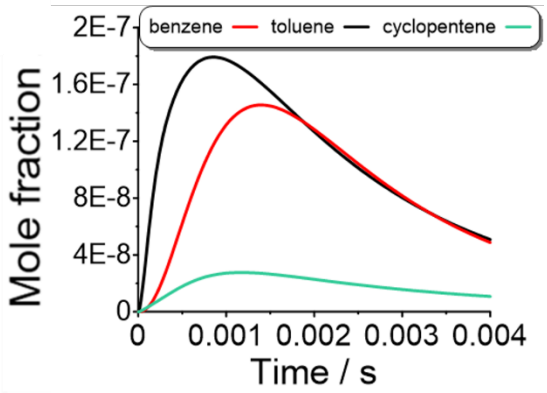

Figure 4.45 *Mole fraction in ppm versus time in seconds of $C_{16}H_{10}$ – benzene in red, toluene in black and cyclopentene in green*

As mentioned above, the HACA route is mainly responsible for the pyrene formation. $C_{14}H_9$ derives from the H-abstraction reactions from $PC_{14}H_{10}$. **Figure 4.46** displays the complex reaction pathways leading to $PC_{14}H_{10}$ formation at T_5 = 1750 K in the pyrolysis of toluene, benzene, and cyclopentene based on the integrated ROP analysis. The percentage numbers (black: toluene, red: benzene, green: cyclopentene) represent the contributions to $PC_{14}H_{10}$ formation by the corresponding reactions. In benzene and cyclopentene pyrolysis, $PC_{14}H_{10}$ mainly comes from the $C_6H_5CCC_6H_5$ isomerization, which is the result of addition elimination reaction $C_6H_5C_2H+C_6H_5$. The reactions $C_9H_7+C_5H_5$ and $C_{13}H_8CH_2$ isomerization also contribute to $PC_{14}H_{10}$ formation in cyclopentene and benzene pyrolysis, respectively. The $PC_{14}H_{10}$ formation in toluene pyrolysis originate from fuel specific reactions: bibenzyl ($C_6H_5C_2H_4C_6H_5$) dehydrogenation steps (52%), $C_{14}H_9+H$ recombination (31%), and fulvenyl (C_7H_5) self-recombination (9%). The first and third pathways derive from the benzyl radical self-recombination.

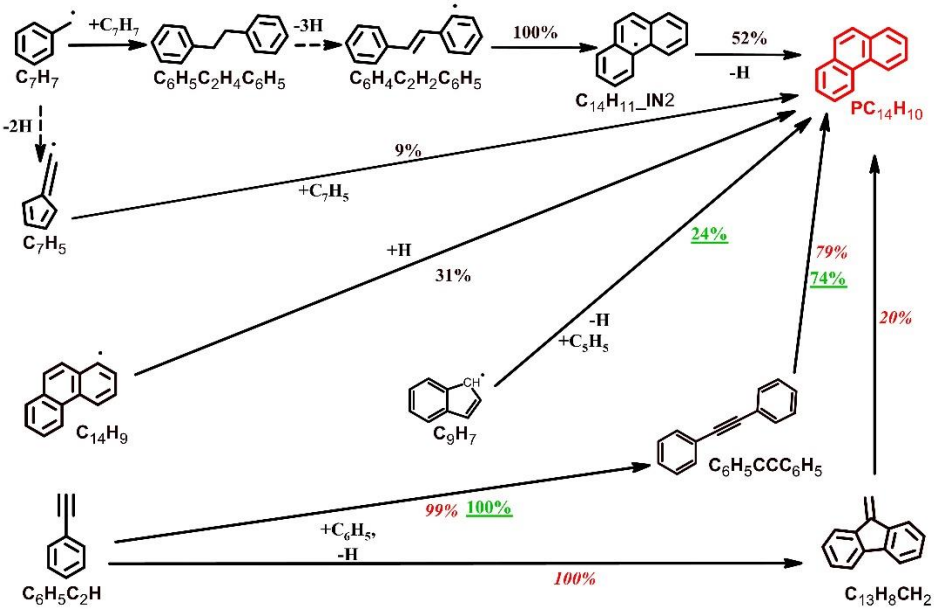

Figure 4.46 *The reaction pathways leading to $PC_{14}H_{10}$ formation at T_5 = 1750 K in the pyrolysis of toluene, benzene and cyclopentene. The percentage numbers (black: toluene, red: benzene and green: cyclopentene) represent the contributions to $PC_{14}H_{10}$ formation by the corresponding reactions*

Second HACA step to $C_{18}H_{10}$ involves fluoranthene. **Figure 4.47** presents the mole fraction versus time of fluoranthene. Contrary to the case of pyrene, fluoranthene is mainly formed in the benzene case (maximum value of around 0.45 ppm, vs 0.2 ppm in toluene pyrolysis and 0.03 ppm in cyclopentene pyrolysis). Thus, the contribution to $C_{18}H_{10}$ formation from fluoranthene in the case of benzene will compensate the greatest contribution of pyrene for toluene.

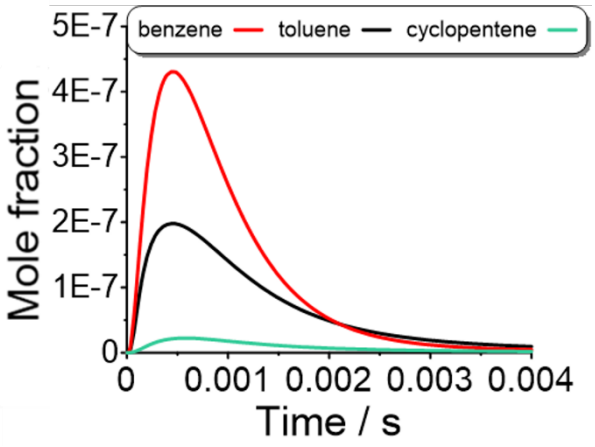

Figure 4.47 *Mole fraction in ppm versus time in seconds of $FC_{16}H_{10}$ – benzene in red, toluene in black and cyclopentene in green*

$FC_{16}H_{10}$ is mainly formed through three pathways:

- $FC_{16}H_9$+H (41% for toluene, 46% for benzene, and 34% for cyclopentene;

- phenyl-naphthalene ($C_{10}H_7C_6H_5$) isomerization and dehydrogenation (20% for toluene, 46% for benzene, and 27% for cyclopentene);
- C_3H_3+ fluorenyl radical ($C_{13}H_9$) (36% for toluene, 3% for benzene, and 36% for cyclopentene).

$C_{10}H_7C_6H_5$ predominantly comes from $C_{10}H_7$-1+C_6H_6 reaction in benzene and cyclopentene. However, this reaction with the pathway starting by C_9H_7+C_7H_7 through the intermediates $C_9H_7C_7H_7$, $C_9H_7CHC_6H_5$, and $C_{10}H_8C_6H_5$ have comparable contribution in toluene pyrolysis. The common pathway involving $C_{10}H_7$-1 requires the formation of this radical species. For the case of toluene, this is possible through H-abstraction reactions from naphthalene (direct or through isomerization of $C_{10}H_7$-2). This is the main pathway also for benzene and cyclopentene, although 20% of the $C_{10}H_7$-1 ROP derives from the C_4H_2+C_6H_5 reaction in the benzene case and 26% from the HACA route C_2H_2+$C_6H_4C_2H$ foe cyclopentene pyrolysis. Reaction pathways leading to naphthalene formation are mapped out based on ROP analyses at 1750 K in the individual cases, as presented in **Figure 4.48**. The percentage numbers (black: toluene, red: benzene, and green: cyclopentene) represent the contributions to $C_{10}H_8$ formation by the corresponding reactions. The formation of $C_{10}H_8$ is governed by the $C_9H_6CH_2$ isomerization and a minor channel through $C_9H_6CH_3$-1 dehydrogenation in toluene and cyclopentene pyrolysis (66% and 78% of the total integrated rate of production, respectively). Both $C_9H_6CH_2$ and $C_9H_6CH_3$-1 are the result of C_9H_7+CH_3 recombination reaction. Other minor channels through C_7H_5+C_3H_3 and $C_{10}H_7$-1+H also lead to $C_{10}H_8$ formation in toluene pyrolysis (14% and 15% of the total ROP, respectively), while the scheme presented in **Figure 4.9** based on the C_5H_5+C_5H_5 recombination is responsible for 21% of naphthalene production from cyclopentene. However, naphthalene formation is different in benzene pyrolysis. It mostly comes from the H-addition reaction to naphthyl radical ($C_{10}H_7$-1, 51%), the abstraction reaction $C_{10}H_7$-1+ C_6H_6 (18%) and the reaction between C_6H_5 and C_4H_2 (15%).

The pathway involved in the formation of $FC_{16}H_{10}$ through $C_{13}H_9$ is a major route only for toluene and cyclopentene, thus the formation of this radical will be analyzed for these two fuels. $C_{13}H_9$ is the result of fluorene **(**$C_{13}H_{10}$) consumption through H-abstraction by H and CH_3. $C_{13}H_{10}$ mainly comes from the H-addition reaction to $C_{13}H_9$ for the two fuels. Additional formation pathways through the two-step ring closure/dehydrogenation of diphenylmethane ($C_6H_5CH_2C_6H_5$, 23% of total ROP) and the recombination reaction of C_4H_4+C_9H_7 (19% of total ROP) also contribute to $C_{13}H_{10}$ formation in toluene and cyclopentene, respectively. Diphenylmethane is formed from the recombination reaction between the benzyl radical and the phenyl radical.

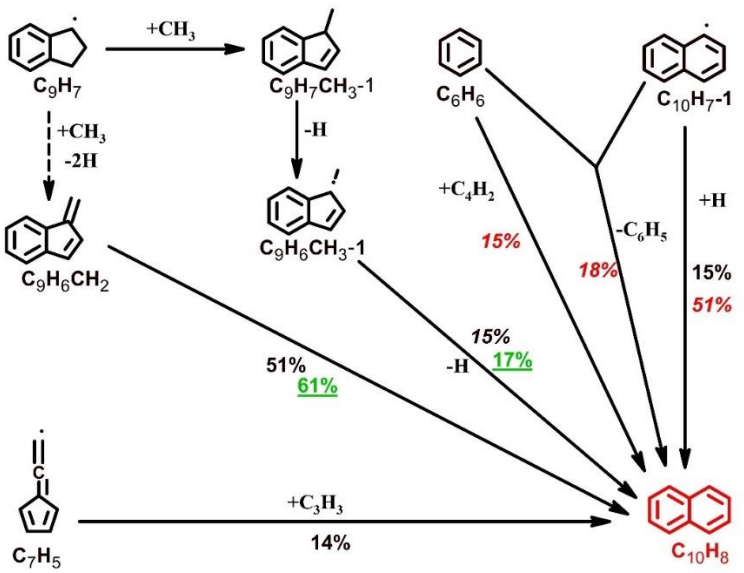

Figure 4.48 *The reaction pathways leading to $C_{10}H_8$ formation at T_5 = 1750 K in the pyrolysis of toluene, benzene and cyclopentene. The percentage numbers (black: toluene, red: benzene and green: cyclopentene) represent the contributions to $C_{10}H_8$ formation by the corresponding reactions*

One of the main intermediate species involved in the formation of $C_{18}H_{10}$, phenanthrene, fluorene, phenylnaphthalene, and naphthalene is the indenyl radical. The C_9H_7 formation originates from different sources as shown in **Figure 4.49**, however the thermal decomposition of methyl indene ($C_9H_7CH_3$-2), the H-abstraction or fragmentation of indene, and $CH_3C_6H_4+C_2H_2/C_2H$ reaction through the intermediate ethynyl-toluene (o-$CH_3C_6H_5C_2H$) governs C_9H_7 formation in toluene pyrolysis (44%, 19%, and 34% of the total integrated ROP, respectively). The first two pathways are also responsible for indenyl formation in the case of benzene, while the latter two in cyclopentene pyrolysis.

Figure 4.50 displays the mole fraction of C_9H_8. Both $C_6H_6+C_3H_3$ reaction (24% for toluene, 58% for benzene, and 60% for cyclopentene) and $C_6H_5C_3H_3$P_1 isomerization (15% for toluene, 1% for benzene and 30% for cyclopentene) contribute to C_9H_8 formation in the three studied mixtures but with different relative importance. Additional pathway through C_9H_7+H leads to the formation of C_9H_8 in toluene pyrolysis. C_6H_6 comes from ipso-substitution reaction $C_7H_8+H=C_6H_6+CH_3$ and propargyl self-recombination reaction in toluene pyrolysis. The latter pathway also contributes to C_6H_6 formation in cyclopentene pyrolysis in addition to fulvene isomerization originating from $C_5H_5+CH_3$ pathways. $C_6H_5C_2H+CH_3$ reaction is the main contributor to $C_6H_5C_3H_3$P_1 formation in both cyclopentene and toluene pyrolysis.

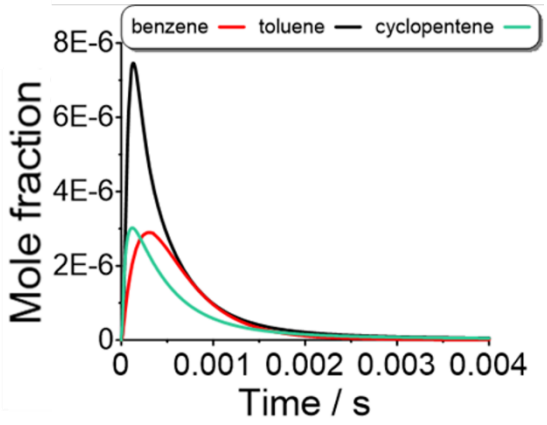

Figure 4.49 *Mole fraction in ppm versus time in seconds of C_9H_8 – benzene in red, toluene in black and cyclopentene in green*

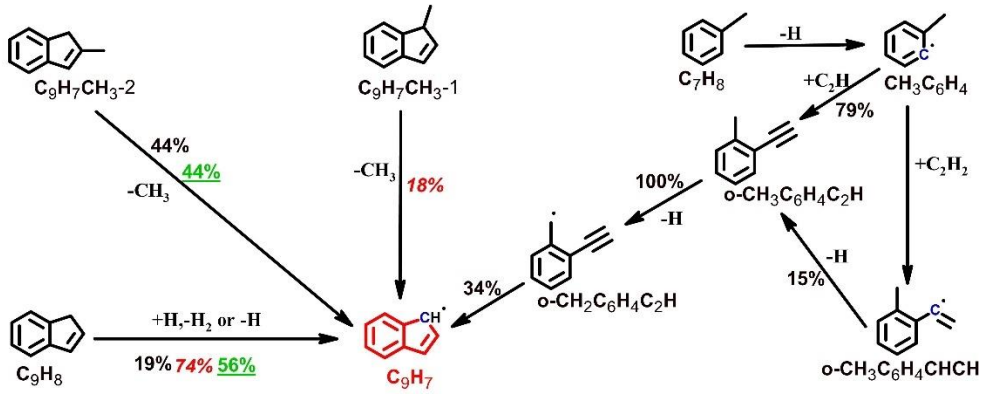

Figure 4.50 *The reaction pathways leading to C_9H_7 formation at T_5 = 1750 K in the pyrolysis of toluene, benzene and cyclopentene. The percentage numbers (black: toluene, red: benzene and green: cyclopentene) represent the contributions to C_9H_7 formation by the corresponding reactions*

4.2.5 TEM Analyses

Complementary to the extinction measurements presented above, the study of soot particles by transmission electron microscopy (TEM) was performed at two enlargements: 2.75×10^4 and 2×10^5. The study of the soot texture (morphology, size of the unitary particles) was carried out in TEM at a magnification of 2.75×10^4 leading to images of medium resolution. The micro-structure of the soot (length of carbonaceous planes carbonaceous planes, distance separating these planes) was instead studied at a magnification of 2×10^5. For the neat fuels (toluene, benzene, and cyclopentene), the samples collected from three experiments at different temperatures were analyzed: minimum temperature, intermediate temperature (corresponding to the maximum optical densities), and maximum temperature. Once C_2H_2 or C_2H_4 was added to the fuel mixture, only the sample corresponding to the intermediate temperature was studied.

4.2.5.1 Diameter of the primary particles

The measurement of the size of the elementary particles of soot was carried out for several fuels in pyrolysis, through the software ImageJ [282]. The first step of the analysis consists on setting a scale for each image. Assuming that the particles are perfectly spherical, the diameter is measured with a digital ruler, as shown in **Figure 4.51**. Several particles (55-100) are measured in order to extract the distribution and calculate their average value and then the standard deviation.

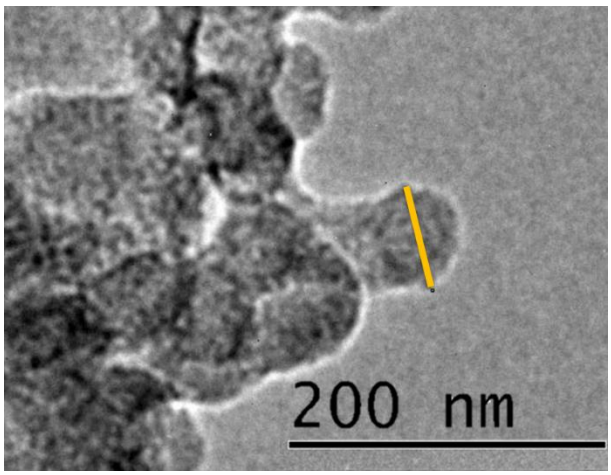

Figure 4.51 *Example of measurement of the diameter of the primary particle*

The first fuel analyzed is toluene. **Figure 4.52** shows the soot cluster observed for T_5 = 1564 K and P_5 = 16.8 bar. The mean diameter is 27.6 nm with a standard deviation of 0.1 nm. These data were obtained with 100 particles measured. The soot appears to be dense, and the individual particles are superimposed. It is also important to consider that the particles are not perfectly spherical, which may cause an uncertainty in the measurements.

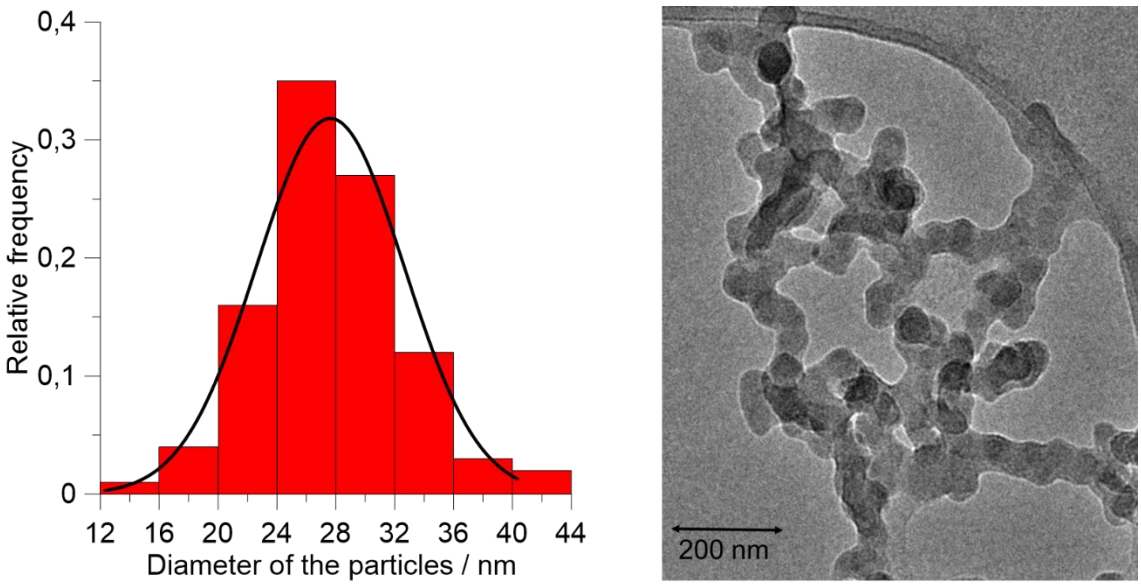

Figure 4.52 *TEM Analysis of toluene pyrolysis, T_5 = 1564 K, P_5 =16.8 bar. Diameter of the primary particles: $\bar{d}$ = 27.6 nm, σ = 0.1, number of particles measured: 100*

Figure 4.53 shows the soot cluster observed for T_5 = 1732 K and P_5 = 18.0 bar. The mean diameter is 15.6 nm with standard deviation of 0.1 nm, a substantial decrease when compared with the previous temperature condition. The soot is well distributed in the space, and the primary particles seem to be more spherical compared to the previous example. Once again 100 particles were measured.

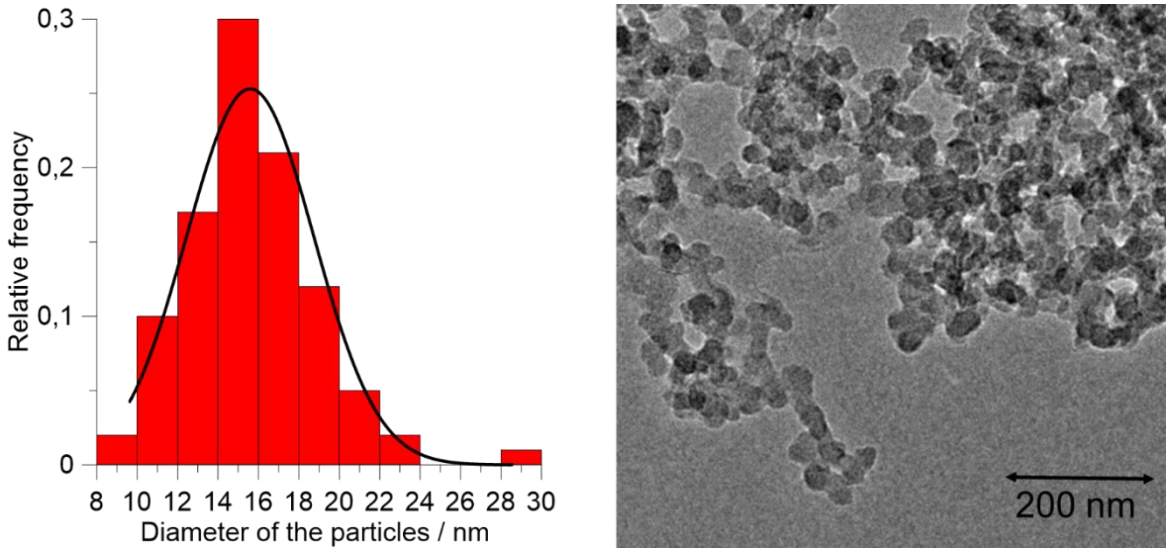

Figure 4.53 *TEM Analysis of toluene pyrolysis, T_5 = 1732 K, P_5 =18.0 bar. Diameter of the primary particles: $\bar{d}$ = 15.6 nm, σ = 0.3, number of particles measured: 100*

For toluene pyrolysis at higher temperature, T_5 = 1931 K and P_5 = 17.5 bar, the decrease of the diameter was almost imperceptible compared to T_5 = 1732 K. The mean diameter is 14.8 nm (σ= 0.1 nm) with 75

particles measured. One remarkable difference is the agglomeration of the particles at the higher temperature, as the primary particles seem mostly superimposed (**Figure 4.54**).

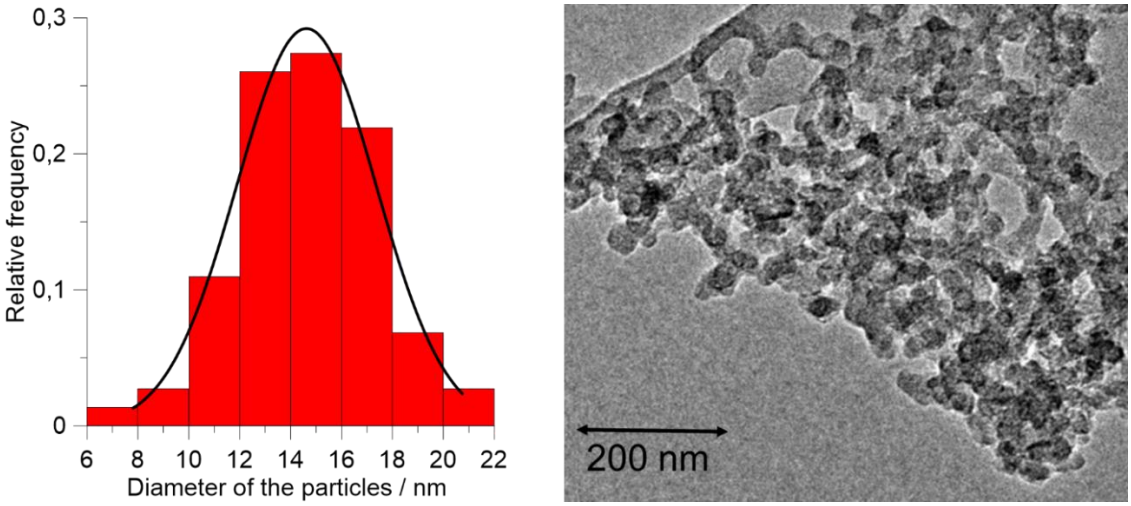

Figure 4.54 *TEM Analysis of toluene pyrolysis, T_5 = 1931 K, P_5 = 17.5 bar. Diameter of the primary particles: $\bar{d}$ = 14.8 nm, σ = 0.1, number of particles measured: 75*

Once acetylene is added to toluene, a different pattern can be observed. At T_5 = 1709 K and P_5 = 17.7 bar (**Figure 4.55**), the average diameter of the primary particles is 17.6 nm with a standard deviation of 1.3 nm (larger distribution compared to the neat toluene). For this set of images, 75 particles were measured. When compared to neat toluene at a similar temperature, the average diameter is significantly larger. Besides, the soot particles seem less dense, and a foam is formed around the soot aggregates. The presence of the foam could be due to PAHs condensing/adsorbing on the particles.

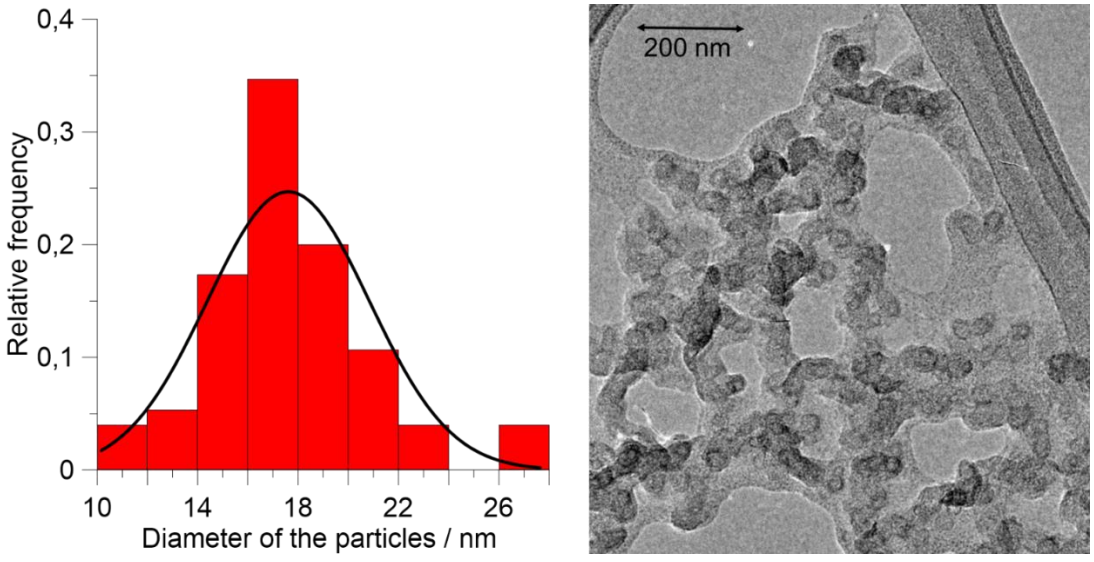

Figure 4.55 *TEM Analysis of C_7H_8+C_2H_2 pyrolysis, T_5 = 1709 K, P_5 = 17.7 bar. Diameter of the primary particles: $\bar{d}$ = 17.6 nm, σ = 1.3, number of particles measured: 75*

This foam could not be detected in the presence of ethylene, as seen in **Figure 4.56**. In this case, the particles are mostly superimposed and their mean diameter decreases but not significantly (considering the standard deviations) when compared to the previous case, $\bar{d}$ = 16.1 nm and σ= 0.8 nm. For this condition, 100 particles were measured at T_5 = 1738 K and P_5 = 17.3 bar.

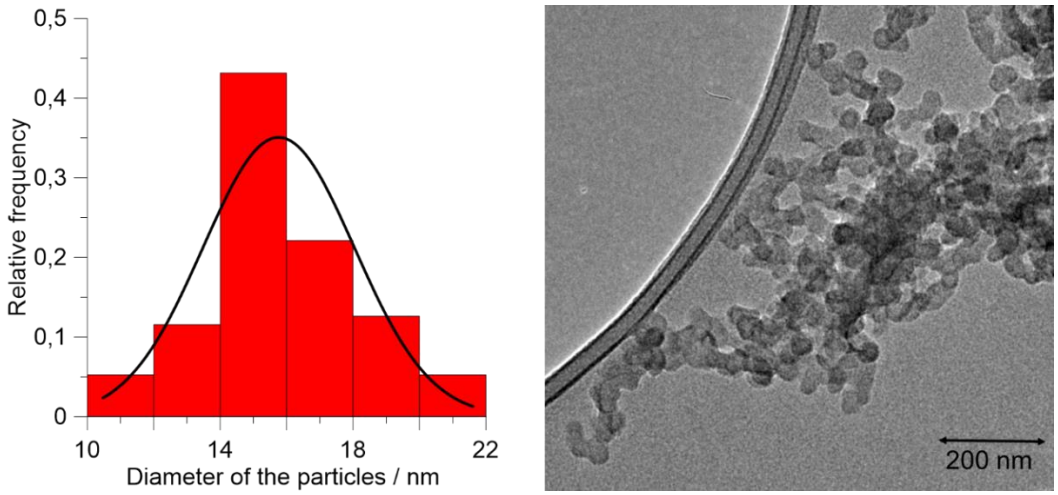

Figure 4.56 *TEM Analysis of C_7H_8+C_2H_4 pyrolysis, T_5 = 1738 K, P_5 = 17.3 bar. Diameter of the primary particles: $\bar{d}$ = 16.1 nm, σ = 0.8, number of particles measured: 100*

Considering neat benzene, **Figure 4.57** shows the TEM for the low temperature fuel sample analyzed. For this particular investigation, 75 particles were measured, the mean diameter is 22.0 nm (σ= 0.2 nm) at T_5 = 1537 K and P_5 = 16.5 bar. This value is significantly lower compared to the toluene case (for which the average diameter is 27.6 nm), but once again it is also important to consider that the particles are not perfectly spherical as for neat toluene. Similarly to the low temperature toluene pyrolysis case, soot appears to be dense, and some of the individual particles are superimposed.

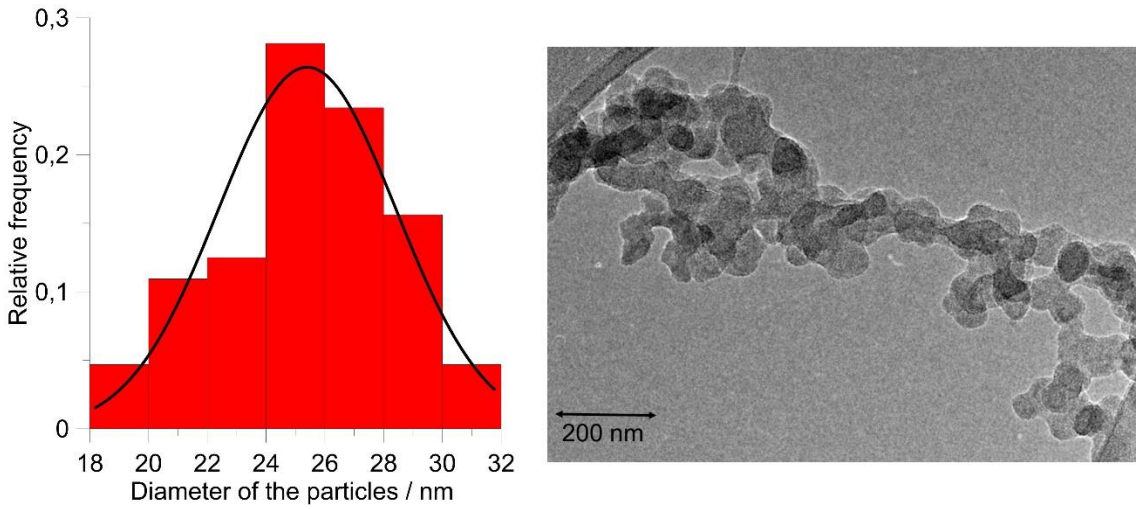

Figure 4.57 *TEM Analysis of benzene pyrolysis, T_5 = 1537 K, P_5 = 16.5 bar. Diameter of the primary particles: $\bar{d}$ = 25.4 nm, σ = 0.2, number of particles measured: 75*

Figure 4.58 shows the soot cluster observed for T_5 = 1714 K and P_5 = 17.9 bar. The mean diameter is 15.5 nm with standard deviation of 0.4 nm (75 particles measured), a significant decrement compared to the previous temperature. The average diameter is the same as the one obtained for toluene pyrolysis at 1732 K. The characteristics of the soot are also similar, the particles are well distributed and more spherical compared to **Figure 4.57**.

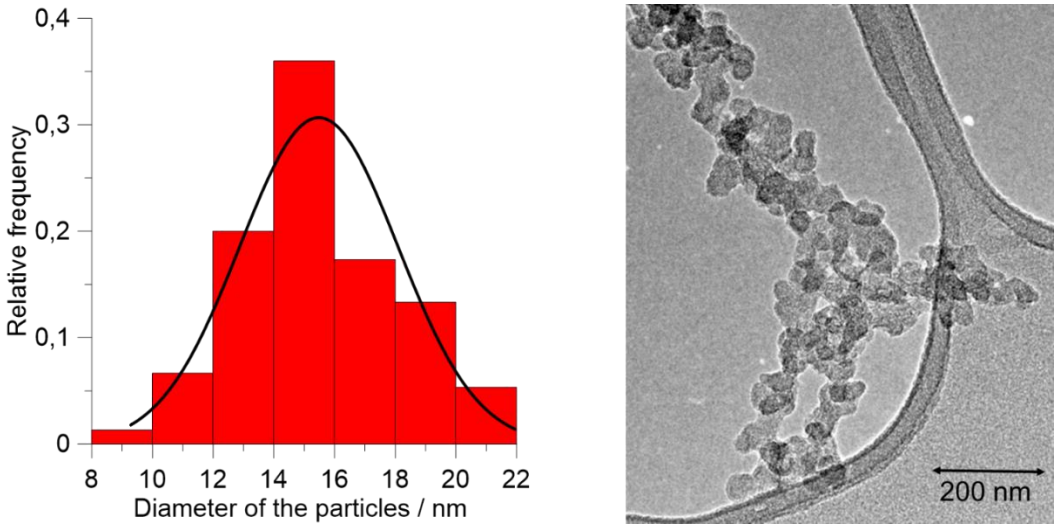

Figure 4.58 *TEM Analysis of benzene pyrolysis, T_5 = 1714K, P_5 = 17.9 bar. Diameter of the primary particles: $\bar{d}$ = 15.5 nm, σ = 0.4, number of particles measured: 75*

For benzene pyrolysis at higher temperature, T_5 = 1920 K and P_5 = 17.4 bar, the decrease of the diameter was minor compared to the case in **Figure 4.58**. The mean diameter is 15.1 nm (σ = 0.3 nm) for 75 particles measured. Thus, the average diameter in **Figure 4.58** and in **Figure 4.59** are similar, however the second

image of the clusters seems to be less defined than the first. This can be explained because the soot was slightly moving inside of the microscope while the images were captured.

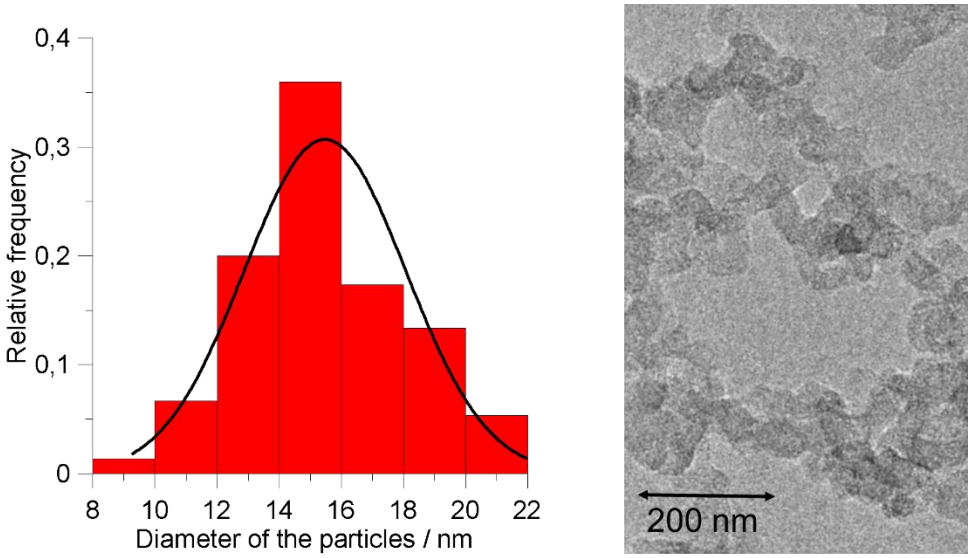

Figure 4.59 *TEM Analysis of benzene pyrolysis, T_5 = 1920 K, P_5 = 17.4 bar. Diameter of the primary particles: $\bar{d}$ = 15.1 nm, σ = 0.3, number of particles measured: 75*

Figure 4.60 shows the TEM analysis of benzene plus acetylene pyrolysis, at T_5 = 1723 K and P_5 = 18.5 bar. The average diameter of the primary particles is 21.5 nm, for 55 particles measured, with a standard deviation of 0.8 nm. What is interesting about this image is the foam formed around the soot agglomerate, which was also observed for the toluene plus C_2H_2 pyrolysis case. However, it is possible to notice a remarkable increase of the mean diameter of the particle when comparing both cases.

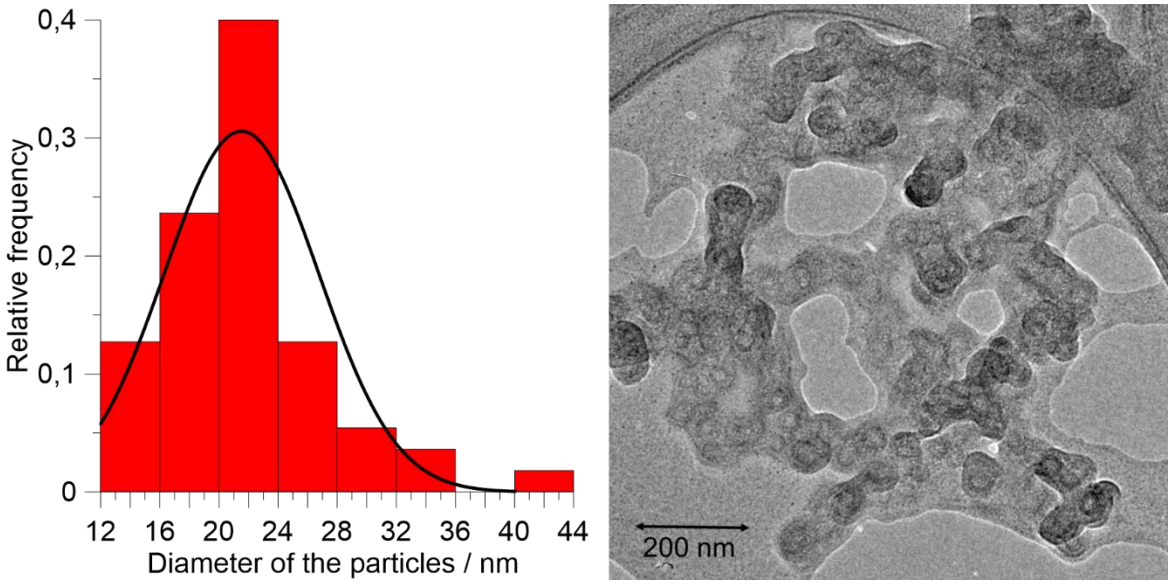

Figure 4.60 *TEM Analysis of C_6H_6+C_2H_2 pyrolysis, T_5 = 1723 K, P_5 = 18.5 bar. Diameter of the primary particles: $\bar{d}$ = 21.52 nm, σ = 0.80, number of particles measured: 55*

Moving to the cyclopentene pyrolysis analysis, **Figure 4.61** shows the soot observed for T_5 = 1551 K and P_5 = 16.6 bar. The mean diameter is 22.3 nm (σ = 0.6 nm) from measurements on 100 particles. Comparing these results with toluene (**Figure 4.52**, T_5 = 1564, average diameter = 27.6 nm) and benzene (**Figure 4.57**, T_5 = 1537, average diameter = 25.4 nm), one can observe a decrease in the average diameter of the particle. The soot appears to be dense, and the individual particles are also superimposed. It is also important to consider that the particles are not perfectly spherical.

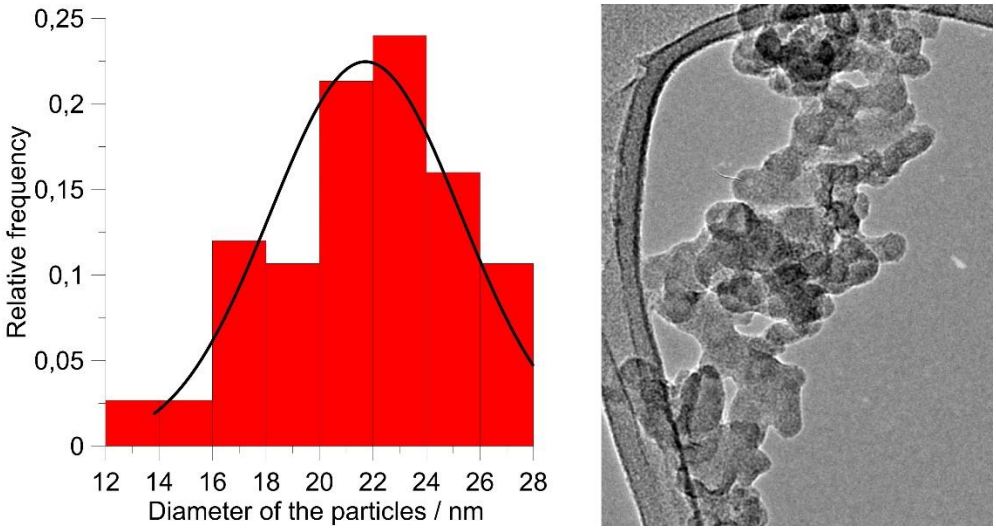

Figure 4.61 *TEM Analysis of cyclopentene pyrolysis, T_5 = 1551 K, P_5 = 16.6 bar. Diameter of the primary particles: $\bar{d}$ = 22.3 nm, σ = 0.6, number of particles measured: 100*

Figure 4.62 shows the soot cluster observed for T_5 = 1739 K and P_5 = 18.1 bar. The mean diameter is 18.4 nm (σ = 0.1 nm) and the soot particles are well distributed, and they seem to be more spherical when compared to the previous example. The average diameter drops compared to the lower temperature case, but it is significantly higher compared to the corresponding cases of toluene (15.6 nm) and benzene (15.5 nm). For the higher temperature case, **Figure 4.63**, T_5 = 1968 K and P_5 = 17.8 bar, the decrease of the diameter was negligible, similarly to the benzene and toluene cases. The mean diameter is 18.3 nm with a standard deviation of 0.8 nm for 55 particles measured.

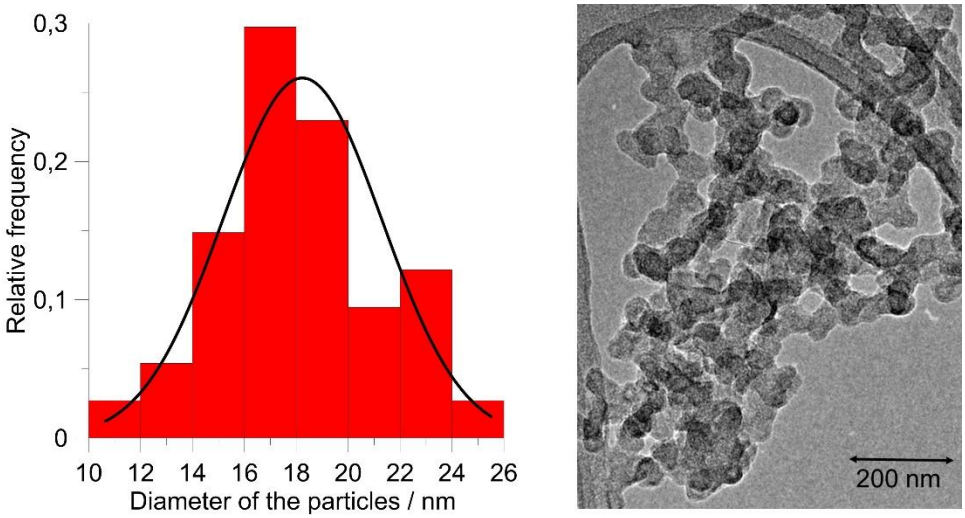

Figure 4.62 *TEM Analysis of cyclopentene pyrolysis, T_5 = 1739 K, P_5 = 18.1 bar. Diameter of the primary particles: $\bar{d}$ = 18.4 nm, σ = 0.1, number of particles measured: 75*

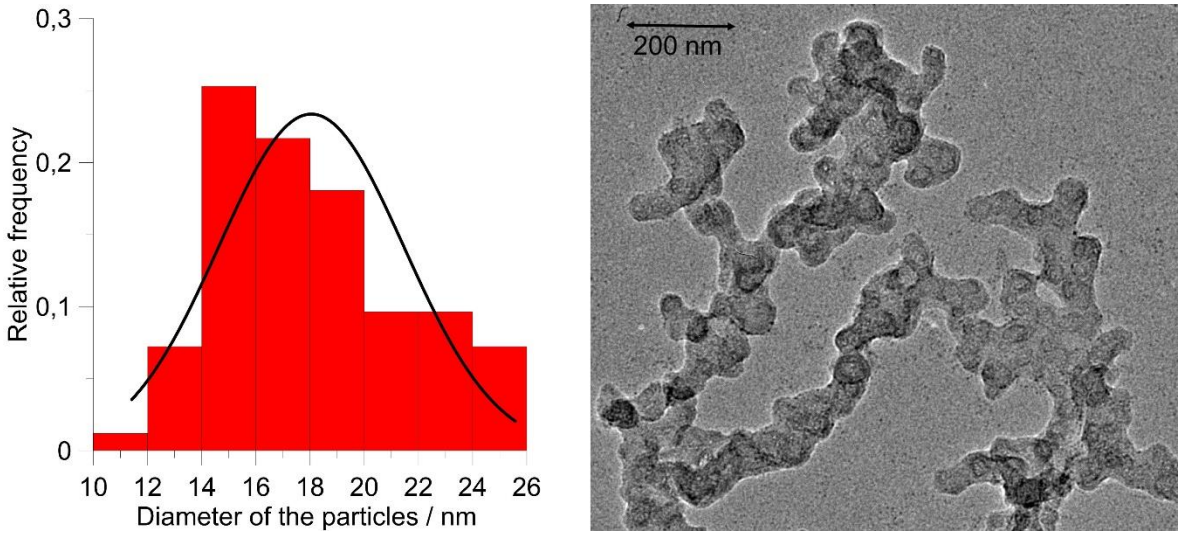

Figure 4.63 *TEM Analysis of cyclopentene pyrolysis, T_5 = 1968 K, P_5 = 17.8 bar. Diameter of the primary particles: $\bar{d}$ = 18.3 nm, σ = 0.8, number of particles measured: 55*

Figure 4.64 shows the TEM analysis of cyclopentene plus acetylene pyrolysis, at T_5 = 1732 K and P_5 = 17.0 bar. The average diameter of the primary particles is 18.4 nm with standard deviation 0.4 nm for 100 particles measured, which is same diameter found for the intermediate case of neat cyclopentene pyrolysis. Thus, the addition of acetylene to cyclopentene does not change significantly the size of the primary particles obtained in the shock tube. In contrast with toluene and benzene binary mixtures with acetylene, the foam is not present in this case.

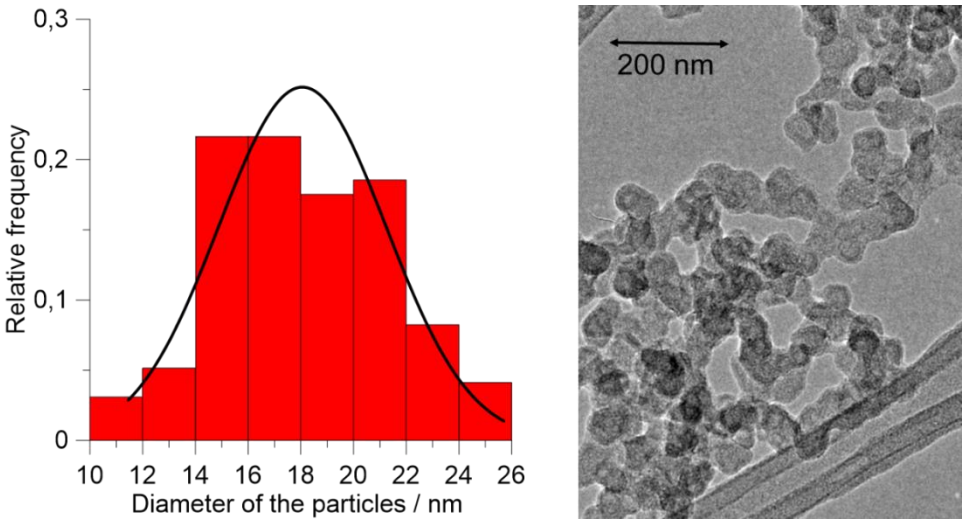

Figure 4.64 *TEM Analysis of C_5H_8+C_2H_2 pyrolysis, T_5 = 1732 K, P_5 = 17.0 bar. Diameter of the primary particles: $\bar{d}$ = 18.4 nm, σ = 0.4, number of particles measured: 100*

The last two cases analyzed were from the same fuel, neat acetylene, at different concentrations and temperatures. **Figure 4.65** shows the TEM analysis of 0.245% C_2H_2, at T_5 = 1989 K and P_5 = 17.4 bar. The diameter of the primary particles is considerably higher than the previous neat fuels, $\bar{d}$ = 23.5 nm with σ = 0.2 nm (100 particles). The particles are superimposed and even in the neat form, a foam is present. This foam could be the source of the increase of the mean diameter of the particles.

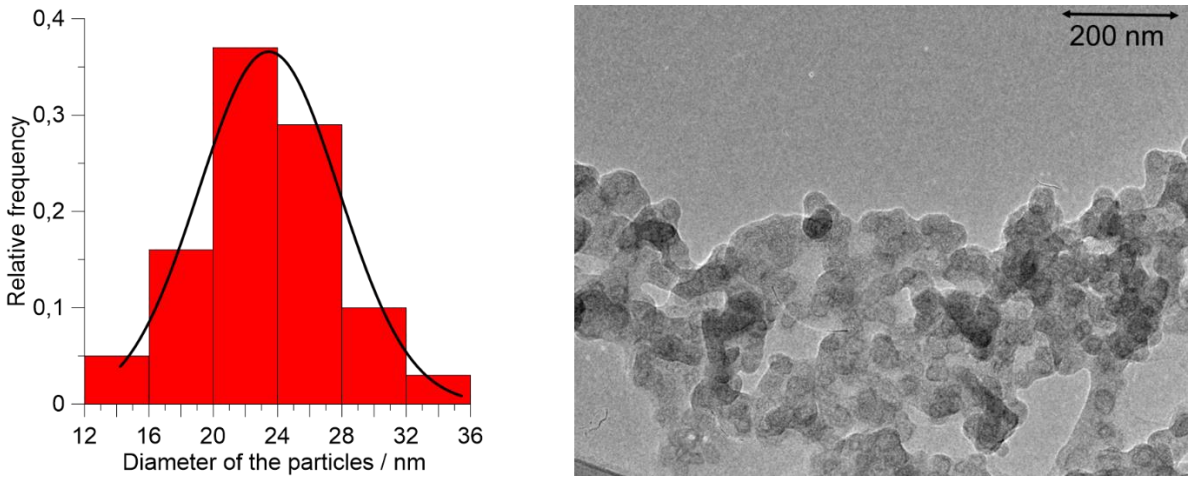

Figure 4.65 *TEM Analysis of 0.245% acetylene pyrolysis, T_5 = 1989 K, P_5 = 17.4 bar. Diameter of the primary particles: $\bar{d}$ = 23.5 nm, σ = 0.2, number of particles measured: 100*

This characteristic is even more visible in **Figure 4.66**. This figure shows the TEM analysis of 0.35% acetylene pyrolysis, at T_5 = 1741 K and P_5 = 17.6 bar. The diameter of the primary particles is 25.2 nm while the standard deviation 0.3 nm (55 particles measured).

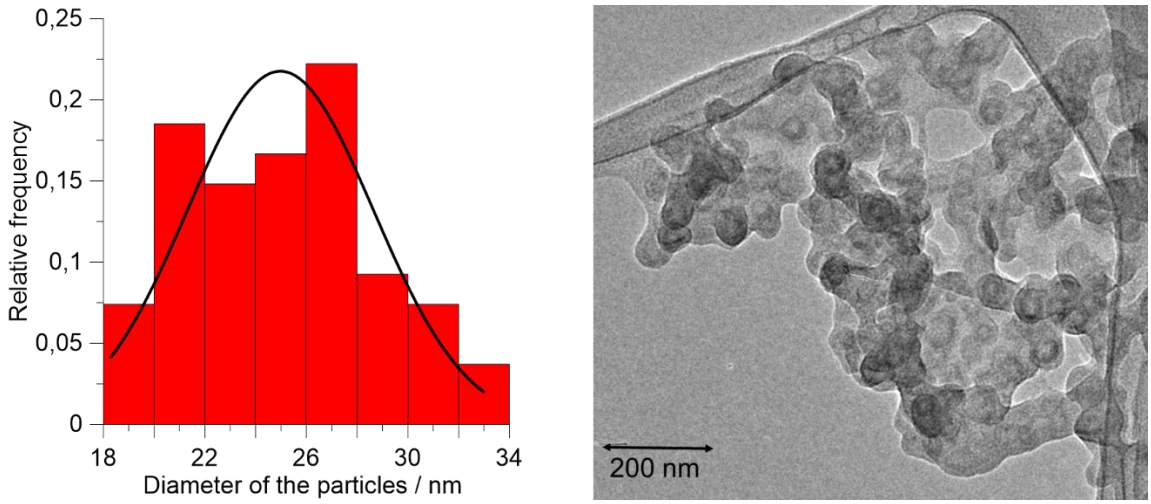

Figure 4.66 *TEM Analysis of 0.35% acetylene pyrolysis, T_5 = 1741 K, P_5 = 17.6 bar. Diameter of the primary particles: $\bar{d}$ = 25.2 nm, σ = 0.3, number of particles measured: 55*

In conclusion, at a magnification of 2 x 10^4, it was possible to observe the arrangement of the primary spheres in aggregates. The aggregates are composed of chains of primary spheres and the mean diameter of the spheres varies with the temperature and the fuel. In the toluene pyrolysis case, the mean diameter of the primary spheres decreased from 28 nm to 15 nm as the temperature increased from 1560 to 1930 K. Analogous behavior was observed in the case of benzene (from 25 to 15 nm). The same observation was made by Douce et al. [226]. The addition of C_2H_2 to toluene increases the mean diameter of the particle by 12%, while for benzene this increase was more dramatic, almost 40%. When ethylene was added to C_7H_8,

it was also possible to observe a slight change in the diameter by 4%. For cyclopentene pyrolysis, the mean diameter decreased from 22 to 18 nm as the temperature increased from 1550 to 1970K, i.e., the variation of the particle size is smaller when compared to toluene and benzene. The addition of C_2H_2 to cyC_5H_8 had no impact on the size of the particle, contrary to the toluene and benzene cases. For these fuels, the addition of acetylene increased the mean diameter of the particle, and a foam was observed around the particles. In summary, **Figure 4.67** shows the mean diameter of the particles versus the temperature.

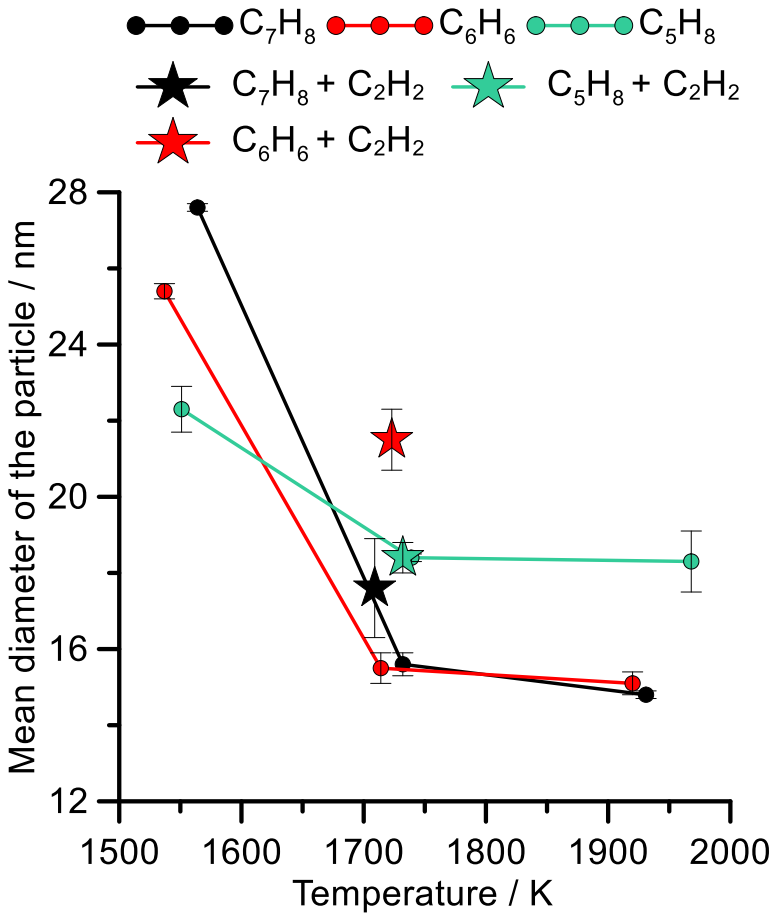

Figure 4.67 *Mean diameter of the particles versus temperature.*

4.2.5.2 Internal organization of the layers

The internal organization of carbon layers was carried out through Gatan's DigitalMicrograph, which is an application used for acquiring, visualizing, analyzing, and processing digital image data [283]. The soot particle is zoomed until a region where the layers are discernable is found, as shown in **Figure 4.68** inside the red circle.

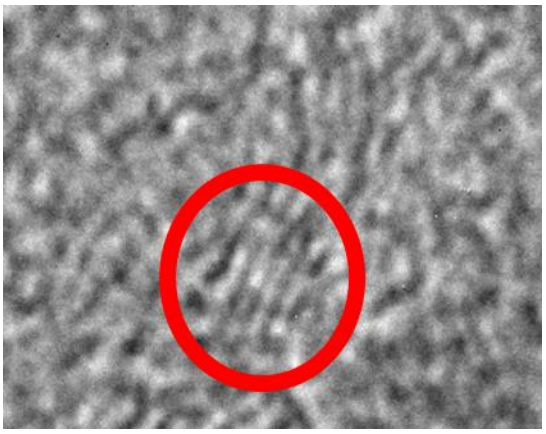

Figure 4.68 *Region of the soot where the layers are discernable.*

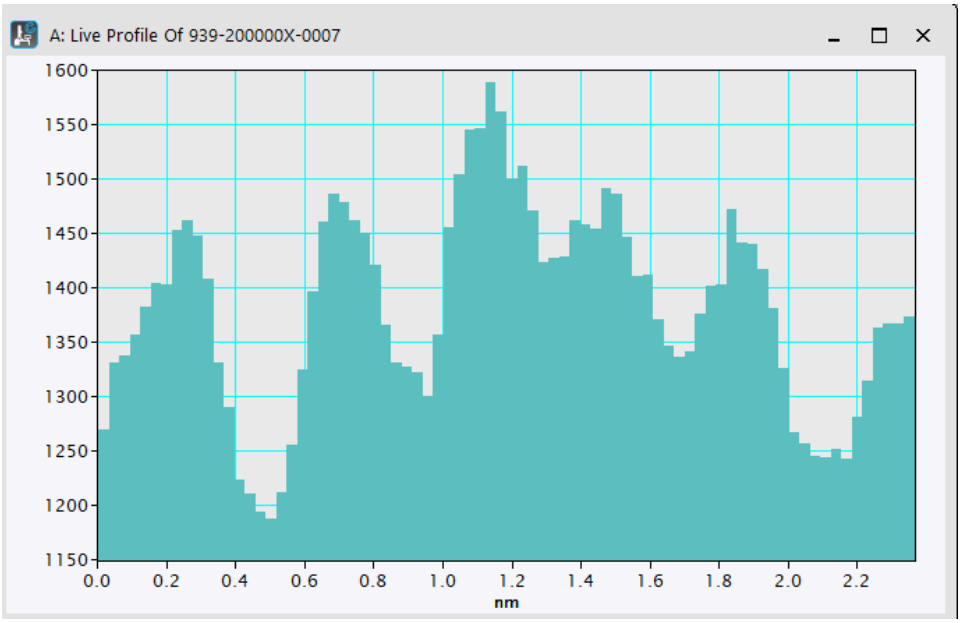

Figure 4.69 *Internal organization of carbon layers – Profile of a typical Live Profile.*

The next step consists of plotting a live profile between these layers (**Figure 4.69**). One must measure the distance between the gaps of the layers and then divide by the number of gaps between the pair/trio of columns and finally it is possible to obtain the space between the carbon layers of the soot particles. The last step consists of plotting histograms and the lognormal distributions in order to analyze the frequency distribution.

The structure (organization at the atomic scale) and the micro texture (spatial organization of the basic structural units) of the particles were observed by TEM at a magnification of 2.5 x 10^5. These two parameters are important because they influence the ability of soot to adsorb gaseous compounds such as

PAHs [206]. The first fuel analyzed is toluene. **Figure 4.70** shows the structure of soot formed at 1564 K from toluene pyrolysis. At this temperature, the soot presents an external crown where the carbon layers are long compared to the core of the particle. However, short carbon planes are discernible, and the structure of the soot is dense and homogeneous. The average d-spacing is 0.435±0.004 nm.

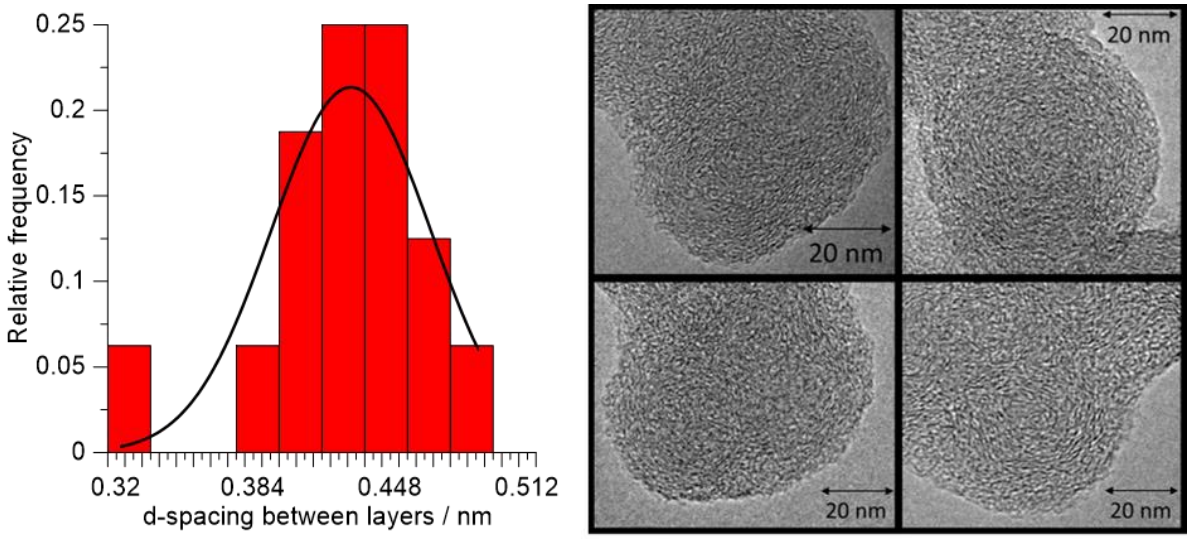

Figure 4.70 *TEM Analysis of toluene pyrolysis, T_5 = 1564 K, P_5 = 16.8 bar. Internal organization of the layers: d-spacing = 0.435 nm, σ = 0.004 nm.*

Figure 4.71 displays the structure of soot formed at 1732 K from toluene pyrolysis. At this temperature the soot particles exhibit a thick, well-organized outer structure with long, parallel planes with different thicknesses. The core of the particle consists of a particulate nucleus (composed of several primary nuclei). The average d-spacing is 0.413±0.007 nm.

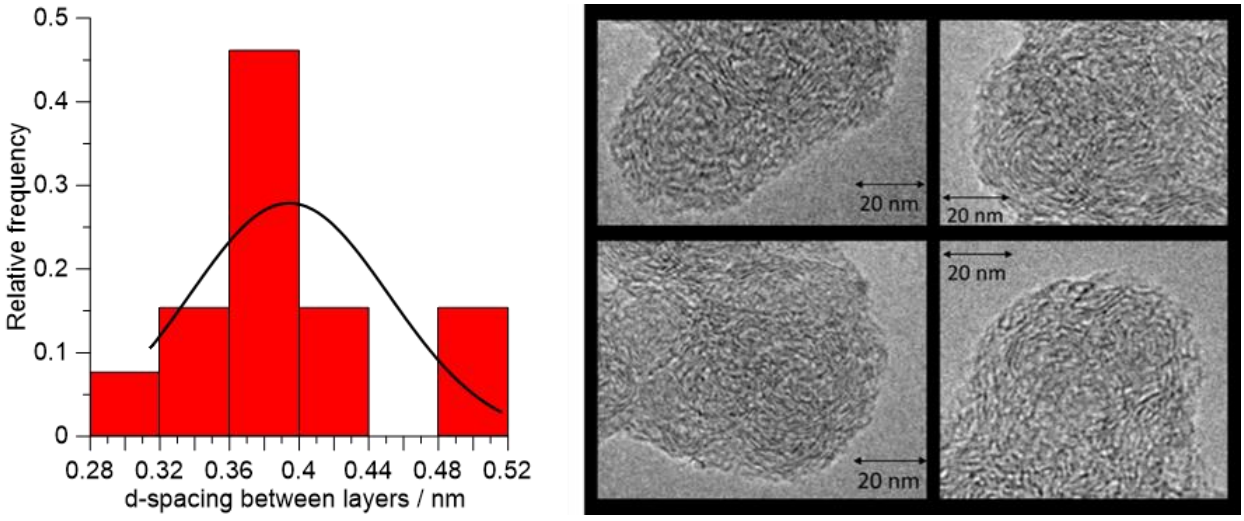

Figure 4.71 *TEM Analysis of toluene pyrolysis, T_5 = 1732 K, P_5 = 18.0 bar. Internal organization of the layers: d-spacing = 0.413 nm, σ = 0.007 nm.*

Figure 4.72 illustrates the structure of soot formed at 1931 K from toluene pyrolysis. The average d-spacing is 0.386±0.003 nm. It is possible to observe well-organized long carbon planes piled parallel to each other. The inner core of these particles is similar to the previous toluene case discussed.

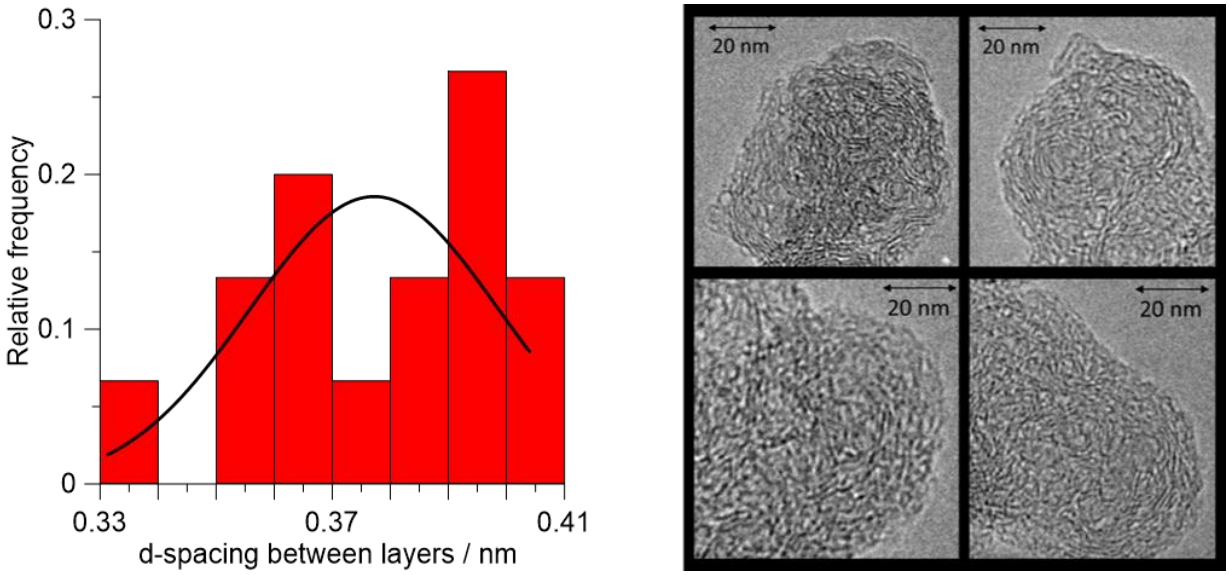

Figure 4.72 *TEM Analysis of toluene pyrolysis, T_5=1931 K, P_5 = 17.5 bar. Internal organization of the layers: d-spacing = 0.386 nm, σ = 0.003 nm.*

Figure 4.73 shows the structure of soot formed at 1709 K of the binary mixture of toluene and acetylene pyrolysis. The soot has short, unorganized carbon layers in the inner and outer areas of the particle. Besides, its thickness seems to remain similar all over the particle. The average d-spacing is 0.420±0.013 nm.

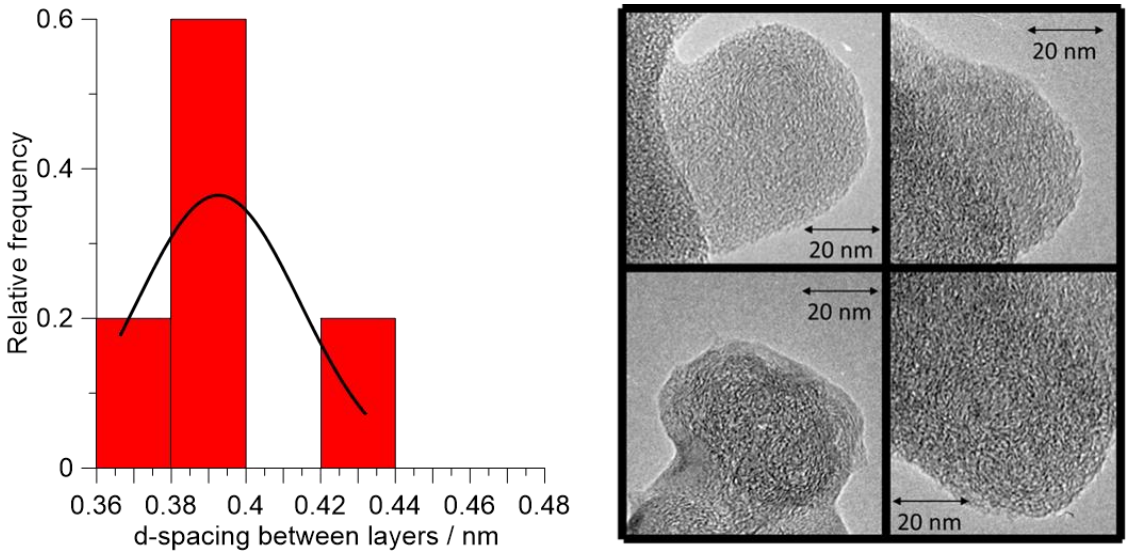

Figure 4.73 *TEM Analysis of C_7H_8+C_2H_2 pyrolysis, T_5 = 1709 K, P_5 = 17.7 bar. Internal organization of the layers: d-spacing = 0.420 nm, σ = 0.013 nm.*

Concerning benzene, **Figure 4.74** shows the structure of soot formed at 1537 K from benzene pyrolysis. At this temperature, the soot has short, unorganized carbon layers in the inner and outer areas of the particle. Nonetheless, short carbon planes are discernible, and the structure of the soot is dense and the average d-spacing is 0.462±0.003 nm, slightly smaller than the toluene case at similar temperature.

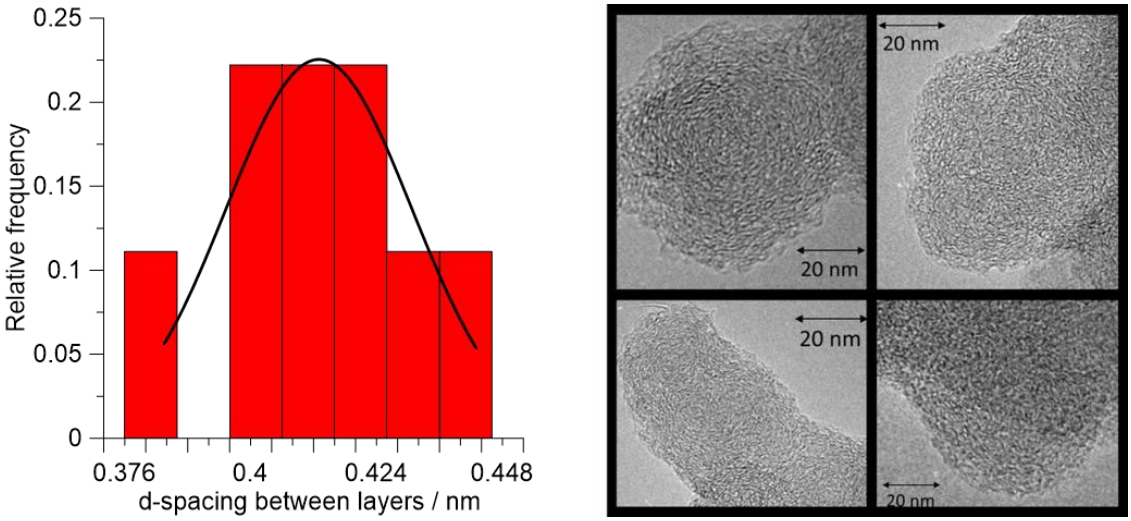

Figure 4.74 *TEM Analysis of benzene pyrolysis, T_5=1537 K, P_5 = 16.5 bar. Internal organization of the layers: d-spacing = 0.462 nm, σ = 0.003 nm.*

Figure 4.75 shows the structure of soot formed at 1714 K from benzene pyrolysis. At this temperature the soot particles exhibit a thick, well-organized outer structure with long, parallel planes with different thicknesses. The average d-spacing is 0.402±0.005 nm, once again this value is slightly smaller than the neat toluene intermediate temperature. Several primary nuclei can be spotted inside the particles.

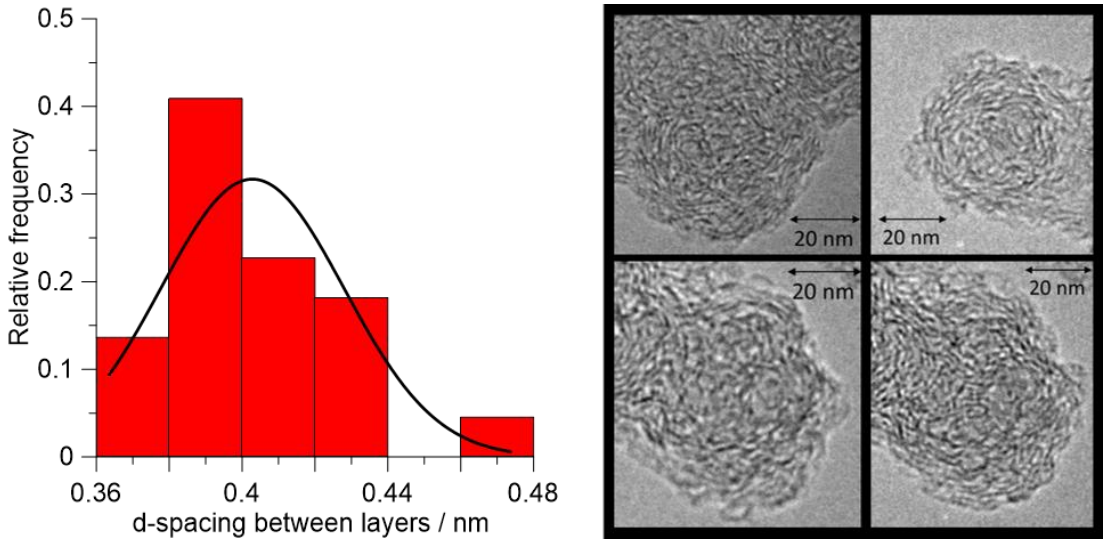

Figure 4.75 *TEM Analysis of benzene pyrolysis, T_5=1714 K, P_5 = 17.9 bar. Internal organization of the layers: d-spacing = 0.402 nm, σ = 0.005 nm.*

Figure 4.76 illustrates the structure of soot formed at 1920 K of benzene pyrolysis. At this temperature the soot particles exhibit even thicker, well-organized outer structure with long, parallel planes. The core of the particle consists of several nuclei and the average d-spacing is 0.374±0.005 nm, similar to neat toluene at high temperature.

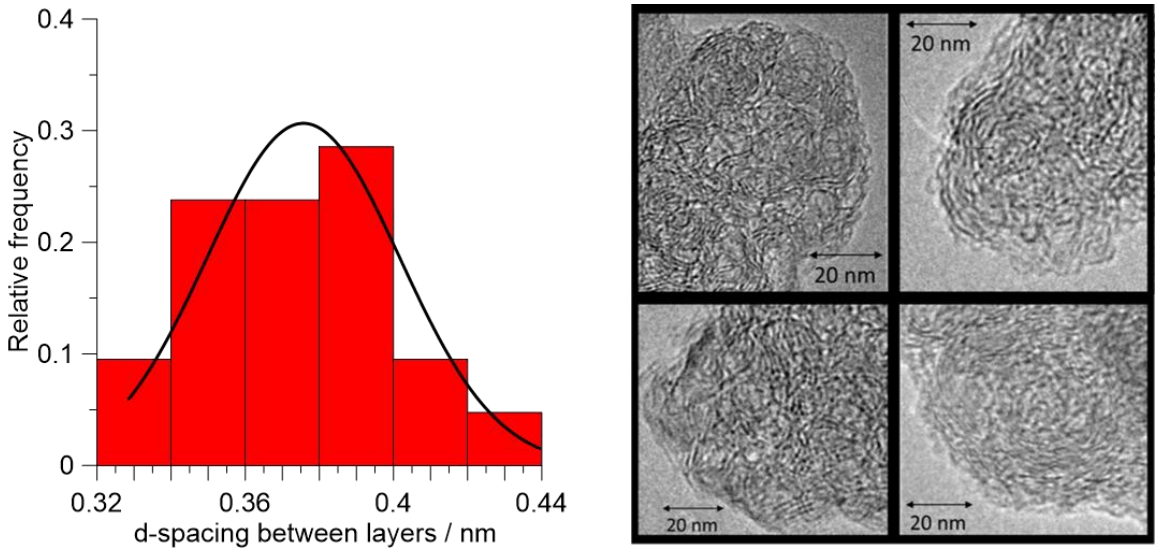

Figure 4.76 *TEM Analysis of benzene pyrolysis, T_5=1920 K, P_5 = 17.4 bar. Internal organization of the layers: d-spacing = 0.374 nm, σ = 0.005 nm*

The last set of fuel analyzed was cyclopentene. **Figure 4.77** shows the structure of soot formed at 1551 K of cyclopentene pyrolysis. It is possible to see the difference between the layers of the core of the particles which are shorter that the layers of the external part of the soot. These external layers are longer when compared to toluene and benzene low-temperature cases. The average d-spacing is 0.404±0.004 nm, similar to the neat toluene and benzene cases.

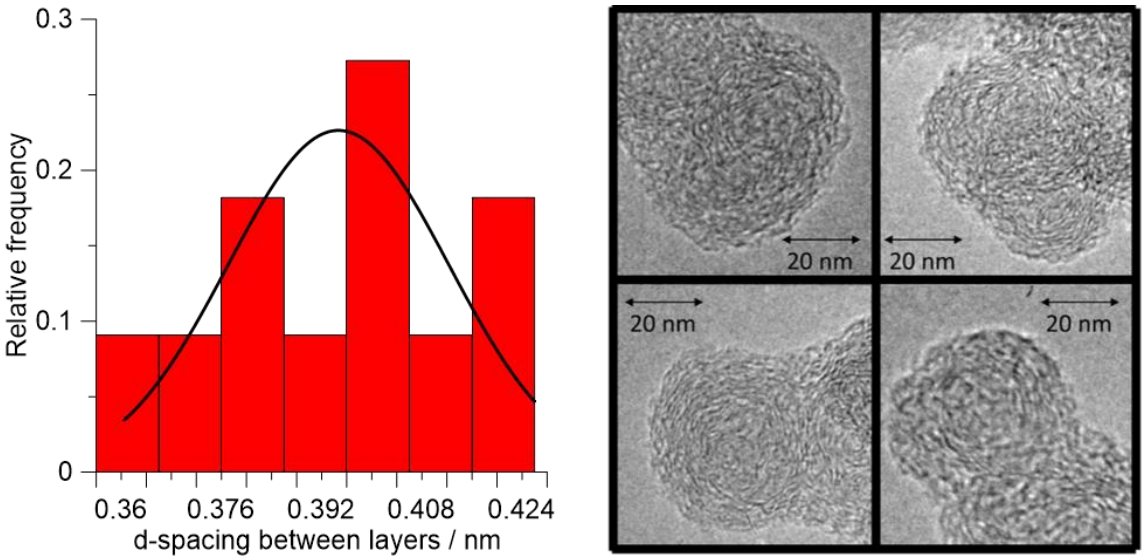

Figure 4.77 TEM Analysis of cyclopentene pyrolysis, T_5=1551 K, P_5 = 16.6 bar. Internal organization of the layers: d-spacing = 0.404 nm, σ = 0.004 nm.

The intermediate temperature is displayed in **Figure 4.78**, at 1739 K. At this temperature the soot particles exhibit a thick, well-organized outer structure with long, parallel planes with different thicknesses, similar to toluene and benzene cases at the intermediate temperature. It is also possible to observe multiple nuclei in these particles. The average d-spacing is 0.393±0.006 nm, very similar to the toluene pyrolysis at similar conditions.

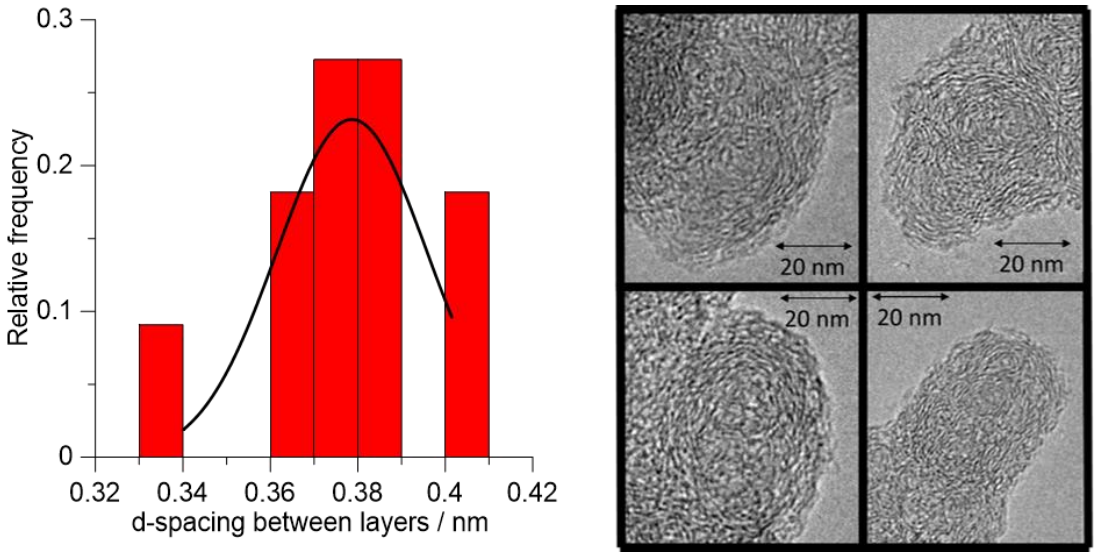

Figure 4.78 TEM Analysis of cyclopentene pyrolysis, T_5=1739 K, P_5 = 18.1 bar. Internal organization of the layers: d-spacing = 0.393 nm, σ = 0.006 nm.

Figure 4.79 shows the structure of soot formed at 1968 K from cyclopentene pyrolysis. The core of the particle consists of several nuclei and the average d-spacing is 0.381±0.007 nm (close to toluene and

benzene). The carbon planes seem to be shorter that the intermediate temperature, which differs from the behavior of the previous fuels studied.

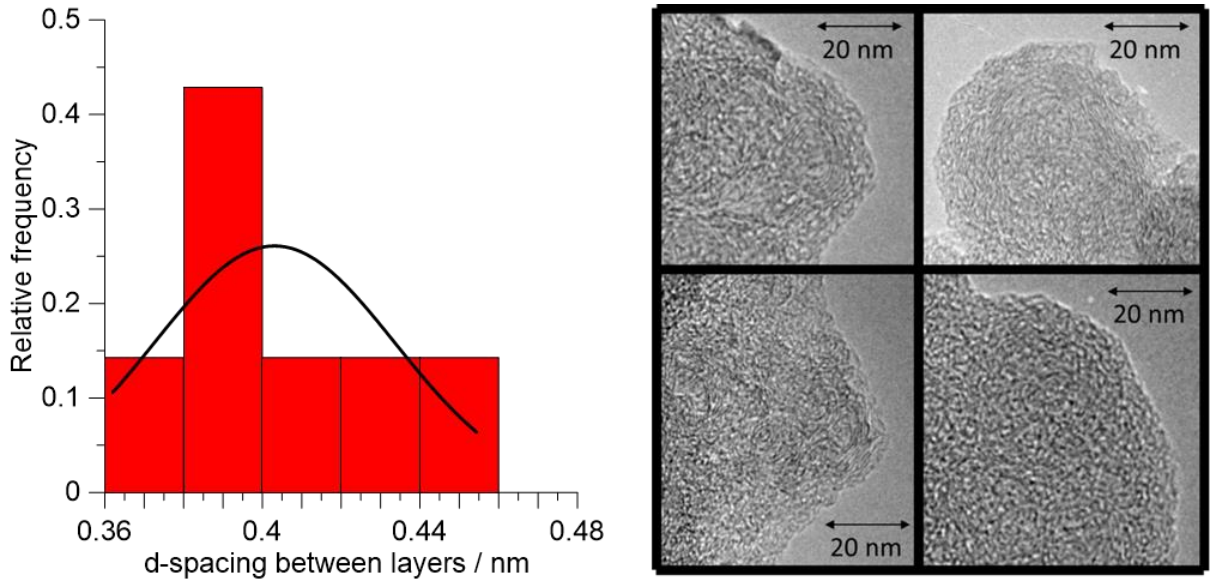

Figure 4.79 *TEM Analysis of cyclopentene pyrolysis, T_5=1968 K, P_5 = 17.8 bar. Internal organization of the layers: d-spacing = 0.381 nm, σ = 0.007 nm.*

The last image to be analyzed is **Figure 4.80**, which shows the structure of soot formed at 1732 K from C_5H_8+C_2H_2 pyrolysis. The soot has short, unorganized carbon layers in the inner and outer areas of the particle. Besides, its thickness seems to remain similar all over the particle. The average d-spacing is 0.390±0.006 nm, similar to the case of neat cyclopentene at this temperature, which mean that the addition of acetylene has minor influence on the internal organization of the layers.

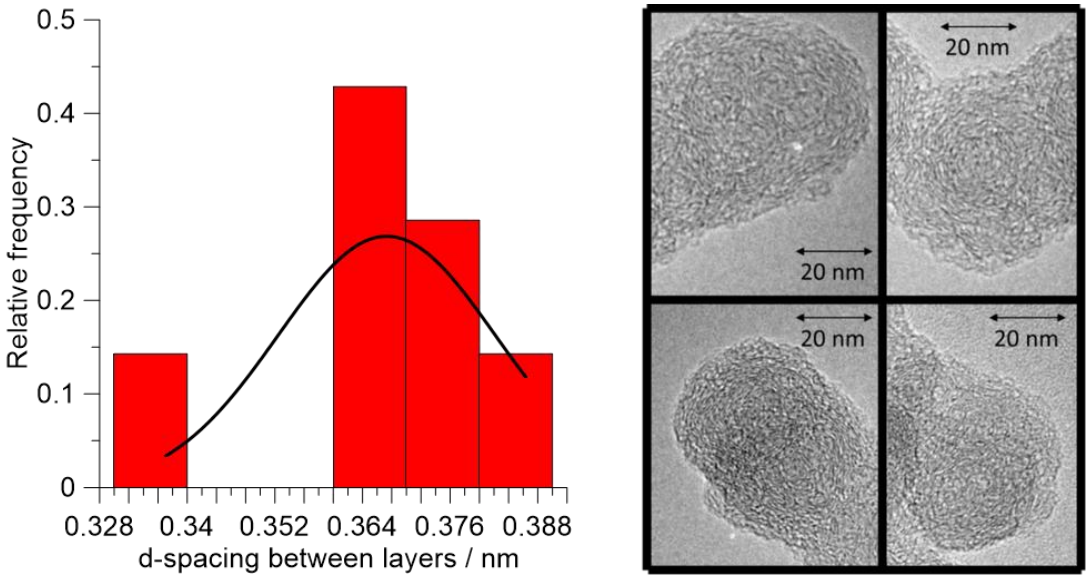

Figure 4.80 *TEM Analysis of C_5H_8+C_2H_2 pyrolysis, T_5=1732 K, P_5 = 17.0 bar. Internal organization of the layers: d-spacing = 0.390 nm, σ = 0.006 nm.*

In summary, the micro-structure and micro-texture of the soot particles were observed in TEM at a magnification of 2.0 x 10^5. From these observations, it is visible that these two factors are strongly influenced by the particle formation temperature. Generally, the organization of the carbonaceous planes (length and parallelism of the planes) on the external crown of the particle increases with temperature. For the intermediate and high temperatures, the core of the particle is constituted of nuclei which seem to be derived from the coalescence of the primary particle nuclei. These observations support the theory postulated for the determination of the growth rate constants according to which the growth of the particles at the beginning is influenced by coagulation and surface growth, while at later stages the surface reactions are predominant.

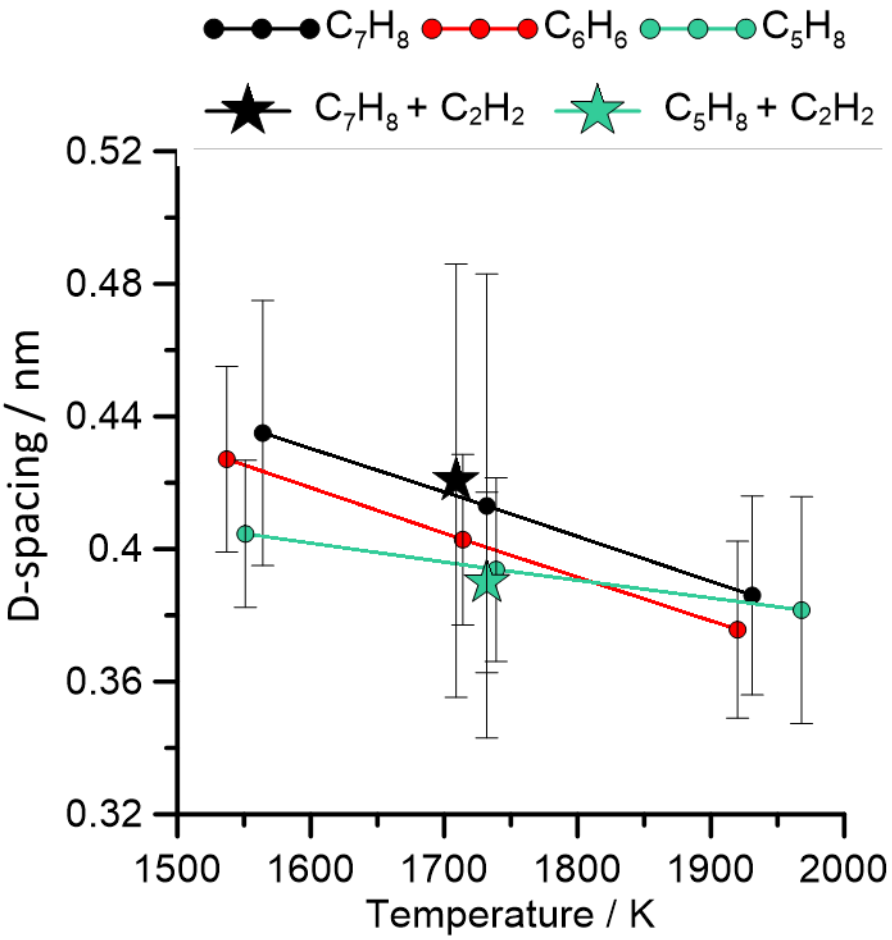

Figure 4.81 *Interspace layers versus the temperature*

The hydrocarbon soot particles presented show a multiscale organization. The micro-texture of these primary particles was constituted of a concentric arrangement of basic structural units (BSU) leading to an onion-like micro-texture [228]. These BSU, made of stacks of 2–3 nanometric polyaromatic layers, are characterized by their lateral extension, and their mean interlayer spacing [227]. The data presented leads to interesting conclusions. Concerning the cyclic fuels, the space between the layers does not vary more than 10 % from one fuel to another (see **Figure 4.81**). The conditions under which the soot was formed are given in **Table 4**, along with the mean particle diameter and interlayer spacing with related uncertainties.

Table 4 *Experimental conditions of TEM Analysis*

Mixture	Run	T_5 (K)	P_5 (bar)	Diameter of the primary particles		Internal organization of the layers	
				$\bar{d}$ (nm)	σ (nm)	d-spacing (nm)	σ (nm)
0.1% C_7H_8	T853	1564	16.8	27.6	0.1	0.435	0.004
	T852	1732	18.0	15.6	0.3	0.413	0.007
	T854	1931	17.5	14.8	0.1	0.386	0.003
0.03% C_7H_8 + 0.15% C_2H_2	T1001	1709	17.7	17.6	1.3	0.420	0.013
0.03% C_7H_8 + 0.15% C_2H_4	T1101	1738	17.3	16.1	0.8	-	-
0.082% C_6H_6	T896	1537	16.5	25.4	0.2	0.462	0.003
	T895	1714	17.9	15.5	0.4	0.402	0.005
	T897	1920	17.4	15.1	0.3	0.374	0.005
0.03% C_6H_6 + 0.15% C_2H_2	T1013	1723	18.5	21.5	0.8	-	-
0.098% C_5H_8	T940	1551	16.6	22.3	0.6	0.404	0.004
	T951	1739	18.1	18.4	0.1	0.393	0.006
	T939	1968	17.8	18.3	0.8	0.381	0.007
0.05% C_5H_8 + 0.23% C_2H_2	T1026	1732	17.0	18.4	0.4	0.390	0.006
0.245% C_2H_2	T998	1989	17.4	23.5	0.2	-	-
0.35% C_2H_2	T973	1741	17.6	25.2	0.3	-	-

5 Conclusions

This work was devoted to study soot formation at typical conditions encountered in modern combustion devices. Soot is a toxic compound, and its toxicity is partially attributed to the presence of PAHs condensed and adsorbed on the surface of the particles. PAHs are also the building blocks for the appearance of the nascent nanoparticles. The denomination PAH encompasses different types of chemical compounds, that have different properties, depending on their chemical structure and number of rings, as function of the fuel and the thermodynamic conditions. Particularly with regards to the morphology of soot and the chemical composition of the adsorbed phase, but also to the fundamental principles of soot formation chemistry, predictions from comprehensive kinetic models are still unsatisfactory. Adequate models are required to comprehend the intricate soot production processes. These models should be tested in well controlled environments against measurements of PAH precursors from fuel molecules and mixtures and particle concentrations, particle size distributions, soot volume fractions, and other parameters which characterize the solid-phase chemistry.

One of the objectives of this thesis is to provide an experimental database on the chemistry of PAH formation from the pyrolysis of important fuel components at high-pressure and high-temperature conditions. In the first part of the work, pyrolysis experiments of n-heptane (from 100 to 2000 ppm in argon bath gas) and cyclopentene with and without the addition of acetylene (100 and 300 ppm cyclopentene and 100 ppm cyclopentene + 500 ppm acetylene in argon bath gas) were carried out using a single-pulse shock tube over a temperature range of 940-1680 K for a nominal pressure of 20 bar and a reaction time of around 4 ms. Chemical compositions of the post shock mixtures were analyzed using the GC/MS techniques. Species mole fraction profiles as a function of T_5 were obtained, the base for the extension of a comprehensive chemical kinetic model for PAH chemistry. n-Heptane dissociates into hydrocarbon products, mainly C2, C3 and C4, at high temperatures. These compounds then react to form larger multi-ring species (PAHs). In general, the model can capture the decomposition and formation temperature windows of the reported pyrolysis species and match their mole fraction profiles while accounting for experimental uncertainties. Analytical modeling techniques such as rate of production (ROP) analyses and sensitivity analyses were used to obtain an understanding of the chemistry of n-heptane fragmentation and aromatics growth. n-Heptane is primarily consumed by the C-C bond scission reaction, which produces n-propyl and 1-butyl radicals, and by hydrogen abstraction reactions, which produce 1-, 2-, 3-, and 4-heptyl radicals. Other C-C bond fission reactions that produce methyl and 1-hexyl radicals, as well as ethyl and 1-pentyl radicals, contribute only slightly to the thermal decomposition of n-heptane. The experimental and simulated mole fraction profiles of several common mono-aromatic hydrocarbons (MAHs) and bicyclic

and tricyclic PAHs were also shown and analyzed. Through the ROP studies, the major pathways of aromatics production were presented and discussed. MAHs species detected include benzene, toluene, phenylacetylene, styrene and ethylbenzene. Concerning the soot precursor PAH molecules, the central tole of indene and the indenyl radical was highlighted for the formation of numerous species including naphthalene, acenaphthylene and fluorene. The naphthyl radical also contributes to the formation of large PAHs products such as 1-methyl naphthalene and 1-ethynyl naphthalene, while the benzyl radical self-recombination is the major reaction contributing to the three-ring structures.

The second fuel studied in the single pulse shock tube was cyclopentene with and without the addition of acetylene. The interest in cyclopentene stems from its role as a precursor to C5 intermediates, including cyclopentadiene, whose chemistry has a significant impact on PAH and soot production. The decomposition reactivity of CYC_5H_8 was studied along with the speciation of small intermediates, followed by the production of aromatic species, from the simplest benzene to the largest PAHs. The model developed accurately describes the fuel reactivity and the formation of the main product with respect to temperature windows and peak concentrations. According to the ROP analysis, CYC_5H_8 is mainly consumed by the dehydrogenation and ring-opening isomerization processes, which result in the generation of C_5H_6 and LC_5H_8, respectively. Smaller hydrocarbons are formed by other reactions of small fragmentation products, consumption of C5 intermediates, or direct interactions of the fuel with hydrogen atoms. The reaction of C_5H_5 with small species leads to the formation of several MAHs including benzene, toluene, phenylacetylene, and styrene, while the C5+C5 mechanisms were validated for the formation of different PAH such as indene and naphthalene. Further growth to acenaphthylene and phenanthrene is the result of the indenyl radical reacting with C_3H_3 and C_5H_5, respectively. Once acetylene is added to cyclopentene, the production pathways for the small hydrocarbons did not significantly change compared to those of pure CYC_5H_8, both qualitatively and quantitatively, though the addition of C_2H_2 to CYC_5H_8 amplifies the concentrations of $C_6H_5C_2H$ and 1-ethynylnaphthalene while reducing the naphthalene concentration.

Another aim of this thesis was to develop, implement and characterize the laser-based technique to study soot formation behind reflected shock waves (scattering + extinction). In order to accomplish this task, it was decided to use the heated shock tube present at ICARE. A new end-section was designed to allow multiple optical fibers to be connected to the shock tube for delivery and collection of two laser beams. The preliminary measurements showed large vibrations in the signals. Several solutions were implemented to improve the method, which resulted in the construction of a rigid frame for blocking the shock tube, and the use of classical optical systems without optical fibers. The extinction technique was completely developed and characterized.

The new technique was then used to measure the time-dependent behavior of the soot volume fraction from numerous fuels and fuel mixtures, including benzene, toluene, cyclopentene, acetylene, ethylene, propylene, propyne, and the mixtures between the cyclic compounds and the C2/C3 intermediates, at temperatures between 1500 and 2000 K, pressures between 16 and 20 bar, and similar carbon concentrations. The first parameter that was examined was the optical density. It was shown that the maximum absolute value of D_{633nm} is reached for the intermediate temperature, hence, it can be inferred that the soot yield has a bell-shaped temperature dependence behavior, which is characteristic of the soot formation process. Similar optical densities were obtained for benzene and toluene, pyrolysis. The third pure fuel analyzed was cyclopentene and the general behavior of this fuel does not differ much from the two aromatic fuels, however, the absolute value of the optical density decreased to around half. The addition of C2 and C3 fuels to toluene, benzene, or cyclopentene lead to a significant decrease in the absolute value the optical densities. Acetylene, propyne and propylene were also studied as single fuels at similar concentrations. The single fuels can be classified as it follows concerning the propensity to form soot particles: toluene = benzene > propyne > cyclopentene > propylene > acetylene. In order to be able to study ethylene, experiments at higher initial fuel concentrations were performed.

Another parameter derived from the extinction measurements was the induction delay time. This is one of the most important parameters to characterize the tendency of a hydrocarbon to form soot, as it is the time necessary for the first soot particles to appear. The induction times as a function of the inverse of the temperature of toluene, toluene + C2 and toluene + C3 were analyzed. The fitted curve of neat toluene was split into two parts, fitting the data in the high-temperature and low-temperature ranges. Their pre-exponential factors and their activation energies differ, suggesting the existence of two mechanisms, probably associated with the aromatic-aromatic reactions at lower T or with aromatic-aliphatic reactions at high T. The addition of C_2H_2 and C_2H_4 increases the induction delay times, especially C_2H_4, and it changes the behavior compared to neat C_7H_8 as the data can be fit with a single curve. The binary mixture of toluene and propyne or propylene shows similar behavior to neat C_7H_8, i.e., the data needs to be described with two curves, although the difference in the activation energies is less significant than for the neat toluene. Again, an increase in the induction times was observed for the mixtures. In the case of benzene, the fitted curve of the neat fuel is divided into two parts, similarly to toluene, but with a less marked difference in the activation energies. The addition of acetylene and ethylene increases the induction times, but it modifies the behavior as only a single curve could be used to fit the data. For cyclopentene, the addition of C_2H_2 had a small impact on the induction delays with a slight increment observed. Considering the C2 and C3 fuels, the order for the tendency to form particles follows a similar trend than the optical densities: toluene > benzene > propyne > cyclopentene > propylene > acetylene. Among the non-cyclic fuels, only propyne shows a

double-stage behavior as the aromatic fuels, possibly due to the formation of large amounts of benzene from the C3+C3 reactions.

After the induction period, the soot volume fraction grows quickly by surface reactions and coagulations. With the assumption that beyond the inflection point of the curve the growth of the volume fraction occurs mainly by surface reactions with the gas phase molecules, the soot growth rate was derived considering a first-order Arrhenius law. The results showed that the addition of C_2H_2 and C_2H_4 to benzene and toluene have the same consequences on the soot growth rates, with a similar decrement in the absolute value. The same for the addition of propyne and propylene to toluene. The comparison between the different single fuels leads to the following ranking in the propensity to form particles toluene > benzene > cyclopentene > propyne > propylene > acetylene. Thus, in this case, cyclopentene has a faster growth rate than propyne. Among the different fuels and mixtures, only the curves for toluene, benzene, and propyne were described by two different fitting curves. The activation energy of the high-temperature regions for such fuels, and the activation energies of the remaining fuels show similar values.

Lastly, the study of soot particles by transmission electron microscopy (TEM) was performed at two magnifications: $2.75x10^4$ (soot texture: morphology, primary particle size) and $2x10^5$ (microstructure: length of carbon planes, distance between these planes). For pure fuels (toluene, benzene and cyclopentene), three temperatures were analyzed: minimum, intermediate (at the maximum optical densities) and maximum. Once C_2H_2 or C_2H_4 was added, only the intermediate temperature was analyzed. The particles are composed of chains of primary spheres and the average diameter of the spheres strongly varies with the temperature. On the other hand, the three cyclic fuels have similar values. For toluene and benzene, the addition of acetylene and ethylene lead to an increase of the particle size, while no significant variation could be obtained when acetylene was added to cyclopentene. The analyses on acetylene pyrolysis showed very large primary particles compared to the other fuels. Concerning the internal organization of the carbon planes, in general, its length and parallelism on the external crown of the particle increases with temperature. For intermediate and high temperatures, the core of the particle is made of different nuclei that seem to come from the coalescence process.

As a perspective work, the Rayleigh scattering measurements will be implemented in the heated shock tube for complementing the extinction and TEM data. This would allow to derive the mean diameter of the particles as a function of time. Another objective to pursue is to do the TEM analysis for other fuels tested, in order to have a more mapping of the influence of the fuel composition on the soot structure. The work of course could be extended to other fuels of interest, including important aromatic intermediates, aliphatics, and naphthenes, as well as real fuels including the new generation biofuels. In addition, with the intention of obtaining a complete understanding of the soot formation, it would be useful for the scientific community

to investigate the soot formation in oxidation conditions. Lastly, the development of a soot code for simulation of the particle formation in pyrolytic conditions is an ongoing effort as part of a different thesis work at ICARE.

Appendix

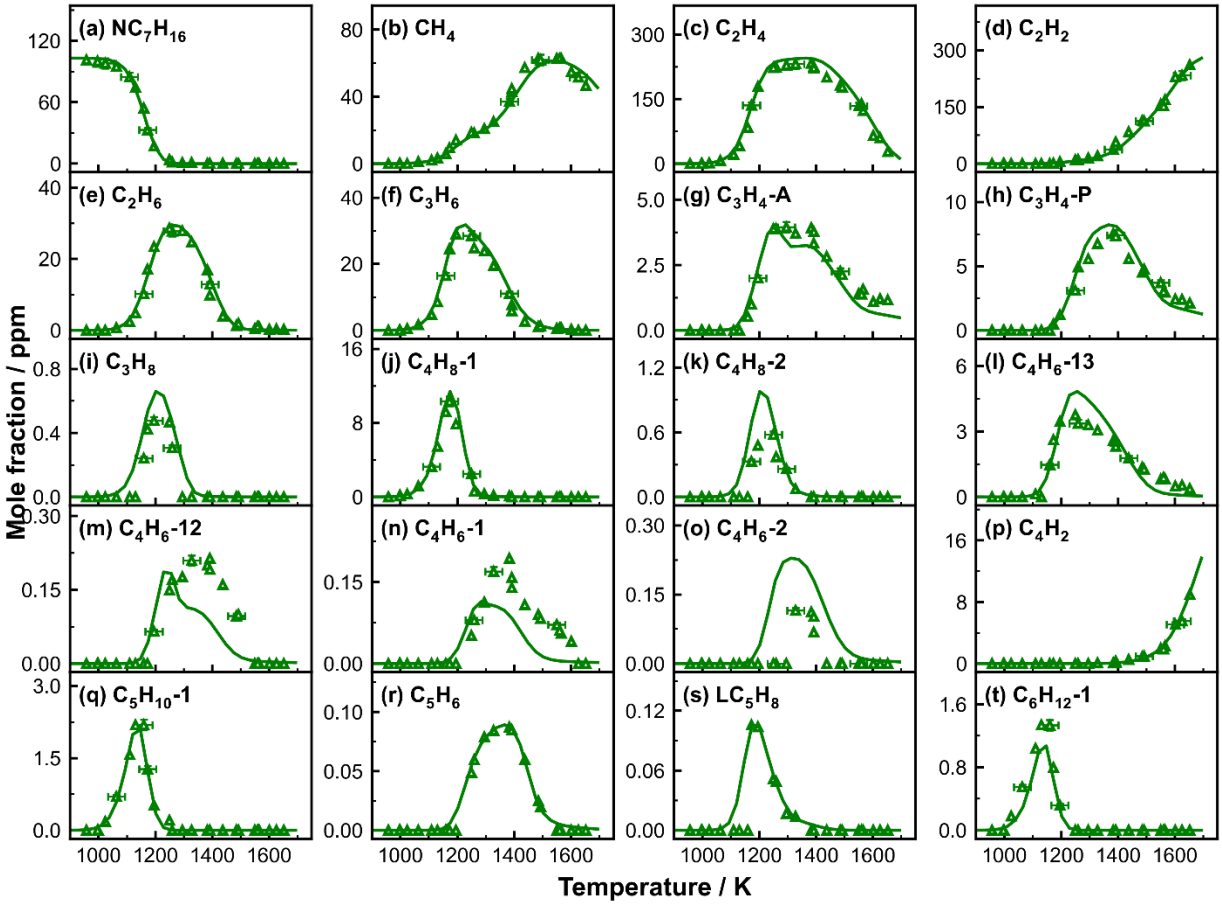

Figure A. 1 *Measured (symbols) and simulated (lines) mole fraction profiles of fuel and small intermediates as a function of post-shock temperature T5 in heptane pyrolysis, 103 ppm*

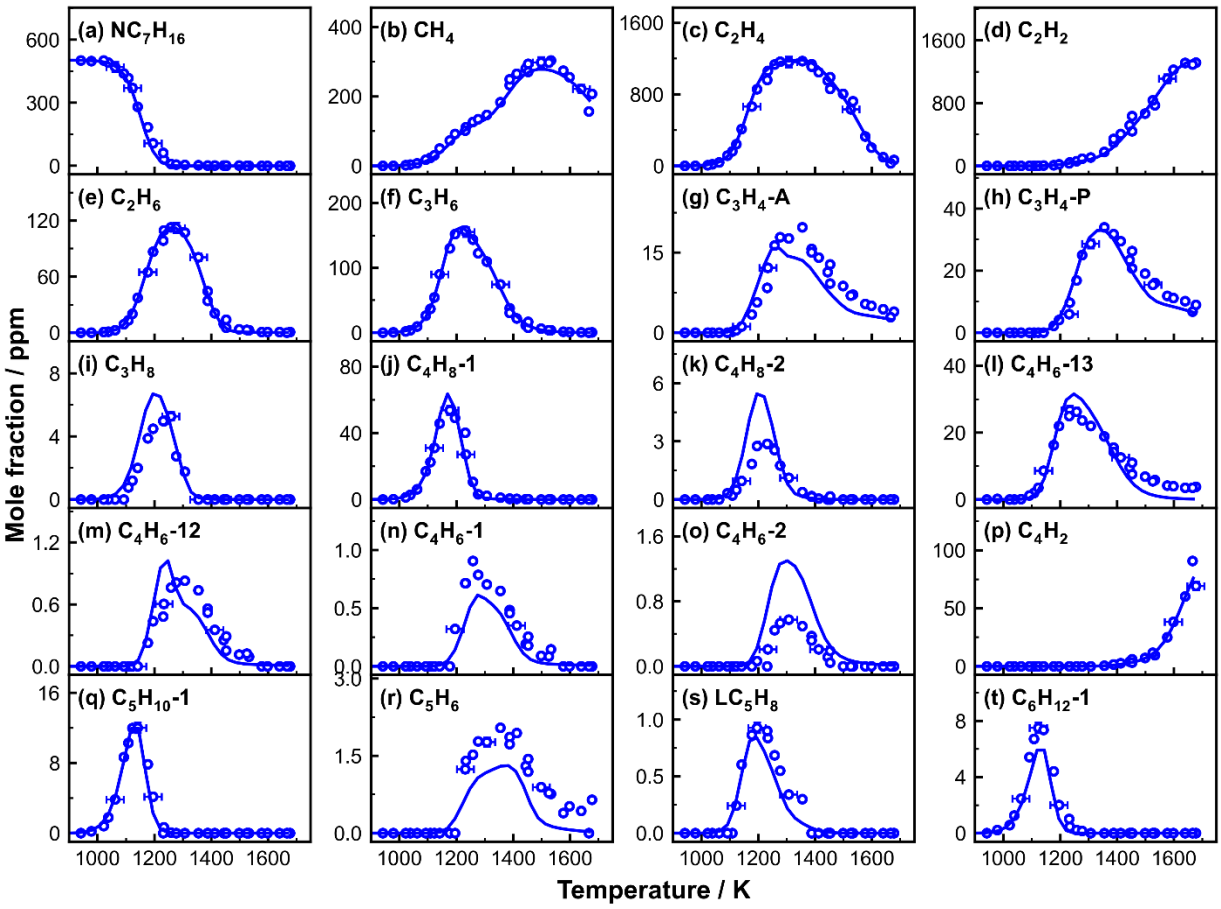

Figure A. 2 *Measured (symbols) and simulated (lines) mole fraction profiles of fuel and small intermediates as a function of post-shock temperature T5 in heptane pyrolysis, 502 ppm*

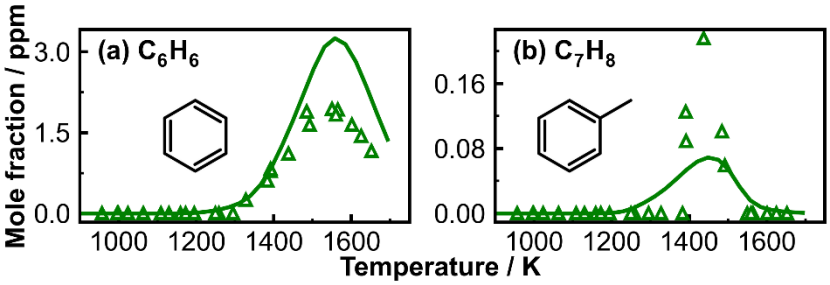

Figure A. 3 *Measured (symbols) and simulated (lines) mole fraction profiles of MAHs and PAHs as a function of post-shock temperature T5 in heptane pyrolysis, 103 ppm*

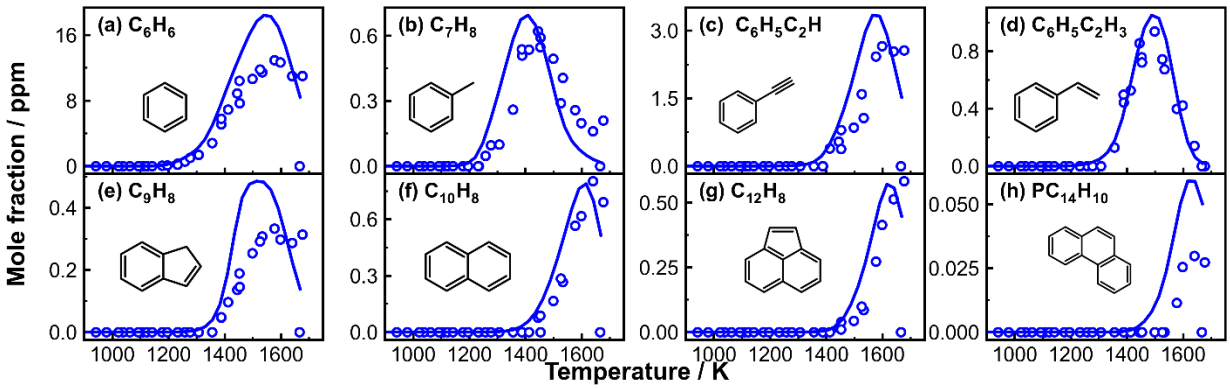

Figure A. 4 *Measured (symbols) and simulated (lines) mole fraction profiles of MAHs and PAHs as a function of post-shock temperature T5 in heptane pyrolysis, 502 ppm*

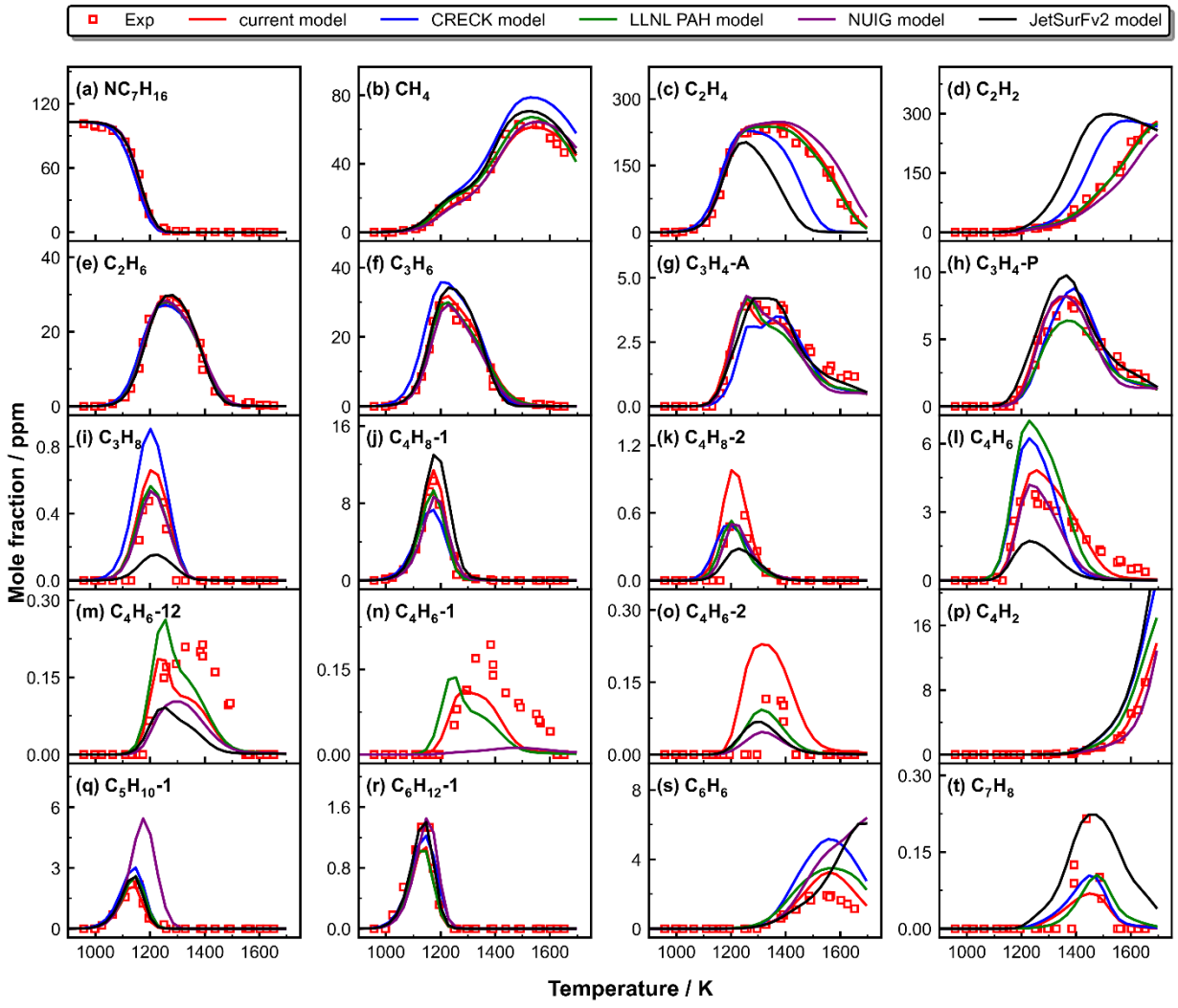

Figure A. 5 *Measured (symbols) and simulated (lines) mole fraction profiles of the fuel and the decomposition products as a function of T5 in 103 ppm heptane pyrolysis. Solid red lines: simulations using the current kinetic model with the constant* P_5 *of*

20 bar and the nominal reaction time of 4 ms; solid blue lines: simulations using the CRECK model [284] with the constant P_5 of 20 bar and the nominal reaction time of 4 ms; solid green lines: simulations using the LLNL PAH model [285] with the constant P_5 of 20 bar and the nominal reaction time of 4 ms; solid purple lines: simulations using the NUIG model [286] with the constant P_5 of 20 bar and the nominal reaction time of 4 ms; solid black lines: simulations using the JetSurFv2 model [179] with the constant P_5 of 20 bar and the nominal reaction time of 4 ms

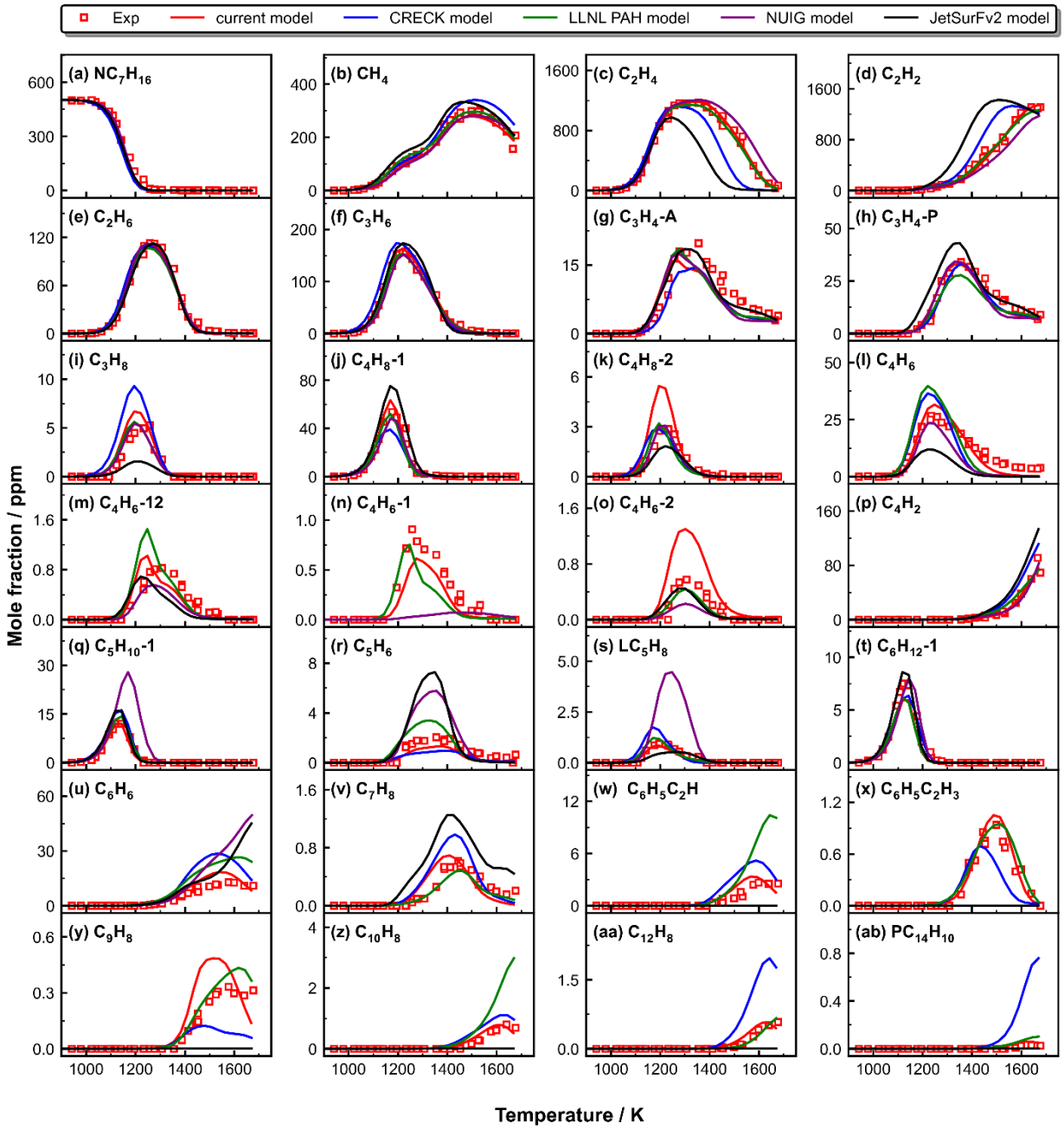

Figure A. 6 *Measured (symbols) and simulated (lines) mole fraction profiles of the fuel and the decomposition products as a function of T5 in 502 ppm heptane pyrolysis. Solid red lines: simulations using the current kinetic model with the constant P_5 of 20 bar and the nominal reaction time of 4 ms; solid blue lines: simulations using the CRECK model [284] with the constant P_5 of 20 bar and the nominal reaction time of 4 ms; solid green lines: simulations using the LLNL PAH model [285] with the constant P_5 of 20 bar and the nominal reaction time of 4 ms; solid purple lines: simulations using the NUIG model [286] with the constant*

P_5 of 20 bar and the nominal reaction time of 4 ms; solid black lines: simulations using the JetSurFv2 model [179] with the constant P_5 of 20 bar and the nominal reaction time of 4 ms

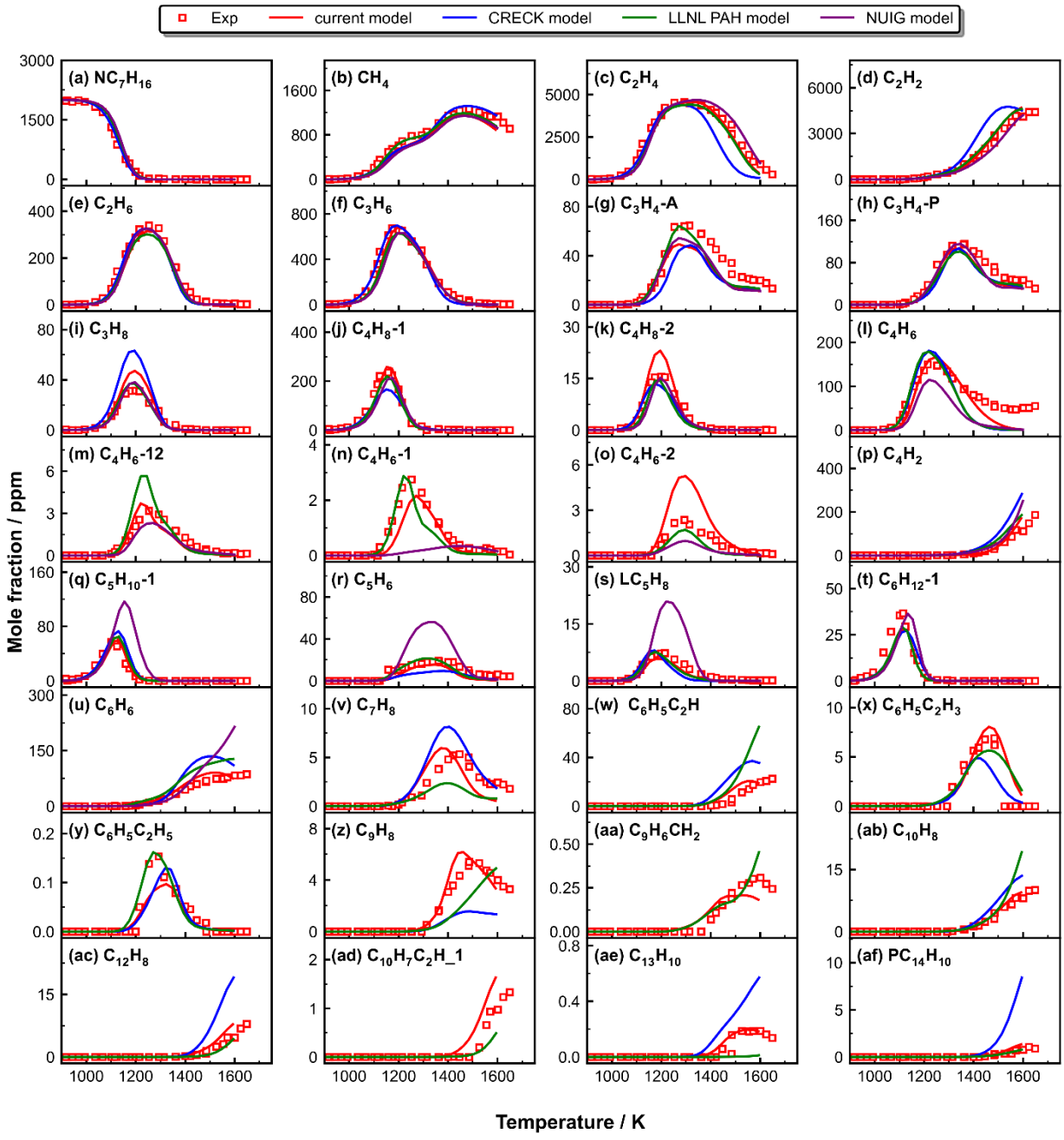

Figure A. 7 *Measured (symbols) and simulated (lines) mole fraction profiles of the fuel and the decomposition products as a function of T5 in 2000 ppm heptane pyrolysis. Solid red lines: simulations using the current kinetic model with the constant P_5 of 20 bar and the nominal reaction time of 4 ms; solid blue lines: simulations using the CRECK model [284] with the constant P_5 of 20 bar and the nominal reaction time of 4 ms; solid green lines: simulations using the LLNL PAH model [285] with the constant P_5 of 20 bar and the nominal reaction time of 4 ms; solid purple lines: simulations using the NUIG model [286] with the constant P_5 of 20 bar and the nominal reaction time of 4 ms; solid black lines: simulations using the JetSurFv2 model [179] with the constant P_5 of 20 bar and the nominal reaction time of 4 ms*

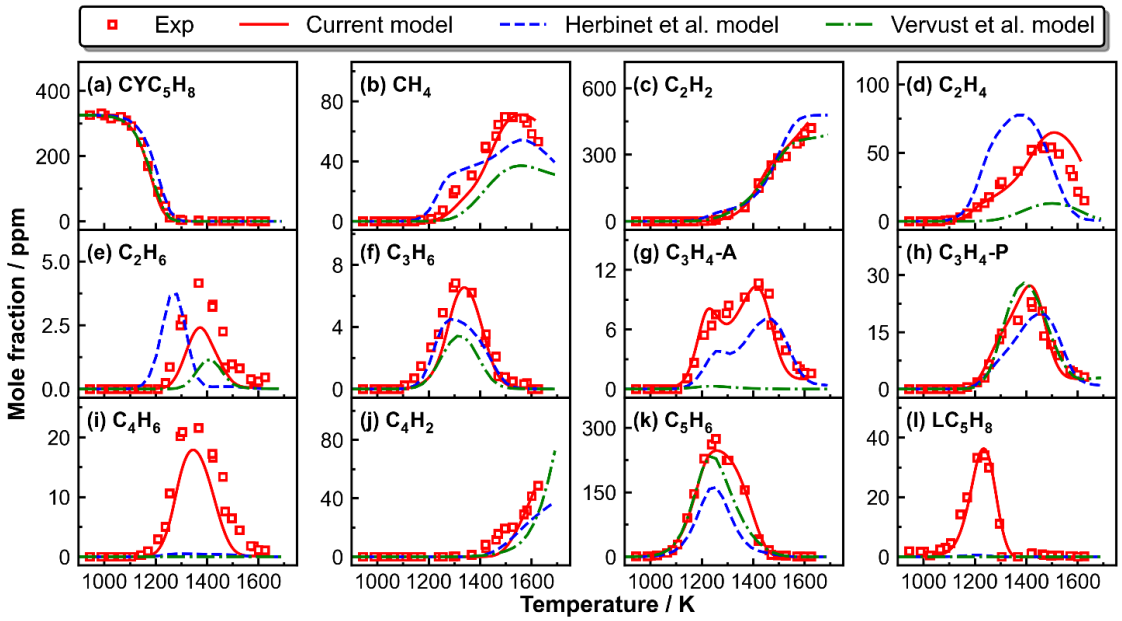

Figure A. 8 *Measured (symbols) and simulated (lines) mole fraction profiles of the fuel and the C0-C5 species as a function of T_5 in 326 ppm cyclopentene pyrolysis. Thick solid red lines: simulations using the current kinetic model; thin dashed blue lines: simulations using the Herbinet et al. [141] model; thin dot dashed green lines: simulations using the Vervust et al. [140] model*

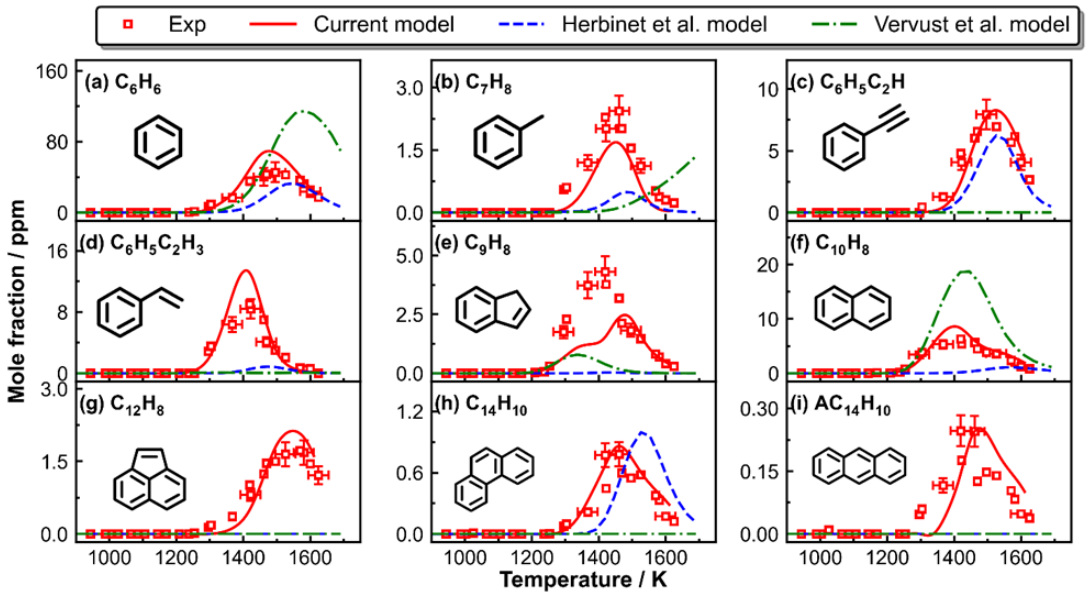

Figure A. 9 *Measured (symbols) and simulated (lines) mole fraction profiles of the aromatic species as a function of T_5 in 326 ppm cyclopentene pyrolysis. Thick solid red lines: simulations using the current kinetic model; thin dashed blue lines: simulations using using the Herbinet et al. [141] model; thin dot dashed green lines: simulations using the Vervust et al. [140] model*

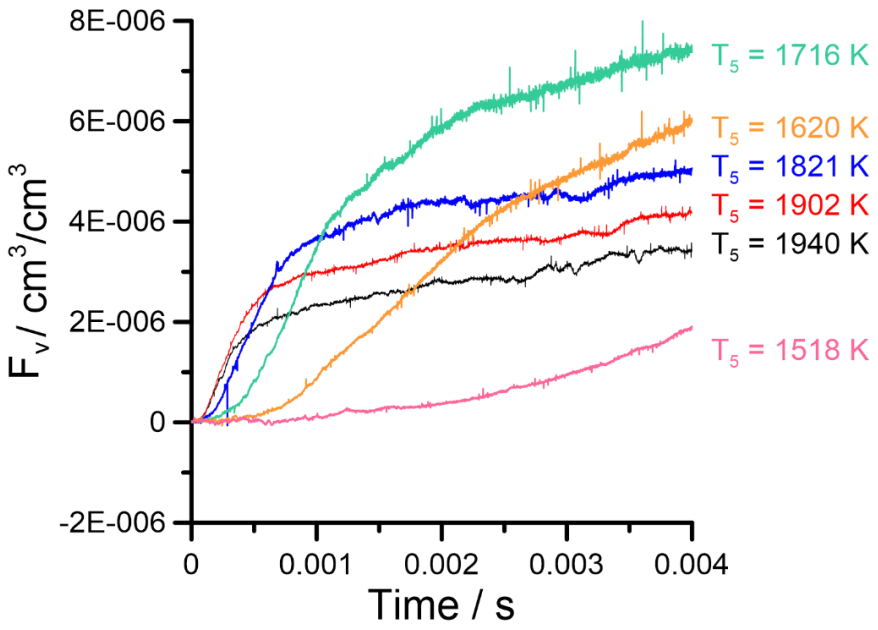

Figure A. 10 *Soot volume fraction versus time of 0.07% C_7H_8 in Argon for different temperatures*

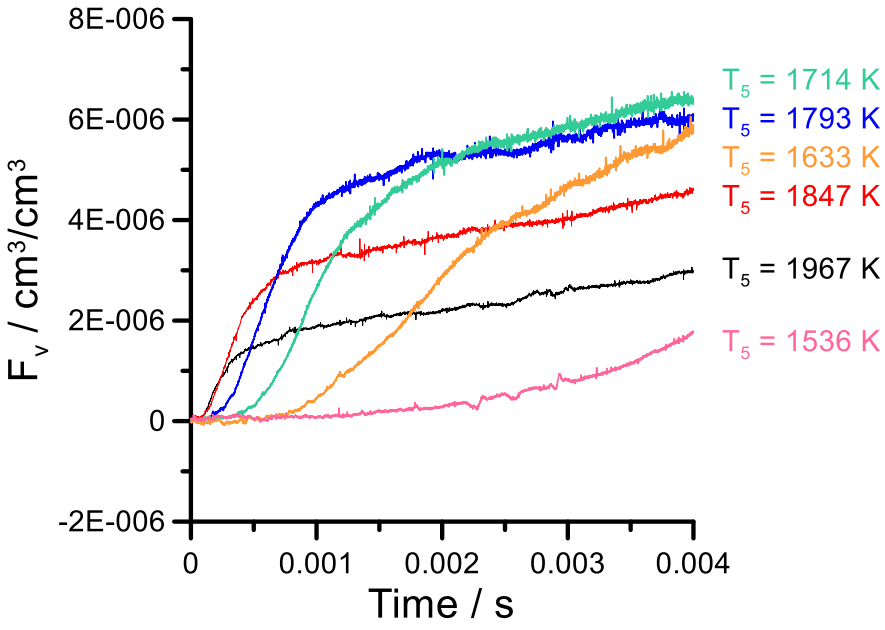

Figure A. 11 *Soot volume fraction versus time of 0.08% C_6H_6 in Argon for different temperatures*

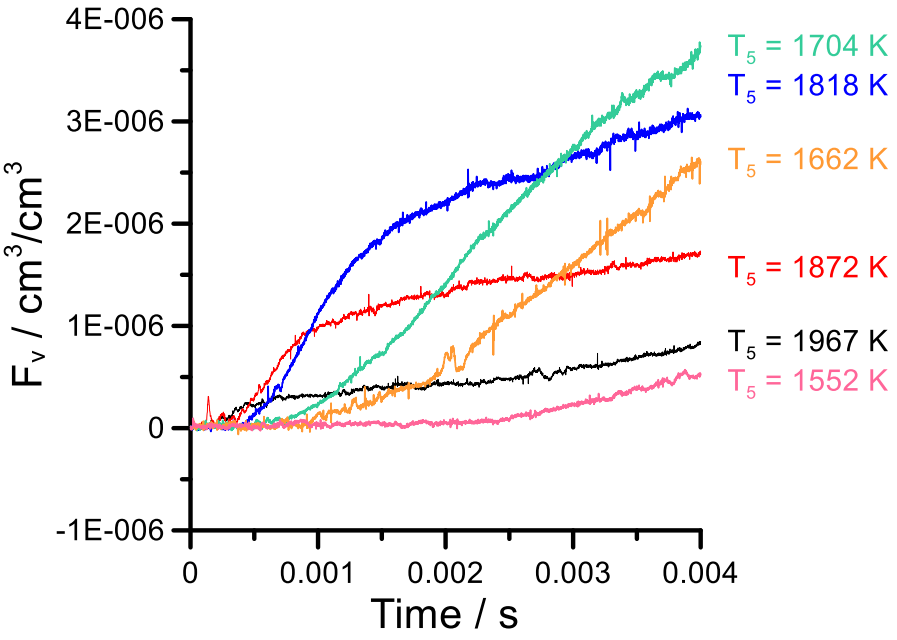

Figure A. 12 *Soot volume fraction versus time of 0.098% C_5H_8 in Argon for different temperatures*

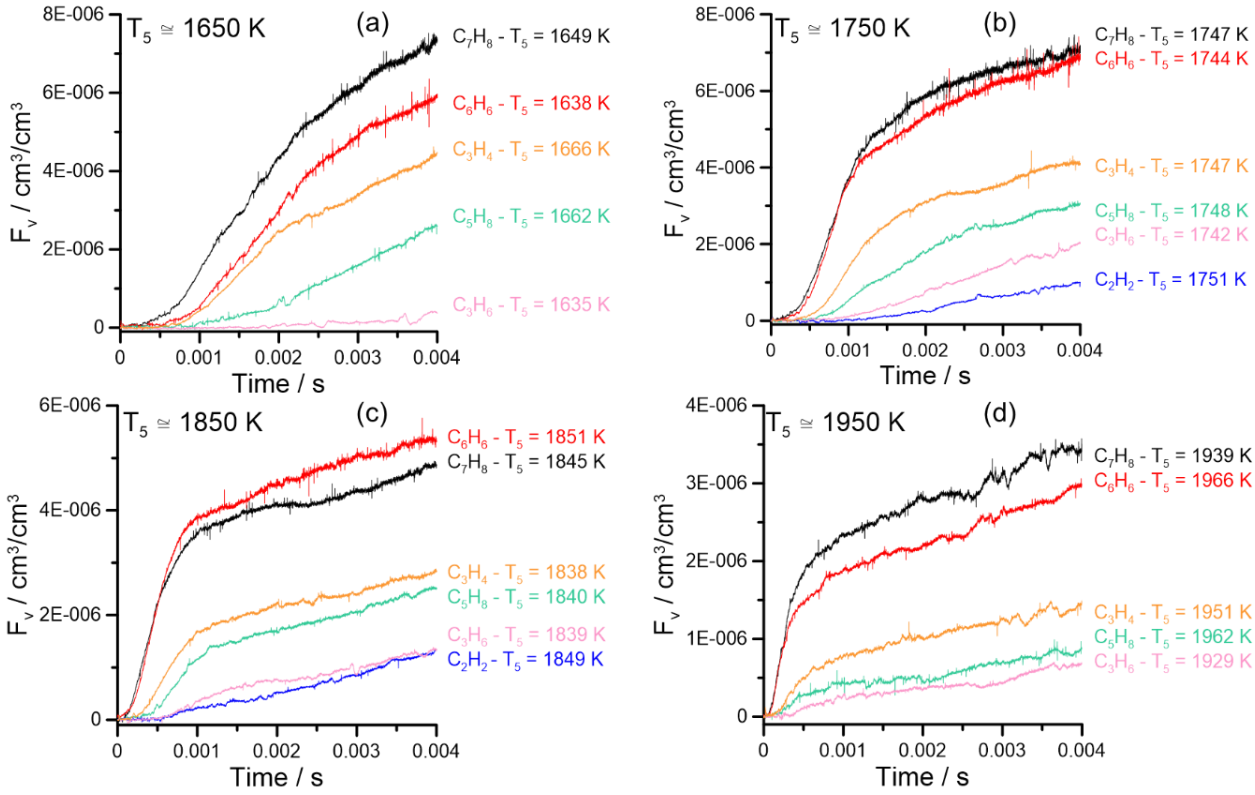

Figure A. 13 *Soot volume fraction versus time of different fuels at similar temperatures - in black: 0.07% C_7H_8 in Ar, in red: 0.08% C_6H_6 in Ar, in orange: 0.16% C_3H_4 in Ar, in green: 0.098% C_5H_8 in Ar, in pink: 0.16% C_3H_6 in Ar and in blue: 0.245% C_2H_2 in Ar.* ***(a)*** *$T_5 \approx 1630K$,* ***(b)*** *$T_5 \approx 1750K$,* ***(c)*** *$T_5 \approx 1850K$ and* ***(d)*** *$T_5 \approx 1950K$*

Bibliography

[1] U.S. Environmental Protection Agency, “What is Particulate Matter?” https://www3.epa.gov/region1/eco/uep/particulatematter.html (accessed Jul. 29, 2019).

[2] R. D. Brook *et al.*, “Particulate Matter Air Pollution and Cardiovascular Disease: An Update to the Scientific Statement From the American Heart Association,” *Circulation*, vol. 121, no. 21, pp. 2331–2378, Jun. 2010, doi: 10.1161/CIR.0b013e3181dbece1.

[3] G. P. Lewis and L. Coughlin, “Lung ‘soot’ accumulation in man,” *Atmospheric Environ. 1967*, vol. 7, no. 12, pp. 1249–1255, Dec. 1973, doi: 10.1016/0004-6981(73)90134-0.

[4] R. Niranjan and A. K. Thakur, “The Toxicological Mechanisms of Environmental Soot (Black Carbon) and Carbon Black: Focus on Oxidative Stress and Inflammatory Pathways,” *Front. Immunol.*, vol. 8, p. 763, Jun. 2017, doi: 10.3389/fimmu.2017.00763.

[5] U. Lohmann, F. Friebel, Z. A. Kanji, F. Mahrt, A. A. Mensah, and D. Neubauer, “Future warming exacerbated by aged-soot effect on cloud formation,” *Nat. Geosci.*, vol. 13, no. 10, pp. 674–680, Oct. 2020, doi: 10.1038/s41561-020-0631-0.

[6] M. Z. Jacobson, “Short-term effects of controlling fossil-fuel soot, biofuel soot and gases, and methane on climate, Arctic ice, and air pollution health,” *J. Geophys. Res.*, vol. 115, no. D14, p. D14209, Jul. 2010, doi: 10.1029/2009JD013795.

[7] D. G. Victor, D. Zaelke, and V. Ramanathan, “Soot and short-lived pollutants provide political opportunity,” *Nat. Clim. Change*, vol. 5, no. 9, pp. 796–798, Sep. 2015, doi: 10.1038/nclimate2703.

[8] H. Bockhorn, “Soot Formation in Combustion: Mechanisms and Models.”

[9] M. Frenklach, “Reaction mechanism of soot formation in flames,” *Phys. Chem. Chem. Phys.*, vol. 4, no. 11, pp. 2028–2037, May 2002, doi: 10.1039/b110045a.

[10] J. C. Fetzer, “THE CHEMISTRY AND ANALYSIS OF LARGE PAHs,” *Polycycl. Aromat. Compd.*, vol. 27, no. 2, pp. 143–162, Apr. 2007, doi: 10.1080/10406630701268255.

[11] U. KC, M. Beshir, and A. Farooq, “Simultaneous measurements of acetylene and soot during the pyrolysis of ethylene and benzene in a shock tube,” *Proc. Combust. Inst.*, vol. 36, no. 1, pp. 833–840, 2017, doi: https://doi.org/10.1016/j.proci.2016.08.087.

[12] S. McAllister, J.-Y. Chen, and A. C. Fernandez-Pello, *Fundamentals of combustion processes*. New York: Springer, 2011.

[13] Y. Bouvier,) É. T., and) P. D., *Caractérisation de suies et de précurseurs de suies dans des flammes par incandescence induite par laser*. 2006. [Online]. Available: https://books.google.fr/books?id=vudQOQAACAAJ

[14] T. Bourdrel, M.-A. Bind, Y. Béjot, O. Morel, and J.-F. Argacha, “Cardiovascular effects of air pollution,” *Arch. Cardiovasc. Dis.*, vol. 110, no. 11, pp. 634–642, 2017, doi: https://doi.org/10.1016/j.acvd.2017.05.003.

[15] H. A. Michelsen, C. Schulz, G. J. Smallwood, and S. Will, “Laser-induced incandescence: Particulate diagnostics for combustion, atmospheric, and industrial applications,” *Prog. Energy Combust. Sci.*, vol. 51, pp. 2–48, Dec. 2015, doi: 10.1016/j.pecs.2015.07.001.

[16] R. P. Bambha, M. A. Dansson, P. E. Schrader, and H. A. Michelsen, “Effects of volatile coatings and coating removal mechanisms on the morphology of graphitic soot,” *Carbon*, vol. 61, pp. 80–96, 2013, doi: https://doi.org/10.1016/j.carbon.2013.04.070.

[17] H. Richter and J. B. Howard, “Formation of polycyclic aromatic hydrocarbons and their growth to soot—a review of chemical reaction pathways,” *Prog. Energy Combust. Sci.*, vol. 26, no. 4, pp. 565–608, Aug. 2000, doi: 10.1016/S0360-1285(00)00009-5.

[18] S. ; P. De Iuliis Claude-Etienne; Coghe, Aldo, “Etude de la vitesse de formation des suies à partir de l’éthylène en présence d’hydrogène par les méthodes du tube à choc et du brûleur au moyen de

différentes techniques optiques," 2009. [Online]. Available: http://www.theses.fr/2009ORLE2082/document
[19] A. Hamadi, "Experimental study on the formation of soot precursors by shock tube techniques," Université d'Orléans, 2021.
[20] H. A. Michelsen *et al.*, "A Review of Terminology Used to Describe Soot Formation and Evolution under Combustion and Pyrolytic Conditions," *ACS Nano*, vol. 14, no. 10, pp. 12470–12490, Oct. 2020, doi: 10.1021/acsnano.0c06226.
[21] M. Frenklach, D. W. Clary, W. C. Gardiner, and S. E. Stein, "Detailed kinetic modeling of soot formation in shock-tube pyrolysis of acetylene," *Symp. Int. Combust.*, vol. 20, no. 1, pp. 887–901, Jan. 1985, doi: 10.1016/S0082-0784(85)80578-6.
[22] M. Frenklach, "Systematic optimization of a detailed kinetic model using a methane ignition example," *Combust. Flame*, vol. 58, no. 1, pp. 69–72, Oct. 1984, doi: 10.1016/0010-2180(84)90079-8.
[23] M. Frenklach and H. Wang, "Detailed modeling of soot particle nucleation and growth," *Symp. Int. Combust.*, vol. 23, no. 1, pp. 1559–1566, Jan. 1991, doi: 10.1016/S0082-0784(06)80426-1.
[24] A. S. Gordon and J. R. McNesby, "Isomerization of Primary *n* -Alkyl Free Radicals," *J. Chem. Phys.*, vol. 31, no. 3, pp. 853–855, Sep. 1959, doi: 10.1063/1.1730483.
[25] W. Sun, A. Hamadi, S. Abid, N. Chaumeix, and A. Comandini, "An experimental and kinetic modeling study of phenylacetylene decomposition and the reactions with acetylene/ethylene under shock tube pyrolysis conditions," *Combust. Flame*, vol. 220, pp. 257–271, Oct. 2020, doi: 10.1016/j.combustflame.2020.06.044.
[26] A. Comandini, T. Malewicki, and K. Brezinsky, "Chemistry of Polycyclic Aromatic Hydrocarbons Formation from Phenyl Radical Pyrolysis and Reaction of Phenyl and Acetylene," *J. Phys. Chem. A*, vol. 116, no. 10, pp. 2409–2434, Mar. 2012, doi: 10.1021/jp207461a.
[27] R. B. Cundall, D. E. Fussey, A. J. Harrison, and D. Lampard, "Shock tube studies of the high temperature pyrolysis of acetylene and ethylene," *J. Chem. Soc. Faraday Trans. 1 Phys. Chem. Condens. Phases*, vol. 74, no. 0, p. 1403, 1978, doi: 10.1039/f19787401403.
[28] R. B. Cundall, D. E. Fussey, A. J. Harrison, and D. Lampard, "High temperature pyrolysis of ethane and propylene," *J. Chem. Soc. Faraday Trans. 1 Phys. Chem. Condens. Phases*, vol. 75, no. 0, p. 1390, 1979, doi: 10.1039/f19797501390.
[29] A. Indarto, "Soot Growth Mechanisms from Polyynes," *Environ. Eng. Sci.*, vol. 26, no. 12, pp. 1685–1691, Dec. 2009, doi: 10.1089/ees.2007.0325.
[30] J. H. Miller, "The kinetics of polynuclear aromatic hydrocarbon agglomeration in flames," *Symp. Int. Combust.*, vol. 23, no. 1, pp. 91–98, Jan. 1991, doi: 10.1016/S0082-0784(06)80246-8.
[31] A. Kazakov, H. Wang, and M. Frenklach, "Detailed modeling of soot formation in laminar premixed ethylene flames at a pressure of 10 bar," *Combust. Flame*, vol. 100, no. 1–2, pp. 111–120, Jan. 1995, doi: 10.1016/0010-2180(94)00086-8.
[32] C. A. Schuetz and M. Frenklach, "Nucleation of soot: Molecular dynamics simulations of pyrene dimerization," *Proc. Combust. Inst.*, vol. 29, no. 2, pp. 2307–2314, Jan. 2002, doi: 10.1016/S1540-7489(02)80281-4.
[33] H. Wang, "Formation of nascent soot and other condensed-phase materials in flames," *Proc. Combust. Inst.*, vol. 33, no. 1, pp. 41–67, 2011, doi: 10.1016/j.proci.2010.09.009.
[34] S. J. Harris and A. M. Weiner, "A picture of soot particle inception," *Symp. Int. Combust.*, vol. 22, no. 1, pp. 333–342, 1989, doi: https://doi.org/10.1016/S0082-0784(89)80039-6.
[35] R. J. Santoro, H. G. Semerjian, and R. A. Dobbins, "Soot particle measurements in diffusion flames," *Combust. Flame*, vol. 51, pp. 203–218, Jan. 1983, doi: 10.1016/0010-2180(83)90099-8.
[36] B. Yang and U. O. Koylu, "Detailed soot field in a turbulent non-premixed ethylene/air flame from laser scattering and extinction experiments," *Combust. Flame*, vol. 141, no. 1–2, pp. 55–65, Apr. 2005, doi: 10.1016/j.combustflame.2004.12.008.
[37] B. Yang and U. O. Koylu, "SOOT PROCESSES IN A STRONGLY-RADIATING TURBULENT FLAME FROM LASER SCATTERING/EXTINCTION EXPERIMENTS," in *Proceeding of the*

4th International Symposium on Radiative Transfer, Istambul, Turkey, 2004, pp. 1–10. doi: 10.1615/ICHMT.2004.RAD-4.410.
[38] S. S. Iyer, T. A. Litzinger, S.-Y. Lee, and R. J. Santoro, "Determination of soot scattering coefficient from extinction and three-angle scattering in a laminar diffusion flame," *Combust. Flame*, vol. 149, no. 1, pp. 206–216, 2007, doi: https://doi.org/10.1016/j.combustflame.2006.11.009.
[39] J. B. Jeffries, R. A. Copeland, G. P. Smith, and D. R. Crosley, "Multiple species laser-induced fluorescence in flames," *Symp. Int. Combust.*, vol. 21, no. 1, pp. 1709–1718, Jan. 1988, doi: 10.1016/S0082-0784(88)80404-1.
[40] U. Westblom and M. Aldén, "Simultaneous multiple species detection in a flame usinglaser-induced fluorescence: Errata," *Appl. Opt.*, vol. 29, no. 33, pp. 4844–4851, Nov. 1990, doi: 10.1364/AO.29.004844.
[41] D. R. Crosley, "Semiquantitative laser-induced fluorescence in flames," *Combust. Flame*, vol. 78, no. 1, pp. 153–167, Oct. 1989, doi: 10.1016/0010-2180(89)90013-8.
[42] D. E. Heard, J. B. Jeffries, G. P. Smith, and D. R. Crosley, "LIF measurements in methane/air flames of radicals important in prompt-NO formation," *Combust. Flame*, vol. 88, no. 2, pp. 137–148, Feb. 1992, doi: 10.1016/0010-2180(92)90048-T.
[43] M. J. Dyer and D. R. Crosley, "Two-dimensional imaging of OH laser-induced fluorescence in a flame," *Opt. Lett.*, vol. 7, no. 8, pp. 382–384, Aug. 1982, doi: 10.1364/OL.7.000382.
[44] K. J. Rensberger, J. B. Jeffries, R. A. Copeland, K. Kohse-Höinghaus, M. L. Wise, and D. R. Crosley, "Laser-induced fluorescence determination of temperatures in low pressure flames," *Appl. Opt.*, vol. 28, no. 17, pp. 3556–3566, Sep. 1989, doi: 10.1364/AO.28.003556.
[45] M. Tamura *et al.*, "Laser-induced fluorescence of seeded nitric oxide as a flame thermometer," *Appl. Phys. B Lasers Opt.*, vol. 66, no. 4, pp. 503–510, Apr. 1998, doi: 10.1007/s003400050425.
[46] K. McManus, B. Yip, and S. Candel, "Emission and laser-induced fluorescence imaging methods in experimental combustion," *Exp. Therm. Fluid Sci.*, vol. 10, no. 4, pp. 486–502, May 1995, doi: 10.1016/0894-1777(94)00078-M.
[47] *Handbook of Fluorescence Spectra of Aromatic Molecules*. Elsevier, 1971. doi: 10.1016/B978-0-12-092656-5.X5001-1.
[48] J. Dunn, "Investigation of premixed sooting flames by combined laser induced incandescence and laser induced fluorescence," University of Strathclyde, 2013. doi: 10.48730/SVAQ-3J17.
[49] M. Mannazhi, S. Török, J. Gao, and P.-E. Bengtsson, "Soot maturity studies in methane-air diffusion flames at elevated pressures using laser-induced incandescence," *Proc. Combust. Inst.*, vol. 38, no. 1, pp. 1217–1224, 2021, doi: 10.1016/j.proci.2020.07.127.
[50] B. Quay, T.-W. Lee, T. Ni, and R. J. Santoro, "Spatially resolved measurements of soot volume fraction using laser-induced incandescence," *Combust. Flame*, vol. 97, no. 3–4, pp. 384–392, Jun. 1994, doi: 10.1016/0010-2180(94)90029-9.
[51] R. L. Vander Wal and K. J. Weiland, "Laser-induced incandescence: Development and characterization towards a measurement of soot-volume fraction," *Appl. Phys. B*, vol. 59, no. 4, pp. 445–452, Oct. 1994, doi: 10.1007/BF01081067.
[52] S. Will, S. Schraml, and A. Leipertz, "Two-dimensional soot-particle sizing by time-resolved laser-induced incandescence," *Opt. Lett.*, vol. 20, no. 22, pp. 2342–2344, Nov. 1995, doi: 10.1364/OL.20.002342.
[53] D. J. Bryce, N. Ladommatos, and H. Zhao, "Quantitative investigation of soot distribution by laser-induced incandescence," *Appl. Opt.*, vol. 39, no. 27, pp. 5012–5022, Sep. 2000, doi: 10.1364/AO.39.005012.
[54] Z. A. Mansurov, "Soot Formation in Combustion Processes (Review)," *Combust. Explos. Shock Waves*, vol. 41, no. 6, pp. 727–744, Nov. 2005, doi: 10.1007/s10573-005-0083-2.
[55] R. Hadef, K. P. Geigle, W. Meier, and M. Aigner, "Soot characterization with laser-induced incandescence applied to a laminar premixed ethylene–air flame," *Int. J. Therm. Sci.*, vol. 49, no. 8, pp. 1457–1467, Aug. 2010, doi: 10.1016/j.ijthermalsci.2010.02.014.

[56] S. De Iuliis, F. Migliorini, F. Cignoli, and G. Zizak, “2D soot volume fraction imaging in an ethylene diffusion flame by two-color laser-induced incandescence (2C-LII) technique and comparison with results from other optical diagnostics,” *Proc. Combust. Inst.*, vol. 31, no. 1, pp. 869–876, Jan. 2007, doi: 10.1016/j.proci.2006.07.149.

[57] P.-E. Bengtsson and M. Aldén, “Soot-visualization strategies using laser techniques: Laser-induced fluorescence in C2 from laser-vaporized soot and laser-induced soot incandescence,” *Appl. Phys. B Laser Opt.*, vol. 60, no. 1, pp. 51–59, Jan. 1995, doi: 10.1007/BF01082073.

[58] H. Bladh, P.-E. Bengtsson, J. Delhay, Y. Bouvier, E. Therssen, and P. Desgroux, “Experimental and theoretical comparison of spatially resolved laser-induced incandescence (LII) signals of soot in backward and right-angle configuration,” *Appl. Phys. B*, vol. 83, no. 3, pp. 423–433, Jun. 2006, doi: 10.1007/s00340-006-2197-y.

[59] H. Bladh *et al.*, “Influence of soot particle aggregation on time-resolved laser-induced incandescence signals,” *Appl. Phys. B*, vol. 104, no. 2, pp. 331–341, Aug. 2011, doi: 10.1007/s00340-011-4470-y.

[60] Q. N. Chan, P. R. Medwell, P. A. M. Kalt, Z. T. Alwahabi, B. B. Dally, and G. J. Nathan, “Simultaneous imaging of temperature and soot volume fraction,” *Proc. Combust. Inst.*, vol. 33, no. 1, pp. 791–798, 2011, doi: 10.1016/j.proci.2010.06.031.

[61] M. Charwath, R. Suntz, and H. Bockhorn, “Influence of the temporal response of the detection system on time-resolved laser-induced incandescence signal evolutions,” *Appl. Phys. B*, vol. 83, no. 3, pp. 435–442, Jun. 2006, doi: 10.1007/s00340-006-2265-3.

[62] Y. N. Mishra *et al.*, “Application of FRAME for Simultaneous LIF and LII Imaging in Sooting Flames Using a Single Camera,” *Sensors*, vol. 20, no. 19, p. 5534, Sep. 2020, doi: 10.3390/s20195534.

[63] L. Xu, M. Zhou, Y. Wang, and D. Liu, “Probing sooting limits in counterflow diffusion flames via multiple optical diagnostic techniques,” *Exp. Therm. Fluid Sci.*, vol. 136, p. 110679, Aug. 2022, doi: 10.1016/j.expthermflusci.2022.110679.

[64] C. S. McEnally, L. D. Pfefferle, B. Atakan, and K. Kohse-Höinghaus, “Studies of aromatic hydrocarbon formation mechanisms in flames: Progress towards closing the fuel gap,” *Prog. Energy Combust. Sci.*, vol. 32, no. 3, pp. 247–294, Jan. 2006, doi: 10.1016/j.pecs.2005.11.003.

[65] M. Sirignano, D. Bartos, M. Conturso, M. Dunn, A. D’Anna, and A. R. Masri, “Detection of nanostructures and soot in laminar premixed flames,” *Combust. Flame*, vol. 176, pp. 299–308, Feb. 2017, doi: 10.1016/j.combustflame.2016.10.009.

[66] R. L. Vander Wal, Z. Zhou, and M. Y. Choi, “Laser-induced incandescence calibration via gravimetric sampling,” *Combust. Flame*, vol. 105, no. 4, pp. 462–470, Jun. 1996, doi: 10.1016/0010-2180(95)00216-2.

[67] Z.-Q. Zhou, T. U. Ahmed, and M. Y. Choi, “Measurement of dimensionless soot extinction constant using a gravimetric sampling technique,” *Exp. Therm. Fluid Sci.*, vol. 18, no. 1, pp. 27–32, Sep. 1998, doi: 10.1016/S0894-1777(98)10005-5.

[68] F. Xu, “Soot formation in laminar premixed ethylene/air flames at atmospheric pressure,” *Combust. Flame*, vol. 108, no. 4, pp. 471–493, Mar. 1997, doi: 10.1016/S0010-2180(96)00200-3.

[69] T. C. Williams, C. R. Shaddix, K. A. Jensen, and J. M. Suo-Anttila, “Measurement of the dimensionless extinction coefficient of soot within laminar diffusion flames,” *Int. J. Heat Mass Transf.*, vol. 50, no. 7–8, pp. 1616–1630, Apr. 2007, doi: 10.1016/j.ijheatmasstransfer.2006.08.024.

[70] M. Y. Choi, G. W. Mulholland, A. Hamins, and T. Kashiwagi, “Comparisons of the soot volume fraction using gravimetric and light extinction techniques,” *Combust. Flame*, vol. 102, no. 1–2, pp. 161–169, Jul. 1995, doi: 10.1016/0010-2180(94)00282-W.

[71] W. Merchan-Merchan, S. G. Sanmiguel, and S. McCollam, “Analysis of soot particles derived from biodiesels and diesel fuel air-flames,” *Spec. Sect. ACS Clean Coal*, vol. 102, pp. 525–535, Dec. 2012, doi: 10.1016/j.fuel.2012.04.029.

[72] R. L. Vander Wal and K. A. Jensen, “Laser-induced incandescence: excitation intensity,” *Appl. Opt.*, vol. 37, no. 9, pp. 1607–1616, Mar. 1998, doi: 10.1364/AO.37.001607.
[73] R. J. Samson, G. W. Mulholland, and J. W. Gentry, “Structural analysis of soot agglomerates,” *Langmuir*, vol. 3, no. 2, pp. 272–281, Mar. 1987, doi: 10.1021/la00074a022.
[74] R. L. Vander Wal, T. M. Ticich, and A. B. Stephens, “Optical and microscopy investigations of soot structure alterations by laser-induced incandescence,” *Appl. Phys. B Lasers Opt.*, vol. 67, no. 1, pp. 115–123, Jul. 1998, doi: 10.1007/s003400050483.
[75] B. Axelsson, R. Collin, and P.-E. Bengtsson, “Laser-induced incandescence for soot particle size measurements in premixed flat flames,” *Appl. Opt.*, vol. 39, no. 21, pp. 3683–3690, Jul. 2000, doi: 10.1364/AO.39.003683.
[76] F. Migliorini, K. A. Thomson, and G. J. Smallwood, “Investigation of optical properties of aging soot,” *Appl. Phys. B*, vol. 104, no. 2, pp. 273–283, Aug. 2011, doi: 10.1007/s00340-011-4396-4.
[77] C. Zhang, Y. Wu, B. Liu, Z. Wang, and L. Zhou, “Investigation of soot particles morphology and size distribution produced in a n-heptane/anisole laminar diffusion flame based on TEM images,” *Combust. Flame*, vol. 244, p. 112234, Oct. 2022, doi: 10.1016/j.combustflame.2022.112234.
[78] B. Zhao *et al.*, “Measurement and numerical simulation of soot particle size distribution functions in a laminar premixed ethylene-oxygen-argon flame,” *Combust. Flame*, vol. 133, no. 1–2, pp. 173–188, Apr. 2003, doi: 10.1016/S0010-2180(02)00574-6.
[79] M. Kasper, K. Siegmann, and K. Sattler, “Evaluation of an in situ sampling probe for its accuracy in determining particle size distributions from flames,” *J. Aerosol Sci.*, vol. 28, no. 8, pp. 1569–1578, Dec. 1997, doi: 10.1016/S0021-8502(97)00031-1.
[80] W. Kim, S. H. Kim, D. W. Lee, S. Lee, C. S. Lim, and J. H. Ryu, “Size Analysis of Automobile Soot Particles Using Field-Flow Fractionation,” *Environ. Sci. Technol.*, vol. 35, no. 6, pp. 1005–1012, Mar. 2001, doi: 10.1021/es001329n.
[81] G. Skillas, H. Burtscher, K. Siegmann, and U. Baltensperger, “Density and Fractal-like Dimension of Particles from a Laminar Diffusion Flame,” *J. Colloid Interface Sci.*, vol. 217, no. 2, pp. 269–274, Sep. 1999, doi: 10.1006/jcis.1999.6370.
[82] S. C. Wang and R. C. Flagan, “Scanning Electrical Mobility Spectrometer,” *Aerosol Sci. Technol.*, vol. 13, no. 2, pp. 230–240, Jan. 1990, doi: 10.1080/02786829008959441.
[83] S. Chowdhury, W. R. Boyette, and W. L. Roberts, “Time-averaged probability density functions of soot nanoparticles along the centerline of a piloted turbulent diffusion flame using a scanning mobility particle sizer,” *J. Aerosol Sci.*, vol. 106, pp. 56–67, Apr. 2017, doi: 10.1016/j.jaerosci.2016.10.012.
[84] L. S. Ruzer and N. H. Harley, *Aerosols handbook: measurement, dosimetry, and health effects*. Boca Raton: Taylor & Francis, 2013. Accessed: Aug. 05, 2022. [Online]. Available: https://doi.org/10.1201/b12668
[85] H. Zhao and N. Ladommatos, “Optical diagnostics for soot and temperature measurement in diesel engines,” *Prog. Energy Combust. Sci.*, vol. 24, no. 3, pp. 221–255, Jan. 1998, doi: 10.1016/S0360-1285(97)00033-6.
[86] Y. Su, Y. Zhang, F. Xie, J. Duan, X. Li, and Y. Liu, “Influence of ethanol blending ratios on in-cylinder soot processes and particulate matter emissions in an optical direct injection spark ignition engine,” *Fuel*, vol. 308, p. 121944, Jan. 2022, doi: 10.1016/j.fuel.2021.121944.
[87] J. Liu, J. Yang, P. Sun, Q. Ji, J. Meng, and P. Wang, “Experimental investigation of in-cylinder soot distribution and exhaust particle oxidation characteristics of a diesel engine with nano-CeO2 catalytic fuel,” *Energy*, vol. 161, pp. 17–27, Oct. 2018, doi: 10.1016/j.energy.2018.07.108.
[88] Y. Wang, Y. Zhuang, M. Yao, Y. Qin, and Z. Zheng, “An experimental investigation into the soot particle emissions at early injection timings in a single-cylinder research diesel engine,” *Fuel*, vol. 316, p. 123288, May 2022, doi: 10.1016/j.fuel.2022.123288.
[89] C.-J. Sung and H. J. Curran, “Using rapid compression machines for chemical kinetics studies,” *Prog. Energy Combust. Sci.*, vol. 44, pp. 1–18, Oct. 2014, doi: 10.1016/j.pecs.2014.04.001.

[90] C. Crua, D. A. Kennaird, and M. R. Heikal, “Laser-induced incandescence study of diesel soot formation in a rapid compression machine at elevated pressures,” *Combust. Flame*, vol. 135, no. 4, pp. 475–488, 2003, doi: https://doi.org/10.1016/S0010-2180(03)00183-4.
[91] I. Kitsopanidis and W. K. Cheng, “Soot Formation Study in a Rapid Compression Machine,” *J. Eng. Gas Turbines Power*, vol. 128, no. 4, pp. 942–949, Oct. 2006, doi: 10.1115/1.2180279.
[92] J. E. Ketterer and W. K. Cheng, “A study of soot formation in a rapid compression machine at conditions representative of cold-fast-idle in spark ignition engines,” *Int. J. Engine Res.*, vol. 20, no. 6, pp. 670–677, Aug. 2019, doi: 10.1177/1468087418777663.
[93] H. C. Hottel, G. C. Williams, and A. H. Bonnell, “Application of well-stirred reactor theory to the prediction of combustor performance,” *Combust. Flame*, vol. 2, no. 1, pp. 13–34, 1958, doi: https://doi.org/10.1016/0010-2180(58)90017-8.
[94] M. Yahyaoui, N. Djebaïli-Chaumeix, P. Dagaut, C.-E. Paillard, and S. Gail, “Experimental and modelling study of gasoline surrogate mixtures oxidation in jet stirred reactor and shock tube,” *Proc. Combust. Inst.*, vol. 31, no. 1, pp. 385–391, Jan. 2007, doi: 10.1016/j.proci.2006.07.179.
[95] P. Dagaut, “On the kinetics of hydrocarbons oxidation from natural gas to kerosene and diesel fuel,” *Phys Chem Chem Phys*, vol. 4, no. 11, pp. 2079–2094, 2002, doi: 10.1039/B110787A.
[96] P. Dagaut *et al.*, “A jet-stirred reactor for kinetic studies of homogeneous gas-phase reactions at pressures up to ten atmospheres (≈1 MPa),” *J. Phys. [E]*, vol. 19, no. 3, pp. 207–209, Mar. 1986, doi: 10.1088/0022-3735/19/3/009.
[97] P. Dagaut, M. Reuillon, and M. Cathonnet, “Experimental study of the oxidation of n-heptane in a jet stirred reactor from low to high temperature and pressures up to 40 atm,” *Combust. Flame*, vol. 101, no. 1–2, pp. 132–140, Apr. 1995, doi: 10.1016/0010-2180(94)00184-T.
[98] O. Herbinet, B. Husson, H. Le Gall, and F. Battin-Leclerc, “An experimental and modeling study of the oxidation of *n*- heptane, ethylbenzene, and *n*- butylbenzene in a jet-stirred reactor at pressures up to 10 bar,” *Int. J. Chem. Kinet.*, vol. 52, no. 12, pp. 1006–1021, Dec. 2020, doi: 10.1002/kin.21417.
[99] M. Pelucchi *et al.*, “Pyrolysis and Combustion Chemistry of Pyrrole, a Reference Component for Bio-oil Surrogates: Jet-Stirred Reactor Experiments and Kinetic Modeling,” *Energy Fuels*, vol. 35, no. 9, pp. 7265–7284, May 2021, doi: 10.1021/acs.energyfuels.0c03874.
[100] S. Arunthanayothin, A. Stagni, Y. Song, O. Herbinet, T. Faravelli, and F. Battin-Leclerc, “Ammonia–methane interaction in jet-stirred and flow reactors: An experimental and kinetic modeling study,” *Proc. Combust. Inst.*, vol. 38, no. 1, pp. 345–353, 2021, doi: 10.1016/j.proci.2020.07.061.
[101] S. Manzello, G. Mulholland, M. Donovan, W. Tsang, M. Zachariah, and S. Stouffer, “On the Use of a Well Stirred Reactor to Study Soot Inception,” Jan. 2005.
[102] S. L. Manzello *et al.*, “Soot particle size distributions in a well-stirred reactor/plug flow reactor,” *Proc. Combust. Inst.*, vol. 31, no. 1, pp. 675–683, 2007, doi: https://doi.org/10.1016/j.proci.2006.07.013.
[103] D. B. Lenhert and S. L. Manzello, “Effects of benzene and naphthalene addition on soot inception in a well-stirred reactor/plug flow reactor,” *Proc. Combust. Inst.*, vol. 32, no. 1, pp. 657–664, 2009, doi: https://doi.org/10.1016/j.proci.2008.07.016.
[104] W. Tsang and A. Lifshitz, “Shock Tube Techniques in Chemical Kinetics,” *Annu. Rev. Phys. Chem.*, vol. 41, no. 1, pp. 559–599, Oct. 1990, doi: 10.1146/annurev.pc.41.100190.003015.
[105] M. Evans and A. Williams, “Shock tube studies on the formation of soot from the combustion and pyrolysis of some hydrocarbons,” *Fuel*, vol. 60, no. 11, pp. 1047–1056, Nov. 1981, doi: 10.1016/0016-2361(81)90048-X.
[106] S. D. Iuliis, N. Chaumeix, M. Idir, and C.-E. Paillard, “Scattering/extinction measurements of soot formation in a shock tube,” *Exp. Therm. Fluid Sci.*, vol. 32, no. 7, pp. 1354–1362, 2008, doi: https://doi.org/10.1016/j.expthermflusci.2007.11.008.

[107] O. Mathieu, N. Djebaïli-Chaumeix, C.-E. Paillard, and F. Douce, “Experimental study of soot formation from a diesel fuel surrogate in a shock tube,” *Combust. Flame*, vol. 156, no. 8, pp. 1576–1586, Aug. 2009, doi: 10.1016/j.combustflame.2009.05.002.
[108] D. Nativel, J. Herzler, S. Krzywdziak, S. Peukert, M. Fikri, and C. Schulz, “Shock-tube study of the influence of oxygenated additives on benzene pyrolysis: Measurement of optical densities, soot inception times and comparison with simulations,” *Combust. Flame*, p. 111985, Jan. 2022, doi: 10.1016/j.combustflame.2022.111985.
[109] W. G. Lovell, “Knocking Characteristics of Hydrocarbons,” May 01, 2002. https://pubs.acs.org/doi/pdf/10.1021/ie50468a033 (accessed Apr. 04, 2020).
[110] C. S. McEnally, L. D. Pfefferle, B. Atakan, and K. Kohse-Höinghaus, “Studies of aromatic hydrocarbon formation mechanisms in flames: Progress towards closing the fuel gap,” *Prog. Energy Combust. Sci.*, vol. 32, no. 3, pp. 247–294, Jan. 2006, doi: 10.1016/j.pecs.2005.11.003.
[111] S. Sinha and A. Raj, “Polycyclic aromatic hydrocarbon (PAH) formation from benzyl radicals: a reaction kinetics study,” *Phys. Chem. Chem. Phys.*, vol. 18, no. 11, pp. 8120–8131, Mar. 2016, doi: 10.1039/C5CP06465A.
[112] R. D. Smith, “A direct mass spectrometric study of the mechanism of toluene pyrolysis at high temperatures,” *J. Phys. Chem.*, vol. 83, no. 12, pp. 1553–1563, Jun. 1979, doi: 10.1021/j100475a001.
[113] K. M. Pamidimukkala, R. D. Kern, M. R. Patel, H. C. Wei, and J. H. Kiefer, “High-temperature pyrolysis of toluene,” *J. Phys. Chem.*, vol. 91, no. 8, pp. 2148–2154, Apr. 1987, doi: 10.1021/j100292a034.
[114] M. B. Colket and D. J. Seery, “Reaction mechanisms for toluene pyrolysis,” *Symp. Int. Combust.*, vol. 25, no. 1, pp. 883–891, 1994, doi: 10.1016/S0082-0784(06)80723-X.
[115] R. Sivaramakrishnan, R. S. Tranter, and K. Brezinsky, “High Pressure Pyrolysis of Toluene. 1. Experiments and Modeling of Toluene Decomposition,” *J. Phys. Chem. A*, vol. 110, no. 30, pp. 9388–9399, Aug. 2006, doi: 10.1021/jp060820j.
[116] R. Sivaramakrishnan, R. S. Tranter, and K. Brezinsky, “High Pressure Pyrolysis of Toluene. 2. Modeling Benzyl Decomposition and Formation of Soot Precursors,” *J. Phys. Chem. A*, vol. 110, no. 30, pp. 9400–9404, Aug. 2006, doi: 10.1021/jp0608224.
[117] S. C. Graham, J. B. Homer, and J. L. J. Rosenfeld, “The formation and coagulation of soot aerosols generated by the pyrolysis of aromatic hydrocarbons,” *Proc. R. Soc. Lond. Math. Phys. Sci.*, vol. 344, no. 1637, pp. 259–285, Jun. 1975, doi: 10.1098/rspa.1975.0101.
[118] T. E. Parker, R. R. Foutter, and W. T. Rawlins, “Soot initiation and particle growth in the pyrolysis of toluene at high inert gas pressures,” in *AIP Conference Proceedings*, 1990, vol. 208, pp. 481–486. doi: 10.1063/1.39378.
[119] A. Alexiou and A. Williams, “Soot formation in shock-tube pyrolysis of toluene, toluene-methanol, toluene-ethanol, and toluene-oxygen mixtures,” *Combust. Flame*, vol. 104, no. 1–2, pp. 51–65, Jan. 1996, doi: 10.1016/0010-2180(95)00004-6.
[120] J. D’Alessio, M. Lazzaro, P. Massoli, and V. Moccia, “Absorption spectroscopy of toluene pyrolysis,” *Opt. Lasers Eng.*, vol. 37, no. 5, pp. 495–508, 2002, doi: https://doi.org/10.1016/S0143-8166(01)00122-1.
[121] L. Xian, Y. Li, J. He, C. Zhang, P. Li, and X. Li, “Measurement of Soot Yield from the Pyrolysis of Toluene at High Temperatures by Laser Extinction Method,” *Guang Pu Xue Yu Guang Pu Fen Xi Guang Pu*, vol. 36, no. 11, pp. 3481–3484, Nov. 2016.
[122] A. Matsugi and A. Miyoshi, “Reactions of o-benzyne with propargyl and benzyl radicals: potential sources of polycyclic aromatic hydrocarbons in combustion,” *Phys. Chem. Chem. Phys.*, vol. 14, no. 27, p. 9722, 2012, doi: 10.1039/c2cp41002h.
[123] A. Matsugi and A. Miyoshi, “Computational study on the recombination reaction between benzyl and propargyl radicals,” *Int. J. Chem. Kinet.*, vol. 44, no. 3, pp. 206–218, Mar. 2012, doi: 10.1002/kin.20625.

[124] A. Matsugi and A. Miyoshi, “Modeling of two- and three-ring aromatics formation in the pyrolysis of toluene,” *Proc. Combust. Inst.*, vol. 34, no. 1, pp. 269–277, Jan. 2013, doi: 10.1016/j.proci.2012.06.032.
[125] T. Yuan, L. Zhang, Z. Zhou, M. Xie, L. Ye, and F. Qi, “Pyrolysis of *n* -Heptane: Experimental and Theoretical Study,” *J. Phys. Chem. A*, vol. 115, no. 9, pp. 1593–1601, Mar. 2011, doi: 10.1021/jp109640z.
[126] W. Yuan, Y. Li, P. Dagaut, J. Yang, and F. Qi, “Investigation on the pyrolysis and oxidation of toluene over a wide range conditions. I. Flow reactor pyrolysis and jet stirred reactor oxidation,” *Combust. Flame*, vol. 162, no. 1, pp. 3–21, Jan. 2015, doi: 10.1016/j.combustflame.2014.07.009.
[127] G. L. Agafonov, I. Naydenova, P. A. Vlasov, and J. Warnatz, “Detailed kinetic modeling of soot formation in shock tube pyrolysis and oxidation of toluene and n-heptane,” *Proc. Combust. Inst.*, vol. 31, no. 1, pp. 575–583, Jan. 2007, doi: 10.1016/j.proci.2006.07.191.
[128] W. Sun, A. Hamadi, S. Abid, N. Chaumeix, and A. Comandini, “Probing PAH formation chemical kinetics from benzene and toluene pyrolysis in a single-pulse shock tube,” *Proc. Combust. Inst.*, vol. 38, no. 1, pp. 891–900, Jan. 2021, doi: 10.1016/j.proci.2020.06.077.
[129] R. D. Kern, H. J. Singh, M. A. Esslinger, and P. W. Winkeler, “Product profiles observed during the pyrolyses of toluene, benzene, butadiene, and acetylene,” *Symp. Int. Combust.*, vol. 19, no. 1, pp. 1351–1358, Jan. 1982, doi: 10.1016/S0082-0784(82)80311-1.
[130] A. Laskin and A. Lifshit, “Thermal decomposition of benene. Single-pulse shock-tube investigation,” *Symp. Int. Combust.*, vol. 26, no. 1, pp. 669–675, Jan. 1996, doi: 10.1016/S0082-0784(96)80274-8.
[131] R. Sivaramakrishnan, K. Brezinsky, and R. Tranter, “A shock-tube study of the high-pressure thermal decomposition of benzene,” *Combust. Sci. Technol.*, vol. 178, pp. 285–305, Jan. 2006, doi: 10.1080/00102200500292340.
[132] R. S. Tranter, S. J. Klippenstein, L. B. Harding, B. R. Giri, X. Yang, and J. H. Kiefer, “Experimental and Theoretical Investigation of the Self-Reaction of Phenyl Radicals,” *J. Phys. Chem. A*, vol. 114, no. 32, pp. 8240–8261, Aug. 2010, doi: 10.1021/jp1031064.
[133] B. Shukla and M. Koshi, “A highly efficient growth mechanism of polycyclic aromatic hydrocarbons,” *Phys. Chem. Chem. Phys.*, vol. 12, no. 10, p. 2427, 2010, doi: 10.1039/b919644g.
[134] R. S. Tranter, S. J. Klippenstein, L. B. Harding, B. R. Giri, X. Yang, and J. H. Kiefer, “Experimental and Theoretical Investigation of the Self-Reaction of Phenyl Radicals,” *J. Phys. Chem. A*, vol. 114, no. 32, pp. 8240–8261, Aug. 2010, doi: 10.1021/jp1031064.
[135] C. Saggese, A. Frassoldati, A. Cuoci, T. Faravelli, and E. Ranzi, “A wide range kinetic modeling study of pyrolysis and oxidation of benzene,” *Combust. Flame*, vol. 160, no. 7, pp. 1168–1190, Jul. 2013, doi: 10.1016/j.combustflame.2013.02.013.
[136] E. Ranzi *et al.*, “Hierarchical and comparative kinetic modeling of laminar flame speeds of hydrocarbon and oxygenated fuels,” *Prog. Energy Combust. Sci.*, vol. 38, no. 4, pp. 468–501, Aug. 2012, doi: 10.1016/j.pecs.2012.03.004.
[137] H. Böhm, H. Jander, and D. Tanke, “PAH growth and soot formation in the pyrolysis of acetylene and benzene at high temperatures and pressures: Modeling and experiment,” *Symp. Int. Combust.*, vol. 27, no. 1, pp. 1605–1612, 1998, doi: https://doi.org/10.1016/S0082-0784(98)80570-5.
[138] G. L. Agafonov, P. A. Vlasov, and V. N. Smirnov, “Soot formation in the pyrolysis of benzene, methylbenzene, and ethylbenzene in shock waves,” *Kinet. Catal.*, vol. 52, no. 3, pp. 358–370, May 2011, doi: 10.1134/S0023158411030013.
[139] A. Drakon, A. Eremin, E. Mikheyeva, B. Shu, M. Fikri, and C. Schulz, “Soot formation in shock-wave-induced pyrolysis of acetylene and benzene with H2, O2, and CH4 addition,” *Combust. Flame*, vol. 198, pp. 158–168, 2018, doi: https://doi.org/10.1016/j.combustflame.2018.09.014.
[140] A. J. Vervust *et al.*, “Detailed Experimental and Kinetic Modeling Study of Cyclopentadiene Pyrolysis in the Presence of Ethene,” *Energy Fuels*, vol. 32, no. 3, pp. 3920–3934, Mar. 2018, doi: 10.1021/acs.energyfuels.7b03560.

[141] O. Herbinet *et al.*, “Study of the Formation of the First Aromatic Rings in the Pyrolysis of Cyclopentene,” *J. Phys. Chem. A*, vol. 120, no. 5, pp. 668–682, Feb. 2016, doi: 10.1021/acs.jpca.5b09203.
[142] M. Salamanca, M. L. Botero, J. W. Martin, J. A. H. Dreyer, J. Akroyd, and M. Kraft, “The impact of cyclic fuels on the formation and structure of soot,” *Combust. Flame*, vol. 219, pp. 1–12, Sep. 2020, doi: 10.1016/j.combustflame.2020.04.026.
[143] V. V. Kislov and A. M. Mebel, “The Formation of Naphthalene, Azulene, and Fulvalene from Cyclic C_5 Species in Combustion: An Ab Initio/RRKM Study of 9-H-Fulvalenyl ($C_5H_5-C_5H_4$) Radical Rearrangements,” *J. Phys. Chem. A*, vol. 111, no. 38, pp. 9532–9543, Sep. 2007, doi: 10.1021/jp0732099.
[144] A. M. Mebel and V. V. Kislov, “Can the $C_5H_5 + C_5H_5 \rightarrow C_{10}H_{10} \rightarrow C_{10}H_9 + H/C_{10}H_8 + H_2$ Reaction Produce Naphthalene? An Ab Initio/RRKM Study,” *J. Phys. Chem. A*, vol. 113, no. 36, pp. 9825–9833, Sep. 2009, doi: 10.1021/jp905931j.
[145] C. Cavallotti and D. Polino, “On the kinetics of the C5H5+C5H5 reaction,” *Proc. Combust. Inst.*, vol. 34, no. 1, pp. 557–564, Jan. 2013, doi: 10.1016/j.proci.2012.05.097.
[146] A. E. Long *et al.*, “Pressure dependent kinetic analysis of pathways to naphthalene from cyclopentadienyl recombination,” *Combust. Flame*, vol. 187, pp. 247–256, Jan. 2018, doi: 10.1016/j.combustflame.2017.09.008.
[147] C. Cavallotti, S. Mancarella, R. Rota, and S. Carrà, “Conversion of C5 into C6 Cyclic Species through the Formation of C7 Intermediates,” *J. Phys. Chem. A*, vol. 111, no. 19, pp. 3959–3969, May 2007, doi: 10.1021/jp067117f.
[148] S. Sharma and W. H. Green, “Computed Rate Coefficients and Product Yields for *c*-$C_5H_5 + CH_3 \rightarrow$ Products,” *J. Phys. Chem. A*, vol. 113, no. 31, pp. 8871–8882, Aug. 2009, doi: 10.1021/jp900679t.
[149] K. Wang, S. M. Villano, and A. M. Dean, “Reactions of allylic radicals that impact molecular weight growth kinetics,” *Phys. Chem. Chem. Phys.*, vol. 17, no. 9, pp. 6255–6273, 2015, doi: 10.1039/C4CP05308G.
[150] V. S. Krasnoukhov, D. P. Porfiriev, I. P. Zavershinskiy, V. N. Azyazov, and A. M. Mebel, “Kinetics of the $CH_3 + C_5H_5$ Reaction: A Theoretical Study,” *J. Phys. Chem. A*, vol. 121, no. 48, pp. 9191–9200, Dec. 2017, doi: 10.1021/acs.jpca.7b09873.
[151] G. da Silva, J. A. Cole, and J. W. Bozzelli, “Kinetics of the Cyclopentadienyl + Acetylene, Fulvenallene + H, and 1-Ethynylcyclopentadiene + H Reactions,” *J. Phys. Chem. A*, vol. 114, no. 6, pp. 2275–2283, Feb. 2010, doi: 10.1021/jp906835w.
[152] S. Fascella, C. Cavallotti, R. Rota, and S. Carrà, “The Peculiar Kinetics of the Reaction between Acetylene and the Cyclopentadienyl Radical,” *J. Phys. Chem. A*, vol. 109, no. 33, pp. 7546–7557, Aug. 2005, doi: 10.1021/jp051508x.
[153] M. R. Djokic, K. M. V. Geem, C. Cavallotti, A. Frassoldati, E. Ranzi, and G. B. Marin, “An experimental and kinetic modeling study of cyclopentadiene pyrolysis: First growth of polycyclic aromatic hydrocarbons,” *Combust. Flame*, vol. 161, no. 11, pp. 2739–2751, 2014, doi: https://doi.org/10.1016/j.combustflame.2014.04.013.
[154] D. H. Kim, J. A. Mulholland, D. Wang, and A. Violi, “Pyrolytic Hydrocarbon Growth from Cyclopentadiene,” *J. Phys. Chem. A*, vol. 114, no. 47, pp. 12411–12416, Dec. 2010, doi: 10.1021/jp106749k.
[155] R. G. Butler and I. Glassman, “Cyclopentadiene combustion in a plug flow reactor near 1150K,” *Proc. Combust. Inst.*, vol. 32, no. 1, pp. 395–402, 2009, doi: 10.1016/j.proci.2008.05.010.
[156] L. Carneiro Piton, A. Hamadi, S. Abid, N. Chaumeix, and A. Comandini, “Combined high-pressure experimental and kinetic modeling study of cyclopentene pyrolysis and its reactions with acetylene,” *Proc. Combust. Inst.*, p. S1540748922000487, Aug. 2022, doi: 10.1016/j.proci.2022.07.023.

[157] K. Roy, C. Horn, P. Frank, V. G. Slutsky, and T. Just, “High-temperature investigations on the pyrolysis of cyclopentadiene,” *Symp. Int. Combust.*, vol. 27, no. 1, pp. 329–336, 1998, doi: https://doi.org/10.1016/S0082-0784(98)80420-7.
[158] R. D. Kern *et al.*, “Pyrolysis of cyclopentadiene: Rates for initial C−H bond fission and the decomposition of c-C5H5,” *Symp. Int. Combust.*, vol. 27, no. 1, pp. 143–150, 1998, doi: https://doi.org/10.1016/S0082-0784(98)80399-8.
[159] S. E. Johnson, D. F. Davidson, and R. K. Hanson, “Shock tube/laser absorption measurements of the pyrolysis of JP-10 fuel,” *Combust. Flame*, vol. 216, pp. 161–173, 2020, doi: https://doi.org/10.1016/j.combustflame.2019.11.026.
[160] F. A. Carey, “ethylene | Encyclopedia Britannica.” https://www.britannica.com/science/ethylene (accessed Jun. 06, 2022).
[161] G. B. Skinner and E. M. Sokoloski, “SHOCK TUBE EXPERIMENTS ON THE PYROLYSIS OF ETHYLENE,” *J. Phys. Chem.*, vol. 64, no. 8, pp. 1028–1031, Aug. 1960, doi: 10.1021/j100837a015.
[162] S. Bauerle *et al.*, “Soot formation at elevated pressures and carbon concentrations in hydrocarbon pyrolysis,” *Symp. Int. Combust.*, vol. 25, no. 1, pp. 627–634, 1994, doi: https://doi.org/10.1016/S0082-0784(06)80694-6.
[163] Y. Hidaka *et al.*, “Shock-tube and modeling study of ethylene pyrolysis and oxidation,” *Combust. Flame*, vol. 117, no. 4, pp. 755–776, 1999, doi: https://doi.org/10.1016/S0010-2180(98)00128-X.
[164] G. L. Pilla, D. F. Davidson, and R. K. Hanson, “Shock tube/laser absorption measurements of ethylene time-histories during ethylene and n-heptane pyrolysis,” *Proc. Combust. Inst.*, vol. 33, no. 1, pp. 333–340, 2011, doi: https://doi.org/10.1016/j.proci.2010.06.146.
[165] S. Mostafalou and H. Bahadar, “Acetylene,” in *Encyclopedia of Toxicology (Third Edition)*, Third Edition., P. Wexler, Ed. Oxford: Academic Press, 2014, pp. 51–53. doi: https://doi.org/10.1016/B978-0-12-386454-3.00362-6.
[166] T. Britannica, “scattering | Encyclopedia Britannica.” https://www.britannica.com/science/scattering (accessed Jun. 06, 2022).
[167] A. Eremin, E. Gurentsov, and E. Mikheyeva, “Experimental study of molecular hydrogen influence on carbon particle growth in acetylene pyrolysis behind shock waves,” *Combust. Flame*, vol. 159, no. 12, pp. 3607–3615, 2012, doi: https://doi.org/10.1016/j.combustflame.2012.07.011.
[168] G. L. Agafonov, I. V. Bilera, P. A. Vlasov, Yu. A. Kolbanovskii, V. N. Smirnov, and A. M. Tereza, “Soot formation during the pyrolysis and oxidation of acetylene and ethylene in shock waves,” *Kinet. Catal.*, vol. 56, no. 1, pp. 12–30, Jan. 2015, doi: 10.1134/S0023158415010012.
[169] M. P. Ruiz, R. Guzmán de Villoria, Á. Millera, M. U. Alzueta, and R. Bilbao, “Influence of Different Operation Conditions on Soot Formation from C_2H_2 Pyrolysis,” *Ind. Eng. Chem. Res.*, vol. 46, no. 23, pp. 7550–7560, Nov. 2007, doi: 10.1021/ie070008i.
[170] N. E. Sánchez, A. Callejas, A. Millera, R. Bilbao, and M. U. Alzueta, “Formation of PAH and soot during acetylene pyrolysis at different gas residence times and reaction temperatures,” *Energy*, vol. 43, no. 1, pp. 30–36, 2012, doi: https://doi.org/10.1016/j.energy.2011.12.009.
[171] C. Esarte, M. Abián, Á. Millera, R. Bilbao, and M. U. Alzueta, “Gas and soot products formed in the pyrolysis of acetylene mixed with methanol, ethanol, isopropanol or n-butanol,” *Energy*, vol. 43, no. 1, pp. 37–46, 2012, doi: https://doi.org/10.1016/j.energy.2011.11.027.
[172] N. E. Sánchez, Á. Millera, R. Bilbao, and M. U. Alzueta, “Polycyclic aromatic hydrocarbons (PAH), soot and light gases formed in the pyrolysis of acetylene at different temperatures: Effect of fuel concentration,” *J. Anal. Appl. Pyrolysis*, vol. 103, pp. 126–133, 2013, doi: https://doi.org/10.1016/j.jaap.2012.10.027.
[173] A. Burcat and K. Radhakrishnan, “High temperature oxidation of propene,” *Combust. Flame*, vol. 60, no. 2, pp. 157–169, May 1985, doi: 10.1016/0010-2180(85)90004-5.
[174] V. S. Rao and G. B. Skinner, “Study of the high-temperature pyrolysis of propene by determination of H and D atoms formed from partially deuterated propenes heated behind shock waves,” *J. Phys. Chem.*, vol. 93, no. 5, pp. 1869–1876, Mar. 1989, doi: 10.1021/j100342a034.

[175] J. H. Kiefer, M. Z. Al-Alami, and K. A. Budach, “A shock tube, laser-schlieren study of propene pyrolysis at high temperatures,” *J. Phys. Chem.*, vol. 86, no. 5, pp. 808–813, Mar. 1982, doi: 10.1021/j100394a043.
[176] Y. Hidaka, T. Nakamura, H. Tanaka, A. Jinno, H. Kawano, and T. Higashihara, “Shock tube and modeling study of propene pyrolysis,” *Int. J. Chem. Kinet.*, vol. 24, no. 9, pp. 761–780, Sep. 1992, doi: 10.1002/kin.550240902.
[177] W.-C. Hung, C.-Y. Tsai, H. Matsui, N.-S. Wang, and A. Miyoshi, “Experimental and Theoretical Study on the Thermal Decomposition of C_3H_6 (Propene),” *J. Phys. Chem. A*, vol. 119, no. 8, pp. 1229–1237, Feb. 2015, doi: 10.1021/jp5102169.
[178] R. X. Fernandes, B. R. Giri, H. Hippler, C. Kachiani, and F. Striebel, “Shock Wave Study on the Thermal Unimolecular Decomposition of Allyl Radicals,” *J. Phys. Chem. A*, vol. 109, no. 6, pp. 1063–1070, Feb. 2005, doi: 10.1021/jp047482b.
[179] H. Wang *et al.*, “A high-temperature chemical kinetic model of n-alkane (up to n-dodecane), cyclohexane, and methyl-, ethyl-, n-propyl and n-butyl-cyclohexane oxidation at high temperatures, JetSurF version 2.0,” Sep. 2010, [Online]. Available: http://web.stanford.edu/group/haiwanglab/JetSurF/JetSurF2.0/index.html
[180] W. Tsang, “Chemical Kinetic Data Base for Combustion Chemistry Part V. Propene,” *J. Phys. Chem. Ref. Data*, vol. 20, no. 2, pp. 221–273, Mar. 1991, doi: 10.1063/1.555880.
[181] S. G. Davis, C. K. Law, and H. Wang, “Propene pyrolysis and oxidation kinetics in a flow reactor and laminar flames,” *Combust. Flame*, vol. 119, no. 4, pp. 375–399, 1999, doi: https://doi.org/10.1016/S0010-2180(99)00070-X.
[182] I. Weber, L. Golka, and M. Olzmann, “Thermal decomposition of propene: A shock-tube/H-ARAS and modeling study,” *Proc. Combust. Inst.*, vol. 36, no. 1, pp. 299–306, 2017, doi: https://doi.org/10.1016/j.proci.2016.06.091.
[183] S. C. Moldoveanu, “Pyrolysis of Hydrocarbons,” in *Pyrolysis of Organic Molecules*, Elsevier, 2019, pp. 35–161. doi: 10.1016/B978-0-444-64000-0.00002-0.
[184] N. Hansen *et al.*, “Isomer-specific combustion chemistry in allene and propyne flames,” *Combust. Flame*, vol. 156, no. 11, pp. 2153–2164, Nov. 2009, doi: 10.1016/j.combustflame.2009.07.014.
[185] J. A. Miller and S. J. Klippenstein, “The Recombination of Propargyl Radicals: Solving the Master Equation,” *J. Phys. Chem. A*, vol. 105, no. 30, pp. 7254–7266, Aug. 2001, doi: 10.1021/jp0102973.
[186] J. A. Miller and S. J. Klippenstein, “The Recombination of Propargyl Radicals and Other Reactions on a C_6H_6 Potential,” *J. Phys. Chem. A*, vol. 107, no. 39, pp. 7783–7799, Oct. 2003, doi: 10.1021/jp030375h.
[187] J. N. Bradley and K. O. West, “Single-pulse shock tube studies of hydrocarbon pyrolysis. Part 4.—Isomerization of allene to methylacetylene,” *J. Chem. Soc. Faraday Trans. 1 Phys. Chem. Condens. Phases*, vol. 71, no. 0, p. 967, 1975, doi: 10.1039/f19757100967.
[188] A. Lifshitz, M. Frenklach, and A. Burcat, “Structural isomerization allene .dblarw. propyne. Studies with a single pulse shock tube,” *J. Phys. Chem.*, vol. 79, no. 12, pp. 1148–1152, Jun. 1975, doi: 10.1021/j100579a002.
[189] Terumitsu. Kakumoto, Toshiaki. Ushirogouchi, Ko. Saito, and Akira. Imamura, “Isomerization of allene .dblarw. propyne in shock waves and ab initio calculations,” *J. Phys. Chem.*, vol. 91, no. 1, pp. 183–189, Jan. 1987, doi: 10.1021/j100285a040.
[190] S. G. Davis, C. K. Law, and H. Wang, “Propyne Pyrolysis in a Flow Reactor: An Experimental, RRKM, and Detailed Kinetic Modeling Study,” *J. Phys. Chem. A*, vol. 103, no. 30, pp. 5889–5899, Jul. 1999, doi: 10.1021/jp982762a.
[191] W. Sun, A. Hamadi, S. Abid, N. Chaumeix, and A. Comandini, “A comprehensive kinetic study on the speciation from propylene and propyne pyrolysis in a single-pulse shock tube,” *Combust. Flame*, vol. 231, p. 111485, 2021, doi: https://doi.org/10.1016/j.combustflame.2021.111485.

[192] S. Panigrahy *et al.*, “A comprehensive experimental and improved kinetic modeling study on the pyrolysis and oxidation of propyne,” *Proc. Combust. Inst.*, vol. 38, no. 1, pp. 479–488, 2021, doi: 10.1016/j.proci.2020.06.320.
[193] S. E. Johnson, Y. Ding, D. F. Davidson, and R. K. Hanson, “Shock tube/laser absorption measurements of the isomerization rates of allene and propyne,” *Combust. Flame*, vol. 238, p. 111962, 2022, doi: https://doi.org/10.1016/j.combustflame.2021.111962.
[194] S. M. Lee, S. S. Yoon, and S. H. Chung, “Synergistic effect on soot formation in counterflow diffusion flames of ethylene–propane mixtures with benzene addition,” *Combust. Flame*, vol. 136, no. 4, pp. 493–500, Mar. 2004, doi: 10.1016/j.combustflame.2003.12.005.
[195] J. Y. Hwang, W. Lee, H. G. Kang, and S. H. Chung, “Synergistic Effect of Ethylene–Propane Mixture on Soot Formation in Laminar Diffusion Flames,” *Combust. Flame*, vol. 114, no. 3, pp. 370–380, Aug. 1998, doi: 10.1016/S0010-2180(97)00295-2.
[196] S. S. Yoon, S. M. Lee, and S. H. Chung, “Effect of mixing methane, ethane, propane, and propene on the synergistic effect of PAH and soot formation in ethylene-base counterflow diffusion flames,” *Proc. Combust. Inst.*, vol. 30, no. 1, pp. 1417–1424, Jan. 2005, doi: 10.1016/j.proci.2004.08.038.
[197] N. B. Poddar, S. Thomas, and M. J. Wornat, “Polycyclic aromatic hydrocarbons from the co-pyrolysis of 1,3-butadiene and propyne,” *Proc. Combust. Inst.*, vol. 34, no. 1, pp. 1775–1783, Jan. 2013, doi: 10.1016/j.proci.2012.05.013.
[198] C. Shao, G. Kukkadapu, S. W. Wagnon, W. J. Pitz, and S. M. Sarathy, “PAH formation from jet stirred reactor pyrolysis of gasoline surrogates,” *Combust. Flame*, vol. 219, pp. 312–326, Sep. 2020, doi: 10.1016/j.combustflame.2020.06.001.
[199] V. G. Knorre, D. Tanke, Th. Thienel, and H. Gg. Wagner, “Soot formation in the pyrolysis of bezene/acetylene and acetylene/hydrogen mixtures at high carbon concentrations,” *Symp. Int. Combust.*, vol. 26, no. 2, pp. 2303–2310, Jan. 1996, doi: 10.1016/S0082-0784(96)80058-0.
[200] W. Sun, A. Hamadi, S. Abid, N. Chaumeix, and A. Comandini, “Influences of propylene/propyne addition on toluene pyrolysis in a single-pulse shock tube,” *Combust. Flame*, vol. 236, p. 111799, 2022, doi: https://doi.org/10.1016/j.combustflame.2021.111799.
[201] W. Sun, A. Hamadi, S. Abid, N. Chaumeix, and A. Comandini, “Detailed experimental and kinetic modeling study of toluene/C2 pyrolysis in a single-pulse shock tube,” *Combust. Flame*, vol. 226, pp. 129–142, 2021, doi: https://doi.org/10.1016/j.combustflame.2020.11.044.
[202] A. Hamadi, W. Sun, S. Abid, N. Chaumeix, and A. Comandini, “An experimental and kinetic modeling study of benzene pyrolysis with C2−C3 unsaturated hydrocarbons,” *Combust. Flame*, vol. 237, p. 111858, 2022, doi: https://doi.org/10.1016/j.combustflame.2021.111858.
[203] A. C. Eckbreth, *Laser Diagnostics for Combustion Temperature and Species*, 1st ed. London: CRC Press, 2022. doi: 10.1201/9781003077251.
[204] R. Di Sante, “Laser extinction technique for measurements of carbon particles concentration during combustion,” *Opt. Lasers Eng.*, vol. 51, no. 6, pp. 783–789, Jun. 2013, doi: 10.1016/j.optlaseng.2013.01.019.
[205] F. Douce, N. Djebaïli-Chaumeix, C.-E. Paillard, C. Clinard, and J. N. Rouzaud, “Pyrolysis Oxidation of Toluene behind Reflected Shock Waves,” Capri 12 – 16 september, 1999, pp. 251–258.
[206] O. Mathieu, “Etude cinétique de la formation des particules de suie dans les conditions de fonctionnement des moteurs automobiles,” 2006.
[207] W. D. Erickson, G. C. Williams, and H. C. Hottel, “Light scattering measurements on soot in a benzene□air flame,” *Combust. Flame*, vol. 8, no. 2, pp. 127–132, Jun. 1964, doi: 10.1016/0010-2180(64)90038-0.
[208] W. H. Dalzell and A. F. Sarofim, “Optical Constants of Soot and Their Application to Heat-Flux Calculations,” *J. Heat Transf.*, vol. 91, no. 1, pp. 100–104, Feb. 1969, doi: 10.1115/1.3580063.
[209] S. Chippett and W. A. Gray, “The size and optical properties of soot particles,” *Combust. Flame*, vol. 31, pp. 149–159, Jan. 1978, doi: 10.1016/0010-2180(78)90125-6.

[210] H. Bockhorn, F. Fetting, U. Meyer, R. Reck, and G. Wannemacher, “Measurement of the soot concentration and soot particle sizes in propane oxygen flames,” *Symp. Int. Combust.*, vol. 18, no. 1, pp. 1137–1147, 1981, doi: https://doi.org/10.1016/S0082-0784(81)80118-X.
[211] S. C. Lee and C. L. Tien, “Optical constants of soot in hydrocarbon flames,” *Eighteenth Symp. Int. Combust.*, vol. 18, no. 1, pp. 1159–1166, Jan. 1981, doi: 10.1016/S0082-0784(81)80120-8.
[212] H. Chang and T. T. Charalampopoulos, “Determination of the wavelength dependence of refractive indices of flame soot,” *Proc. R. Soc. Lond. Ser. Math. Phys. Sci.*, vol. 430, no. 1880, pp. 577–591, Sep. 1990, doi: 10.1098/rspa.1990.0107.
[213] A. Emelianov *et al.*, “Time and temperature dependence of carbon particle growth in various shock wave pyrolysis processes,” *Proc. Combust. Inst.*, vol. 30, no. 1, pp. 1433–1440, Jan. 2005, doi: 10.1016/j.proci.2004.08.155.
[214] A. Emelianov, A. Eremin, H. Jander, and H. Gg. Wagner, “To the Temperature Dependence of Carbon Particle Formation in Shock Wave Pyrolysis Processes,” *Z. Für Phys. Chem.*, vol. 217, no. 7, pp. 893–910, 2003, doi: 10.1524/zpch.217.7.893.20396.
[215] M. Aldén, J. Bood, Z. Li, and M. Richter, “Visualization and understanding of combustion processes using spatially and temporally resolved laser diagnostic techniques,” *Proc. Combust. Inst.*, vol. 33, no. 1, pp. 69–97, 2011, doi: https://doi.org/10.1016/j.proci.2010.09.004.
[216] C. Schulz, A. Dreizler, V. Ebert, and J. Wolfrum, “Combustion Diagnostics,” in *Springer Handbook of Experimental Fluid Mechanics*, C. Tropea, A. L. Yarin, and J. F. Foss, Eds. Berlin, Heidelberg: Springer Berlin Heidelberg, 2007, pp. 1241–1315. doi: 10.1007/978-3-540-30299-5_20.
[217] D. J. Lockwood, “Rayleigh and Mie Scattering,” in *Encyclopedia of Color Science and Technology*, R. Luo, Ed. Berlin, Heidelberg: Springer Berlin Heidelberg, 2015, pp. 1–12. doi: 10.1007/978-3-642-27851-8_218-1.
[218] M. Kerker, *The Scattering of Light and Other Electromagnetic Radiation*. Elsevier, 1969. doi: 10.1016/C2013-0-06195-6.
[219] R. A. Dobbins, R. J. Santoro, and H. G. Semerjian, “Analysis of light scattering from soot using optical cross sections for aggregates,” *Symp. Int. Combust.*, vol. 23, no. 1, pp. 1525–1532, 1991, doi: https://doi.org/10.1016/S0082-0784(06)80422-4.
[220] U. O. Ko¨ylu¨ and G. M. Faeth, “Optical Properties of Soot in Buoyant Laminar Diffusion Flames,” *J. Heat Transf.*, vol. 116, no. 4, pp. 971–979, Nov. 1994, doi: 10.1115/1.2911473.
[221] D. F. G. Dur??o, J. H. Whitelaw, and P. O. Witze, *Instrumentation for Combustion and Flow in Engines*. Dordrecht: Springer Netherlands, 1989. Accessed: Jun. 01, 2022. [Online]. Available: https://doi.org/10.1007/978-94-009-2241-9
[222] L. A. Melton, “Soot diagnostics based on laser heating,” *Appl. Opt.*, vol. 23, no. 13, pp. 2201–2208, Jul. 1984, doi: 10.1364/AO.23.002201.
[223] S. A. Reggeti, A. K. Agrawal, and J. A. Bittle, “Two-color pyrometry system to eliminate optical errors for spatially resolved measurements in flames,” *Appl. Opt.*, vol. 58, no. 32, pp. 8905–8913, Nov. 2019, doi: 10.1364/AO.58.008905.
[224] C. M. Megaridis and R. A. Dobbins, “Morphological Description of Flame-Generated Materials,” *Combust. Sci. Technol.*, vol. 71, no. 1–3, pp. 95–109, May 1990, doi: 10.1080/00102209008951626.
[225] R. L. Vander Wal and A. J. Tomasek, “Soot nanostructure: dependence upon synthesis conditions,” *Combust. Flame*, vol. 136, no. 1, pp. 129–140, Jan. 2004, doi: 10.1016/j.combustflame.2003.09.008.
[226] F. Douce, N. Djebaïli-Chaumeix, C.-E. Paillard, C. Clinard, and J.-N. Rouzaud, “Soot formation from heavy hydrocarbons behind reflected shock waves,” *Proc. Combust. Inst.*, vol. 28, no. 2, pp. 2523–2529, Jan. 2000, doi: 10.1016/S0082-0784(00)80668-2.
[227] T. Ishiguro, Y. Takatori, and K. Akihama, “Microstructure of diesel soot particles probed by electron microscopy: First observation of inner core and outer shell,” *Combust. Flame*, vol. 108, no. 1, pp. 231–234, Jan. 1997, doi: 10.1016/S0010-2180(96)00206-4.

[228] J. N. Rouzaud and A. Oberlin, “Structure, microtexture, and optical properties of anthracene and saccharose-based carbons,” *Carbon*, vol. 27, no. 4, pp. 517–529, 1989, doi: https://doi.org/10.1016/0008-6223(89)90002-X.
[229] O. Mathieu *et al.*, “Characterization of adsorbed species on soot formed behind reflected shock waves,” *Proc. Combust. Inst.*, vol. 31, no. 1, pp. 511–519, 2007, doi: https://doi.org/10.1016/j.proci.2006.07.190.
[230] Michael L. Norman and K.-H. A. Winkler, “Shock Waves versus Sound Waves,” *Los Alamos Sci.*, vol. 12, pp. 42–43, 1985.
[231] A. G. Gaydon and I. R. Hurle, *The Shock Tube in High-temperature Chemical Physics*. Reinhold Publishing Corporation, 1963. [Online]. Available: https://books.google.fr/books?id=5B46AQAAIAAJ
[232] G. Ben-Dor, O. Igra, and T. Elperin, *Handbook of Shock Waves, Three Volume Set: Three Volume Set*. Saint Louis: Elsevier Science, 2014. Accessed: Jul. 12, 2022. [Online]. Available: http://qut.eblib.com.au/patron/FullRecord.aspx?p=299438
[233] J. Kurian, “Shock Tube,” Dept. of Aerospace Engg., Indian Institute of Technology, Madras. Accessed: Aug. 11, 2022. [Online]. Available: https://dokumen.tips/documents/shock-tube-nptel.html?page=12
[234] “XV. On the thermodynamic theory of waves of finite longitudinal disturbance,” *Philos. Trans. R. Soc. Lond.*, vol. 160, pp. 277–288, Dec. 1870, doi: 10.1098/rstl.1870.0015.
[235] P. H. Hugoniot, “Sur la Propagation du Mouvement dans les Corps et Spécialement dans les Gaz Parfaits (deuxième partie),” *J. Ecole Polytech*, vol. 58, pp. 1–125, 1889.
[236] P. H. Hugoniot, “Sur la Propagation du Mouvement dans les Corps et Spécialement dans les Gaz Parfaits (première partie),” *J. Ecole Polytech*, vol. 57, pp. 3–97, 1887.
[237] A. Lifshitz, S. H. Bauer, and E. L. Resler, “Studies with a Single-Pulse Shock Tube. I. The *Cis—Trans* Isomerization of Butene-2,” *J. Chem. Phys.*, vol. 38, no. 9, pp. 2056–2063, May 1963, doi: 10.1063/1.1733933.
[238] F. Battin-Leclerc, J. M. Simmie, and E. Blurock, Eds., *Cleaner Combustion: Developing Detailed Chemical Kinetic Models*. London: Springer London, 2013. doi: 10.1007/978-1-4471-5307-8.
[239] R. S. Tranter, K. Brezinsky, and D. Fulle, “Design of a high-pressure single pulse shock tube for chemical kinetic investigations,” *Rev. Sci. Instrum.*, vol. 72, no. 7, pp. 3046–3054, Jul. 2001, doi: 10.1063/1.1379963.
[240] A. Lifshitz, “The single pulse shock tube: its Odyssey in chemical kinetics,” in *Shock Waves*, Z. Jiang, Ed. Berlin, Heidelberg: Springer Berlin Heidelberg, 2005, pp. 57–64. doi: 10.1007/978-3-540-27009-6_6.
[241] W. J. Hooker, “Testing Time and Contact-Zone Phenomena in Shock-Tube Flows,” *Phys. Fluids*, vol. 4, no. 12, p. 1451, 1961, doi: 10.1063/1.1706243.
[242] Z. Hong, D. F. Davidson, and R. K. Hanson, “Contact surface tailoring condition for shock tubes with different driver and driven section diameters,” *Shock Waves*, vol. 19, no. 4, pp. 331–336, Aug. 2009, doi: 10.1007/s00193-009-0212-z.
[243] N. M. Reddy, “An analytical method for real gas tailoring in a shock tube.,” *AIAA J.*, vol. 9, no. 12, pp. 2458–2460, Dec. 1971, doi: 10.2514/3.6532.
[244] A. R. Amadio, M. W. Crofton, and E. L. Petersen, “Test-time extension behind reflected shock waves using CO2–He and C3H8–He driver mixtures,” *Shock Waves*, vol. 16, no. 2, pp. 157–165, Dec. 2006, doi: 10.1007/s00193-006-0058-6.
[245] J. English, “What is fiber optics?,” *TechTarget*. https://www.techtarget.com/searchnetworking/definition/fiber-optics-optical-fiber (accessed Jul. 12, 2022).
[246] C. Y. Tang and Z. Yang, “Transmission Electron Microscopy (TEM),” in *Membrane Characterization*, Elsevier, 2017, pp. 145–159. doi: 10.1016/B978-0-444-63776-5.00008-5.
[247] F. Warmont, “Microscopie électronique en transmission.” http://www.icmn.cnrs-orleans.fr/?Microscopie-electronique-en&lang=fr

[248] H. J. Curran, P. Gaffuri, W. J. Pitz, and C. K. Westbrook, “A Comprehensive Modeling Study of n-Heptane Oxidation,” *Combust. Flame*, vol. 114, no. 1–2, pp. 149–177, Jul. 1998, doi: 10.1016/S0010-2180(97)00282-4.
[249] W. G. Appleby, W. H. Avery, and W. K. Meerbott, “Kinetics and Mechanism of the Thermal Decomposition of n-Heptane [1],” *J. Am. Chem. Soc.*, vol. 69, no. 10, pp. 2279–2285, Oct. 1947, doi: 10.1021/ja01202a012.
[250] M. Murata and S. Saito, “PREDICTION OF INITIAL PRODUCT DISTRIBUTION FROM n-PARAFFIN PYROLYSIS AT HIGHER TEMPERATURES BY CONSIDERING ETHYL RADICAL DECOMPOSITION,” *J. Chem. Eng. Jpn.*, vol. 7, no. 5, pp. 389–391, 1974, doi: 10.1252/jcej.7.389.
[251] M. Bajus, V. Veselý, P. A. Leclercq, and J. A. Rijks, “Steam Cracking of Hydrocarbons. 1. Pyrolysis of Heptane,” *Ind. Eng. Chem. Prod. Res. Dev.*, vol. 18, no. 1, pp. 30–37, Mar. 1979, doi: 10.1021/i360069a007.
[252] D. S. Aribike and A. A. Susu, “Kinetics and mechanism of the thermal cracking of n-heptane,” *Thermochim. Acta*, vol. 127, pp. 247–258, May 1988, doi: 10.1016/0040-6031(88)87501-4.
[253] D. S. Aribike and A. A. Susu, “Mechanistic modeling of the pyrolysis of n-heptane,” *Thermochim. Acta*, vol. 127, pp. 259–273, May 1988, doi: 10.1016/0040-6031(88)87502-6.
[254] K. K. Pant and D. Kunzru, “Pyrolysis of n-heptane: kinetics and modeling,” *J. Anal. Appl. Pyrolysis*, vol. 36, no. 2, pp. 103–120, Jun. 1996, doi: 10.1016/0165-2370(95)00925-6.
[255] T. J. Held, A. J. Marchese, and F. L. Dryer, “A Semi-Empirical Reaction Mechanism for n-Heptane Oxidation and Pyrolysis,” *Combust. Sci. Technol.*, vol. 123, no. 1–6, pp. 107–146, Jan. 1997, doi: 10.1080/00102209708935624.
[256] D. F. Davidson, M. A. Oehlschlaeger, and R. K. Hanson, “Methyl concentration time-histories during iso-octane and n-heptane oxidation and pyrolysis,” *Proc. Combust. Inst.*, vol. 31, no. 1, pp. 321–328, Jan. 2007, doi: 10.1016/j.proci.2006.07.087.
[257] J. P. Chakraborty and D. Kunzru, “High pressure pyrolysis of n-heptane,” *J. Anal. Appl. Pyrolysis*, vol. 86, no. 1, pp. 44–52, Sep. 2009, doi: 10.1016/j.jaap.2009.04.001.
[258] S. Garner, R. Sivaramakrishnan, and K. Brezinsky, “The high-pressure pyrolysis of saturated and unsaturated C7 hydrocarbons,” *Proc. Combust. Inst.*, vol. 32, no. 1, pp. 461–467, 2009, doi: 10.1016/j.proci.2008.06.217.
[259] P. Zámostný, Z. Bělohlav, L. Starkbaumová, and J. Patera, “Experimental study of hydrocarbon structure effects on the composition of its pyrolysis products,” *J. Anal. Appl. Pyrolysis*, vol. 87, no. 2, pp. 207–216, Mar. 2010, doi: 10.1016/j.jaap.2009.12.006.
[260] S. H. Pyun, W. Ren, D. F. Davidson, and R. K. Hanson, “Methane and ethylene time-history measurements in n-butane and n-heptane pyrolysis behind reflected shock waves,” *Fuel*, vol. 108, pp. 557–564, Jun. 2013, doi: 10.1016/j.fuel.2012.12.034.
[261] K. Yasunaga, S. Etoh, H. Yamada, H. Oshita, and Y. Hidaka, “Modeling and Experimental Study on Pyrolysis of Isooctane and *n* -Heptane behind Reflected Shock Waves,” *Chem. Lett.*, vol. 47, no. 6, pp. 747–750, Jun. 2018, doi: 10.1246/cl.180154.
[262] K. Yasunaga, H. Yamada, H. Oshita, K. Hattori, Y. Hidaka, and H. Curran, “Pyrolysis of n-pentane, n-hexane and n-heptane in a single pulse shock tube,” *Combust. Flame*, vol. 185, pp. 335–345, Nov. 2017, doi: 10.1016/j.combustflame.2017.07.027.
[263] X. Li, Z. Ma, E. Lv, Y. Dong, and X. Wang, “Experimental and kinetic study of hydrocarbon fuel pyrolysis in a shock tube,” *Fuel*, vol. 304, p. 121521, Nov. 2021, doi: 10.1016/j.fuel.2021.121521.
[264] J. A. Miller and S. J. Klippenstein, “The Recombination of Propargyl Radicals and Other Reactions on a C6H6 Potential,” *J. Phys. Chem. A*, vol. 107, no. 39, pp. 7783–7799, Oct. 2003, doi: 10.1021/jp030375h.
[265] H. Jin *et al.*, “A chemical kinetic modeling study of indene pyrolysis,” *Combust. Flame*, vol. 206, pp. 1–20, Aug. 2019, doi: 10.1016/j.combustflame.2019.04.040.
[266] W. Sun, A. Hamadi, S. Abid, N. Chaumeix, and A. Comandini, “An experimental and kinetic modeling study of phenylacetylene decomposition and the reactions with acetylene/ethylene under

shock tube pyrolysis conditions," *Combust. Flame*, vol. 220, pp. 257–271, Oct. 2020, doi: 10.1016/j.combustflame.2020.06.044.
[267] K. Wang, S. M. Villano, and A. M. Dean, "Fundamentally-based kinetic model for propene pyrolysis," *Combust. Flame*, vol. 162, no. 12, pp. 4456–4470, Dec. 2015, doi: 10.1016/j.combustflame.2015.08.012.
[268] A. E. Long *et al.*, "Pressure dependent kinetic analysis of pathways to naphthalene from cyclopentadienyl recombination," *Combust. Flame*, vol. 187, pp. 247–256, Jan. 2018, doi: 10.1016/j.combustflame.2017.09.008.
[269] A. J. Vervust *et al.*, "Detailed Experimental and Kinetic Modeling Study of Cyclopentadiene Pyrolysis in the Presence of Ethene," *Energy Fuels*, vol. 32, no. 3, pp. 3920–3934, Mar. 2018, doi: 10.1021/acs.energyfuels.7b03560.
[270] W. Sun, A. Hamadi, S. Abid, N. Chaumeix, and A. Comandini, "A comprehensive kinetic study on the speciation from propylene and propyne pyrolysis in a single-pulse shock tube," *Combust. Flame*, vol. 231, p. 111485, Sep. 2021, doi: 10.1016/j.combustflame.2021.111485.
[271] J. X. J. Zhang and K. Hoshino, "Optical Transducers," in *Molecular Sensors and Nanodevices*, Elsevier, 2014, pp. 233–320. doi: 10.1016/B978-1-4557-7631-3.00005-3.
[272] M. Frenklach, S. Taki, and R. A. Matula, "A conceptual model for soot formation in pyrolysis of aromatic hydrocarbons," *Combust. Flame*, vol. 49, no. 1–3, pp. 275–282, Jan. 1983, doi: 10.1016/0010-2180(83)90170-0.
[273] M. Frenklach, S. Taki, M. Durgaprasad, and R. Matula, "Soot formation in shock-tube pyrolysis of acetylene, allene, and 1,3-butadiene☆," *Combust. Flame*, vol. 54, no. 1–3, pp. 81–101, Dec. 1983, doi: 10.1016/0010-2180(83)90024-X.
[274] T. Wang, R. Matula, and R. Farmer, "International Symposium on Combustion, 18th, 1980," *Combust. Inst. Pittsburgh PA*, p. 1149, 1981.
[275] B. S. Haynes and H. Gg. Wagner, "Soot formation," *Prog. Energy Combust. Sci.*, vol. 7, no. 4, pp. 229–273, Jan. 1981, doi: 10.1016/0360-1285(81)90001-0.
[276] H. Mätzing and H. Gg. Wagner, "Measurements about the influence of pressure on carbon formation in premixed laminar C2H4-air flames," *Symp. Int. Combust.*, vol. 21, no. 1, pp. 1047–1055, Jan. 1988, doi: 10.1016/S0082-0784(88)80335-7.
[277] H. Böhm, ChR. Feldermann, Th. Heidermann, H. Jander, B. Lüers, and H. Gg. Wagner, "Soot formation in premixed C2H4-air flames for pressures up to 100 bar," *Symp. Int. Combust.*, vol. 24, no. 1, pp. 991–998, Jan. 1992, doi: 10.1016/S0082-0784(06)80117-7.
[278] V. G. Knorre, D. Tanke, Th. Thienel, and H. Gg. Wagner, "Soot formation in the pyrolysis of bezene/acetylene and acetylene/hydrogen mixtures at high carbon concentrations," *Symp. Int. Combust.*, vol. 26, no. 2, pp. 2303–2310, 1996, doi: 10.1016/S0082-0784(96)80058-0.
[279] F. Douce, "Etude de la formation des particules de suie à partir de constituants représentatifs du gazole," Université d'Orléans, 2011. [Online]. Available: http://www.theses.fr/2001ORLE2022
[280] R. J. Kee *et al.*, "CHEMKIN collection, release 3.6, reaction design," *Inc San Diego CA*, vol. 20, no. 0, p. 0, 2000.
[281] H. Richter, S. Granata, W. H. Green, and J. B. Howard, "Detailed modeling of PAH and soot formation in a laminar premixed benzene/oxygen/argon low-pressure flame," *Proc. Combust. Inst.*, vol. 30, no. 1, pp. 1397–1405, Jan. 2005, doi: 10.1016/j.proci.2004.08.088.
[282] J. M. Mateos Pérez and J. Pascau, *Image processing with imageJ: discover the incredible possibilities of ImageJ, from basic image processing to macro and plugin development*, 1. publ. Birmingham: Packt Publishing, 2013.
[283] I. Gatan, "DigitalMicrograph 3.4 User's Guide," Pleaseton, CA, Nov. 1999. [Online]. Available: https://www.gatan.com/installation-instructions
[284] W. Pejpichestakul *et al.*, "Examination of a soot model in premixed laminar flames at fuel-rich conditions," *Proc. Combust. Inst.*, vol. 37, no. 1, pp. 1013–1021, Jan. 2019, doi: 10.1016/j.proci.2018.06.104.

[285] C. Shao, G. Kukkadapu, S. W. Wagnon, W. J. Pitz, and S. M. Sarathy, “PAH formation from jet stirred reactor pyrolysis of gasoline surrogates,” *Combust. Flame*, vol. 219, pp. 312–326, 2020, doi: https://doi.org/10.1016/j.combustflame.2020.06.001.
[286] K. Zhang *et al.*, “An updated experimental and kinetic modeling study of n-heptane oxidation,” *Combust. Flame*, vol. 172, pp. 116–135, Oct. 2016, doi: 10.1016/j.combustflame.2016.06.028.